Université Joseph Fourier

Thèse

présentée par

Lucia Alianelli

Pour obtenir le titre de docteur

de l'Université Joseph Fourier de Grenoble

Specialité: **Physique**

Characterization and modelling of imperfect crystals for thermal neutron diffraction.

Soutenance publique le 20 novembre 2002

Composition du Jury :

Pierre Bastie, Président
Rober McGreevy, Rapporteur
Francesco Sacchetti, Rapporteur
Marc Bée, Directeur de Thèse
Ian Anderson, Tuteur
Roberto Felici, Tuteur
Manuel Sánchez del Río, Tuteur

Acknowledgments

I would like first of all to thank Manuel Sánchez del Río (ESRF). During the time of this thesis, he has been always available for guiding me in the scientific and technical tasks. He has transmitted to me his experience, enthusiam and original ideas that have been decisive for the accomplishment of this thesis.

Many thanks to Roberto Felici (INFM) for his continuous support, his scientific guidance, and for all frequent and helpful advices and ideas on how to improve my work.

It is great pleasure to thank Ian Anderson. He has played a fundamental role in many aspects: he was at the origin of the idea that has led to this thesis. He has conducted negotiations and administrative tasks that created the position that I benefit. He has welcomed me to the Neutron Optics Group of the Institut Laue Langevin. I fully acknowledge that he always found the time to help me whenever I needed. And finally, he always teached me how to work in a very rigorous way, organise my time, and to focus on fundamental aspects.

I wish to thank professor Marc Bée, who has accepted to follow my work as thesis director at the Université Joseph Fourier and has often listened to my reports without complaining for my bad French.

I acknowledge professor Robert McGreevy who has shown interest in our study, carefully read the thesis and accepted to be *rapporteur*.

I am indebted to the *rapporteur* professor Francesco Sacchetti for the discussions about some important thesis subjects.

Special thanks to Pierre Bastie for accepting to be the *président du jury*.

I acknowledge the complete staff of the Monochromator Laboratory of the ILL. I am grateful to Bernard Hamelin and Pierre Courtois for providing the samples, for allowing the access to the T13A-C instruments and the hard x-ray diffractometer and for the frequent discussions about crystals and experiments. Many thanks to Catherine Menthonnex, Erwin Hetzler, Roland Hehn, Ali Elaazzouzi, Michel Berneron and Alain Escoffier for their technical assistance and for welcoming me with kindness in every occasion. I wish to thank the members of the Service for Neutron Optics and Françoise Giraud for having warmly welcomed me since my first days at the ILL.

It is a pleasure to thank Alexandre Ivanov, who gave me the possibility to measure the temperature dependent reflectivity of a copper crystal on IN1 and who introduced me to the theory of phonon scattering.

Thanks to professors F. Frontera and M. Gambaccini ant their colleagues from Ferrara University for lending us the graphite sample and for the collaboration during one of the experiments at BM5.

I am grateful to the ESRF, in particular the staff of the ID15A and BM5 beamlines for their professional help and assistance during the synchrotron experiments and their preparation.

Many thanks to Giovanni Bruno (who has also read and commented the thesis during the last rainy August in Grenoble), J. Saroun and Th. Pirling for providing me with material on the Strain Imager instrument and for discussions on the simulations.

Thanks also to the many friends and kind people I have met here, those who have left and those who are still here: they have contributed to the happiness of these three years spent in Grenoble.

Last but not least, I fully acknowledge the organizations that funded my thesis: the Istituto Nazionale per la Fisica della Materia and the Institut Laue Langevin.

I finally thank the SCANS RTD network (supported by the Access to Research Infrastructures activity, Improving Human Potential programme, of the European Commission under contract HPRI-CT-1999-50013) that supports the continuation of this work.

Un pensiero speciale a mamma, a papà e a tutti quelli che sono riusciti a farmi sentire vicina nonostante la distanza.

Contents

Introduction

Les sources de neutrons prévues pour le nouveau millénaire fourniront un flux sans précédent qui pourra être utilisé dans de vastes domaines, de la recherche fondamentale à l'industrie. L'instrumentation liée à ces sources inclut des éléments optiques complexes et chers. Par conséquent, il est souhaitable de modéliser et simuler exactement ces dispositifs afin d'optimiser leur fonctionnement et coût.

Les neutrons sont une sonde fondamentale pour l'étude de la physique de la matière condensée, de la chimie et de la biologie. Les arrangements des noyaux dans la matière sont étudiés dans des expériences de diffraction en analysant la dépendance angulaire du faisceau de neutrons diffracté par l'échantillon. Le diffractomètre le plus simple est un instrument à deux axes : le cristal monochromateur, placé sur le premier axe, sélectionne l'énergie ; le mouvement du deuxième axe (axe de l'échantillon et/ou du détecteur) permet d'enregistrer les spectres angulaires.

Dans les expériences en temps de vol, la direction du faisceau incident est fixe et la monochromatisation est achevée par des dispositifs mécaniques, comme des *choppers*. Ces dispositifs sélectionnent des bandes de longueur d'ondes en exploitant la vitesse réduite des neutrons thermiques (liée à leur énergie).

Les spectres énergétiques des excitations dans la matière solide et molle peuvent être étudiés par la dispersion non élastique et quasiélastique des neutrons : un spectromètre typique est le *trois axes* dans lequel le troisième axe correspond au cristal analyseur. Il y a également des spectromètres basés sur l'utilisation soit de cristaux soit d'éléments à temps de vol.

Un grand nombre d'instruments de neutrons sont équipés avec des collimateurs et des cristaux. Les collimateurs sont des assemblages faits avec les lames absorbantes, qui réduisent la divergence et améliorent ainsi la résolution angulaire. Le cristaux monochromatisent les faisceaux de neutrons selon la loi de Bragg $\lambda = 2\, d_h \sin\theta_B$.

Les cristaux focalisants, en outre, augmentent l'intensité à l'échantillon. Des méthodes plus spécifiques sont employées quand une résolution d'énergie plus élevée est nécessaire. La monochromatisation d'un faisceau par des cristaux en rétro-diffusion permet une résolution d'énergie de ~ 1 μeV. La technique de l'écho de spin, basée sur la mesure du déphasage entre les ondes de deux états de rotation du neutron dans un champ magnétique, permet une résolution d'énergie de ~ 1 neV.

Le spin de 1/2 des neutrons implique qu'ils peuvent être employés pour des investigations du spin nucléaire. D'ailleurs, le moment magnétique du neutron interagit avec le moment magnétique des électrons permettant la mesure des structures et des excitations

magnétiques. Pour ces expériences, les dispositifs utilisés pour détecter la polarisation des faisceaux sont les suivants : cristaux magnétiques de Heusler, champs magnétiques non homogènes, multicouches magnétiques, filtres d'hélium basés sur l'absorption sélective des neutrons dans des états de spin différents.

Les sources de neutrons produisent des faisceaux isotropes et dans des domaines de longueur d'ondes relativement grands. Ces faisceaux doivent être transportés, puis monochromatisés et collimatés. Le degré de monochromatisation et de collimation dépend de la résolution et de l'intensité nécessaires à l'expérience. Une intensité élevée et une bonne résolution sont deux conditions contradictoires : par exemple, une bonne résolution angulaire peut être réalisée en utilisant des collimateurs qui réduisent l'intensité. Dans beaucoup de cas, le dessin final de l'instrument est un compromis entre l'optimisation de l'intensité et de la résolution.

La technique la plus utilisée pour choisir une bande $\Delta\lambda$ de longueur d'onde à partir du faisceau incident est basée sur la diffraction de Bragg par un cristal. Il y a également des monochromateurs faits par des multicouches : ils produisent des réflectivités intégrées élevées et sont employés particulièrement quand des paramètres de maille élevés sont nécessaires. Les multicouches ont l'avantage de pouvoir être fabriqués avec des paramètres de maille et, dans certains cas, des matériaux plus adaptées au besoins expérimentaux.

Cette discussion montre qu'il y a une variété d'instruments de neutrons dans lesquels la combinaison d'éléments différents peut être très complexe. Le grand effort technique et économique requis pour construire ou remplacer un instrument exige de connaître précisément la fonction de chaque élément optique. D'ailleurs, l'amélioration (en termes d'intensité, par exemple) d'un élément optique, tel qu'un cristal ou un multicouche, ne peut être comparé à celui nécessaire pour augmenter l'intensité de la source. Ce sont les raisons de l'importance de modéliser les éléments optiques de neutrons.

Un des objectifs de cette thèse est celui de contribuer à la description et à la simulation des instruments de neutrons, en particulier de cristaux imparfaits qui sont habituellement utilisés comme monochromateurs ou analyseurs. On sait que la réflectivité expérimentale de cristaux réels est souvent en désaccord avec celle calculée en utilisant les modèles analytiques standard. Notre but est de : 1) étudier les méthodes existantes et définir leurs limites d'applicabilité pour calculer la diffraction par des cristaux réels. Ceci implique un travail expérimental pour la mesure des profils de réflectivité dans les meilleures conditions possibles en termes de qualité du faisceau incident; 2) développer de nouveaux algorithmes de simulation Monte Carlo donnant une description réaliste de ces cristaux.

Chapter 1

Introduction

Neutron sources under development for the new millennium will provide unprecedented neutron beam fluxes for applications covering a wide range of pure and applied science and industrial research. The instrumentation associated with these sources includes complex and expensive optical elements. Therefore, it is highly desirable to accurately model and simulate these devices in order to achieve an optimum design in terms of performance and cost. At the same time a big effort in refurbishing instruments is being made in some neutron laboratories operating "old" neutron sources. One example is the ILL Millenium Programme [1] in which the renewal of existing instruments and the building of new ones is upgrading the facility with the most advanced neutron optics technology (supermirror guides, polarizing devices, focusing monochromators).

Neutrons are a fundamental probe for the study of condensed matter physics, chemistry and biology. The spatial arrangements of nuclei in ordered and disordered matter is investigated in *diffraction experiments* by studying the angular dependence of the neutron beam scattered by the sample. The most simple diffractometer is a two axes instrument in which the crystal monochromator, placed on the first axis, selects the energy and the angular scans are recorded by moving the sample and/or detector (second axis). In *time of flight instruments* the incoming beam angle is fixed and the beam is monochromated by a mechanical device, exploiting the fact that the low speed of thermal neutrons (linked to energy) allows selection of energy using rotating choppers. The energy spectra of excitations in solid and soft matter can be investigated with *inelastic and quasielastic scattering*: a typical spectrometer is the triple axis instrument in which the third axis holds the crystal analyser. There are also spectrometers based on the combination of crystal and time of flight optical elements. Almost all neutron instruments are equipped with devices such as collimators and crystals. Collimators are made of thin channels with absorbing blades, which reduce divergence and thus improve the angular resolution. Crystals monochromate the neutron beam according to the Bragg's law $\lambda = 2\, d_H \sin\theta_B$,

with d_H being the d-spacing of the diffracting planes and θ_B the Bragg angle. Focusing crystals, in addition, increase the intensity at the sample. More specific methods are used when high energy resolution is needed. Beam monochromatization by crystals at almost normal incidence allows high energy resolution, based on the fact that the wavelength range selected by the crystal is $\Delta\lambda/\lambda = \Delta d_H/d_H + \cot\theta_B \Delta\theta \sim \Delta d_H/d_H$, thus giving a resolution of approximately ~ 1 μeV. The *spin-echo technique*, based on measurement of the phase shift between the waves of two spin states of the neutron in a magnetic field, allows an energy resolution of ~ 1 neV.

The neutron has a spin of 1/2 which implies that neutron scattering is spin dependent and can be used for investigations of nuclear spin. Moreover, the neutron magnetic moment interacts with the magnetic moment of electrons thus allowing the measure of magnetic structures and excitations. For these experiments, instrumentation aiming at modifying and detecting the polarization of the beams is used: Heusler magnetic crystals, inhomogeneous magnetic fields, magnetic multilayers and polarizing helium filters based on the selective absorption of neutrons with different spin states are some of the methods.

Neutron sources produce neutron beams with isotropic intensity distributions and with relatively large wavelength bands. These beams have to be transported and then monochromated and collimated before reaching the sample. The degree of monochromatization and collimation depends on the resolution and intensity needed for the experiment. High intensity and resolution are two contrasting requirements: for example high angular resolution can be achieved using collimators which remove neutrons from the beam thus decreasing intensity. In many cases the instrument design is a compromise between the optimization of intensity and resolution. The most widespread technique used for selecting a wavelength band $\Delta\lambda$ from the incident beam is based on Bragg diffraction from a given set of lattice planes in a single crystal. There are also monochromators made of multilayers: they show high integrated reflectivities and are used especially when high d-spacings are needed. The advantages which multilayers offer with respect to crystals is that they can be manufactured with d-spacings, and in some cases materials, which fit the experimental needs. Instruments exploiting the time of flight technique can be based on mechanical tools such as phased choppers and Fermi choppers.

This discussion shows that there are a variety of neutron instruments in which the combination of elements can be very complex. The large technical and economical effort needed to build or renew an instrument requires us to have a precise and accurate idea of the effect of each element on the neutron beam and the combination between them. Moreover, the cost needed for improving (in terms of intensity, for example) a given optical element such as a crystal or multilayer, cannot be compared with that needed to increase the source intensity. These are the principal reasons for the importance of modelling neutron optical elements.

One of the aims of this thesis is to contribute to the description and simulation of neutron instruments, in particular of the crystal element, which is usually the "heart" of a neutron instrument. It is known that the experimental reflectivity of real crystals often disagrees substantially with that calculated using standard analytical models. Our goal is twofold: 1) To study existing methods and define their limits of applicability to predict the diffracting properties of real crystals. This implies experimental work for recording reflectivity profiles in the best conditions in terms of incident beam. 2) Develop new Monte Carlo algorithms aimed at giving a description of reflectivity and related parameters as close as possible to the experimental values.

In the rest of this Chapter we will give a review of the general models used for describing optical elements (section 1.1) and then introduce the differences and complementarity between analytical, graphical and numerical methods. Section 1.2 is an introduction to non-perfect crystals and their use in neutron instrumentation: this thesis will be focused on them. Finally, in section 1.3, a short account of the development of ray-tracing packages for simulating complete neutron instruments is given.

An important part of this thesis looks into the detailed modelling of crystal monochromators and analyzers. In Chapter 2 we review the analytical models which describe diffraction and absorption by crystals and show typical reflectivity, transmission and absorption curves calculated using the computer codes that we have developed. From the practical point of view, these models have been implemented in a friendly computer environment, the software package XOP [2], and a dedicated version for neutron optics will be made available [3] to the scientific community.

In our opinion, modelling of a complete neutron instrument can be done in several stages: as a first step one can make a pre-calculation of the effect of the individual optical elements. For this, the *XOP for neutrons* code that we have developed, can help. It contains all the crystal models described in this thesis. More precise calculations are usually made by means of Monte Carlo methods: in Chapter 3 we present an original simulation tool for describing Bragg diffraction by crystals in a realistic way. The novelty of our method consists in the accurate microscopical description of the interaction of the "rays", representing the neutron beam, with the microscopic crystal regions. The difference with respect to other ray-tracing crystal modules is that our code calculates the full history of the rays and does not use any average or macroscopic law. Thus it is very realistic, allows an accurate control of all the calculation parameters and can also be used for crystals having any kind of distortion, for example inhomogeneities. In the same Chapter, applications of the possible uses of the code are given, for example the different behaviour of mosaic and bent crystals, or the calculation of important quantities such as multiple scattering. A full benchmarking of the code against analytical models is made for some well defined cases, with monochromatic and collimated incident beams. Our code can

represent a crystal module for instrument simulations, and we have used it for calculating the efficiency and resolution of the new Strain Imager instrument which is being built at the ILL. The resulting intensity and resolution, using a mosaic bent germanium crystal as monochromator, are summarised in Chapter 4. Another important feature of the code is that one can monitor the ray properties at any stage of the calculation, and it allows computation of images of the beam which can also be measured in an experiment, such as topographs. The comparison between the measured and simulated topographs for copper and germanium non-perfect crystals will be reported in Chapters 5 and 6.

In order to compare the calculations to the diffraction properties of real crystals we have studied experimentally the neutron and x-ray reflectivity of copper, germanium and graphite non-perfect crystals. In Chapters 5 and 6 we present the experimental results and discuss the advantages and disadvantages of current models for interpreting the results.

1.1 General methods for modelling neutron optical elements

A generic distinction between models for the description of neutron optical elements is obtained by classifying them as graphical, analytical and numerical.

The graphical methods allow an intuitive understanding and prediction of optical components: the so-called DuMond [4] diagrams used for the interpretation of wavelength-angle diagrams after diffraction by a system of two or more crystals and the acceptance diagrams describing the transfer function of other modules such as guides or phased choppers [5]. In Bragg diffraction, the wavelength λ and the reflection angle θ are to be considered as independent variables because of the non-zero width of the angular diffraction profile of crystals. Then, in a (λ, θ) diagram, the Bragg's law is represented by a band (or blurring), rather than a segment, due to the Darwin width or to mosaicity. This simple consideration makes the interpretation of the combined effect of two or more crystals very easy: the final diagram will be given by the intersection of the diagrams of two or more crystals.

Acceptance diagrams are widely used in the design of optical elements such as neutron guides and mechanical velocity selectors [5]: the transfer function of the optical element under consideration is written as a product of functions each depending on a variable or group of variables such as coordinates, angles, wavelength and time. This method is very well suited to the calculation of the beam passing through apertures or phased disk choppers in high resolution time of flight spectrometers. It has also been applied to the calculation of guide illumination by a given source and to the prediction of the

performance of converging and supermirror guides. This is also called the phase-space method as the analysis is done in a multidimensional space (coordinates, angles, energy). The DuMond analysis can be considered as a two dimensional acceptance diagram in the variables (λ, θ).

In the case of bent crystals, the graphical approach becomes a matrix-approach [6]: the neutron state before diffraction is specified by the spatial and angular coordinates and also by the relative wave-vector deviation; the neutron state after diffraction is found by simply applying the lens equation where the focal length is a function of the crystal bending radius, of the Bragg and asymmetry angles. This method uses the approximation that the coordinates describing the neutron state in the two planes (parallel and perpendicular to the diffraction plane) are not correlated. Moreover, the crystal thickness and mosaicity are neglected, as well as the aberrations (chromatic and geometrical) produced by the focusing surface.

Analytical methods are generally used for calculation of the resolution in neutron scattering experiments [7, 8]: the effect of Soller collimators, mosaic monochromators, and analysers are usually described by Gaussian functions with characteristic widths in the horizontal and vertical planes; the sample cross-section is then convoluted with these "transmission" functions.

Ray-tracing and Monte Carlo are numerical methods used when a more detailed description is needed both for designing or up-grading neutron instruments and when calculating the experimental resolution. Almost all simulation codes, which will be mentioned in the next section, work using the sequential ray-tracing method. The *source*, i.e. the starting point for the simulation, is generated by *random sampling* the ray distribution (in terms of energy, position and angles). The other elements are modelled assuming that the neutron tracks are linear (or parabolic, if gravity is included) segments between one element and the next. At each instrument stage, the neutron trajectory is modified according to a macroscopic law governing reflection/transmission/diffraction by this element.

Let us consider the simulation of diffraction by a mosaic crystal as represented in Fig. 1.1. The crystal is composed of an agglomeration of small perfect crystallites with their angular orientation following a distribution $W(\theta, \phi)$ not shown explicitly in the figure. The ray-tracing calculation of diffraction by this crystal uses a macroscopic approach [9, 10, 11]: 1) the particle penetration depth τ is sampled by a probability distribution depending on the secondary extinction and absorption depths; 2) the value of the angle θ formed by the Bragg planes and the emerging particle is sampled using the W distribution and considering that the Bragg's law must be satisfied; the emerging angle ψ is determined by θ and by the the asymmetry angle between the Bragg planes and the crystal surface; 3) the azimuthal angle ϕ is also calculated by using W, or a constant probability distribution if

the W distribution is isotropic, i.e. not dependent on ϕ; 4) finally the *probability* or *weight* of the emerging particle being diffracted is sampled from analytical formulas depending on the absorption coefficient, strenght of the reflection, Debye Waller factor etc.

The use of the Monte Carlo method for the mosaic crystal, sketched in Fig. 1.1 (right), does not require any assumption on the macroscopic laws mentioned above. Monte Carlo simulations can provide numerical solutions of the equations describing the transport of neutrons or x-rays in crystals. For example, this means that the *Darwin's equations*, that govern the reflectivity of mosaic crystals, can be numerically solved by using the Monte Carlo technique. The input parameters are the crystal geometrical and physical properties (size, set of Bragg planes, W distribution, size of the perfect domains and, if necessary, imperfections). The particle trajectory is followed step by step: each step represents the interaction with a small perfect crystallite and this interaction is governed by the laws of *dynamical diffraction*. We have discussed the two different approaches for the case of a mosaic crystal because this is usually the optical element that requires a full physical description in a neutron instrument. We have used the Monte Carlo method and developed an original computer code for mosaic crystals which also includes other kinds of deformation (i.e. bending). By definition, Monte Carlo methods permit modelling of a large range of phenomena that are difficult to describe otherwise. For example, in the case of crystals, the effect of inhomogeneities in the mosaic structure can be simulated. Our code will be extensively described in Chapter 3: it will be shown that it can be inserted as a *crystal module* into any neutron (and also x-ray) ray-tracing program. Moreover, it can be used for calculating other important parameters, such as the number of scattering events in a non-perfect crystal, which cannot be determined analytically. Knowledge of this quantity is important expecially, when computation of the crystal efficiency as a monochromator for high resolution instruments is needed.

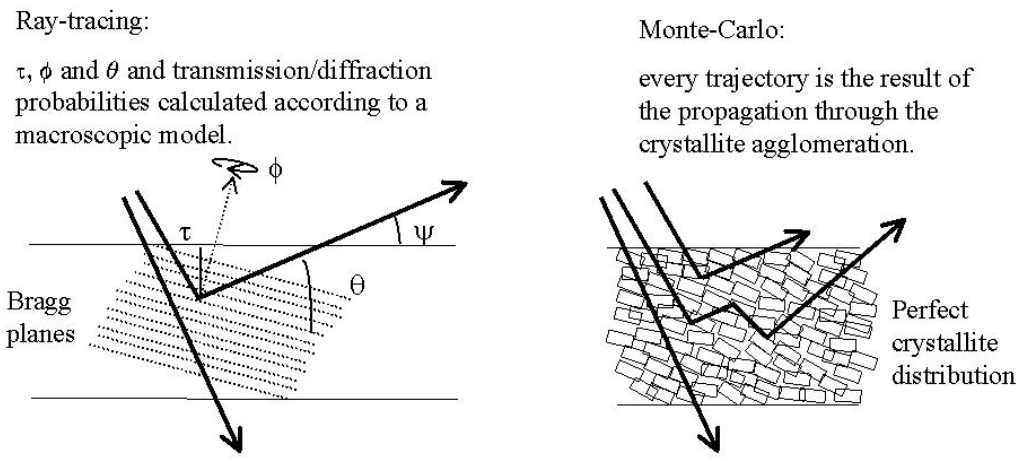

Figure 1.1: *Schematic representation of modelling diffraction by a mosaic crystal: ray-tracing (left) and Monte Carlo method (right).*

1.2 Crystals for neutron monochromators

The first requirement for the choice of material for a crystal monochromator is that the coherent scattering cross-section be the dominant part of the total cross-section and that other contributions such as incoherent scattering, nuclear absorption and inelastic processes, contributing to background and absorption, are negligible. Since relatively large crystals (volumes of about 50 cm^3) are needed, the use of isotopes is practically impossible because of the cost.

Another important parameter for the choice of material is the value of the d-spacing: the mosaic crystal reflectivity is proportional to the square of the scattering length density, so the unit cell volume has to be kept small, but at the same time the d-spacing has to be appropriate for the value of wavelength and suitable Bragg angles.

Perfect crystals are not suitable in most cases because of their narrow angular acceptance. Therefore, crystals with some kind of "imperfections" or "distortion" of the Bragg planes, have to be considered. The most common imperfections are those due to the so-called *mosaicity*, i.e. the misorientation with respect to the nominal direction of the crystal perfect blocks. In the next Chapters we will point out that, except for some materials such as highly oriented pyrolitic graphite, the mosaic structure of real crystals (usually artificially obtained) differs significantly from the homogeneous distributions assumed in theoretical models. The case of mosaic copper was pointed out in the 1970's by Schneider [12] and Freund [13] who used γ-rays for measuring the real mosaic distribution: they found that this was not a smooth Gaussian or Lorentzian distribution but rather an irregular one.

Among flat mosaic crystals, those used often are copper and highly oriented pyrolitic graphite: we will present some experimental results on their diffraction properties in Chapters 5 and 6. Beryllium is also a very good candidate as a neutron monochromator because of the small incoherent scattering and nuclear absorption cross sections, high coherent scattering length density and high Debye temperature. The drawbacks are that it is difficult to produce mosaic crystals, and its hcp structure makes its deformation behaviour very complex. Moreover, the toxicity of beryllium requires special care and equipment for the growth and preparation stages. However, beryllium crystals with suitable mosaicity have been obtained by assembling plastic deformed wafers [14].

Finally, bent crystals are used both for increasing the flux at the sample via spatial focusing and for achieving a better resolution via focusing in reciprocal space. However, phase-space volume conservation as stated by the Liouville theorem puts limitations on the use of focusing, which is suitable only for a limited number of samples investigated. When large samples are studied, and the resolution requirements are not so stringent, large copper

mosaic monochromators are preferred. Elastically bent perfect silicon monochromators have been implemented successfully in neutron diffraction, both for the measurement of strain in materials [15] and in triple axis instruments [16].

Bent perfect germanium would give higher relectivity than silicon and efforts are being made in several neutron laboratories to obtain plastically bent germanium. In Chapter 6 we shall present some results concerning a bent germanium crystal.

Other crystals are used in back-scattering geometry: one example is the calcium fluoride monochromator of IN13 at the ILL [17]. Natural mica is used for the monochromatization of cold neutrons [18] or as an analyzer in low-energy inelastic spectroscopy [19]. The neutron reflectivity of mica crystals with different compositions has been studied by Crow [20]. The large d-spacing allows their use as ultracold neutron monochromators. The presence of several orders of reflection having high structure factors allows the extension of the applicability range. Moreover, high quality bent crystals can be obtained [21].

In Chapters 5 and 6 the experimental results for a wide range of non-perfect crystal samples (copper, germanium and graphite) and their comparison with theory will be discussed. The aim of the experimental tests was to address the limitations in applicability of the theory and the differences between real and ideal crystals. The samples we used were of good quality, produced for use as parts of monochromators, and previously characterized by other techniques. Therefore they should produce results close to the best avalaible. Our experiments were performed with both neutrons and x-rays. As will be shown in Chapter 2, the equations governing neutron and x-ray Bragg diffraction by crystals, are the same. Moreover, the use of neutrons and x-rays produced by synchrotron radiation, give complementary information on the reflectivity and homogeneity of the crystals we have analyzed.

1.3 Computer simulation of neutron instruments. An overview.

The increasing number of neutron simulation programs produced recently reflects the efforts of the neutron community to push the performance of instruments, which are already in use or are under construction. Some of these codes are programmed for specific classes of instruments and they allow a precise computation of the response in terms of resolution and intensity: one example is the Restrax program [22] implemented for triple axis spectrometers. On the other hand, multi-purpose, Monte Carlo transport and ray-tracing codes provide a collection of optical elements which can be assembled to simulate any kind of instrument. The Los Alamos Monte Carlo code NISP [23], with its Web

library and interface [24], has been under development for about 20 years and provides a collection of optical elements and pre-defined instruments. The Vitess package [25, 10] is specially designed for the simulation of instruments at the future European Spallation Source. The McStas code [26, 27] is widely used, flexible and well supported.

The standard simulation tool used by the x-ray community is the Shadow code [28, 29]: it allows the simulation of a complete x-ray instrument and the detailed description of synchrotron sources, and of a large range of focusing and/or diffracting devices such as crystals, multilayers and gratings. In this thesis we have used the Shadow capability to generate sources with different geometries, then inserted our Monte Carlo codes for simulating non-perfect crystals, and finally used the powerful graphical tools implemented in ShadowVUI [2] for analyzing the simulation results.

The packages mentioned above are often used as black boxes whose output gives the user the response of a complex instrument in terms of neutron flux, angular and spectral resolution. In many cases, the ray-tracing or Monte Carlo calculations involve many elements (crystals, collimators, samples, detectors, etc.) and the final result is influenced by all these elements. It can be difficult to address the individual effect of each component when wanting to analyse the final result. The final accuracy depends on the precision used to describe the individual components. Therefore, a possible approximation in the simulation of one of the elements affects the accuracy of the result. Hence the code reliability depends on the models used for simulating the source and the components and also on the statistical error inherent to any Monte Carlo simulation. It may be difficult to explain the origin of some results and, more importantly, to address the problem of their reliability. Ray-tracing and Monte Carlo methods should be used for accurate computations, after considering the possible use of analytic or graphic approaches. It is crucial to verify the precision of the description of each optical element before modelling the complete instrument and understand the effect of each component.

The starting element in a simulation is the source. It contains all the information on the neutrons at a given starting region: energy, position, direction, probability of presence (or weight). The exact computation of the neutron spectra emitted by a reactor or a spallation source cannot be performed analytically. In practice, the source characteristics can be input in three ways: 1) From direct measurements of flux. 2) Using data coming from a Monte Carlo particle transport simulation of the reactor core, beam tube and shielding materials (an example is MCNP [30, 31], developed at the Los Alamos National Laboratory and containing neutron cross-sections in a wide energy range). 3) Using geometrical models, such as used in McStas (simple geometrical and energy distribution with an euristical time distribution in the time of flight case) and Vitess (Maxwellian distribution from the moderator and pulse shape function of input parameters). A development of a database containing experimental and calculated (e.g. Monte Carlo) sources would

be desirable for a ray-tracing simulation. Careful modelling of the source is also of great importance for the final result. The geometry and divergence of the neutron beam at the starting point of the instrument define the shape of the phase-space that will be transformed by the optical elements. Therefore, the simulation results depend on the source characteristics, and the problem of designing and optimising the instrument is reduced to preserving its *brightness* (i.e. the neutron flux per solid angle per unit of energy) whilst minimizing losses. The lack of analytical models describing neutron sources (reactors and spallation sources), and the poor quantity of data avalaible (measured and calculated), represent a limiting factor for the reliability of the simulation results. For this reason, a considerable effort should be made in the field. On the contrary, synchrotron sources (bending magnets, wigglers and undulators) can be exactly computed using analytical functions and ray-tracing is a well established method in this field.

Among the optical elements, one can distinguish those having a geometrical role (such as slits and Sollers) and others having more physical effects requiring a description in terms of reflectivity or transmission: multilayer and supermirror guides, filters, attenuators, crystal monochromators and analysers. The creation of a database containing the measured response of real optical elements would serve as a base for real reflectivities and a benchmark for ab-initio simulations (i.e. simulations in which the measured properties such as reflectivity or transmission profiles are inserted in the calculations instead of the theoretical profiles).

A debated question is the transport of polarized neutrons and the description of those elements which are concerned with the state of polarisation of the beam: Heusler monochromators, magnetic multilayers, polarising filters. A method for tracing thr neutron spin in a simulation program dealing with polarised neutron scattering is described by Seeger *et al.* [32] and makes use of the Bloch's equations for the precession of neutron spin in a magnetic field.

Simulation of the scattering properties of the sample is often required, both when calculating the instrument resolution or the flux which is expected to hit the detector. In order to simulate the sample one can simply use an effective source in its place or insert a detailed description of the $S(\mathbf{q}, \omega)$ as obtained by calculation or experiment. We recall that $S(\mathbf{q}, \omega)$ represents the probability for the neutron to undergo an energy change $\hbar\omega$ at a wave vector transfer $\mathbf{q}$, while interacting with the sample.

Finally, it is often desirable to include the detector resolving power and point spread function in the simulations. However, these effects can be calculated by post-processing the ideal results produced by ray-tracing.

Chapter 2

Analytical models for mosaic, gradient and bent crystals

This Chapter contains a review of the models describing neutron diffraction and absorption by perfect and non-perfect crystals. Our contribution in this field was the implementation of the analytical formulas for crystal reflectivities, transmission and absorption in numerical codes.

2.1 Introduction

There are two methods which may be used to account for the intensities observed in neutron and x-ray diffraction by crystals. The *kinematical theory* describes the transport of intensity in a crystal and treats the scattering from each volume element as being independent on that of other volume elements, except for incoherent power losses in that particular volume element. The *dynamical theory*, instead, completely describes the wave amplitude, and takes into account all wave interactions within the crystal volume elements: it considers the total wavefield inside a crystal while diffraction is taking place as a single entity. In other words, it accounts for the strong coupling between the incident and diffracted beams and the continuous energy exchange between them. Intuitively, the dynamical theory has to be used when the size of the perfect crystal or the strength of the reflection are not negligible. In other cases, as for example for fine powders, both theories lead to the same expression for the diffracted intensity, although *primary extinction* corrections (which are a dynamical diffraction effect) have to be included when measuring strong reflections. One of the drawbacks of the kinematical theory is that it violates energy conservation because it does not take into account multiple diffraction. So it is valid only in the very small crystal limit. If we denote by d the crystal thickness and

t_{ext} the primary extinction depth (which represents the perfect crystal depth over which the beam is attenuated of $1/e$ because diffraction is taking place), the condition for the kinematical thery to be valid is

$$d \ll t_{ext} \tag{2.1}$$

The value of t_{ext} ranges between 1 μm and 100 μm depending on the strength of the reflection. Soon after the discovery of the diffraction of x-rays by crystals it was found that the observed Bragg reflections in single crystals differed significantly from the theoretical predictions [33]. For example, the measured integrated intensities and widths of the Bragg peaks were larger than those expected for perfect crystals. It was recognised that the assumption that the crystals were perfect was incorrect and that instead real crystals had to be viewed as composed of *mosaic blocks*, slightly displaced and misoriented relative to one another. In the case of mosaic crystals, for the kinematical theory to be valid, the small mosaic blocks have to fulfill the condition in Eq. (2.1) and, at the same time, the crystal has to be small, less than 1 μm, in order to ensure that multiple reflections between different blocks are negligible. As the reflectivity of neutron crystal monochromators has to be saturated using multiple reflections, i.e. by increasing the crystal volume, the kinematical theory is not applicable to this case.

A mosaic crystal can be seen as an agglomeration of *perfect small crystallites*. The coherence effects which can be observed in the diffraction by perfect crystals are lost in the case of mosaic crystals because of the randomness in the crystallite distribution. The phenomenon of the attenuation of the beam due to diffraction by mosaic crystals is called *secondary extinction*. This attenuation is weaker than primary extinction in perfect crystals and involves larger crystal volumes. When describing diffraction by mosaic crystals (analytically or numerically), one has also to be able to model the effect of these crystallites. For example, a knowledge of their size is essential for computing the effect of primary extinction in the crystal. As a matter of fact, the presence of primary extinction competes with secondary extinction and therefore decreases the reflectivity. For these reasons we will briefly describe the dynamical theory of diffraction for perfect crystals in section 2.3. A more detailed mathematical derivation of the formulas describing the perfect crystal reflectivity is reported in the Appendix. In the following paragraphs the analytical reflectivity of non-perfect crystals, and some examples of their implementation in the XOP code, will be reported.

2.2 Neutron scattering by matter. Bragg scattering.

The dominant interactions between a neutron and an atom are the strong interaction with the nucleus and the magnetic dipole interaction with the unpaired electrons. In the following we will neglect the magnetic dipole interaction, because it is much smaller than the nuclear interaction and also because we will not deal with magnetic materials. The basic quantity measured in a neutron scattering experiment is the partial differential cross-section $d^2\sigma/d\Omega dE'$. This gives the fraction of neutrons of incident energy E and wave vector $\mathbf{k}$ scattered into an element of solid angle $d\Omega$ with an energy between E' and $E' + dE'$ and with wave vector $\mathbf{k}'$. The wavevector is related to the neutron mass and velocity according to the relation $\mathbf{k} = m\mathbf{v}/\hbar$. The energy is $E = (\hbar k)^2/2\,m$ or, as a function of the wavelength, $E = 81.8/\lambda^2$, with E and λ measured in meV and Å respectively. Thermal neutrons have energies of the order of a few tens of meV, hence they are used for measuring excitations in materials, having similar energies. Moreover, their wavelength, of the order of $\lambda \sim 1$ Å, are comparable to the interatomic distances. These properties make neutrons an excellent probe for the study of static structures and collective excitations.

The incident and scattered neutron states are represented by the two plane waves $\psi_{\mathbf{k}}$ and $\psi_{\mathbf{k}'}$. The direction of propagation of the scattered neutron is determined by the angles θ and ϕ as schematically shown in Fig. 2.1.

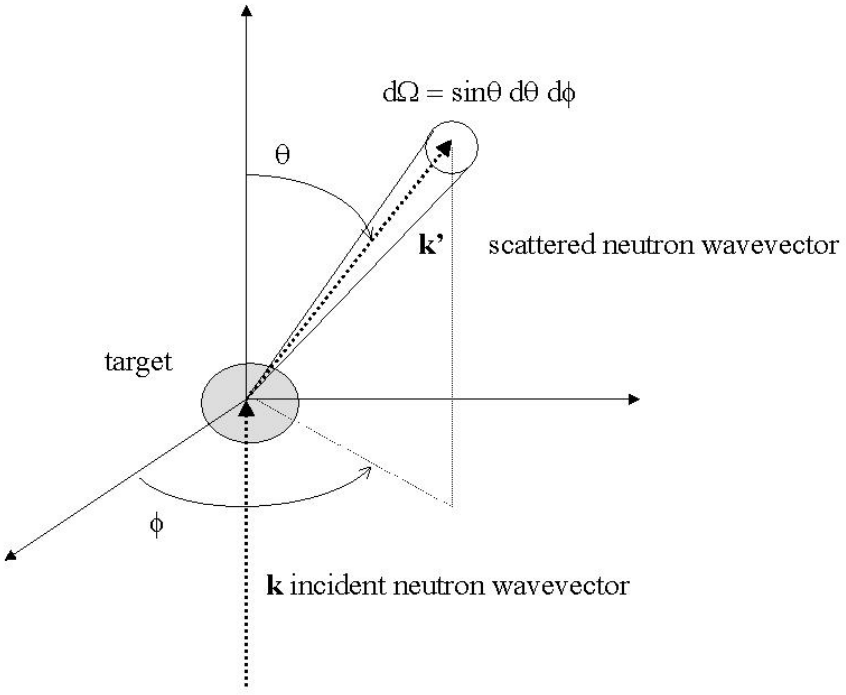

Figure 2.1: *Geometry of scattering.*

When no energy is transferred to the sample, the fraction of neutrons scattered in the solid angle $d\Omega$, is given by the *differential cross-section* $d\sigma$. $d\sigma$ is determined by the probability of transition $W_{k,k'}$ from one state described by $\psi_{\mathbf{k}}$ to another state $\psi_{\mathbf{k'}}$, both having the same energy E:

$$d\sigma = \frac{W_{k,k'}}{incident\, flux} \tag{2.2}$$

with $W_{k,k'}$ obtained by applying the Fermi's Golden rule [34]

$$W_{k,k'} = \frac{2\pi}{\hbar} | \int d\mathbf{r} \psi^*_{k'} \tilde{V} \psi_k |^2 \rho_{k'}(E) \tag{2.3}$$

In the last equation $\tilde{V}$ is the interaction potential which causes the transition and $\rho_{k'}(E)$ is the density of final scattering states per unit energy. Denoting by $|\mathbf{k}>$ and $|\mathbf{k'}>$ the neutron wave functions before and after scattering, having the necessary normalization (see [34] for details), the Eq. (2.3) becomes

$$\frac{d\sigma}{d\Omega} = | < \mathbf{k'} | \tilde{V} | \mathbf{k} > |^2 \tag{2.4}$$

The inelastic scattering is described by the partial differential cross-section. The neutron energy change is usually denoted by $\hbar\omega$. The state of the sample is denoted by the symbol $\tilde{\lambda}$, its energy is $E_{\tilde{\lambda}}$ and the state of the neutron and sample system is represented by a product state function $|\mathbf{k}\,\tilde{\lambda}>$. An approximated expression for the partial differential cross-section, obtained by applying the perturbation theory, is the following average:

$$\left(\frac{d^2\sigma}{d\Omega dE'} \right) = \frac{k'}{k} < \sum_{\tilde{\lambda}\,\tilde{\lambda}'} p_{\tilde{\lambda}} | < \mathbf{k}'\, \tilde{\lambda}' | \tilde{V} | \mathbf{k}\, \tilde{\lambda} > |^2 \delta \left(\hbar\omega + E_{\tilde{\lambda}} - E_{\tilde{\lambda}'} \right) > \tag{2.5}$$

where $p_{\tilde{\lambda}}$ is a weight for the state $\tilde{\lambda}$. The partial differential cross-section will be recalled when introducing, in section 2.6, the inelastic processes due to the vibration of the atoms in crystals.

Turning back to elastic events, and introducing the concept of *scattering amplitude* $f\,(\mathbf{k} - \mathbf{k'}) = - < \mathbf{k'} | \tilde{V} | \mathbf{k} >$ we can write

$$\frac{d\sigma}{d\Omega} = | f\,(\mathbf{k} - \mathbf{k'})\,|^2 \tag{2.6}$$

Since the neutron scattering by a bound nucleus is a very short range interaction, it can be considered to be isotropic and characterised by a single parameter b, called the

scattering length. The scattering length can be a complex quantity and its value depends on the particular nucleus involved in the scattering and on the relative orientation of the neutron and the nuclear spin (if it exists). The scattering length of different isotopes belonging to the same atomic species can have different values. The imaginary part of b represents absorption by the nucleus. Since the scattering is isotropic, the effective interaction between the neutron and the nucleus sitting at $\mathbf{R}$ is described by the Fermi pseudo-potential

$$\tilde{V}(\mathbf{r}) = \frac{2\pi\hbar^2}{m}\, b\, \delta(\mathbf{r} - \mathbf{R}) \tag{2.7}$$

Then, substituting into Eq. (2.4)

$$\frac{d\sigma}{d\Omega} = |b|^2 \tag{2.8}$$

and the total cross-section is

$$\sigma = 4\pi|b|^2 \tag{2.9}$$

We now consider a rigid array of N nuclei, each nucleus sitting at $\mathbf{R}_l$. It can be shown that, due to the dependence of b on the particular nucleus, isotope, or relative spin state, the cross-section can be written as

$$\left(\frac{d\sigma}{d\Omega}\right) = \left(\frac{d\sigma}{d\Omega}\right)_{coh} + \left(\frac{d\sigma}{d\Omega}\right)_{incoh} \tag{2.10}$$

where the *coherent scattering* cross-section $(d\sigma/d\Omega)_{coh}$ represents interference between the waves scattered from each nucleus

$$\left(\frac{d\sigma}{d\Omega}\right)_{coh} = |<b>|^2\, |\sum_l e^{i(\mathbf{k}-\mathbf{k}')\cdot\mathbf{R}_l}|^2 \tag{2.11}$$

and the *incoherent scattering* cross-section $(d\sigma/d\Omega)_{incoh}$ is given by

$$\left(\frac{d\sigma}{d\Omega}\right)_{incoh} = N\left(<|b|^2> - |<b>|^2\right) \tag{2.12}$$

Bragg scattering by a rigid lattice is usually described by the *unit cell structure factor* F_τ

$$F_\tau = \sum_m < b_m > \; e^{i\tau \cdot \mathbf{m}} \tag{2.13}$$

where τ is the reciprocal lattice vector and $\mathbf{m}$ the position vector of the atom m in the unit cell. The Bragg scattering cross-section is then

$$\left(\frac{d\sigma}{d\Omega}\right)_{coh} = N\frac{(2\pi)^3}{V_0}\sum_\tau \delta\left(\mathbf{k} - \mathbf{k}' - \tau\right)|F_\tau|^2 \tag{2.14}$$

with V_0 the unit cell volume.

Finally, the reduction in the number of neutrons that are forward scattered by a system of N nuclei, is determined by the absorption cross-section [35]

$$\sigma_{abs} = -N\frac{4\pi}{k} Im\ (b) \tag{2.15}$$

A collection of neutron cross-section and scattering lengths has been compiled by Sears and published in Neutron News [36]. We have used it as a database in the *XOP for neutrons* code in order to be able to calculate reflectivity and absorption by crystals.

2.3 The dynamical theory of neutron diffraction

The method commonly used to find the solutions for the neutron wave diffracted by a crystal has many similarities with X-rays. In the latter case the solutions for the electromagnetic field are found by solving Maxwell's equations after writing them in terms of the charge density, while for neutrons we determine the behaviour of the coherent wave ψ by solving the Schrödinger equation with an effective potential determined by the average coherent scattering length. The coherent wave representing neutron optical phenomena satisfies the one-body Schrödinger equation

$$\left[-\frac{\hbar^2}{2m}\Delta + v\left(\mathbf{r}\right)\right]\psi\left(\mathbf{r}\right) = E\psi\left(\mathbf{r}\right) \tag{2.16}$$

The optical potential $v\left(\mathbf{r}\right)$ represents the effective interaction of the neutron with the medium and is given in the elementary theory of dispersion by

$$v\left(\mathbf{r}\right) = \frac{2\pi\hbar^2}{m}\rho\left\langle b\left(\mathbf{r}\right)\right\rangle, \tag{2.17}$$

where $b(\mathbf{r})$ is the bound coherent scattering length and ρ is the number density. In the Appendix we give the solution of the previous equations using the formalism of Sears [35]. This is also called *Laue's method* and consists in finding a solution of Eq. (2.16) such that $\psi(\mathbf{r})$ and $\nabla\psi(\mathbf{r})$ are continuous at the crystal boundary and that $\psi(\mathbf{r})$ has the correct asymptotic behaviour at infinity. This method is approximated because the optical potential in Eq. (2.17) neglects local effects. One consequence of this approximation is that the attenuation of the coherent wave results from absorption by the nuclei and ignores diffuse scattering. The approximation is overcome using the *Ewald method*, which consists in applying a rigorous theory of dispersion for diffraction by a regular atomic lattice. This rigorous theory handles the microscopic multiple scattering (local-field problem), while the dynamical theory that we are going to analyse deals with the macroscopic multiple scattering. However, the corrections to Eq. (2.17) due to local field effects are of the order of 10^{-4} or less, and can be disregarded in most cases [35].

According to the formalism of Zachariasen [37] and Sears [35], as shown in the Appendix, the perfect crystal diffraction profiles are written in terms of two dimensionless parameters x and y whose values can be computed from the Eqs. (A.42). The x coefficient represents, apart from a constant, the ratio between the crystal thickness d and the primary extinction coefficient t_{ext}, whose values can range between 1 and 100 μm. The y coefficient is, apart from an additive constant, the ratio between the deviation from the exact Bragg angle $(\theta - \theta_B)$ and the *Darwin width* χ_D defined in the Appendix, which represents the angular range of total reflection for a perfect thick crystal and is of the order of 10 μ rads.

Thin crystal case. If the crystal thickness is much smaller than the primary extinction depth, i.e. if $d \ll t_{ext}$, the reflectivity, for both the Laue and Bragg case is

$$R(x,y) = \left(\frac{\sin xy}{y}\right)^2 \tag{2.18}$$

The result of the implementation of this theory in XOP is shown in Fig. 2.2: the figure shows the neutron reflectivity, versus $(\theta - \theta_B)$, of a perfect Si $< 111 >$ crystal, 5 μm thick, in Bragg symmetric geometry with $\lambda = 1.8$ Å.

It can be seen that, if the crystal is so thin that primary extinction can be neglected, the integrated reflectivity I_R is proportional to the crystal volume δV, and to the scattering factor Q:

$$I_R = Q\,\delta V \tag{2.19}$$

with:

$$Q = \lambda^3 F_{hkl}^2 / \left(V_0^2 \sin 2\theta_B \right) \tag{2.20}$$

with λ representing the wavelength, F_{hkl} the structure factor and V_0 the unit cell volume. The result in Eq. (2.19) is valid when the limited crystal thickness and/or structure factor make primary extinction negligible. Hence the decrease of the amplitude of the incident beam is negligible and the crystal is supposed to be uniformely bathed by radiation. This result is also valid for mosaic crystals: in this case, however, the limits of validity are larger, because of the more extended volume concerned by diffraction and secondary extinction.

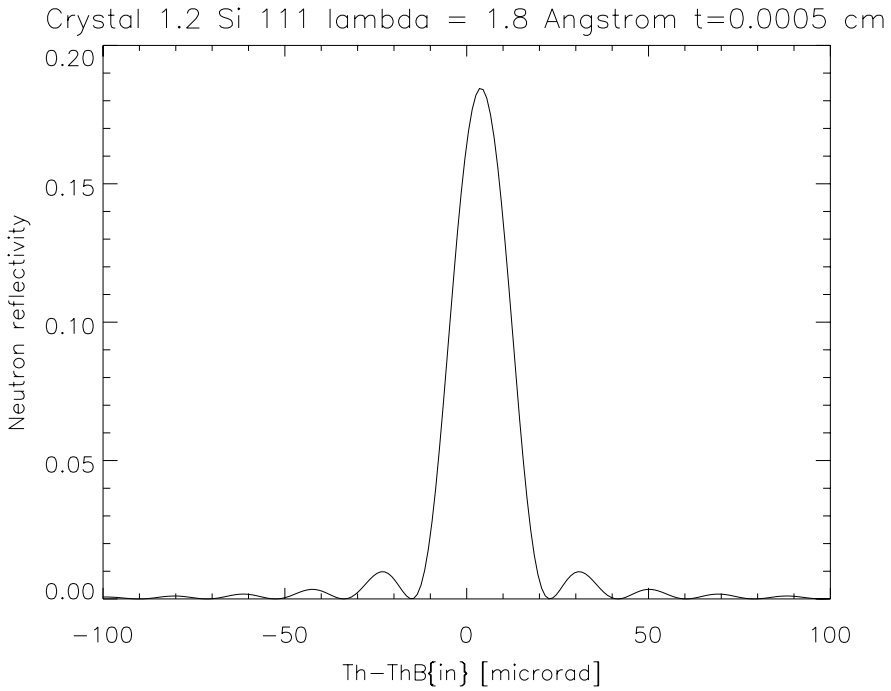

Figure 2.2: *Thin perfect crystal reflectivity: Si <111> in Bragg symmetric geometry at* $\lambda = 1.8$ *Å,* $d = 5$ μm.

Thick crystal case. If the crystal is thick, i.e. $d \gg t_{ext}$, the reflectivity is non zero in a small interval $|y| \leq 1$, or $|\theta - \theta_B| \leq \chi_D \sim 10$ μ rad. As reported in Fig. 2.3, $R(x, y)$ has a very narrow peak and oscillates very rapidly as a function of y. By averaging these oscillations, one can retrieve what would be the measured reflectivity profile of a perfect crystal. The result is that for $x \gg 1$, in Bragg geometry, the reflectivity is equal to 1 for $|y| \leq 1$. This peak width is equal to the *Darwin width*. In the Laue case the reflectivity has a Lorentzian shape with a height equal to 0.5 and a FWHM equal to χ_D. The oscillations appearing in the figure are due to the so-called *Pendellösung interference*: the energy flow of the wave field beneath the crystal surface changes periodically because there is an energy transfer between the forward diffracted and the diffracted wave. Thus this effect

can be observed when absorption is weak. The period of the oscillations is related to χ_D and to the product between the crystal thickness d and the absorption coefficient μ. The phenomenon of *primary extinction*, which we will often mention in the following Chapters, is the total reflection of neutrons or x-rays in the narrow angular range around the peak of the diffraction profile, with a consequent rapid exponential decay of the wave in the crystal.

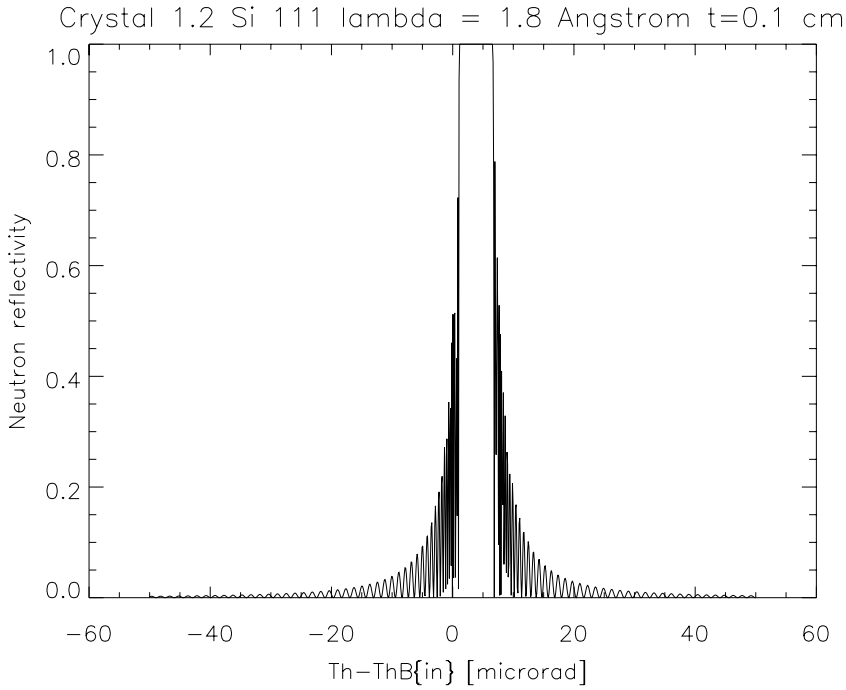

Figure 2.3: *Perfect crystal reflectivity: Si <111> in Bragg symmetric geometry at $\lambda = 1.8$ Å, $d = 1$ mm.*

Anomalous absorption. This effect, also called *Borrmann effect*, was first observed by Borrmann in 1943 [38]: a thick perfect crystal with large absorption, $\mu d \gg 1$, set for x-ray diffraction in Laue symmetric geometry, showed two spots on a photographic film: one corresponding to the diffracted beam and the other in the direction of the incident beam, i.e. separated by $2\theta_B$ with respect to the first beam. The two peaks were found to have comparable intensity. It was clear that the second spot was due to diffraction and was called the *forward diffracted beam*. The reason for this is the presence in the crystal of a standing wave with one wave component having nodes at the Bragg planes and another having antinodes. This means that the absorption of this second component is zero. It can be seen analytically that the standing wave patterns are parallel to the diffracting planes: the absorption by a given atom is proportional to the intensity of the neutron wave at that atom, then if the nodal planes are coincident with the diffracting planes, absorption is very much decreased.

Parasitic multiple Bragg scattering. Simultaneous diffraction occurs when a single

crystal is orientated in a neutron or x-ray monochromatic beam so that two, or more, sets of planes simultaneously satisfy Bragg's law. This can be observed experimentally when the crystal is orientated to diffract from a particular set of Bragg planes, and is rotated slowly around the the diffraction vector: changes in the intensity can be observed because the Bragg's law can be simultaneously satisfied for a different set of planes [39]. In the case of mosaic crystals this effect is observed on a wavelength range larger than that of perfect crystals because of the presence of misoriented blocks. The consequences for the reflectivity of mosaic crystals are discussed in [40].

2.4 The reflectivity of mosaic crystals

The typical angular spread with which a neutron beam exiting a guide or a beam tube reaches the instrument is of the order of 1^o or less. In order to design efficient optical instruments, the angular acceptance of a neutron monochromator has to be coupled to the divergence of the incident beam: this can be achieved by the use of non-perfect crystals. Perfect crystals, as shown in Fig. 2.3, have a non-zero reflectivity in an angular range of the order of 10 μ rad, while typical mosaic crystals, such as copper in Fig. 2.4, have the right angular acceptance, i.e., a fraction of a degree. Therefore, the standard neutron monochromator is a mosaic crystal, i.e., a crystal which is considered to be formed by a large number of small perfect crystallites of microscopical or submicroscopical size oriented almost but not exactly, parallel to one another. The drawback is the increased divergence of the beam reflected in the plane of scattering. The discussion on production and performance of crystals with a gradient in the lattice spacing, which could eliminate the disadvantage of the beam widening by mosaic crystals, dates back to the 1960's [41, 42, 43]. The difficulties in achieving a controlled gradient which give the same reflected intensity as a mosaic crystal, with a reasonable thickness and without any mosaicity, has so far prevented the application of gradient crystals. Mosaic crystals show a much broader diffraction profile as compared to perfect crystals and have a lower peak reflectivity. The diffraction profiles can be calculated using the theory of Bacon [44] or Zachariasen [37] which are equivalent. They assume that the crystallites are oriented almost parallel to the crystal surface (for the Bragg case) following a distribution $W(\theta - \theta_B)$, θ being the angle formed by the incident beam and the Bragg planes and θ_B the Bragg angle. The full-width-at-half-maximum η of this distribution is called the intrinsic mosaic spread or intrinsic mosaicity.

The multiple Bragg reflections in a mosaic crystal and the concept of secondary extinction are summarised by the Darwin's equations [44]. An exact and general solution of these equations has been given by Sears [45]. The physical quantities which govern diffraction by a mosaic crystal are the scattering coefficient $\sigma = Q\,W(\theta - \theta_B)$ and the absorption

coefficient μ, which we will define and describe in detail in section 2.6. If we define $a = \mu d/\sin\psi$ and $s = \sigma d/\sin\psi$, with d being the crystal thickness and ψ the angle formed by the incident beam and the surface, the Sears' equations [45] for the reflected and transmitted beam in symmetric Laue (transmission) and Bragg (reflection) geometries are:

$$R_{Laue\,symm} = \frac{1}{2}e^{-a}\left(1 - e^{-2s}\right) \tag{2.21}$$

$$T_{Laue\,symm} = \frac{1}{2}e^{-a}\left(1 + e^{-2s}\right) \tag{2.22}$$

$$R_{Bragg\,symm} = \frac{s}{\sqrt{a(a+2s)}\coth\sqrt{a(a+2s)} + (a+s)} \tag{2.23}$$

$$T_{Bragg\,symm} = \frac{\sqrt{a(a+2s)}}{\sqrt{a(a+2s)}\cosh\sqrt{a(a+2s)} + (a+s)\sinh\sqrt{a(a+2s)}} \tag{2.24}$$

The model is valid if the mosaicity is much larger than the Darwin width of the perfect crystal and if the thickness of the mosaic blocks t is much smaller than the primary extinction depth t_{ext}. According to Zachariasen [37] the correction for primary extinction consists of a smaller scattering factor Q. The actual Q is decreased by a factor $f(A)$, where $A \sim t/t_{ext}$. Freund *et al.* [46] pointed out that the phenomenon of the complete extinction of the beam in a mosaic block may as well have the effect of a local increase of the absorption cross-section, and that a correction in Q is not sufficient. We will return to this point when presenting the experimental results.

One consequence of Eqs. (2.21) to (2.24) is that anomalous absorption, which is not to be confused with the Borrmann anomalous absorption observed in perfect crystals, is present in Bragg geometry, but not in Laue geometry:

$$[R(\psi) + T(\psi)]_{Laue\,symm} = e^{-\mu d/\sin\psi} \tag{2.25}$$

$$[R(\psi) + T(\psi)]_{Bragg\,symm} \neq e^{-\mu d/\sin\psi} \tag{2.26}$$

The mosaic crystal calculations were implemented in the XOP code. An example of the calculation of the intensities reflected and transmitted by an ideal mosaic copper crystal with $\eta = 0.1^o$ are reported in Fig. 2.4. The presence of anomalous absorption (see Eq. (2.26)) around the peak position is shown in the plot representing absorption, calculated

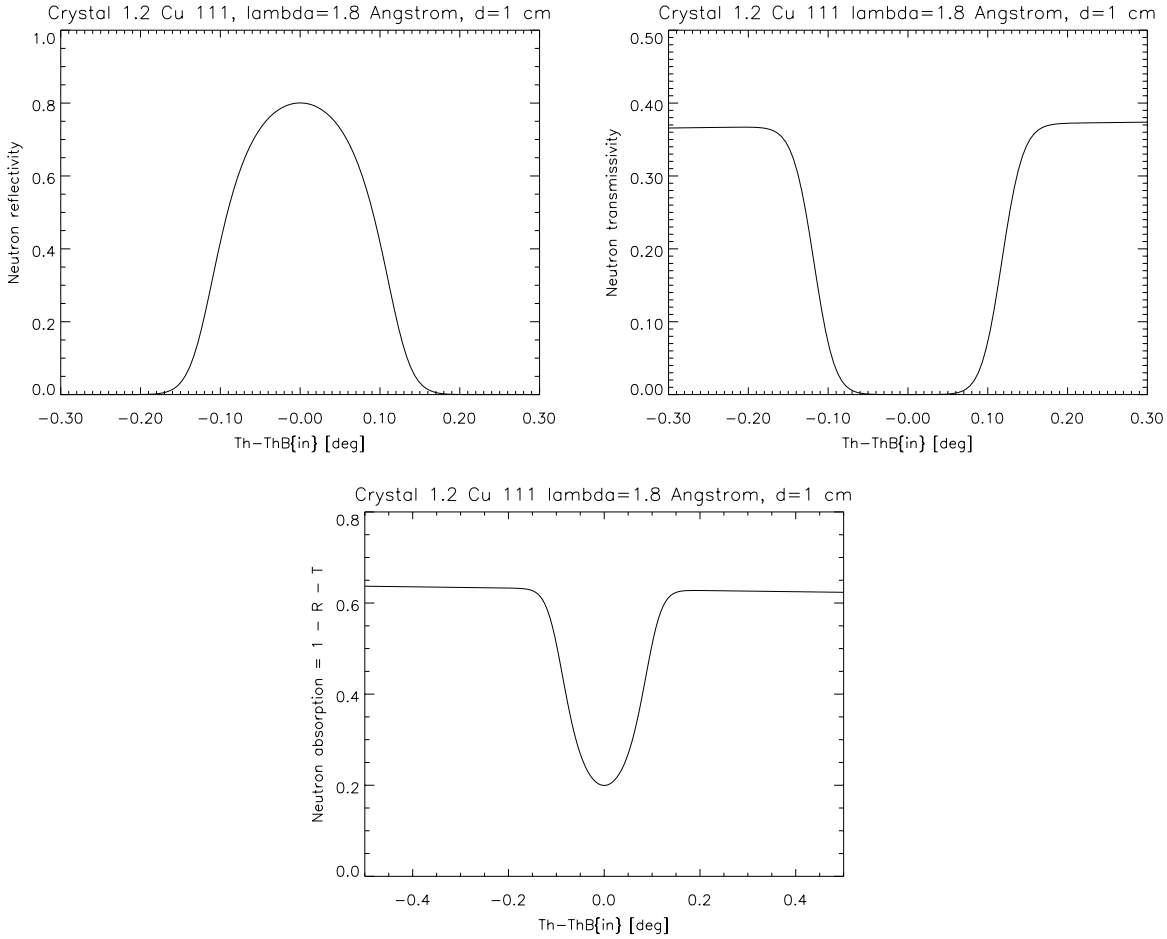

Figure 2.4: *Mosaic crystal reflectivity, transmission and attenuation as a function of* $(\theta - \theta_B)$ *for Cu <111> in Bragg symmetric geometry at* $\lambda = 1.8$ *Å.*

as $A = 1 - R - T$, on the bottom. In Fig. 2.4 the x-axis represents $(\theta - \theta_B)$: the angle formed by the Bragg planes and the crystal surface is zero, hence $\theta \equiv \psi$.

When the mosaic crystal is very thin and multiple reflections of the beam are negligible, the reflectivity calculated with the Darwin's equations is equal to the result of the dynamical theory. Hence, the integrated reflectivity is proportional to the crystal volume, as stated by Eq. (2.19). As a consequence of secondary extinction, when the crystal volume increases and multiple scattering appears, the crystal is no longer uniformely immersed in the beam. Hence, the integrated reflectivity is no longer proportional to the volume.

2.5 Modelling the reflectivity of bent and gradient crystals

Let us suppose that we have a white neutron beam and want to reduce the spectral band to $\Delta\lambda$ using crystal diffraction. This spectral band can be represented in a $(2d_H, \sin\theta)$ diagram as a surface delimited by two hyperbolas representing the Bragg's law as shown in Fig. 2.5.

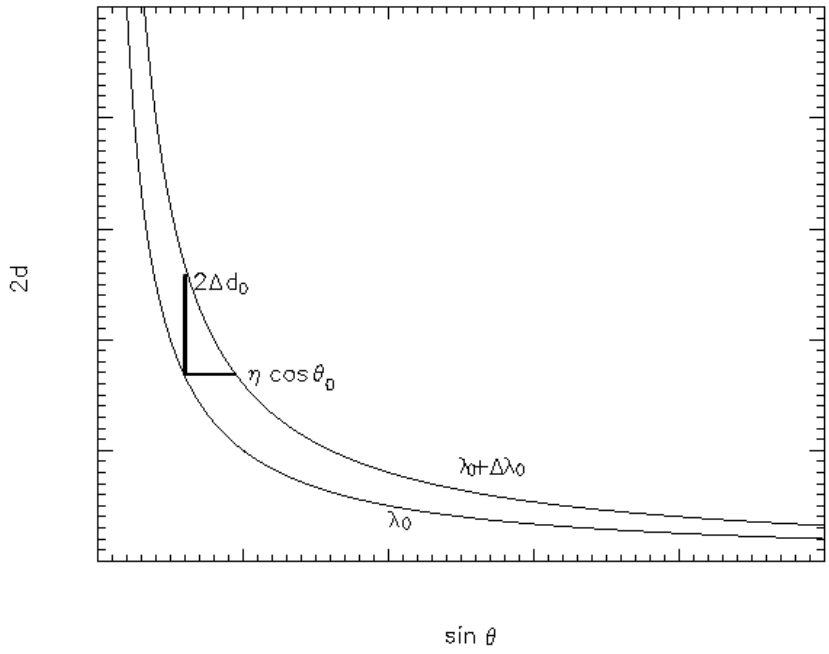

Figure 2.5: *Selection of a range of wavelengths by a mosaic or gradient crystal.*

Calculating the derivative of Bragg's law $\lambda = 2d_H \sin\theta$ we obtain the equation

$$\frac{\Delta\lambda}{\lambda} = \frac{\Delta d_H}{d_H} + \cot\theta\Delta\theta \tag{2.27}$$

from which we see that the wavelength bandwidth can be selected using crystals with Bragg planes misoriented due to a mosaicity η. In this case $\Delta\lambda/\lambda$ is equal to the second term on the right in Eq. (2.27), with $\Delta\theta$ depending on the mosaicity η. A different way to select $\Delta\lambda/\lambda$ is to use crystals having a very small mosaicity and a variation of the d-spacing Δd_H along one direction. The most important feature of gradient crystals is that the reflected beam has the same divergence as the incident beam. This is of decisive importance when high angular resolution is needed. Some technical details about the growth of gradient crystals are discussed in [47]. The improvement that these crystals

would give and the optimal values for the d-spacing gradient are discussed in [48]. The value of $\Delta d_H/d_H$ has to be optimised by requiring that extinction is maximized. By using Eq. (2.27) again we see that, when using gradient crystals, in order to obtain diffracted intensities similar to those of mosaic crystals, we need $\Delta d_H \sim 1\%\, d_H$. The major difficulty is obtaining such large values of the gradient. A variety of techniques can be used for the production of a gradient of the d-spacing (sound-excited crystals, temperature gradient [43]). A good example is that of $Si_{1-x}Ge_x$ [49, 50] binary alloys: the lattice constant of germanium exceeds that of silicon by 4%. With current crystal growth technology [51], a Ge concentration gradient up to $1\,\%$ cm^{-1} can be achieved: this gives a gradient of $\Delta d_H/d_H = 0.04\%$ cm^{-1}, which is too small for neutron use.

An alternative to mosaic or gradient crystals, suitable when focusing at the sample is required, is the use of crystals with bent Bragg planes. In this case, the variation in orientation of the Bragg planes along the crystal depth allows the selection of a wavelength bandwidth similar to that of mosaic crystals, and which depends on geometry because the bending of the Bragg planes effectively "seen" by the neutron depends on the incoming angle. The x-ray and neutron dynamical diffraction by bent and gradient perfect crystals can be obtained by writing the Maxwell's equations (for x-rays) or the Schrödinger equation (for neutrons) in the most general form [52, 53, 54]. An approximate solution, valid for small deformations, is found by assuming the crystal to be ideally divided into regions whose properties remain locally unchanged and that the final crystal reflectivity is the sum of the reflectivities of these small regions, also called *lamellae*. The reflecting properties of mosaic bent crystals, instead, are described by the *layer-coupling model* [56]: an *optical matrix* for the crystal is written, with which the Darwin's equations assume a discrete form. The solution is found by recursively multiplying the matrices for the different layers and by applying the boundary conditions. These two models cannot be compared as they apply to different kinds of crystals: perfect for the *lamellar theory* and mosaic for the *layer-coupling model*. Nevertheless, the *lamellar model* suffers the approximation that the exchanges between transmitted and diffracted beam, from one layer to the next, are neglected. The *layer-coupling model*, instead, deals with multiple diffraction, as it comes from the Darwin's equations, hence is more realistic.

2.5.1 The lamellar theory

The dynamical diffraction of x-rays by ideally deformed crystals was developed by Takagi and Taupin [52, 53]. We report here the basic equations, in the two beam case, in the form derived by Gronkowsky [55]. The crystal is treated as a medium having a dielectric constant with periodicity in the three dimensions

$$\epsilon = \epsilon_0(1 + \chi) \tag{2.28}$$

where ϵ_0 is the dielectric constant in vacuum and χ is the dielectric susceptibility, a three-dimensionally periodic function of position. The electric and magnetic quantities are defined at each point and the solutions are found by solving Maxwell's equations in this medium

$$\mathbf{\Delta D} + rot\, rot\, \chi \mathbf{D} + 4\pi^2 k^2 \mathbf{D} = 0 \tag{2.29}$$

where $\mathbf{D}$ is the electric induction and k the wave vector modulus inside the crystal. The basic assumption of the theory is that, when the crystal is deformed by some displacement vector $\mathbf{w}(\mathbf{r})$, then $\chi(\mathbf{r}) = \chi_0(\mathbf{r} - \mathbf{w}(\mathbf{r}))$, with χ_0 being the susceptibility before the deformation. We will denote by χ_h and $\mathbf{D}_h$ respectively the Fourier components of susceptibility and electric induction and introduce the notion of a *local reciprocal lattice vector* $\mathbf{h}'$

$$\mathbf{h}' = \mathbf{h} - \nabla(\mathbf{h} \cdot \mathbf{w}(\mathbf{r})) \tag{2.30}$$

Using the last equation (2.30) we can write an equivalent of the Bragg relation, as in the perfect crystal

$$\mathbf{K}' = \mathbf{K}_0 + \mathbf{h}' \tag{2.31}$$

where $\mathbf{K}_0$ and $\mathbf{K}'$ are respectively the wave vectors of the incident and diffracted waves. Finally, the Maxwell's equations can be written, in the case of perpendicular, or σ-polarization, as

$$\begin{aligned} \left(\frac{K_0^2 - k^2}{k^2} - \chi_0\right) D_0 - \chi_{\bar{h}} D_h &= -\frac{i}{\pi k}\frac{\partial D_0}{\partial s_0} \\ -\chi_h D_0 + \left(\frac{K_{h'}^2 - k^2}{k^2} - \chi_0\right) D_h &= -\frac{i}{\pi k}\frac{\partial D_h}{\partial s_h} \end{aligned} \tag{2.32}$$

where the partial derivatives of the scalar amplitudes D_0 and D_h are calculated along the forward diffracted $\mathbf{s}_0$ and diffracted $\mathbf{s}_h$ directions respectively. The Takagi-Taupin equations (2.32) can be solved analytically in few cases: the application of numerical solutions in a wide range of cases is reported in [55]. The theory and equations of Takagi-Taupin were extended to neutrons by Klar and Rustichelli [54]. They verified that the

hypotheses which are needed for solving the equations are also fulfilled for neutrons. Then they supposed that the principle of equivalence between neutron and x-ray diffraction, for the case in which the polarization vector is perpendicular to the plane of incidence, is also valid for curved crystals. They made the following assumptions on the kind of crystal deformation: first, the displacement vector $\mathbf{w}(\mathbf{r})$ has to be small

$$|\frac{\partial w}{\partial x_i}| \ll 1 \tag{2.33}$$

and, second, its variation from one atom to the next has to be smaller than the deformation itself

$$|\frac{\partial^2 w}{\partial x_i \partial x_j}\lambda| \ll |\frac{\partial w}{\partial x_i}| \tag{2.34}$$

A particular and very important case is when the deformation is only a function of the Z coordinate along the crystal depth [57]. This is the case for bent or gradient crystals. With these assumptions the Takagi-Taupin equations (2.32) become

$$i\frac{dX}{dA} = X^2\,(1+ik) - 2X\,(y+ig) + (1+ik) \tag{2.35}$$

where X is proportional to the ratio between the diffracted and incident wave amplitudes. The other (dimensionless) quantities appearing in the previous equations are the same as defined by Zachariasen [37]: y is the deviation from Bragg conditions in the Darwin width units, A the dimensionless depth of the reflecting planes inside the crystal, g and k the absorption of the incident and diffracted wave respectively. The y parameter changes with crystal depth:

$$y = y\,(0) + cA \tag{2.36}$$

where c is the crystal curvature (in general it is related to the crystal deformation, and is proportional to the d-spacing gradient in the case of a gradient crystal). The reflectivity of the crystal, in Bragg geometry, is:

$$R = |X\,(0)\,|^2 \tag{2.37}$$

$|X\,(0)\,|^2$ as a function of $y\,(0)$ represents the rocking curve. The Eq. (2.35) can be solved numerically [54, 57], however, in the limit of small deformations, i.e. small c, the

reflectivity R of a curved or gradient perfect crystal can be calculated using the simple *lamellar model* [58]. The bent crystal is divided into many perfect undeformed crystal layers, each of thickness $A_l = 2/c$. As shown in Fig. 2.6, at a certain depth inside the crystal, there can be a layer whose orientation fulfills Bragg's law: this layer is then in the condition of total reflection and has $-1 \leq y \leq 1$. The crystal reflectivity is obtained by adding the reflectivity of the layers (calculated using the dynamical theory results, see section 2.3) and the rocking curve is then given by the reflectivity as a function of $y\,(0)$. It is clear that the assumption of having a layer that, if correctly oriented, totally diffracts in the range $-1 \leq y \leq 1$ is valid only if the deformation is not too large, i.e. if $c \leq 1$.

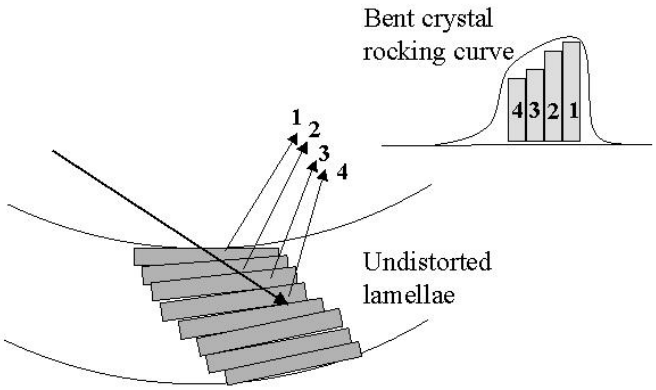

Figure 2.6: *Lamellar model: the bent crystal is divided into many undistorted layers whose orientation follows the Bragg planes curvature. The diffraction profile is wider than that of the perfect crystal because different orientations of the incident beam can satisfy the Bragg's law at different depths.*

The calculation of the reflectivity by bent perfect crystals according to the *lamellar model*, already inplemented in XOP for the x-ray case, was extended by us to the case of neutrons and one example is shown in Fig. 2.7. The model, in the case of x-rays, has been verified by measuring the rocking curves of several thin bent quartz crystal for several diffraction orders. The experimental set-up will be described in Chapter 5 and the curves are shown in Fig. 2.8. The experimental data and the lamellar model are in very good agreement for these samples.

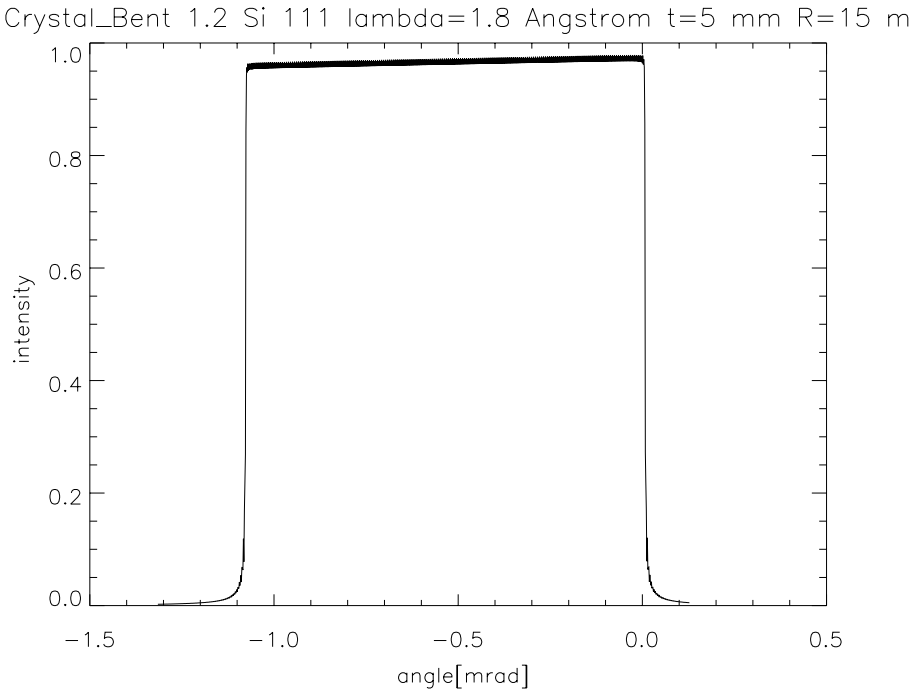

Figure 2.7: *Bent crystal reflectivity: Si <111> in Bragg symmetric geometry at* $\lambda = 1.8$ *Å. The radius of curvature is* $R = 15$ *m.*

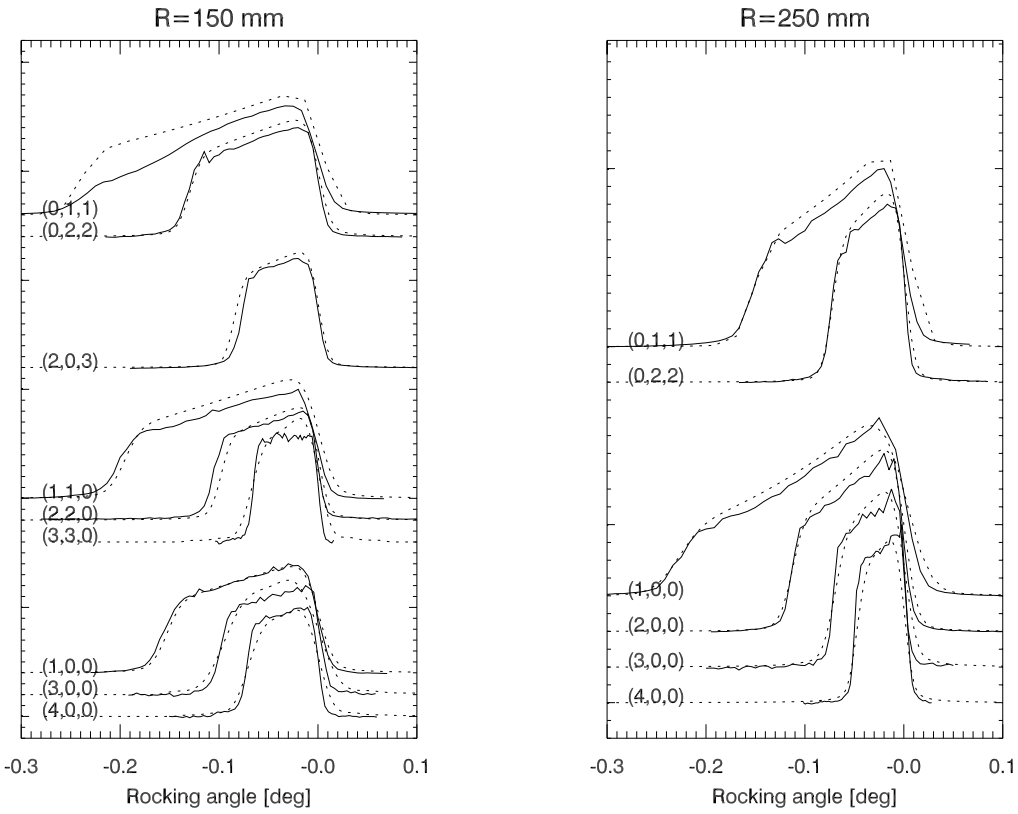

Figure 2.8: *LEFT: experimental x-ray rocking curves (solid lines) and lamellar model (dotted lines) for four different samples bent to $R = 150$ mm. RIGHT: the same for samples with $R = 250$ mm. The crystal thickness is $d \sim 60$ μm for all the samples. The x-ray energy was $E = 20$ keV and the labels indicate the reflection indices. The experimental peak reflectivities were all normalised to unity for ease of representation.*

2.5.2 The layer-coupling model

The *layer coupling model* [56] is the discrete form of the Darwin's equations. We recall that the Darwin's equations describe the transport of the diffracted and transmitted intensities in a mosaic crystals. If the mosaic crystal is also bent or has a d-spacing gradient, then the diffraction planes change orientation or d-spacing from one layer to the next and the Darwin's equations have to be rewritten in a matrix form because the physical parameters depend on the depth. In this section we will use the bent crystal formalism. The equations for a gradient crystal require only a slight modification.

$P_{0,n}$ and $P_{H,n}$ are the power of the incident and diffracted beam at the n-th layer. In Bragg geometry the equations are the following:

$$\begin{aligned} P_{0,n} &= T_{0,n}P_{0,n-1} + D_{H,n}P_{H,n} \\ P_{H,n-1} &= D_{0,n}P_{0,n-1} + T_{H,n}P_{H,n} \end{aligned} \tag{2.38}$$

where: $D_{0/H,n}$ is the probability of the incident/reflected beam being diffracted and not being absorbed by the n-th layer; $T_{0/H,n}$ is the probability of the beam being transmitted by the n-th layer. The previous equations can be expressed by the matrix:

$$\begin{pmatrix} P_{0,n} \\ P_{H,n} \end{pmatrix} = \begin{pmatrix} T_{0,n} - \frac{D_{0,n}D_{H,n}}{T_{H,n}} & \frac{D_{H,n}}{T_{H,n}} \\ -\frac{D_{0,n}}{T_{H,n}} & \frac{1}{T_{H,n}} \end{pmatrix} \begin{pmatrix} P_{0,n-1} \\ P_{H,n-1} \end{pmatrix} \tag{2.39}$$

The solution at the last layer is:

$$\begin{pmatrix} P_{0,N} \\ P_{H,N} \end{pmatrix} = \begin{pmatrix} M_{11} & M_{12} \\ M_{21} & M_{22} \end{pmatrix} \begin{pmatrix} P_{0,0} \\ P_{H,0} \end{pmatrix} \tag{2.40}$$

where the M_{ij} matrix is obtained by iterating the Eq. (2.39). In the Bragg geometry we have $P_{H,N} = 0$, then the reflecting power is:

$$\frac{P_{H,0}}{P_{0,0}} = -\frac{M_{21}}{M_{22}} \tag{2.41}$$

Finally, the diffraction and transmission probabilities can be written as:

$$D_{0,n} = \frac{\sigma_n t_n}{\cos\theta_0} e^{-\frac{\mu t_n}{\cos\theta_0}} \tag{2.42}$$

$$\begin{aligned} D_{H,n} &= \frac{\sigma_n t_n}{|\cos\theta_H|} e^{-\frac{\mu t_n}{|\cos\theta_H|}} \\ T_{0,n} &= (1 - D_{0,n})\, e^{-\frac{\mu t_n}{\cos\theta_0}} \\ T_{H,n} &= (1 - D_{H,n})\, e^{-\frac{\mu t_n}{|\cos\theta_H|}} \end{aligned} \tag{2.43}$$

where: μ is the absorption coefficient, t_n the thickness of the n-th layer, θ_0 the angle of incidence, θ_H the angle of reflection, $\sigma_n = Q \times W(\Delta\theta_n)$ the equivalent of the secondary extinction coefficient for the n-th layer, with Q the scattering coefficient already defined in section 2.4, $\Delta\theta_n$ the deviation from Bragg angle, and W the mosaic distribution:

$$W(\Delta\theta_n) = \frac{1}{\eta_n 2\pi^{\frac{1}{2}}} e^{-\frac{{\Delta\theta_n}^2}{2{\eta_n}^2}} \tag{2.44}$$

$$\Delta\theta_n = \Delta\theta_1 + \epsilon_n \tag{2.45}$$

$$\epsilon_n = \frac{1}{R} \sum_{i=1}^{n} t_i \left[\tan\theta_0 + \left(\sin^2\chi - \nu\cos^2\chi \right) \tan\theta_B + \frac{1}{2}(1+\nu)\sin 2\chi \right] \tag{2.46}$$

In the last equation χ is the asymmetry angle, ν the Poisson ratio and θ_B the Bragg angle. The calculation of the neutron reflectivity by a mosaic bent germanium crystal is shown in Fig. 2.9. The main difference with respect to the perfect bent crystal example in Fig. 2.7 is that the peak reflectivity is smaller and the shape is smoother: these effects are both due to mosaicity.

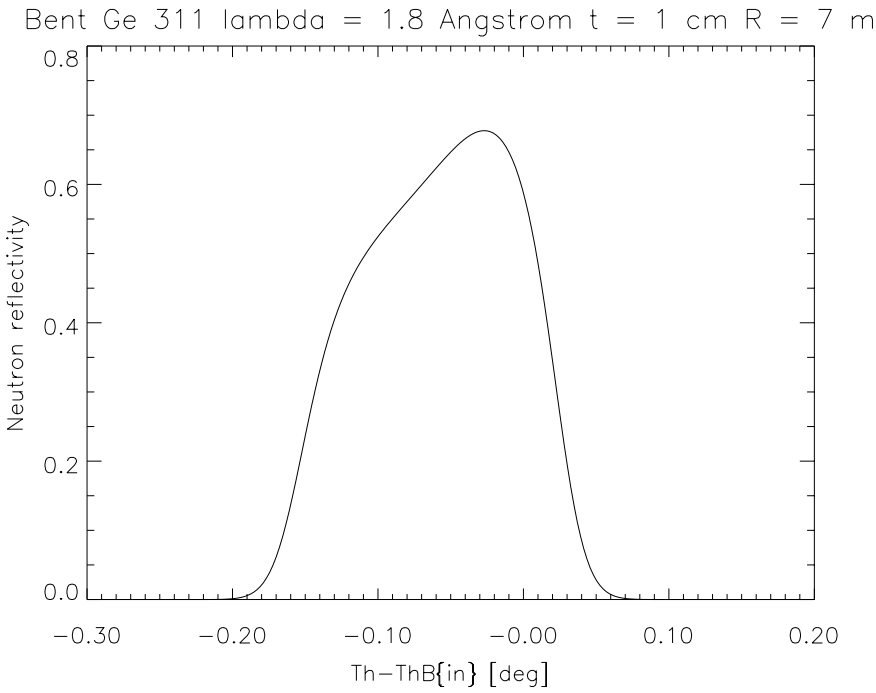

Figure 2.9: *Bent mosaic crystal reflectivity: Ge <311> in Bragg symmetric geometry at* $\lambda = 1.8$ *Å. The radius of curvature is* $R = 7$ *m and the mosaicity is* $\eta = 0.05^o$.

2.6 Neutron removal in crystals - Thermal diffuse scattering

The need for a correct description of the neutron reflectivity of mosaic crystals and the search for new ideas for improving the efficiency of neutron monochromators and analysers, both lead to the problem of determining the cross-sections that mainly contribute to the attenuation coefficient μ of the neutron beam. This is the sum of three parts: nuclear absorption as defined in section 2.2, parasitic Bragg scattering, and thermal diffuse scattering (TDS):

$$\mu = \frac{n}{V_0}(\sigma_{abs} + \sigma_{par} + \sigma_{TDS}) \tag{2.47}$$

where n/V_0 is the number of atoms or molecules per unit cell volume. The nuclear absorption cross-section σ_{abs} does not depend on the temperature and has a simple dependence on energy except for some well known resonant cases. The parasitic Bragg scattering cross-section σ_{par}, already mentioned in section 2.3, is of difficult calculation. Nevertheless, it can have an important role in the decrease of the diffracted intensity, especially at higher energy, as we will see in Chapter 5. The TDS cross-section can be calculated as the sum of single phonon and multiple phonon cross-sections:

$$\sigma_{TDS} = \sigma_{single-ph} + \sigma_{multi-ph} \tag{2.48}$$

The calculation of TDS has been an important task for neutron scatterers since the early years of neutron research [59]. There are two main reasons for being interested in TDS cross-sections:

i) Computing, via a knowledge of the differential cross-section, the improved resolution and background of cooled analysers, a solution which has been adopted for the graphite analysers of the time of flight spectrometer IRIS [60] at ISIS.

ii) Assessing the behaviour of the total cross-section as a function of temperature and incident neutron energy, in order to accurately compute the reflectivity of mosaic crystals, especially at energies greater than the Debye energy of the monochromator crystal.

We have not dealt with the precise computation of the differential cross-section, which requires having a complete model of the lattice dynamics of the crystal under consideration. This is an important subject, also because the amount of TDS is not constant, but changes with changing the Bragg indices and is stronger in the vicinity of the Bragg peak [61]. We aimed at studying the energy and temperature dependence of the total cross-section

σ_{TDS}, for some materials, and try to compute and also measure the improved reflectivity of these materials, when used as cooled monochromators. For this reason, we used two different ways for calculating σ_{TDS}: an empirical formula developed by Freund [62] and the numerical integral of $d^2\sigma/d\Omega\, dE$, discussed in the last section of this Chapter.

There are different approaches and approximations to the problem of TDS [59, 63, 64, 65]: all the authors, except for Binder [65] who gives the coherent cross-section for a polycrystal, use the incoherent approximation for the multi-phonon processes, i.e. they disregard all restrictions coming from the momentum conservation and give a non-zero partial differential cross-section in all scattering directions. This gives the correct result at energies much higher than the Debye energy. At lower energy the main contribution to σ_{TDS} is the single phonon scattering cross-section $\sigma_{single-ph}$ which can be calculated without approximations. At intermediate energies coherence effects, i.e. interference of scattering from different sites have to be considered, but they amount to only a few percent of the total cross-section [63]. We report here the formula given by Freund [62] for the total multi-phonon cross-section:

$$\sigma_{multi-ph} = \sigma_0 \left\{1 - \exp\left[-C_2 E \left(B_0 + B\left(T\right)\right)\right]\right\} \tag{2.49}$$

In this equation σ_0 is the sum of the coherent and incoherent cross-sections for the nucleus, the C_2 parameter has to be determined experimentally for each material and $B_0 + B\left(T\right)$ is the mean square atomic displacement. The energy dependence of σ_{abs} and of $(\sigma_{abs} + \sigma_{TDS})$ for copper at $15\,K$ and $290\,K$, calculated using Eq. (2.49) for the multi-phonon contribution, is plotted in Fig. 2.10. The figure shows that, by neglecting the temperature effect, the calculation of attenuation is far from being realistic, even at low temperature. The behaviour of the TDS contribution, without true absorption, will be shown in the next section.

2.6.1 The partial differential cross-section for single and multiple phonon interactions

The simultaneous emission or absorption of two or more different phonons is called a multi-phonon process. Knowledge of multi-phonon effects is useful for two main reasons: estimating diffuse scattering for correcting the measured data and calculating its influence at high neutron energy. This calculation is difficult because the partial differential cross section is very slowly convergent with increase in the number of phonons involved. However, there is an important consideration made first by Placzek: when two or more phonons are involved, the multi-phonon cross section tends to be a smoothly varying function of scattering angle and incident energy, because energy and momentum conservation

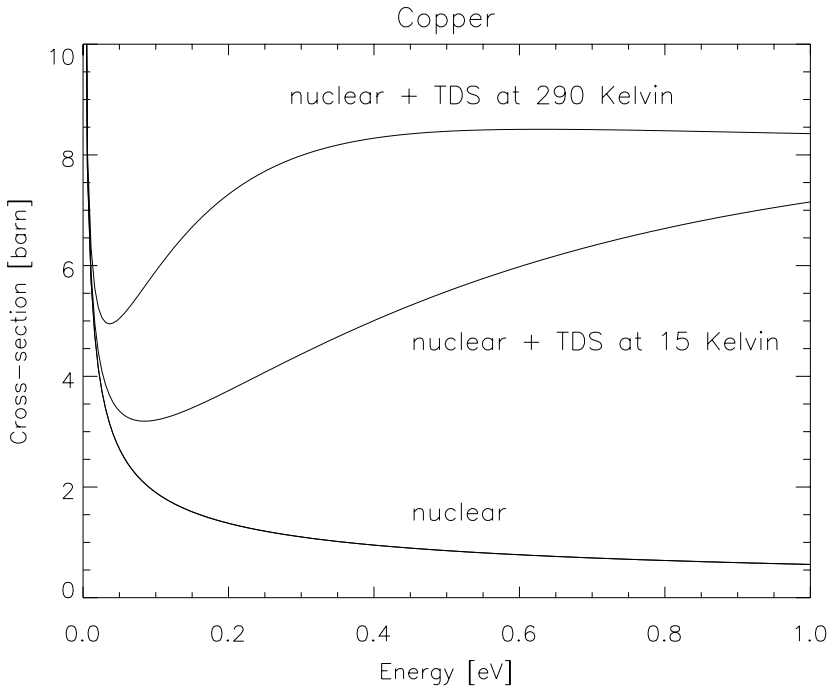

Figure 2.10: *Total cross-sections $\sigma_{abs}+\sigma_{TDS}$ for copper. The line on the bottom represents the true absorption cross-section σ_{abs}. The temperature dependent σ_{TDS} was calculated using the model developed by Freund [62].*

are less restrictive. This means that all scattering can be treated as if it was incoherent and, in the multi-phonon cross section, terms with $l^{'} \neq l$ can be ignored (the index l denotes the lattice site). This is known as the *incoherent approximation*. A detailed discussion of the validity and convergence of the results of this method can be found in the book by Turchin [64]. A further idea is that the multi-phonon cross section can be rearranged in a form which has the correct behaviour at high incident energy. This leads to the so-called *Gaussian approximation*. Here we will report only the theory for a Bravais lattice. We will use the harmonic approximation which consists in truncating the expansion of the displacements at quadratic terms. The starting point is the partial differential incoherent cross-section (see Eq. 2.5) written as a sum of terms involving one, two, ..., n phonons. The nth term, according to Marshall and Lovesey [63], is:

$$\left(\frac{d^2\sigma_n}{d\Omega dE'}\right)_{inc}^{inel} = \frac{\sigma_{inc}}{4\pi}\frac{k^{'}}{k}\frac{N}{2\pi\hbar}\int_{-\infty}^{\infty} dt\, e^{-i\epsilon t/\hbar}\, e^{-2W(\kappa)}\frac{1}{n!} < \kappa\cdot\hat{\mathbf{u}}(l,0)\times\kappa\cdot\hat{\mathbf{u}}(l,t) >^n \qquad (2.50)$$

In Eq. (2.50) the sum over l is implicitly assumed. We have: $\kappa = \mathbf{k}^{'} - \mathbf{k}$, N is the number of nuclei, $\epsilon = E^{'} - E$ is the exchanced energy, $W(\kappa)$ is the Debye Waller factor and $\hat{\mathbf{u}}(l,t)$ the displacement at time t from the equilibrium position of the atom located at l.

Using the formalism of Turchin [64] we obtain for the scattering from a free nucleus, in the incoherent approximation:

$$\frac{d^2\sigma}{d\Omega dE'} = \frac{\sigma_0}{4\pi}\left(1+\frac{1}{\mu}\right)^2 \frac{k'}{k} e^{-\gamma\kappa^2} \sum_{n=0}^{\infty} \left(\frac{h^2\kappa^2}{2M}\right)^n \frac{f_n(\epsilon)}{n!}, \tag{2.51}$$

where the l index has been omitted. In the last equation $\sigma_0 = \sigma_{inc} + \sigma_{coh}$ and μ is the reduced mass of the atom. For a monatomic crystal γ and $f_n(\epsilon)$ can be calculated in terms of the phonon spectrum $g(\epsilon)$ as

$$\gamma = \int_0^{\infty} \frac{\hbar^2}{2M\epsilon} \coth\left(\frac{\epsilon}{2K_BT}\right) g(\epsilon)d\epsilon \tag{2.52}$$

$$f(\epsilon) = \frac{g(|\epsilon)|}{\epsilon\left[1-\exp\left(-\epsilon/K_BT\right)\right]} \tag{2.53}$$

$$f_n(\epsilon) = \int_{-\infty}^{+\infty} f(\epsilon_1)d\epsilon_1 \int_{-\infty}^{+\infty} f(\epsilon_2)d\epsilon_2 ..... \int_{-\infty}^{+\infty} f(\epsilon_n)d\epsilon_n\, \delta(\epsilon_1+\epsilon_2+.....+\epsilon_n-\epsilon) \tag{2.54}$$

Since the $f_n(\epsilon)$ function is obtained by convoluting the $f(\epsilon)$ function n times, it can be replaced, for large n, by a Gaussian with average values for ϵ and for the dispersion which are n times as large as the those for $f(\epsilon)$, which are given by:

$$\epsilon_{aver} = \frac{\int_{-\infty}^{+\infty} \epsilon f(\epsilon)d\epsilon}{\int_{-\infty}^{+\infty} f(\epsilon)d\epsilon} \tag{2.55}$$

$$\Delta^2 = \frac{\int_{-\infty}^{+\infty} \epsilon^2 f(\epsilon)d\epsilon}{\int_{-\infty}^{+\infty} f(\epsilon)d\epsilon} - \epsilon_{aver}^2 \tag{2.56}$$

Consequently, in the Gaussian approximation:

$$f_n(\epsilon) = \frac{1}{\sqrt{2\pi n}\Delta} \frac{1}{\epsilon_{aver}^n} \exp\left[-\frac{(\epsilon - n\epsilon_{aver})^2}{2n\Delta^2}\right] \tag{2.57}$$

Finally, we can separate the cross section Eq. (2.51) into the elastic term, the one-phonon cross section, and the multi-phonon cross section. The first two terms can be calculated with allowance for interference and the last one, with the approximations here discussed, becomes:

$$\frac{d^2\sigma_{multi-ph}}{d\Omega dE'} = \frac{\sigma_0}{4\pi}\left(1+\frac{1}{\mu}\right)^2 \frac{k'}{k} e^{-\gamma\kappa^2} \sum_{n=2}^{\infty} \left(\frac{h^2\kappa^2}{2M}\right)^n \frac{1}{n!} \frac{1}{\sqrt{2\pi n}\Delta} \frac{1}{\epsilon_{aver}^n} \exp\left[-\frac{(\epsilon - n\epsilon_{aver})^2}{2n\Delta^2}\right] \tag{2.58}$$

Eq. (2.58) can be rewritten in a more compact form as:

$$\frac{d^2\sigma_{multi-ph}}{d\Omega dE} = \frac{\sigma_0}{4\pi}\left(1+\frac{1}{\mu}\right)^2 \frac{k'}{k} e^{-\gamma\kappa^2} \exp\left[\frac{\epsilon_{aver}}{\Delta^2}\epsilon\right] \frac{1}{\Delta} F(z,x) \tag{2.59}$$

with:

$$z = \frac{h^2\kappa^2}{2M\epsilon_{aver}} \exp\left(-\frac{\epsilon_{aver}^2}{2\Delta^2}\right) \tag{2.60}$$

$$x = \frac{\epsilon}{\Delta} \tag{2.61}$$

$$F(z,x) = \sum_{n=2}^{\infty} \frac{z^n}{n!} \frac{\exp\left\{-x^2/(2n)\right\}}{\sqrt{2\pi n}} \tag{2.62}$$

In Fig. 2.11 we show the numerical results for the multi-phonon cross section, in the case of copper, obtained calculating the last formulas (left) compared to a semi-empirical model [62] (right). It is not clear if the strong disagreement between the two models depend on the approximation or on numerical limits in the calculation and integration of Eq. (2.59). It is true that, by definition, Eq. (2.59) is only valid for energies much higher than the crystal Debye energy. However, the numerically integrated $\sigma_{multi-ph}$ plotted versus the energy, reaches the saturation value very slowly and also its "high energy" behaviour does not agree with the Freund's model. We will return to this point in Chapter 5, when interpreting the measured temperature dependent reflectivity of a mosaic copper crystal.

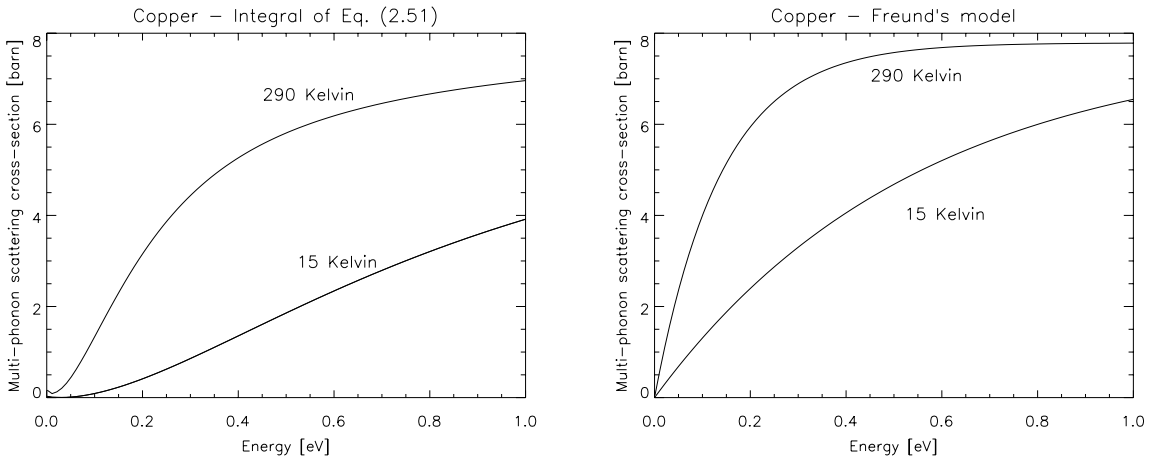

Figure 2.11: *Multi-phonon total cross-section versus energy for copper. LEFT:* $\sigma_{multi-ph}$ *numerically calculated from Eq. (2.59), which is obtained after applying the incoherent and gaussian approximations. RIGHT:* $\sigma_{multi-ph}$ *calculated using Freund's model [62].*

2.7 Summary and conclusions

Our aim is to well understand the physical models describing the diffraction by crystals used as monochromators and analysers, in order to be able to accurately determine the parameters which influence the diffraction properties in terms of resolution and flux.

In this chapter we have outlined the "state of the art" of theoretical models for describing neutron reflectivity by imperfect (mosaic, bent and gradient) crystals.

The chapter has been divided in several sections, where the models to predict the diffraction profiles for different types of crystals have been clearly described:

1) Dynamical theory of diffraction for perfect crystals. The study of perfect crystals is important because imperfect crystals are always built using simple "perfect" elementary crystallites. In addition, primary extinction is a dynamical diffraction effect. Hence, if we want to describe real mosaic crystals in a realistic way, we have to calculate the corrections due to primary extinction using the formal results of the dynamical theory that we presented in this Chapter. Moreover, the Takagi-Taupin equation describing the waves diffracted by perfect bent (or gradient) crystals is a result obtained in the frame of the dynamical theory.

2) The "standard" model for mosaic crystals. We follow the formulation of Sears, the most used in the neutron community, and the most general (Bragg and Laue symmetric and asymmetric cases). This theory supplies analytical formulas for describing the diffraction profiles, which are the analytical solutions of the Darwin's equations. These are the transport equations for the neutron intensity in the crystal. The Sears's solution implies some restrictions: the distribution of the crystallites has to be uniform in the whole crystal; moreover primary extinction inside a single crystallite is neglected. The concept of secondary extinction has been introduced and will be recalled (also with giving numerical values) in the next Chapter.

3) Bent crystals (i.e., having the Bragg planes bent in the plane of scattering) are increasingly used not only to focus the beam, but also to increase the integrated intensity of the diffraction profile with respect to that of perfect crystals. This is because the curvature produces a lack of perfection in the crystal, that starts to behave "imperfectly". This effect can also be combined with an intrinsic crystal mosaicity. Two theoretical models have been described, the lamellar theory, for bent perfect crystals, and the layer-coupling model, for bent crystals having an additional mosaic spread. It is important to calculate the reflectivity as a function of the various parameters, as Bragg angle, thickness and bending radius, and also compare the results for a perfect bent crystal (which is the case of the elastically bent silicon wafers) to those for a mosaic one (as plastically bent

germanium).

4) For any crystal, it is important to study the temperature dependent neutron reflectivity. In order to take into account this effect, we have reported the model developed by Freund [62] for calculating the effect that moving nuclei have on the neutron attenuation length. According to this model, in some cases the effect of cooling the crystal to low temperature can improve the reflectivity as much as 50%. We have tried to quantitatively compare this model to the analytical, approximated incoherent multi-phonon cross-section. There is a strong disagreement between the model and the approximated theory, hence, in our opinion, further work is necessary in this field. These theories will be used for discussing the copper neutron reflectivity versus temperature reported in Chapter 5.

All the models have been implemented in computer codes, and are applied for the analysis of experimental data.

Chapter 3

Numerical solutions for mosaic and bent crystals

We developed two original Monte-Carlo programs for the simulation of Bragg diffraction by non-perfect (flat and bent) crystals: these programs have practical applications, as they can be used as crystal modules in any ray-tracing simulation of neutron instruments. Since they use a detailed description of the particle interaction with the microscopic homogeneous regions composing the crystal, they can be used also for the calculation of quantities having a conceptual interest, as multiple scattering, or for the interpretation of crystal diffraction topographs, as we will show in Chapters 5 and 6.

3.1 The *MOSAIC* Monte Carlo code

The *MOSAIC* program allows the numerical solution of the Darwin's equations [44] for the reflected and transmitted beam in a mosaic crystal. It computes quantities such as the beam distribution at the exit surface, the divergence, the number of scattering events and the total path length inside the crystal for each trajectory. These quantities are difficult to calculate using analytical approaches. The method consists in following a given number of trajectories inside a crystal of thickness d, which is formed by an agglomeration of perfect crystallites. The angular distribution of the normal vectors of the crystallites is given by the usual mosaic distribution $W(\Theta, \Phi)$. The fundamental physical quantities used in the program are the FWHM, η, of the mosaic distribution and the crystallite thickness t. The crystallite transmittivity and reflectivity are calculated according to the dynamical theory of diffraction and depend on the material, the Bragg planes, and the thickness t. The simulation of the particle trajectory is done in steps; a pictorial view was shown in Fig. 1.1 (right) in the Introduction. At each step the particle interacts with a crystallite

as drawn in Fig. 3.1. The crystallite's orientation $\mathbf{N}(\Theta, \Phi)$ is sampled by the distribution $W(\Theta, \Phi)$ thus giving the angle θ formed by the incident direction and the crystallite surface. θ is then used for calculating $R(\theta)$ and $T(\theta)$ according to the dynamical theory of diffraction (Section 2.3 and Eqs. (A.35) in Appendix A). They are respectively the probability of the particle being reflected or transmitted. The reflection or transmission events are decided by generating a random number. The particle is followed until it intersects one of the crystal surfaces. The effect of absorption is included by assigning a *weight* or *probability* to the particle, which is calculated as $weight = e^{-path \times \mu}$, with *path* being the total path length and μ the absorption coefficient. This method of accounting for the effect of absorption is not an approximation: at the stage of the particle-crystallite interaction the absorption is present in $R(\theta)$ and $T(\theta)$. A schematic representation of the code structure is shown in Fig. 3.2

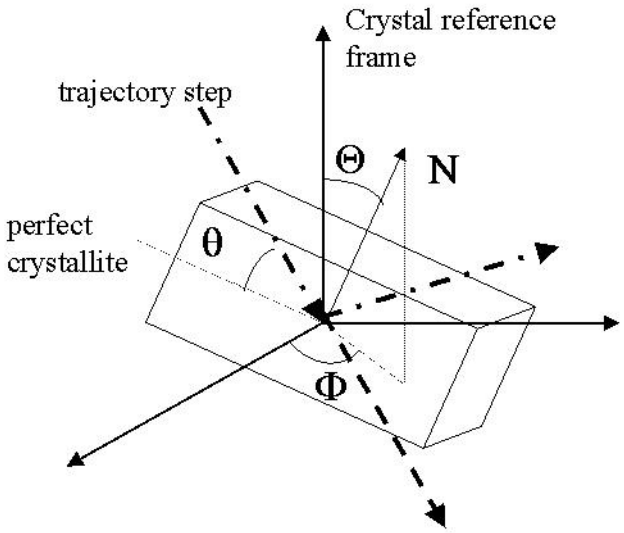

Figure 3.1: *Geometrical view of the interaction between the particle and the crystallite. The two possible events (diffraction or transmission) are shown and their probability is calculated according to the dynamical theory of diffraction. The* Θ *and* Φ *angles are sampled, for each crystallite met by the particle, by the mosaic distribution* $W(\Theta, \Phi)$*.*

By definition, this method allows us to know the complete history of each particle: how many scattering events it has undergone (and also at what spatial coordinates), the maximum depth it has reached in the crystal slab, and the total path length. These important quantities are related to multiple scattering and secondary extinction.

The final values of the particle coordinates (x, y, z), direction cosines (V_x, V_y, V_z), path length *path*, and number N_{multi} of reflection events inside the crystal are written in a file.

The case of an anisotropic mosaic distribution is handled, in the *MOSAIC* program, by using the following probability distribution for the polar and azimuthal angles:

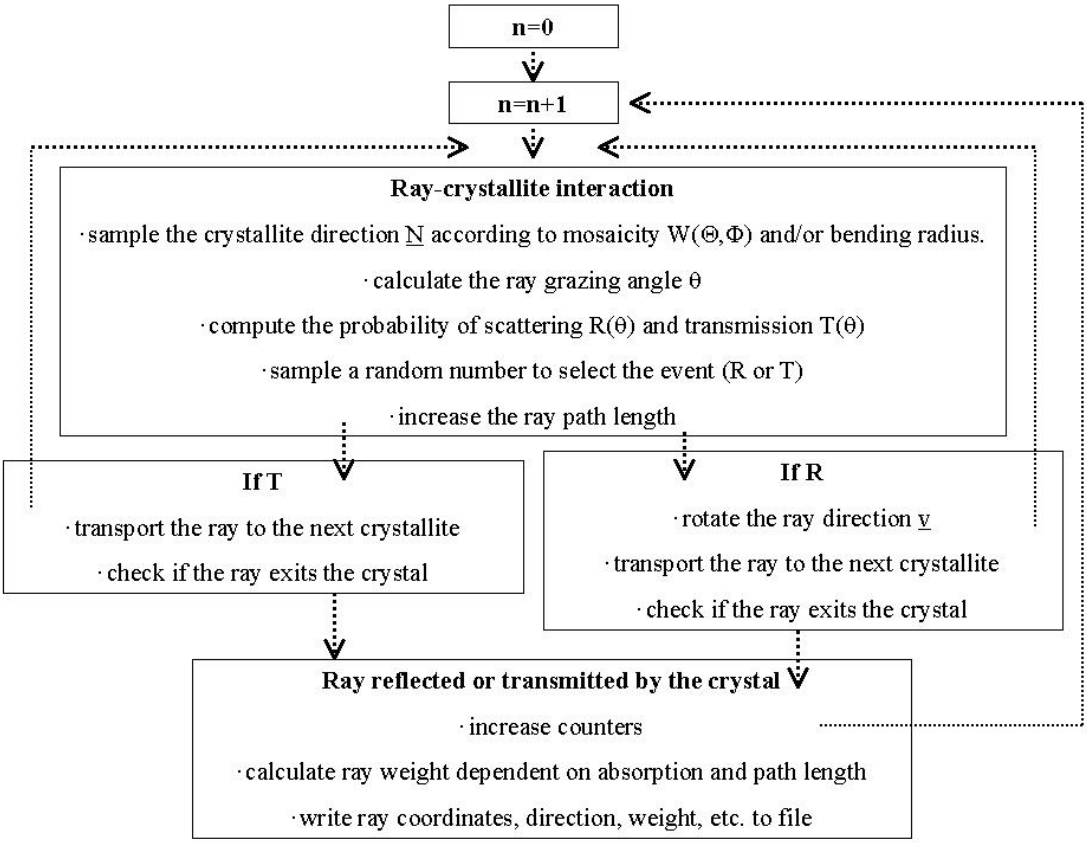

Figure 3.2: *Structure of the MOSAIC and BENT Monte Carlo codes.*

$$W(\Theta,\Phi) = e^{-4\log 2\,\Theta^2\,[\frac{\sin^2\Phi}{\eta_s^2}+\frac{\cos^2\Phi}{\eta_p^2}]} \tag{3.1}$$

where η_s and η_p are the FWHMs in the scattering plane and perpendicular to it, respectively.

The limits of applicability of the *MOSAIC* program are found in those cases where the description of the beam amplitude, rather than the intensity, is needed. In other words, when we talk of *simulated trajectories* or *simulated particles* we deal with something which resembles energy transport (intensity) in the crystal, rather than waves (amplitudes). Therefore these simulations cannot be used to calculate interference effects, such as appear in perfect crystals or crystals having a very small mosaicity, which is of the order of the perfect crystal Darwin width χ_D (defined in Appendix A).

3.1.1 Examples

An essential benchmark for the code is a comparison of diffraction profiles with those predicted by the theory. Fig. 3.3 shows the reflectivity of a copper mosaic crystal in

Bragg and Laue symmetric geometries. The primary extinction depth for copper at this wavelength is calculated by using the dynamical theory of diffraction: $t_{ext} = 6.7$ μm. It is worth noting that this value is not used directly in the code. Nevertheless the simulated reflectivity is strongly dependent on it: for a crystallite size t such that $t \ll t_{ext}$, the reflectivity is not affected by primary extinction; for $t \geq t_{ext}$ the simulated rocking curve will be fitted by the analytical one only if a correction to the Q scattering factor is made. The simulated reflectivity obtained using a crystallite thickness $t = 2$ μm is in very good agreement with that obtained using the analytical formulas in Eqs. (2.23) and (2.21). The result with $t = 10$ μm (top in Fig. 3.3, Bragg symmetric case) is well reproduced by introducing a correction factor $Q^{'} = 0.58 \times Q$ to the scattering factor. By using Eq. (4.46a) of Zachariasen's book [37], we find $Q^{'} = 0.61 \times Q$. Anomalous absorption, discussed in section 2.4, and shown in Fig. 3.4, is also found to be in good agreement with the theory.

Finally, the application of *MOSAIC* to diffraction by a crystal having an asymmetric mosaic distribution, such as that in Eq. (3.1) is shown in Fig. 3.5.

3.1.2 Secondary extinction and multiple scattering

The presence of *secondary extinction* is the reason for the high integrated reflectivity of mosaic crystals. This is due to the fact that the mosaic blocks are misoriented and the beam penetration τ_{ext} (not to be confused with t_{ext}, the primary extinction depth) before extinction can be of the order of several mm, therefore large crystal volumes (when compared to perfect crystals), can take part in diffraction. As the beam path before re-emerging at the crystal surface is long, many scattering events can take place. This *multiple scattering* phenomenon has nothing to do with the concepts discussed in section 2.3 as it concerns diffraction by the same set of Bragg planes. The presence of secondary extinction and multiple scattering makes the reflectivity of the mosaic crystal dependent on the crystal thickness. The optimal values for the thickness d can be calculated analytically [45] but a very precise estimation of the effects of multiple scattering can be done only by simulating the diffraction process. In particular, neither the theory for the mosaic crystal nor a ray-tracing simulation give numerical values for the number of scattering events N_{multi} in the crystal.

The task of calculating of N_{multi} can only be carried out by using a full Monte-Carlo simulation. Therefore, the *MOSAIC* code can be used not only as a crystal-module for any neutron instrument simulation package, but also for studying the behaviour of important parameters such as N_{multi} which have a conceptual importance. In Fig. 3.6 we show the secondary extinction depth τ_{ext} for copper $< 220 >$ in Bragg symmetric geometry as a function of mosaicity η. The solid line represents theory, i.e. $\tau_{ext} = \sin\theta_B/\sigma$ (with the secondary extinction coefficient σ defined in section 2.4). The dashed lines with symbols

are the simulation results: they were obtained by averaging the maximum penetration depths reached by each reflected ray. As is obvious, if we perform the average only on those rays which have been reflected after having undergone only one scattering event (diamond symbols), we do not retrieve the theoretical extinction depth. We can conclude that the simulation of multiple scattering with the *MOSAIC* program is very accurate. The discrepancy at larger values of mosaicity is due to the smaller number of reflected rays, which increases the statistical error. In Fig. 3.7 the histograms of rays versus the maximum penetration depth τ are shown for all the scattering events (top) and for rays with only one scattering event (bottom). These plots have only a "didactic" purpose since they shown that if we consider all scattering events, then extinction is not governed by an exponential law (top). If, instead, only single scattering events are counted, then we can fit the histograms with an exponential function (bottom) which, however, does not give the real extinction cefficients. The number of multiple scattering events undergone by the reflected rays, for several values of mosaicity and as a function of the maximum depth reached inside the crystal, are shown in Fig. 3.8. We see that for a copper crystal 1 mm thick with a mosaicity of 0.1^o in Bragg symmetric geometry at 1.8 Å, the number of events can be of the order of ~ 50 or more.

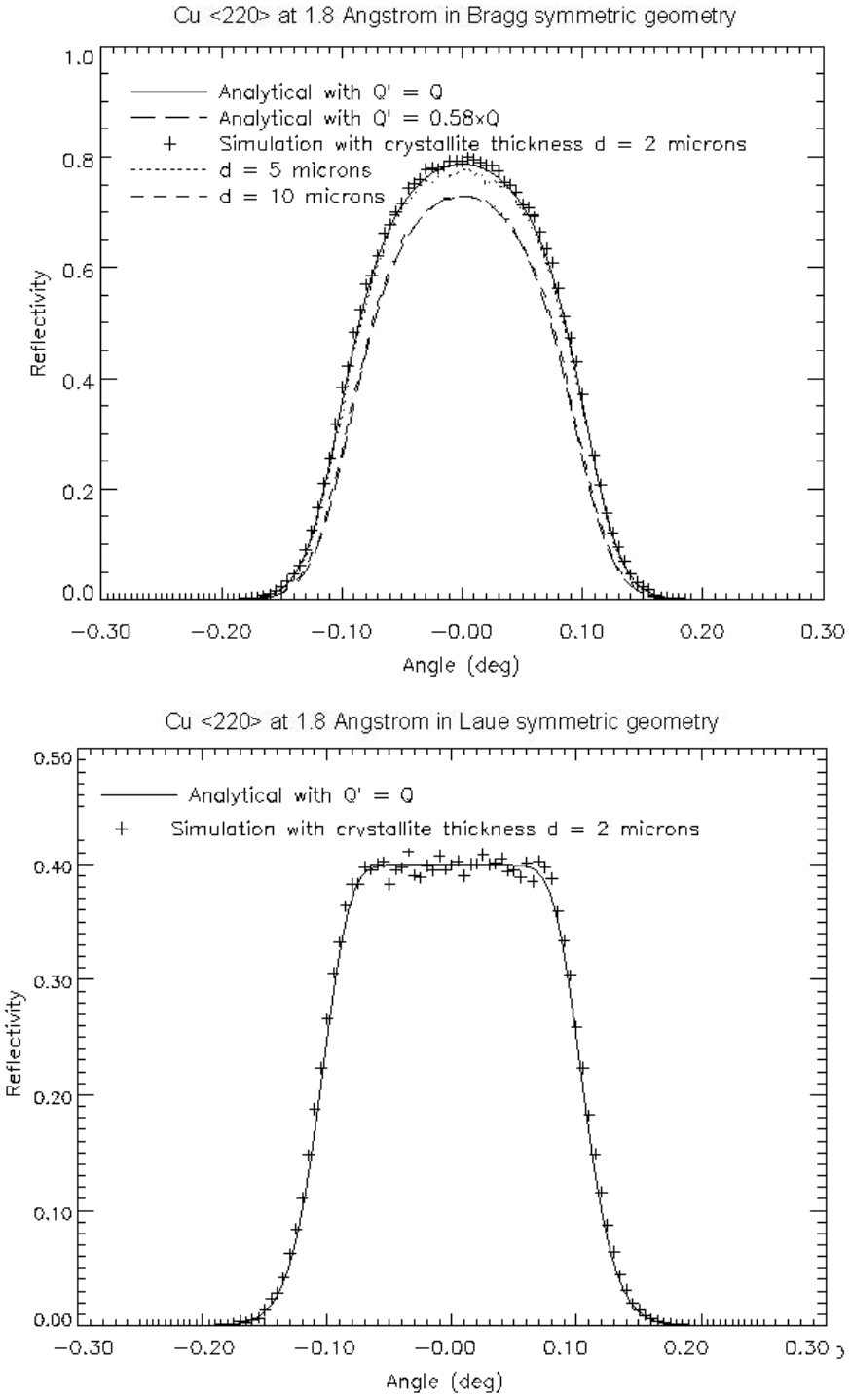

Figure 3.3: *Neutron reflectivity of copper versus* $(\theta - \theta_B)$*, with* $\theta_B = 44.8^o$*,* $\eta = 0.1^o$*, d = 1 cm. TOP: Bragg geometry. The simulations were performed using several values for the crystallite size:* $t = 2\ \mu m$ *(+ symbols),* $t = 5\ \mu m$ *(dotted line) and* $t = 10\ \mu m$ *(dashed line). The analytical curves with* $Q' = Q$ *(solid line) and* $Q' = 0.58 \times Q$ *(long dashed line) fit well the simulations with* $t = 2\ \mu m$ *and* $t = 10\ \mu m$ *respectively. BOTTOM: Laue symmetric geometry.*

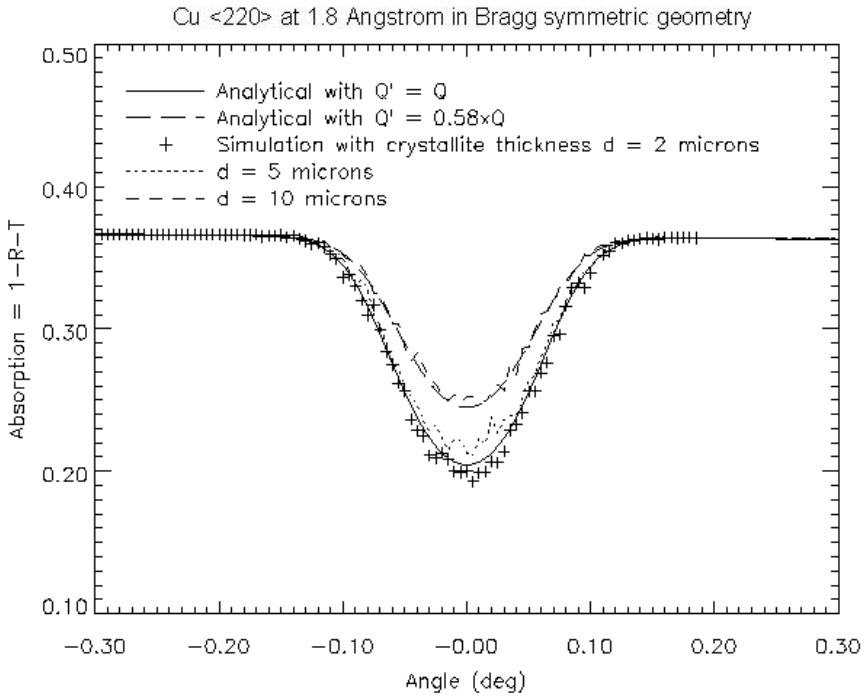

Figure 3.4: *Attenuation for the same case reported in Fig. 3.3 (top).*

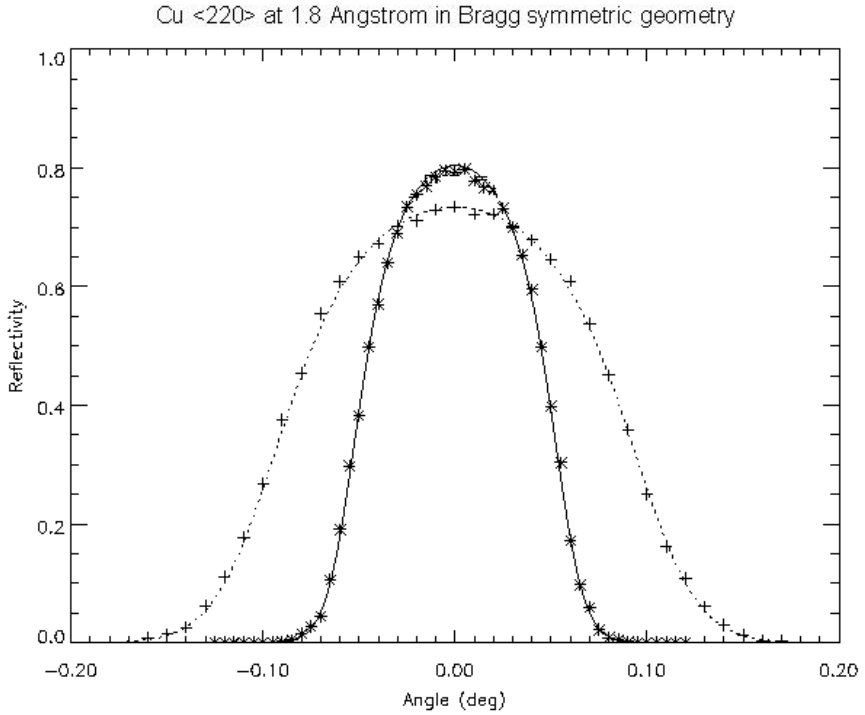

Figure 3.5: *Reflectivity of a copper crystal with an asymmetric mosaic distribution given by Eq. (3.1). The two rocking curves correspond to the two perpendicular planes of diffraction with $\eta_s = 0.1^o$ (+ symbols) and $\eta_p = 0.05^o$ (* symbols). The crystallite size was 10 μm and the analytical curves (dotted and solid lines respectively) were calculated using $Q' = 0.6 \times Q$.*

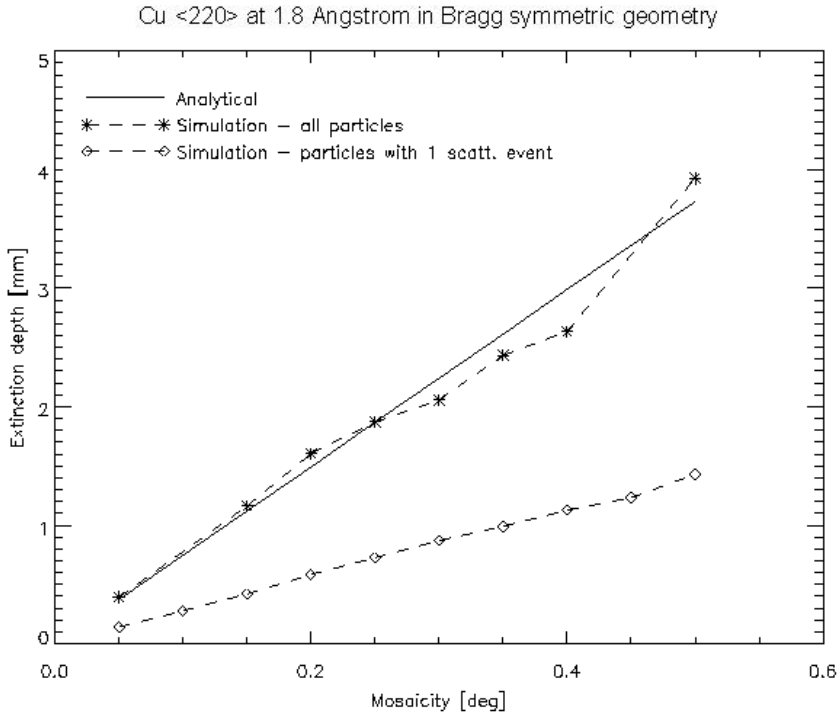

Figure 3.6: *Secondary extinction depth τ_{ext} versus mosaicity η for copper with $\lambda = 1.8$ Å. Data correspond to the exact Bragg position for the Bragg symmetric geometry. The analytic result is the solid line and the * symbols are the result of the simulation, obtained as the averaged maximum penetration depth reached by the reflected particles. The results with only one scattering event (diamond symbols) do not give the correct extinction depth.*

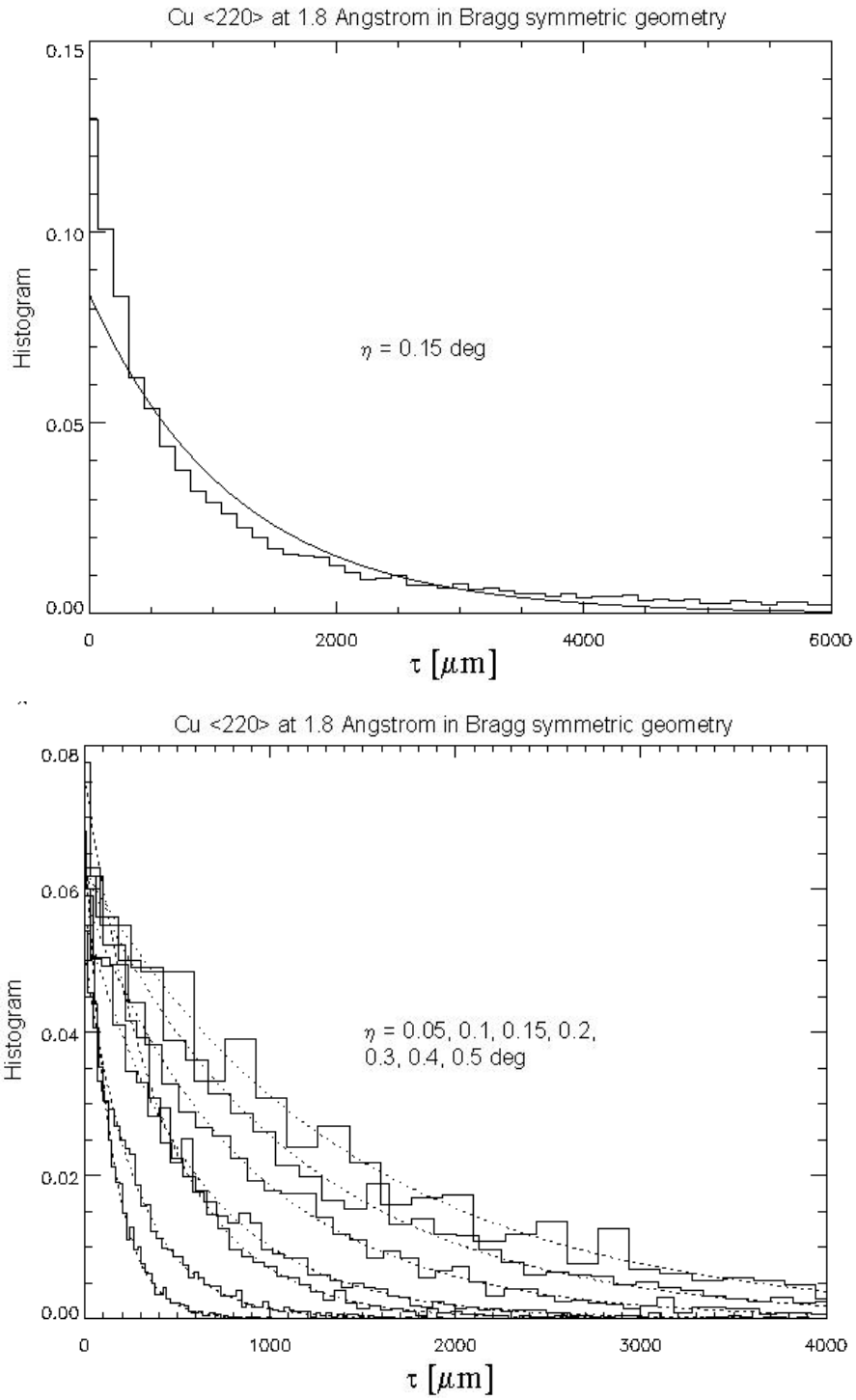

Figure 3.7: *Histograms of the maximum depth τ reached by the reflected particles inside the crystal at the exact Bragg angle and in Bragg symmetric geometry. TOP: the histogram is the result of the simulation for all rays. The solid line is the fit with an exponential function showing that this shape is not appropriate. BOTTOM: the histograms are the simulation result for several values of mosaicity (increasing values of η from top to bottom). Only rays having undergone one scattering event are considered. The exponential fit (dotted lines) shows that for these rays the extinction law follows an exponential law.*

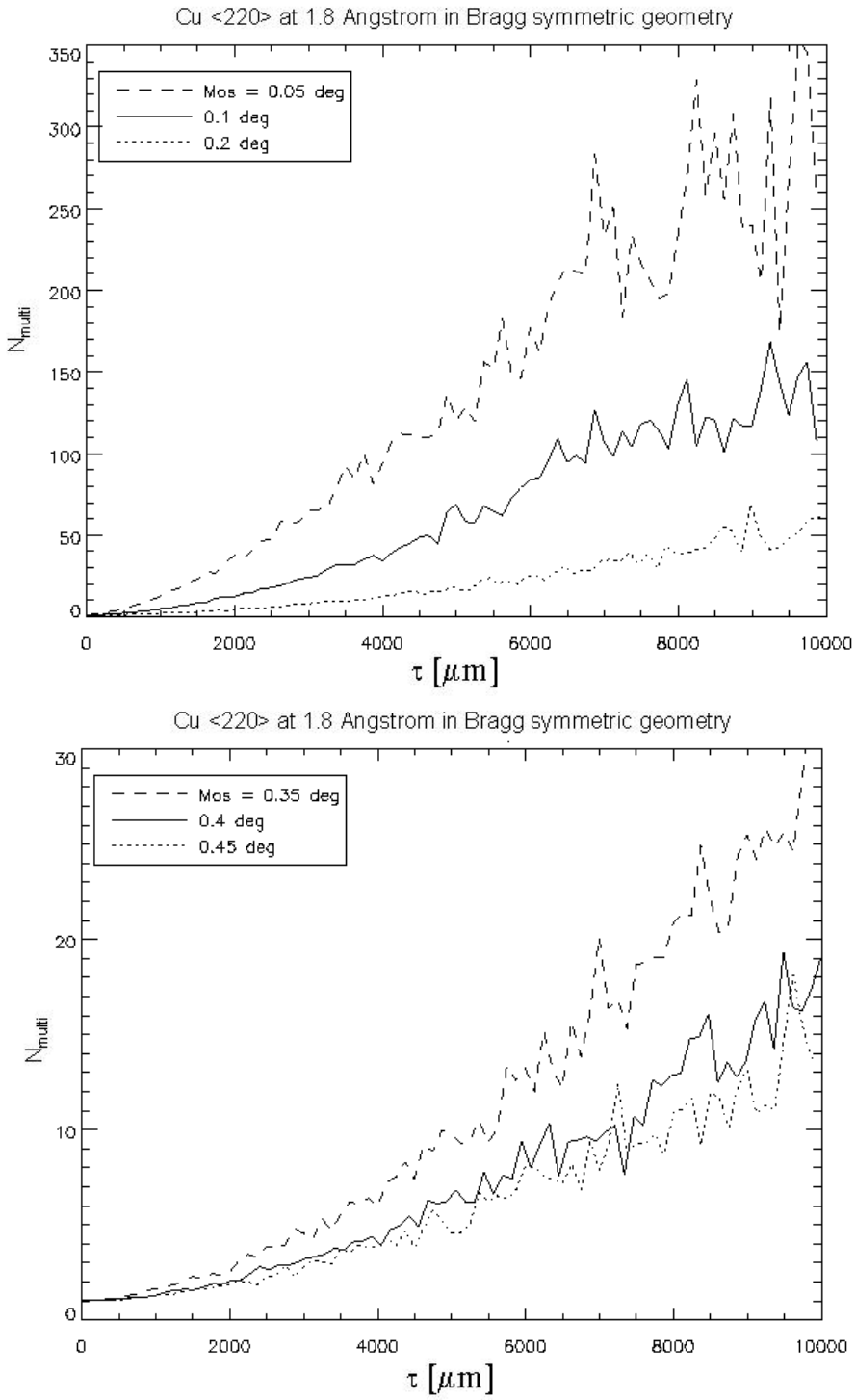

Figure 3.8: *Number of scattering events N_{multi} versus the maximum depth τ reached by the reflected particles. These data correspond to the exact Bragg angle and Bragg symmetric geometry. TOP: $\eta = 0.05^o$, 0.1^o and 0.2^o. BOTTOM: $\eta = 0.35^o$, 0.4^o and 0.45^o.*

3.1.3 Inhomogeneous crystals

The presence in mosaic crystals of regions in which the Bragg planes have a macroscopic misorientation with respect to the nominal value, and also with respect to the usual mosaic distribution, is a very common problem. In these cases a lower peak reflectivity and a splitting of the Bragg peak can be observed. The first effect can be easily explained by the reduced diffracting volume inside the crystal. Using the Monte Carlo method we can give a rather precise estimation of it, if the shape and distribution of the inhomogeneities are known. Let us suppose that the inhomogeneous zones have spherical shapes with radius r (or with r following a given probability distribution) and are distributed randomly with a number density N. We will use a general method for sampling the probability that the particle trajectory meets one of these regions [66]. The probability of collision with a sphere after travelling a short distance dx is

$$dp = N\sigma dx \tag{3.2}$$

where $\sigma = \pi r^2$ is the geometrical cross section. Then the probability $p(x)$ that the particle travels a distance x before meeting the sphere is

$$p(x) = \frac{1}{\lambda} e^{-\frac{x}{\lambda}} \tag{3.3}$$

where $\lambda = 1/N\sigma$ is the mean free path. We can sample x using Eq. (3.3) and, when the trajectory length equals x, determine what is the sphere position with respect to the particle's motion line, with the angles drawn in Fig. 3.9. The probability distribution for α is [66]

$$p(\alpha) = 2\,\mathrm{sin}\alpha\,\mathrm{cos}\alpha \tag{3.4}$$

α can vary between 0 and $\pi/2$, corresponding to tangential and head-on collisions respectively. The angle γ is sampled uniformly in the interval $(0, 2\pi]$. The coordinates of the center of the sphere are calculated and the propagation inside the sphere is followed in the usual way, except for the fact that now a new sampling of the macroscopic misorientation has to be carried out. When the particles exit the inhomogeneous region, the process of sampling the path length before a new intersection is started again.

The plots shown in Fig. 3.10 are obtained by forcing the particle to meet one inhomogeneity immediately close to the incidence surface. When this condition is not applied, the peak reflectivity is not decreased with respect to the theoretical value, but the tails are still larger.

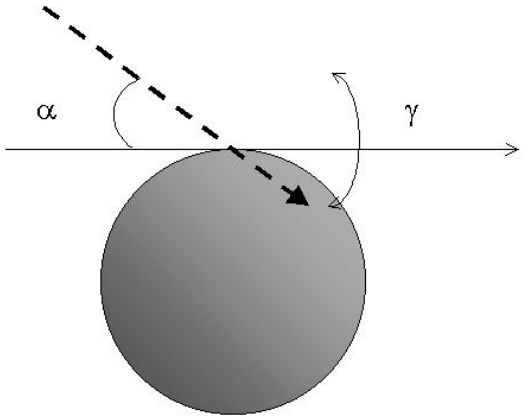

Figure 3.9: *Intersection between the simulated trajectory and the sphere representing an inhomogeneity.*

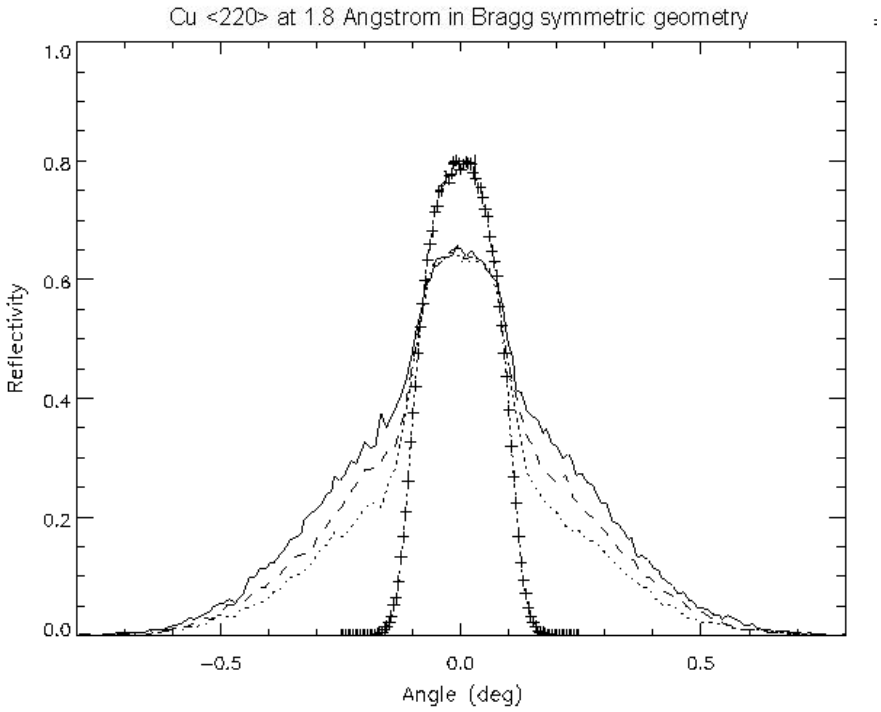

Figure 3.10: *Diffraction profiles of copper with $\eta = 0.1^o$. The + symbols represent the ideal homogeneous crystal and the other lines are the results for crystals with inhomogeneities (i.e. regions with a larger mosaicity η_i =0.5°) of spherical shape with r = 1 mm. The different curves correspond to different inhomogeneity densities: 0.02 mm^{-3} (dotted line), 0.05 mm^{-3} (dashed line), 0.01 mm^{-3} (solid line).*

3.2 Ray-tracing using *MOSAIC*

The simulation results presented in this and the following Chapters were viewed and analyzed using the graphical and manipulation tools of the x-ray simulation code Shadow [28, 29] and its user interface ShadowVUI [2]. In order to do this the data files generated by *MOSAIC* were re-written in the Shadow format and, in some cases, were used as a Shadow input file for carrying out the ray-tracing from the crystal element to the image plane or other instrument positions. This allowed: 1) linking *MOSAIC* to sources created by Shadow; 2) re-tracing rays from the crystal to other planes, for instance to the image plane; 3) visualising the beam characteristics using the powerful ShadowVUI graphical tools. We will call *Crystal* the Shadow file containing the beam properties at the crystal optical element and *Image* those at the image plane.

In order to understand the pictures which will follow, one has to remember that in Shadow the reference frame changes from one optical element to the next and also from the optical element to the image plane. In other words, the ray coordinates are always written in a local reference frame in which: the x-axis is always normal to the scattering plane; the y-axis is directed along the local optical axis in the case of image planes and lies on the crystal surface in the case of a crystal element; the z-axis is always in the plane of scattering, normal to the surface in the case of a crystal element.

This implies that the *Crystal* file is easily written by simply translating the *MOSAIC* data file. The *Image* file, instead, is obtained by re-tracing the rays of *Crystal* to the image plane, then by re-writing their coordinates and direction cosines in the new reference frame.

The following sections report some ray-tracing results using *MOSAIC* as Shadow module.

3.2.1 Diffraction of a collimated monochromatic beam

When an ideal mosaic crystal and an ideally collimated and monochromatic incident beam are set for exact Bragg reflection, the reflected beam will have the following properties: 1) intensity equal to the theoretical peak reflectivity; 2) divergence approximately equal to the Darwin width in the plane of scattering; 3) divergence approximately equal to $\delta\theta_\perp \sim 2\eta \sin\theta_{Bragg}$ in the perpendicular plane. Here we show the results for a 2 mm thick Cu crystal with $\eta = 0.2^o$. The theoretical peak reflectivity is $r = 0.57$. The simulated intensity, normalised to the total number of events, is $I/I_0 = 5570/10000 = 0.557$ with a statistical error $\sigma_I = 2.34\%$. The distribution of the reflected beam direction cosines are shown in Fig. 3.11. The divergence in the scattering plane is approximately $\delta\theta_\parallel = 58\,\mu$rad, which is the Darwin width of the crystallite. In the perpendicular direction it is equal

to $\delta\theta_{\perp} = 4.68$ mrad $= 0.268^{o} \sim 2\eta \sin\theta_{Bragg}$. The average number of diffraction events inside the crystal slab, at the peak position, is $N_{multi} = 10.3$ and the average penetration depth is $< \tau >= 1.25$ mm. Following Zachariasen [37], if the effect of primary extinction is neglected, the secondary extinction coefficient can be calculated as $\sigma_{ext} = Q \times W\,(\theta = \theta_B)$. In our case the theoretical value is $\sigma_{ext} = 6.69$ cm^{-1}, thus giving $\tau_{ext} = 1.5$ mm. This value matches well with the simulation result for $< \tau >$, as the order of magnitude is the same and they are directly comparable from a conceptual point of view.

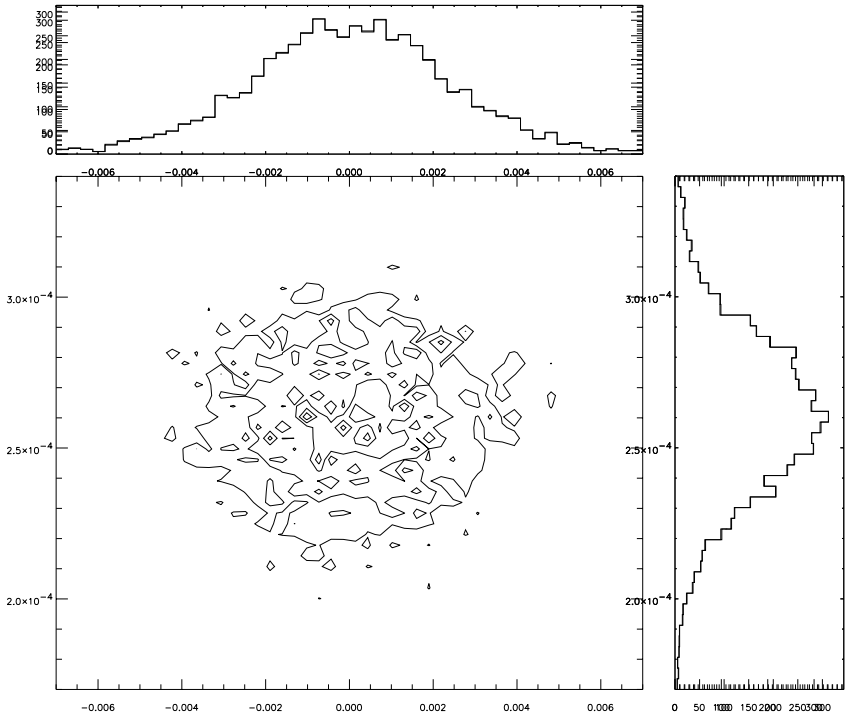

Figure 3.11: *Reflected beam divergence for an incident collimated monochromatic beam. The x-axis and y-axis represent respectively divergence in the direction perpendicular and parallel to the diffraction plane. The Bragg angle is $\theta_B = 44.8^{o}$. Units are radians. Note the different scales in the horizontal and vertical axes.*

3.2.2 Parafocusing properties of mosaic crystals

As shown in Fig. 3.12 flat mosaic crystals produce an interesting pseudo-focusing effect in the plane of scattering in the presence of a monochromatic divergent incident beam [67, 68]. This means that, if we use a point source and p is the source to crystal distance, then the image at a distance $q = p$ is a segment perpendicular to the diffraction plane. An example is shown in Fig. 3.13 where we have $p = q = 100$ cm. The point source emits rays in a cone of aperture $\alpha = 2^{o}$. Its image at a distance q from the crystal is a approximately 0.3 cm wide and 8 cm high. The broadening is due to the finite crystal

thickness (2 mm in the simulation). The image of the same kind of source, but with two separated values of wavelength, can be observed in Fig. 3.14. A qualitative comparison between the simulation and measured data for x-ray diffraction by HOPG is shown in Fig. 3.15.

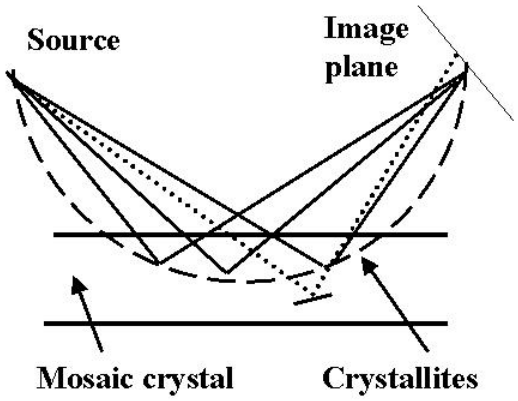

Figure 3.12: *Schematic view of the parafocusing effect by mosaic crystals.*

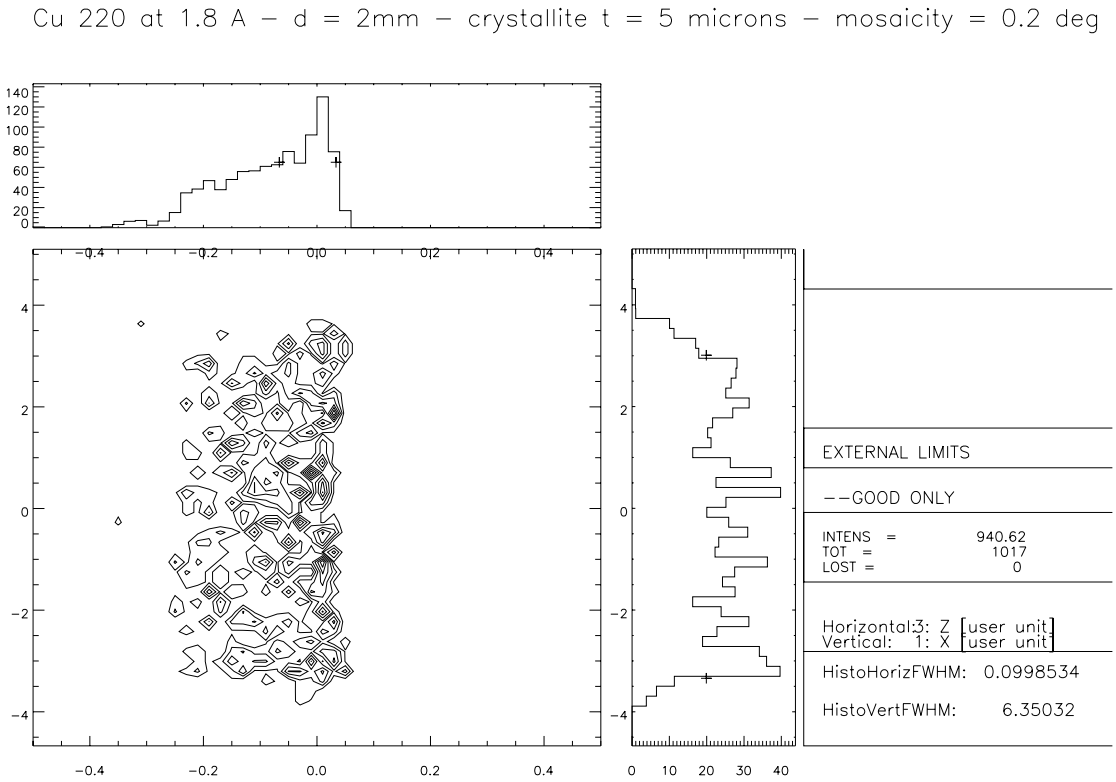

Figure 3.13: *Image of a point divergent monochromatic source. The x-axis and y-axis are respectively parallel and perpendicular to the diffraction plane. Units are cm. The Bragg angle is* $\theta_B = 44.8^o$.

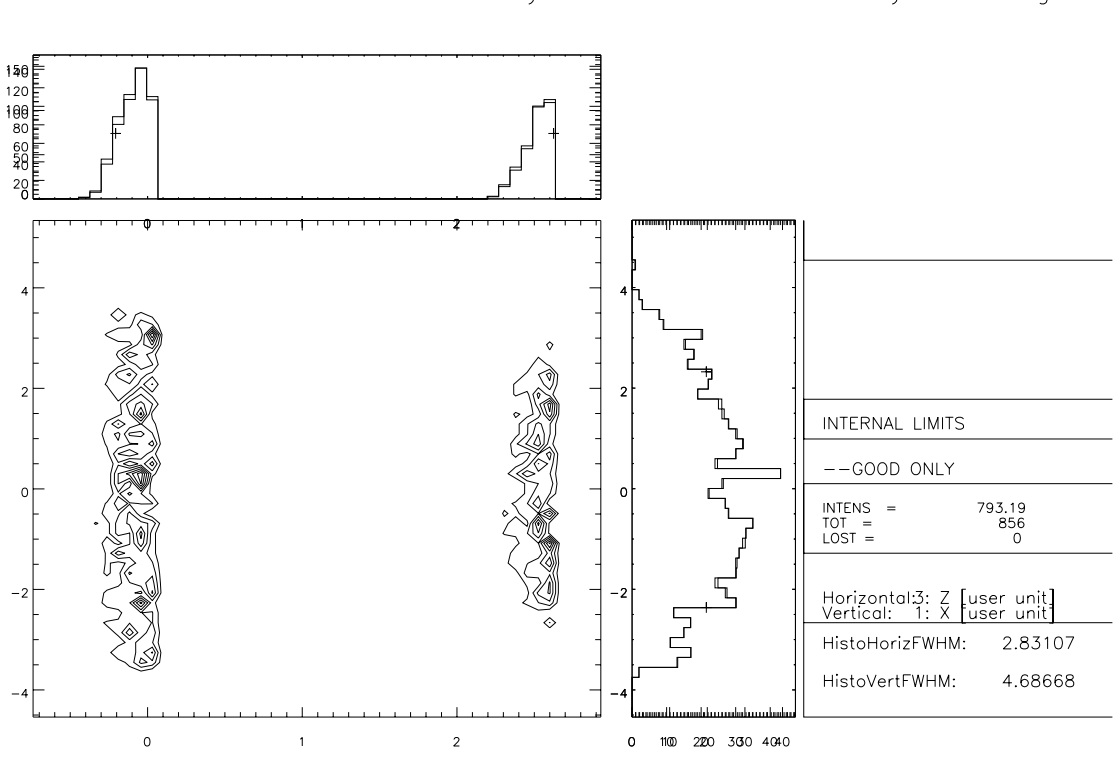

Figure 3.14: *Image of a point divergent monochromatic source with two wavelength lines. Units are cm.*

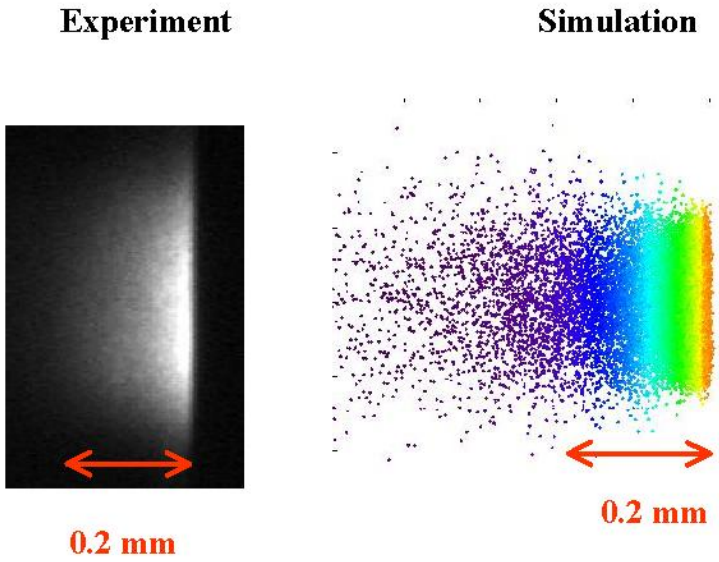

Figure 3.15: *Graphite* $< 002 >$, $\lambda = 0.86$ *Å*, $\theta_B = 7.4^o$. *Image of a divergent and highly monochromatic x-ray source. The source size is 30* μm.

3.3 The *BENT* Monte Carlo code

The *BENT* code used for simulating the diffraction properties of bent perfect and bent mosaic crystals is similar to the *MOSAIC* code described in section 3.1 for the undistorted mosaic crystal. It has simply been modified in the part concerning the surface and Bragg plane orientations. If we suppose that the crystal is cylindrically (and elastically) bent to a radius R, then the deviation of the Bragg planes from the orientation they have in the undistorted crystal will be [56, 69]:

$$\epsilon = \frac{|z|}{R}(\cot\theta - \nu\tan\theta_{Bragg}) \tag{3.5}$$

where θ is the ray grazing angle, ν the Poisson's ratio and $|z|$ the depth below the incidence crystal surface. The first term on the right side of Eq. (3.5) is geometrical and the second accounts for the fact that, if the crystal density stays constant, then there is a linear variation of the d-spacing.

The code can also be used for simulating bent perfect crystals: in this case the ray trajectory is no longer determined by interactions with the crystallite agglomeration as described in section 3.1. The fundamental steps of the trajectory take place between one *perfect lamella* and the next. The lamella thickness is an input parameter for the simulation, it is a function of R, ν (deformation), Bragg angle and Darwin width, and is calculated as in the *lamellar model* described in section 2.5.1. Then the fundamental assumption is that each lamella is homogeneous, that it diffracts as a small perfect crystal according to the dynamical theory, with the Bragg plane orientation following Eq. (3.5). The *BENT* code can therefore also be used for *gradient crystals*, provided that Eq. (3.5) is replaced by an expression accounting for the deformation due to the d-spacing gradient. In this thesis we have not used this application for simulating gradient crystals, so we will only report on the case of deformation due to bending.

Fig. 3.16 shows the reflectivity curve for a mosaic bent Ge crystal in Bragg symmetric geometry. The bending radius is $R = 5$ m and the mosaicity is $\eta = 0.03^o$. The primary extinction depth inside the perfect undistorted crystal is $t_{ext} = 12$ μm. The simulated reflectivity using a crystallite thickness $t = 2$ μm is very well fitted by the theoretical curve calculated with the *layer coupling model*.

In the case of bent crystals the analytical calculation of an *equivalent secondary extinction depth* is not straightforward. However, as we did in section 3.1.1 for mosaic copper, we can calculate the parameters $< \tau >$ and N_{multi}, which are related to extinction. For the exact Bragg angle (peak of the reflectivity curve in Fig. 3.16), the simulation gives an average path length $path = 1.9$ mm and an average value for the multiple diffraction events $N_{multi} = 1.5$. The average penetration depth is $< \tau >= 0.76$ mm. When compared

to the copper data in section 3.1.2 (mosaicity $\eta = 0.1^o$: approximately the same FWHM and peak reflectivity as that of bent germanium, but a different Bragg angle), we see that the values of $< \tau >$ are similar, but for bent germanium N_{multi} is approximately two orders of magnitude less.

3.4 Ray-tracing using *BENT*

In order to understand how resolution and intensity are changed when the crystal is bent we will look at the reflected images obtained by using different kinds of sources. We will always consider Ge $< 311 >$ at 2.4 Å, bent to $R = 7$ m. The theoretical peak reflectivity is $r = 0.81$ and the FWHM of the diffraction profile is $w = 0.12^o$. The Bragg angle is $\theta_B = 44.7^o$. This value for the Bragg angle has been chosen because the geometry is similar to that of Cu $< 220 >$ at 1.8 Å, with $\theta_B = 44.8^o$, analysed in section 3.2.1. Thus we will do a short comparison between the two crystals without discussing the (different) applications that they have in neutron instrumentation. Furthermore, we will not mention the focusing effect of bent crystals, although this is of primary interest when they are used as monochromators.

3.4.1 Diffraction of a collimated monochromatic beam

When a bent crystal and an ideally collimated and monochromatic incident beam are set for exact Bragg reflection (with respect to the crystal pole), the reflected beam will have an intensity equal to the theoretical peak reflectivity only in the limit of a pencil incident beam. When the beam size increases the intensity decreases due to the fact that the correct orientations of Bragg planes for different parts of the beam are found at different depths and at different positions in the crystal plane. Therefore, absorption plays an important role and there may be particles which never meet the Bragg condition due to the finite crystal thickness. These restrictions are less important when the crystal has a mosaicity, as in the case of our simulations, because the effect of mosaicity is that of "convoluting" the reflectivity of the small perfect lamellae of which the crystal is composed (according to the schematization used in the model) with the mosaic distribution. The simulation with a circular source of radius $\rho = 5$ mm gives a normalised intensity equal to $I/I_0 = 10840/25000 = 0.43$ with a statistical error $\sigma_I = 1.59\%$, where the theoretical peak reflectivity is $r = 0.81$. The reflected beam divergence is $\delta\theta \sim 0.1^o$ in the directions both parallel and perpendicular to scattering. If we use a source with $\rho = 1$ mm then the reflected intensity is $I/I_0 = 17437/25000 = 0.7$, much closer to the theoretical value. The divergence along the diffraction plane is much lower than before: $\delta\theta \sim 0.0355^o$.

3.4.2 Diffraction of a polychromatic divergent incident beam

In order to compare the intensity and resolution diffracted by a mosaic crystal and a bent crystal, we have to choose: 1) realistic values for the properties of the source, i.e. wide enough wavelength and angle ranges; 2) similar geometrical conditions, i.e. Bragg angles. For the sake of simplicity we will always use a point source. In a full simulation of an instrument or part of an instrument the actual source size has to be used instead. As mentioned before, this is just an example of the possible applications of the *MOSAIC* and *BENT* codes, not at assessment of the general performance of the two types of crystals, since they have different purposes. The crystal parameters, theoretical peak reflectivities and angular widths, and the simulation results, are shown in Table 1. The two crystals have comparable theoretical peak reflectivities, but the germanium diffraction profile is $\sim 60\%$ that of copper. The integrated diffracted intensities as obtained by the simulation are $I_{Ge}/I_{Cu} \sim 60\%$ (see column n^0 10), and the resolution is better in the case of germanium.

Table 1. *Comparison between intensity and resolution of the beam diffracted by mosaic copper and mosaic bent germanium. The source is non monochromatic, with an incident wavelength spread of* $\pm$ *3 %. It emits 25000 rays following a conical angular distribution with aperture* $\alpha = 2.64^o$*. The last three columns are the simulation results: normalised intensity, angular and wavelength spread of the reflected beam.*

Crystal	λ Å	θ_B deg	R m	η deg	Theor. peak reflect.	Theor. width deg	I/I_0	$\Delta\theta$ deg	$\Delta\lambda/\lambda$ %
Cu 220	1.8	44.8	∞	0.1	0.79	0.19	0.023	1.2	3.5
Ge 311	2.24	44.7	7	0.05	0.81	0.12	0.014	0.81	2.2

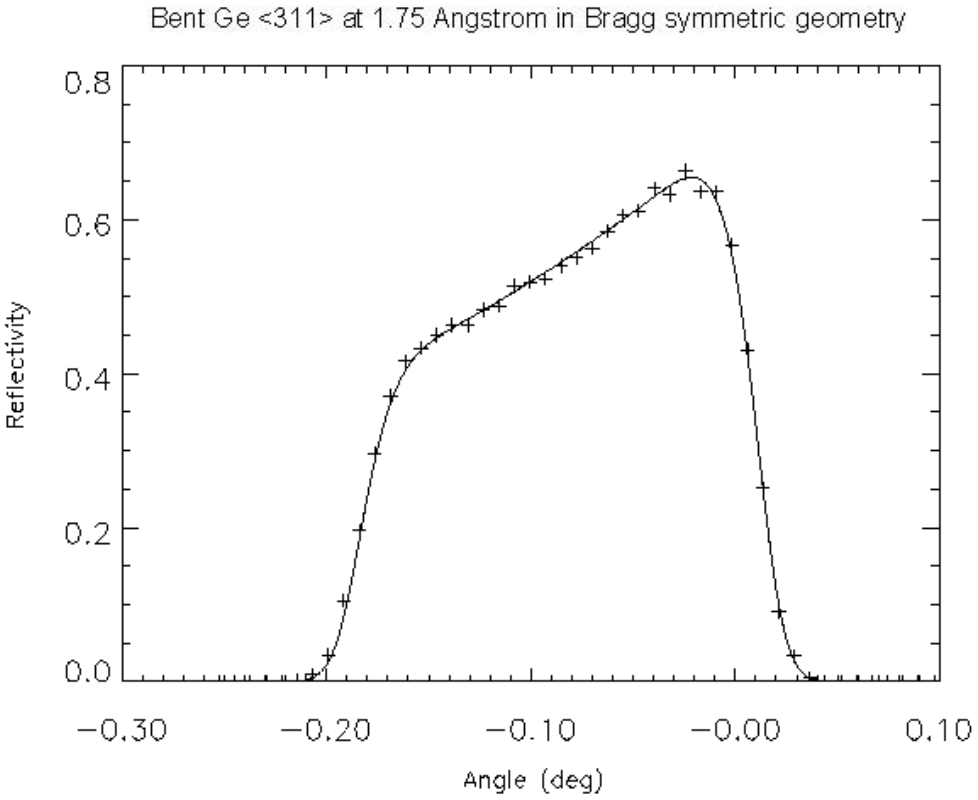

Figure 3.16: *Reflectivity of a bent mosaic germanium crystal versus* $(\theta - \theta_B)$ *in Bragg symmetric geometry.* $R = 5$ *m and* $\eta = 0.03^o$*. The + symbols are the simulation result and the solid line is the diffraction profile calculated using the layer coupling model.*

3.5 Summary and conclusions

One of the aims of this thesis is to try to improve the existing methods employed for describing neutron diffraction by crystal monochromators or analyzers. Accurate and intensive calculations are needed for the simulation and optimisation of neutron instruments. The theoretical models described in Chapter 2 and the derived equations may be not sufficient for these purposes, because they use some assumptions that are not generally satisfied. Moreover, they describe only partially the crystal behaviour, for example they allow computing the diffracted intensity, while other important parameters as the beam penetration into the crystal, the change in beam divergence, etc. are not available.

In this Chapter we have tried to develop general methods for accurately describing the imperfect crystals of interest for neutron optics. We have presented two codes, the first one to simulate neutron or x-ray Bragg diffraction by mosaic crystals, and the second for bent (perfect or mosaic) ones. Their extension to gradient crystals has not been discussed, but is straightforward.

The technique we exploit is the full Monte Carlo method to solve the transport equations. Therefore, our codes allow us to control all the geometrical and physical parameters governing scattering by the crystals. The main application is the modelling of the crystal element in a neutron scattering instrument and we will describe the results of the new *Strain Imager* instrument simulation in the next Chapter. This code could be integrated in new or existing ray-tracing codes, and it is supposed to be more accurated than existing "macroscopic" models. Our MC code has been fully benchmarked against the analytical models described in Chapter 2. It can also be used to model crystal inhomogeneities, an option that is not available in analytical models. Moreover, we show that it can be applied to some cases which probably cannot be simulated by simple ray-tracing. In this Chapter we have shown the case of the parafocusing effect of mosaic crystals, by comparing the simulations with the experimental x-ray data. In Chapter 6 we will use the MC code to analyze the shape of x-ray diffraction topographs, obtaining a very good agreement with the experiments.

Chapter 4

Simulation of the Strain Imager instrument

4.1 The Strain Imager instrument at the ILL.

The new *Strain Imager* instrument at the ILL, which is being built on the H22 guide, will be a high resolution diffractometer allowing the measurement of strain in materials [71]. The neutron strain scanning technique is a powerful tool for the determination of residual stress in materials and mechanical components. The method exploited by this technique is the measurement of the displacement $\delta\theta$ of a given Bragg peak in the crystal bulk, caused by a strain ϵ. By differentiating the Bragg's law, one sees that strain is related to $\delta\theta$ and to the the strain-free Bragg angle $\theta_{B,0}$ by the relation:

$$\epsilon = \frac{d_H - d_{H,0}}{d_{H,0}} = -\delta\theta \cot\theta_{B,0} \tag{4.1}$$

The high penetration depth of neutrons in materials allows measuring strain in small and big samples, which may be of interest for material scientists (new materials development) and for industrial users (control of component treatments as hardening or welding).

The requirements for a strain imaging instrument are high flux and good angular resolution for the beam at the sample and expecially at the detector position. The angular resolution is needed for separating neighbouring peaks and for precisely determining their position. Moreover, the *gauge volume*, i.e. the diffraction volume "seen" by the incoming beam and contributing to the diffracted beam reaching the detector, has to be carefully determined. A schematic layout of the *Strain Imager* is shown in Fig. 4.1: the beam, transported by the guide and monochromatized by the crystal monochromator, is then

focused at the sample position by a radial Soller collimator made of absorbing blades; the slit after the sample selects a portion of the diffracted beam which hits the position sensitive detector. The shape of the gauge volume is determined by the optical elements before the sample (primary optics) and by the slit (or collimator, depending on the design) after it. The ideal monochromator for this instrument would be a perfect crystal with a d-spacing gradient or with elastical bending. This would eliminate the disadvantages of mosaic crystals: large penetration depth with consequent large absorption and the reflected beam affected by the possible inhomogeneities in the mosaic distribution. The production of crystals with a suitable gradient cannot yet be achieved. Hence, a possible choice is that of bent crystals. These crystals allow focusing the beam at the sample position, but strongly influence the angular (and energy) resolution. Current technology allows bending silicon and germanium with success. Previous studies of the instrument efficiency have suggested which reflections, bending radii and crystal dimensions have to be used [72, 73, 74, 75]. For the most used samples, a wavelength range from 1.5 to 3.5 Å is suitable. The monochromator Bragg angles suitable for residual stress analysis lie between 35^o and 60^o. In order to fit these needs to the geometrical constraints (limited crystal length) and to the resolution requirements (depending both on the monochromator and sample Bragg angle) two crystals have been chosen: a mosaic germanium $< 422 >$ and a perfect elastically bent silicon $< 111 >$ made of a "packet" of 4 crystal wafers 2 mm thick. Elastic bending, without mosaicity, becomes inefficient in some geometrical conditions, i.e. when the angle between the Bragg planes normal and the incident beam direction, is small. In these conditions the incident beam does not "see" the bending of the diffracting planes, hence the integrated reflectivity is small. For this reason, the germanium crystal will have a mosaic spread $\eta = 6'$ (FWHM). Other Bragg planes, with asymmetric angles α with respect to the crystal surface, might be used for the germanium crystal. The asymmetric cut allows to condense the reflected beam or to use a more extended crystal monochromating volume depending on the value of α (the so-called *Fankuchen* and *anti Fankuchen* set-ups).

In the following discussion and calculations we will not deal with vertical focusing. This is necessary for focusing in the vertical plane at the sample position, but does not, to a first approximation, influence the energy resolution and the angular resolution in the scattering plane.

The equations governing vertical and horizontal focusing by a bent crystal can be written by assuming simple specular reflection from the lattice planes [76, 77, 78]. This model, which is only valid to a first order, says that a perfectly monochromatic beam, emitted by a source placed at a distance p from the crystal, is focused at a distance q according to the equations:

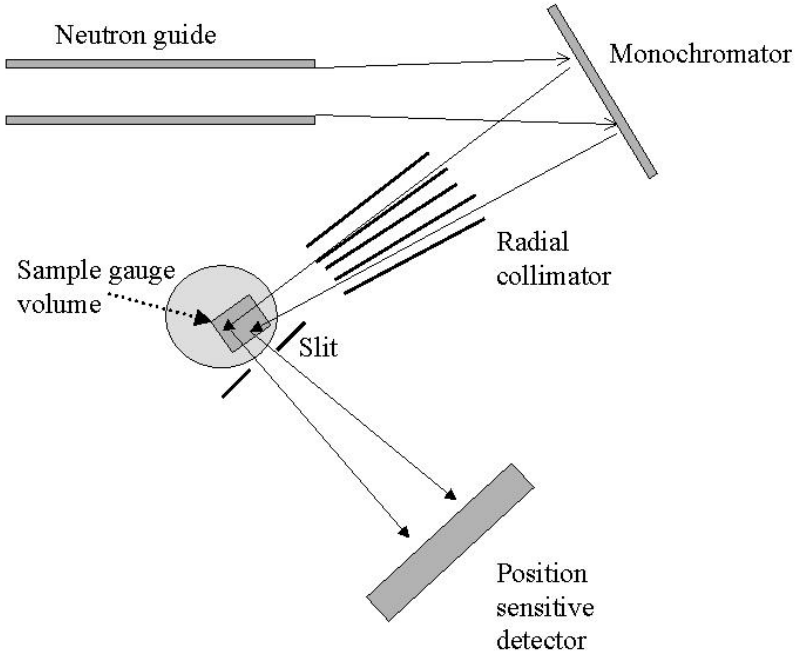

Figure 4.1: *Schematic layout of the Strain Imager as seen from the top. The design of the radial collimator before the sample and of the slit just after it allow choosing a well defined scattering volume inside the sample.*

$$\frac{1}{p} + \frac{1}{q} = \frac{\sin\theta_1 + |\sin\theta_2|}{R_s} \tag{4.2}$$

$$\frac{\sin^2\theta_1}{p} + \frac{\sin^2\theta_2}{q} = \frac{\sin\theta_1 + |\sin\theta_2|}{R_t} \tag{4.3}$$

In the previous equations θ_1 and θ_2 are the incoming and outgoing angles, measured with respect to the crystal surface; R_s and R_t are the radii of curvature in the sagittal and tangential planes. As we do not consider vertical focusing, $R_s = \infty$. The application of the Eqs. (4.2) and (4.3) to neutron beams is seldom possible. The reason is the uncertainty in the position at which the *effective source* is placed. It could be possible to use, as source to crystal distance p, the end of guide or the beam shutter position. In this case we would have $p = 9$ m. However, this would be justified only in the pinhole approximation, i.e. with the source defined by a thin aperture. This is not our case because the beam is 3×20 cm wide, then the crystal sees a source which is difficult to model, as it depends on the full neutron path before exiting the guide. In order to give an idea of the tangential bending radius needed to focus the beam at the sample position ($q = 2.2$ m), we give in Table 1 the R_t values obtained by applying Eq. (4.3) to some typical values of the monochromator Bragg angle. These values were calculated for the Bragg symmetric geometry and for $p = 9$ m and $p = \infty$.

Table 1. *Values of the curvature in the scattering plane obtained using Eq. (4.3). The image to monochromator distance is q = 2.2 m and the Bragg planes are parallel to the crystal surface. The Bragg angles (in the second column) correspond to Ge <422>.*

λ Å	Bragg angle [deg]	R_t [m] for $p = 9$ m	R_t [m] for $p = \infty$
1.2	31.3	6.8	8.5
1.4	37.3	5.8	7.3
1.6	43.85	5.1	6.35
1.8	51.2	4.5	5.65

Of course, focusing and performance of the monochromator (in terms of reflectivity and resolution) depend not only on R_t, but also on other effects such as non monochromaticity of the incident beam, crystal mosaicity and finite thickness. The angular spread $\Delta\theta$ of the beam after the monochromator is determined by the divergence of the incident beam, the radius R_t, the mosaicity η and the crystal thickness. The energy resolution is then $\Delta\lambda/\lambda = \cot\theta_B\,\Delta\theta$ (without considering the smaller effect of the d-spacing spread). Moreover, the final intensity and resolution at the detector depend on the effect of the radial collimator and slits and on the sample scattering angle. This shows that an assessment of the behaviour of the instrument is not straightforward. As we said in the Introduction, there exist both graphical and analytical methods which are able to calculate these parameters. Just to give an example, Cussen [79] has developed a very useful pictorial view of the resolution of neutron scattering instruments, produced using phase-space calculations. However, these methods are not able to account for other effects coming from neutron diffraction in the real monochromator crystal. For this reason the instrument design has already been optimised by using ray-tracing techniques [72]. In the next section we will describe our simulations.

4.2 The simulation

The diagram in Fig. 4.1 shows the elements which the *Strain Imager* is composed of and which have to be simulated. This has already been made by Saroun and Pirling [72] by means of ray-tracing using the RESTRAX program. They have simulated the following elements: a curved supermirror guide made of several sections and with the coating allowing an increase of the angle of total reflection by a factor of two (m=2) when compared with the existing Ni coated guide (m=1) ; the monochromator crystal; the oscillating convergent Soller collimator between monochromator and sample; the ideal polycrystalline sample; the slit between sample and detector.

We made more simulation on a general scale. We focused our attention on the following cases: 1) the dependence on the crystal bending of the intensity and angular resolution of the beam diffracted by the crystal and transmitted by the collimator. The simulations were performed for mosaic bent germanium $< 111 >$ at a monochromator Bragg angle $\theta_B^M = 40^o$. 2) the intensity and the resolution (in energy and angle) at the sample and detector for a bent mosaic germanium $< 422 >$ in the wavelength range $[1.2 - 1.8]$ Å and for two values of mosaicity η. This wavelength range is interesting for the instrument applications.

In this section, we describe the simulation of each optical element. The simulation results will be shown in the next section.

The effective source. This is the starting point for the simulation. As we do not simulate the guide, our source is placed at the end of the guide. As specified in the internal reports, the incident beam will have a width of 30 mm and a divergence of $\sim 0.4^o$, depending on the wavelength and with an almost flat angular distribution [80]. Apart from this, in our simulations, the polychromaticity of the beam is included by choosing also a flat wavelength distribution for the incident beam. The λ range is obviously sufficiently extended for covering all the energy band-width of the primary optics. We use Shadow [28] to generate the source and to trace the polychromatic, extended and divergent beam up to the bent crystal monochromator.

The monochromator. The bent mosaic crystal monochromator is simulated using the *BENT* Monte Carlo code described in section 3.3. We recall that this program can be used for both perfect and mosaic bent crystals. In the present case, i.e. mosaic, it reproduces the reflectivity calculated by using the layer-coupling model. The input parameters are Bragg angle, crystal thickness (no lateral limits were set, although this would be necessary), crystal bending radius, mosaicity, absorption coefficient and the size of the microscopic crystallite. This parameter was set to 1 μm in all the simulations.

The collimator. In order to have a better focus at the sample, the monochromator is followed by a converging collimator made of 44 channels with completely absorbing blades. This is 0.45 m long and its entrance is placed 1.4 m from the crystal monochromator. The blades are 0.08 mm thick and are separated by 2 mm at the entrance and 0.5 mm at the exit. The range of angles accepted by the channel is then approximately $\pm 0.16^o$. The global field of view of the collimator is of 8^o. The entrance surface is 8.8 cm wide. Moreover, in order to eliminate the beam pattern at the collimator exit due to the absorbing blades, it oscillates by $\pm 1^o$ around the zero position. We simulate the collimator in the following way: the rays, after diffraction by the crystal, are traced until they meet the planes corresponding to the collimator entrance and exit. The equations of the points belonging to these planes and corresponding to the collimator channels are written. The

good rays, i.e. those transmitted by the collimator, are found by requiring that they cross the two planes while belonging to the same channel. This method neglects the fact that the real absorbing blades may have a non-zero transmission probability. Concerning the oscillations, these have been included by repeating the calculation we have just discussed over 100 different angular positions of the collimator, covering a range of $\pm 1^o$. The resulting transmitted beam is therefore the average over 100 similar calculations.

The sample. It is essential, for this kind of instrument, to know the resolution at the detector. For this reason the sample and slit also have to be simulated. The sample is treated as a perfect polycrystal. We assume that the it has a size of 4 mm. The first step for simulating the sample is the calculation of a random penetration depth for each ray. We simulate the sample Bragg peak located at a scattering angle of 90^o. The nominal sample Bragg angle is then $\theta_B^{s,N} = 45^o$, the d-spacing is fixed to $d_H = \lambda^N / 2 \sin \theta_B^{s,N}$, with λ^N being the nominal wavelength. The actual Bragg angle for each ray is easily calculated by using its wavelength: $\theta_B^s = \sin^{-1}(\lambda / 2\, d_H)$. The second step in the calculation is the rotation of the direction of each ray by an angle $2\theta_B^s$ in the horizontal plane.

Finally, the *slit*, 1 mm large, is used for defining the sample diffracting volume "seen" by the detector.

The simulation results will be shown in terms of intensity I/I_0, with I being the number of rays weighted by absorption and I_0 the number of rays in the source. Moreover, the typical widths of the spatial, angular and wavelength distributions will be characterised by the FWHMs Δx, $\Delta\theta$ and $\Delta\lambda$, respectively.

4.3 Efficiency and resolution versus bending radius and wavelength

The germanium < 111 > monochromator versus $\mathbf{R_t}$. In the first part of this section we show how the intensity and resolution at the sample position are influenced by the value of the crystal bending radius R_t and by the presence of the collimator. The case discussed here is that of a germanium < 111 > monochromator at $\lambda = 4.2$ Å, with the Bragg angle $\theta_B^M = 40^o$. We will show how intensity and resolution are influenced by R_t and by the presence of the collimator. The results of the monochromator and collimator simulation, as a function of the bending radius, are summarised in Fig. 4.2. The intensity, wavelength spread (not shown) and angular divergence of the beam diffracted by the monochromator monotonically decrease with increasing R_t. The angle and wavelength resolution reach the asymptotic value, that they would have in the case of a flat crystal, for $R_t = 21$ m. The smallest beam size at the sample position, without the collimator, at 2.2 m from the

crystal, is achieved for $R_t = 5$ m and is equal to 1.5 cm (see the image on the top of Fig. 4.3). Then the best focusing conditions are met for $R_t = 5$ m. As shown in the image on the bottom of Fig. 4.3, for $R_t = 5$ m, the collimator reduces the width of the beam at the sample position to ~ 1 mm.

The width (FWHM) of the beam impinging on the collimator entrance ranges from 1 to 2.5 cm (the total width instead ranges from 3 to 6 cm) depending on R_t. It is clear that, in this geometry, not all of the collimator surface is used. The histograms of the transmitted angles before and after the collimator, shown in Fig. 4.4, demonstrate that the collimator reduces the beam divergence only for $R_t \leq 5$ m. For larger values of R_t the angular spread is not decreased. On the other hand, the intensity decreases (see Fig. 4.2) because of the focusing effect. In practice, the collimator absorbs those neutrons whose trajectory does not fulfill the focusing conditions. The absorbed neutrons are those whose diffraction by the crystal monochromator suffers the effects of mosaicity and finite thickness. The collimator geometry is optimised for a bending radius of approximately 5.5 m: the histograms in Figs. 4.4 and the plot of intensity in Fig. 4.2 show that, for $R_t \geq 5$ m, the number of neutrons passing through the collimator decreases dramatically. For $R_t = 5$ m the transmitted intensity ratio is $I_{coll}/I_{mono} \sim 4\%$.

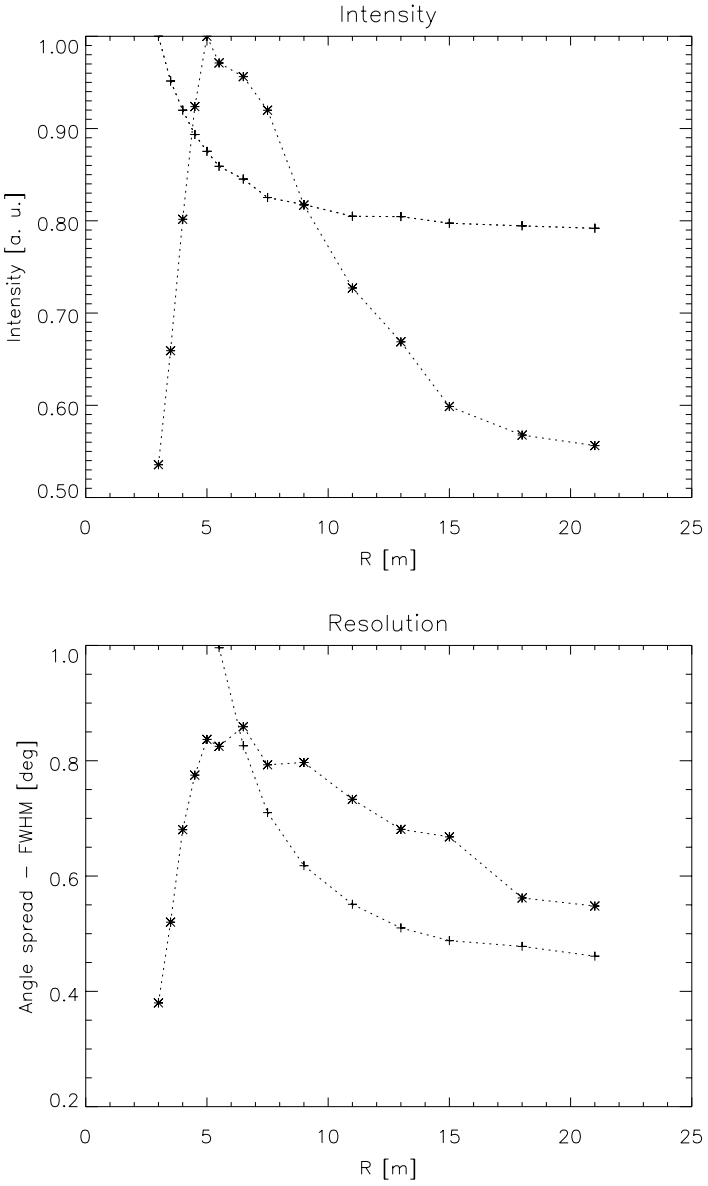

Figure 4.2: *Intensity I/I_0 and angular spread versus the tangential bending radius R_t. The $+$ symbols represent the beam reflected by the monochromator and the $*$ symbols that transmitted by the radial collimator. The intensity after the monochromator and collimator have respectively the maximum values $I_{mono}/I_0 = 7.86\%$ (for $R_t = 3$ m) and $I_{coll}/I_0 = 0.252\%$ (for $R_t = 5$ m). The crystal is Ge <111> with $\theta_B^M = 40^o$.*

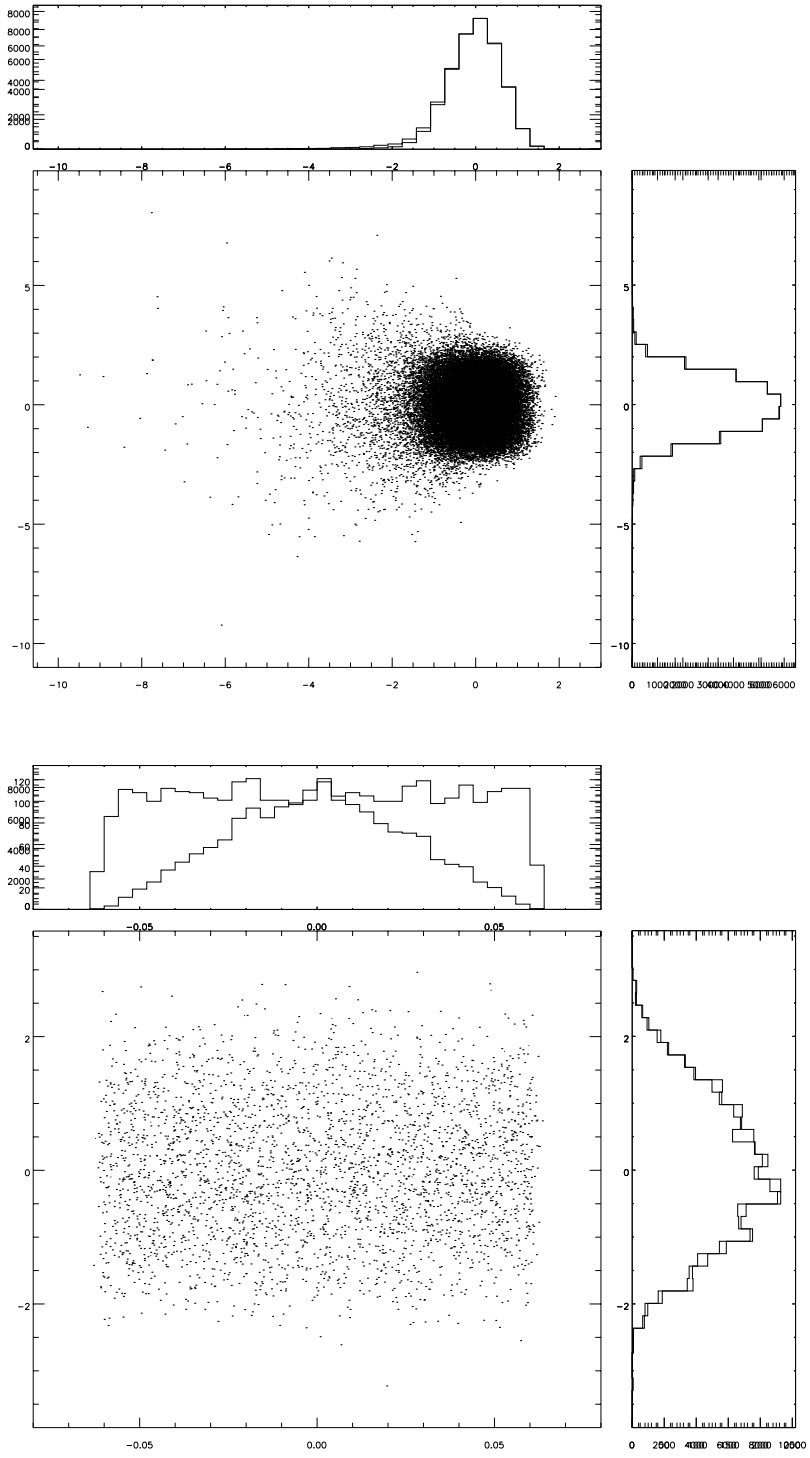

Figure 4.3: *Beam spot at the sample position without (top) and with (bottom) the collimator. The x-axis corresponds to the scattering plane, the y-axis to the perpendicular one. Note the change in scale between the two figures. The histograms show the beam distribution with and without the weight due to absorption. Units are cm.* $R_t = 5$ *m.*

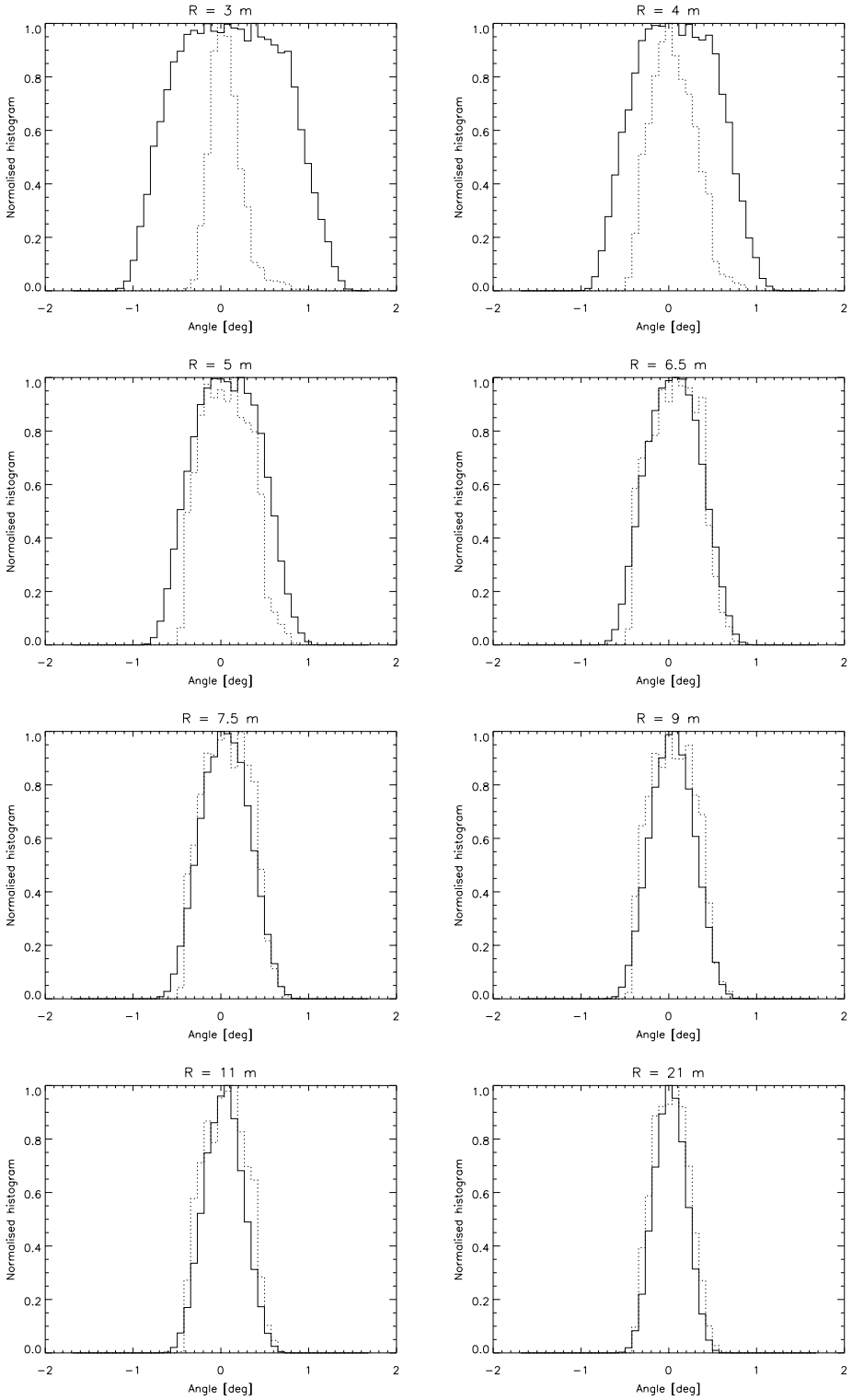

Figure 4.4: *Normalised histograms of angular spread before (solid line) and after the radial collimator (dotted line). The angles are calculated with respect to the optical axis, i.e. the normal to the image plane. The crystal is Ge <111> with* $\theta_B^M = 40^o$.

The germanium < 422 > monochromator versus λ and η. In Fig. 4.5 we show the theoretical rocking curves, calculated using the layer-coupling model discussed in section 2.5.2, for $\lambda = 1.2$ ($\theta_B = 31.3^o$) and 1.8 Å ($\theta_B = 51.2^0$). The bending radius is $R_t = 7$ m. The plots show that, for a mosaicity $\eta = 1'$, the width and shape of the diffraction profiles are determined by the bending of the Bragg planes. The peak reflectivity increases with increasing λ, while the FWHM descreases. When mosaicity is important, $\eta = 6'$, the diffraction profiles hardly show the effect of bending.

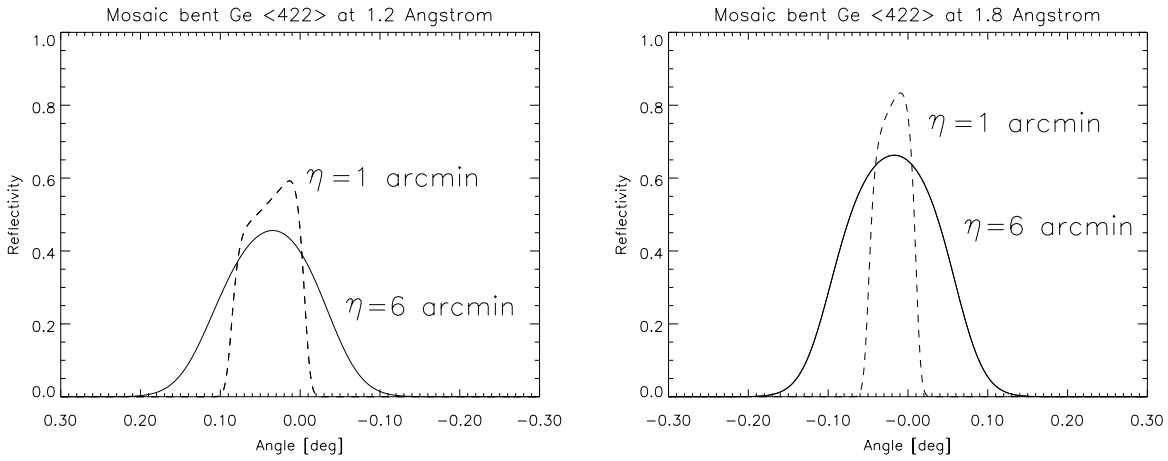

Figure 4.5: *Theoretical reflectivity of germanium <422> with $R_t = 7$ m at $\lambda = 1.2$ Å (left) and 1.8 Å (right). The crystal thickness is d = 0.6 cm and mosaicity is $\eta = 6'$ (solid lines) and $\eta = 1'$ (dashed lines).*

The simulations were made for $\lambda = 1.2$, 1.4, 1.6 and 1.8 Å with a source emitting rays in a wavelength range of ± 0.05 Å about λ. The average incident angular spread was $\sim 0.17^o$ with a slight variation with λ, which should approximately reproduce the guide simulation results [80]. The intensity and resolution (in angle and energy) versus λ, for two different values of mosaicity, are shown in the Figs. 4.6 and 4.7. The intensity at the sample and detector monotonically decreases with increasing λ, i.e. the monochromator Bragg angle. The strong improvement of resolution observed at the detector for higher λ is produced by two effects: 1) the increasing Bragg angle of the monochromator, which increases the crystal intrinsic resolution from 0.93^o at $\lambda = 1.2$ Å to 0.61^o at $\lambda = 1.8$ Å (-34%); 2) the focusing effect by the sample [79]. The increase of the scattered intensity of about 30 to 60% is compensated by a poorer resolution, -25% to -28%, when going from $\eta = 1'$ to $\eta = 6'$.

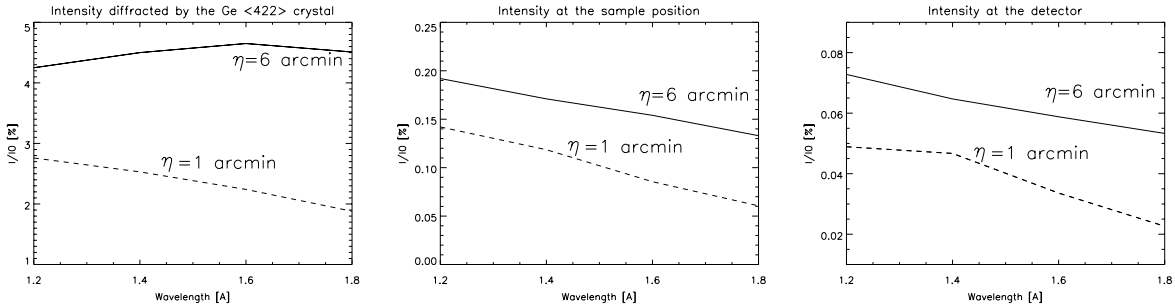

Figure 4.6: *Intensity I/I_0 versus λ diffracted by the bent mosaic Ge <422> monochromator (left), transmitted by the collimator at the sample position (center) and hitting the detector after scattering by the sample (right). The crystal monochromator thickness is* 6 *mm and mosaicity is $\eta = 6$' (solid lines), $\eta = 1$' (dashed lines).*

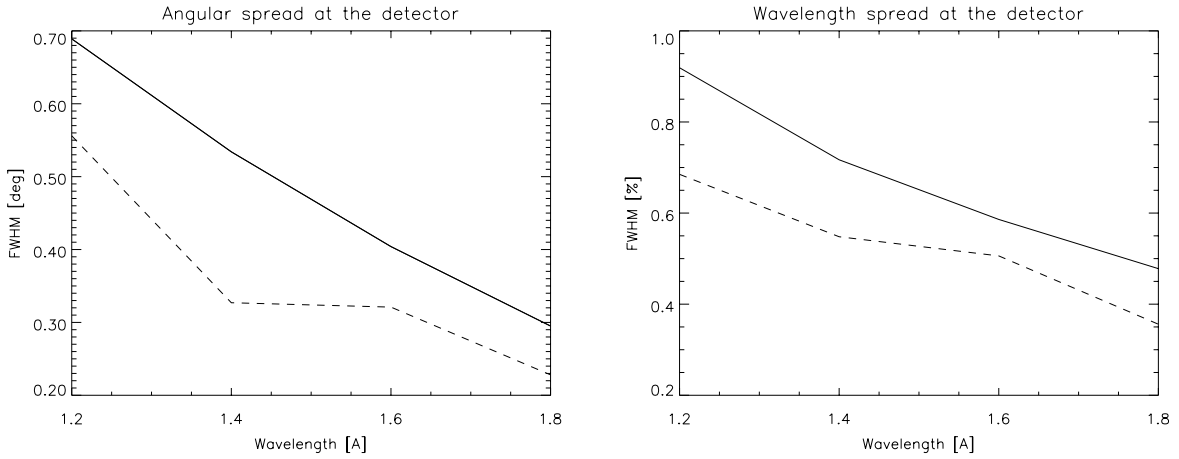

Figure 4.7: *Angular resolution $\Delta\theta$ (left) and wavelength resolution (right) versus λ at the detector. The solid line represents the case with $\eta = 6$', the dotted line with $\eta = 1$'.*

4.4 Summary and conclusions

In this Chapter we have shown an application of the *BENT* monte Carlo code to the simulation of a complete instrument. The complication arising from other optical elements other than the crystal (the radial collimator) and the presence of the sample (which has to be simulated in order to know the final resolution) make the Monte Carlo technique valuable for this kind of calculation. The *Strain Imager* instrument will work, in principle, in a wavelength and angular range much wider than that analysed here. For this reason our results are limited and should be extended. Nevertheless, they show the following points:

1) There is an optimum value for the horizontal bending radius, which can be calculated with our *BENT* code.

2) A large mosaicity of the germanium crystal may not help improving the performance of the instrument, expecially if we take into account that the real reflectivity of plastically deformed mosaic germanium (cfr. Chapter 6) does not agree with the theory.

3) The distribution of the beam at the sample calculated here corresponds to the triangular shapes measured in [81] and gives better details than the geometrical calculation presented therein. Furthermore, we have shown how big is the loss in intensity necessary to obtain the spatial resolution needed on a strain scanner instrument. All these elements may give a valid input for the instrument design.

Further work could be done for making the complete simulation code for this instrument more flexible and easy to use by other users. As we have mentioned, similar and more complete calculations were performed using the RESTRAX [22] code. The comparison of that work with ours would be very useful and instructive.

Chapter 5

Experimental - Copper

As was stated in the Introduction, one of the aims of this thesis was to assess the limits of applicability of the crystal models described in Chapter 2 and to develop Monte-Carlo algorithms able to give a precise description of real crystals. In this Chapter we will focus on the experimental reflectivity of mosaic copper. The temperature dependence of the attenuation coefficient and its influence on the low temperature reflectivity will be reported first. Then, an x-ray study of the homogeneity and limited ideality of two samples will be discussed.

5.1 Introduction

Artificial mosaic crystals are produced by different fabrication processes. Highly oriented pyrolitic graphite (HOPG) is a layered structure manufactured by decomposition of a hydrocarbon gas at very high temperature in vacuum: it has been found that its reflectivity is affected both by inhomogeneities of the mosaic structure and primary extinction. Copper mosaic crystals can be obtained by plastic deformation of grown crystals at room or high temperature. Recently a new technique, the onion-peel method [82], has been developed at the ILL for the production of copper monochromators with an anisotropic mosaic distribution. Other methods exist for the production of deformed germanium monochromators. Perfect germanium wafers are deformed by alternate bending in a furnace and then assembled to obtain the desired thickness and mosaicity. In other cases, the wafers can be assembled to a cylindrical shape with virtually negligible mosaicity. As the presence of dislocations or other kinds of defects depends on these processes, the diffraction properties will be different and will only partially agree with theory. In many cases, modelling may be improved by considering a layered mosaic structure [83]. The reference [13] contains an overview and a discussion of the non-ideality of artificial mosaic

crystals.

Our measurements were performed with both x-rays and neutrons because we had several purposes:

1) Record rocking curves and compare them with theory, in order to verify the crystal quality and the applicability of the models for these crystals.

2) Study the effect of the crystal temperature on neutron diffraction, in order to improve the monochromator efficiency by cooling the crystal.

3) Analyse the homogeneity of crystals by means of x-ray topography and by recording rocking curves at different positions.

The high degree of collimation and monochromaticity presented by third generation synchrotron radiation beams allows the measurement of diffraction profiles in almost ideal conditions. Moreover, using the small size of the beam, one can measure the diffracting properties on a very small scale: this means that we can see details that a neutron beam does not see because of large size and divergence. In the case of bent crystals, finally, the measured rocking curves are the result of the convolution of the large divergent incident beam and the crystal reflectivity. Thus, using the synchrotron beam, it is easier to compare the measured rocking curves with the calculated diffraction profiles.

In the next Chapter the X-ray reflectivity of assembled germanium crystals and HOPG will be reported. The measured samples will be identified by abbreviated names, i.e. Cu-A, Ge-A. Some details are reported in Table A. All the data were measured in Bragg symmetric geometry, except for the neutron reflectivity experiments as a function of temperature, which were in Laue geometry.

Table A. *Samples analysed. The copper and germanium crystals were produced and assembled at the ILL monochromator laboratory. The experimental data on germanium and HOPG are reported in Chapter 6.*

Name	Material	Thickness [mm]	Mosaicity [arcmin]	Bending radius [m]	Production and ref. n^o	Instruments
Cu-A	Copper	8	3	none	ILL	IN1, T13A
Cu-D	Copper	6	8	none	ILL 165-3	ID15A
Cu-E	Copper	6	13	none	ILL 165-2	ID15A
HOPG	HOPG	0.5	19	none	Optigraph	BM5
Ge-A	Germanium	10	1.4	5.7	ILL assembled	T13A, ID15A
Ge-B	Germanium	10	5	none	ILL assembled	T13A, ID15A

5.2 Experimental stations

A simple diagram of the set-up used for measuring the crystal rocking curve $R(\theta - \theta_B)$ is shown in Fig. 5.1: the detector was kept at a scattering angle equal to $2\,\theta_B$ and the crystal was rotated around the exact Bragg position. In order to measure the beam attenuation in some cases the detector was placed in front of the incident beam and the transmitted intensity $T(\theta - \theta_B)$ was recorded. The profiles were normalized by measuring the incident beam intensity after removing the crystal. The neutron tests were performed at the IN1

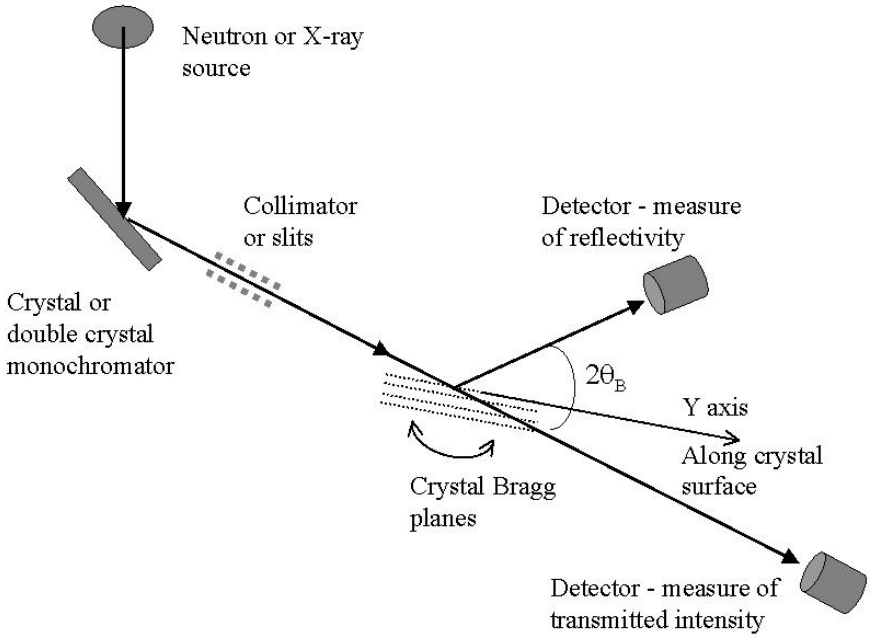

Figure 5.1: *Schematic diagram of the geometry used for recording curves of reflected or transmitted intensity. The Y axis is parallel to the crystal surface.*

[84], T13A and T13C instruments of the ILL. In all these experiments we simply recorded the reflected or transmitted intensity as a function of the crystal rocking angle. IN1 is a hot neutron inelastic spectrometer, but in our experiment, we did not perform any energy analysis. Thus the instrument was used as a simple two axes machine. The beam was collimated to $30'$ before and after the sample. We used IN1 for recording the mosaic copper reflectivity at high neutron energy as a function of temperature, so the sample was mounted in a He displex cryorefrigerator. T13A and T13C are two axes instruments used for crystal tests: they are equipped with germanium and silicon perfect crystal monochromators using several sets of Bragg planes. Therefore it is usually possible to choose a monochromator orientation having the same d-spacing as that of the sample. This is essential when we want to avoid the effect of beam divergence on the measured reflectivity. The beam size was reduced by the use of absorbing diaphragms after the monochromator. Thanks to the low flux at T13A and T13C, it was always possible to measure the incident beam intensity. Thus the rocking curves could easily be normalised

and we will always present them on an absolute scale. This could not be done at IN1, where the high flux prevented a reliable measure of the incident beam.

The x-ray measurements on copper and germanium were performed at the beamline ID15A of the ESRF [85], where x-rays with energies typically higher than 80 keV are available. The use of high energy photons has the advantage of decreasing the attenuation due to the photoelectric absorption. On the other hand, Compton scattering is more important at these energies: see Fig. 5.2 for details of attenuation as a function of energy. The x-ray source of ID15A is an asymmetric wiggler. The white beam was monochromated by a perfect bent silicon crystal in Laue geometry. The energy resolution $\Delta E/E$ was of order $\sim 10^{-3}$.

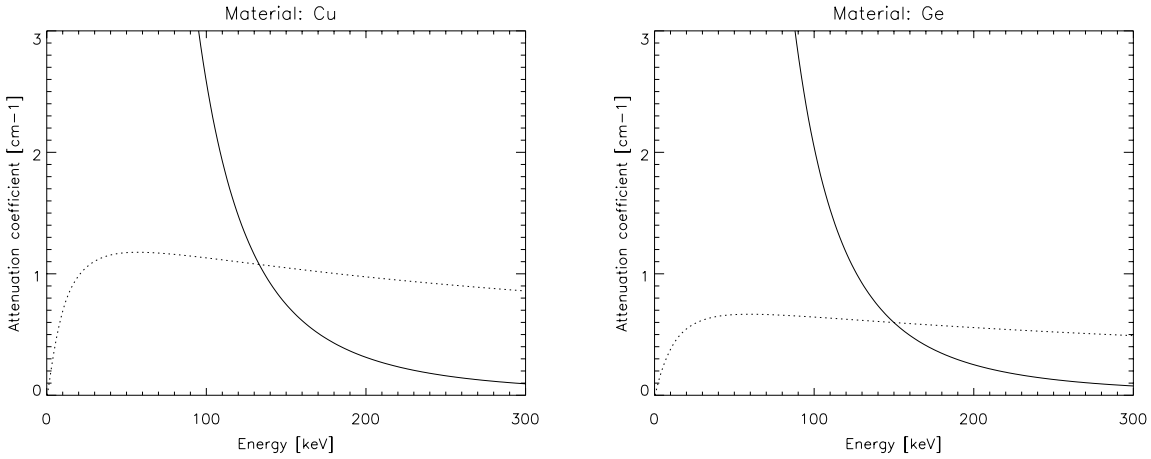

Figure 5.2: *Photoelectric (solid line) and Compton (dotted line) attenuation coefficients for copper and germanium as a function of the x-ray energy.*

A pictorial view of the method of recording diffraction topographs is reported in Fig. 5.3. The incident x-ray beam width is defined by absorbing slits to a few tens of μm. The Bragg diffracted beam is recorded using a CCD camera perpendicular to the reflected beam. In principle, if an incident lamellar beam is used, the camera records the intensity diffracted by the Bragg planes along the beam path in the crystal bulk. In practice, however, the beam has a finite width and the image will be the convolution of the finite beam size and the local crystal properties. If the crystal is homogeneous so will the image be, except for a decrease of intensity measured in the direction of scattering because of attenuation and secondary extinction.

The x-ray reflectivity of graphite and quartz were measured at the BM5 beamline at ESRF [86]. The source is a bending magnet with a critical energy of 20 keV. The beamline was equipped with a flat double crystal Si <111> monochromator (giving an energy resolution of about $\Delta E/E \sim 10^{-4}$) placed 30 m from the source. The sample was mounted 40 m from the source on a three axes diffractometer using the horizontal plane as the diffracting plane.

The divergence of the beam in the scattering plane could be considered as negligible.

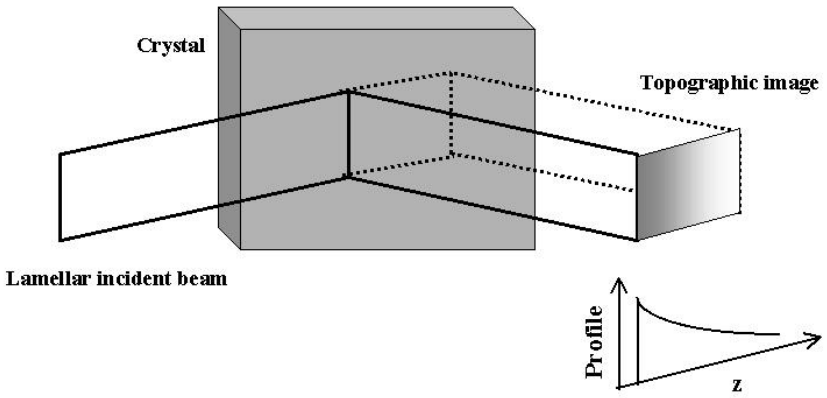

Figure 5.3: *Schematic diagram of a topographic image recording. The dotted line represents the part of the beam which is diffracted after propagating in the crystal bulk. The schematic profile drawn at the bottom is obtained by integrating the image pixel values and represents the attenuation of the diffracted beam due to secondary extinction and absorption.*

5.3 Temperature effects on the neutron peak reflectivity

The typical extinction lengths in mosaic crystals are of the order of some mm. The peak and integrated reflectivities of these crystals are strongly dependent on the attenuation coefficient μ, as it can be seen looking at Eqs. (2.21) and (2.23). For thermal neutrons, in crystals usually employed as monochromators, the μ values are fractions of cm^{-1}. An important contribution to the attenuation coefficient comes from the true absorption by nuclei. We have already mentioned that there are other effects which are responsible for the decrease of the beam intensity: parasitic Bragg scattering (see the end of section 2.3) and thermal diffuse scattering (see section 2.6). In this section we want to describe some measurements of reflectivity and attenuation as a function of temperature. The data analysis was done by using the temperature dependent attenuation (and reflectivity) as discussed in Chapter 2. We did not compute the effect of parasitic Bragg reflections and this is probably the reason for the disagreement with theory.

The reflectivity of a copper single crystal (sample Cu-A) as a function of temperature was measured on the hot neutron three axes spectrometer IN1 ($T = [15\,K,\ 285\,K]$) and on the T13 diffractometer ($T = [77\,K,\ 289\,K]$) of the ILL [87, 88]. The goal was to measure both the attenuation coefficient μ and the diffracted intensity as a function of temperature. The crystal had previously been characterised on the hard x-ray Laue diffractometer at the ILL [89] and its mosaicity was 3'. The crystal thickness was $d = 0.8$ cm. Measurements have been performed at 48 meV ($\lambda = 1.3$ Å), 100 meV ($\lambda = 0.9$ Å) and 250 meV ($\lambda = 0.57$ Å) in Laue geometry. The experimental conditions have been described in section 5.2. As was shown in section 2.6, for neutron energies above the crystal Debye energy $E_D = K_B T_D \sim 26$ meV for copper, the predominant part of the attenuation comes from multiphonon scattering, if the effect of parasitic reflections is neglected. The decrease of absorption (with consequent increase of reflectivity) due to phonons is more important at higher neutron energies and of course at low temperature. The values of measured and calculated gain in the peak reflectivity at low temperature, with respect to the room temperature reflectivity, are reported in Table 1. The values in the third column were calculated using, for the absorption cross-section, the Freund's model in Eq. (2.49) for multi-phonon absorption. Those in the last column were obtained using the numerical integral of $d^2\sigma/d\Omega dE'$ as reported in Eq. (2.59). By looking at the values in Table 1 and the multi-phonon scattering cross-section plotted in Fig. 2.11 we may conclude that the multi-phonon cross section, calculated in the frame of the incoherent approximation, is underestimated at $E = 48$ (these data are discussed later in this section) and 100 meV, thus in the following we will consider only Freund's model. The data measured at $E = 250$ meV disagree with the formulas in both cases, although a good agreement is found for

the $< 331 >$ asymmetric reflection.

Table 1. *Measured and calculated increase of the neutron reflectivity for copper at* 77 *K for* $E = 48$ *meV (T13 data) and at* 15 *K for* $E = 100$ *and* 250 *meV (IN1 data).*

Reflection	Energy meV	Experiment	Freund's model	Approximated multi-phonon
220	48	12%	17%	3%
	100	18%	24%	13%
	250	18%	35%	33%
331	100	31%	34%	14%
	250	33%	55%	35%

Fig. 5.4 shows the peak reflectivity vs. temperature for the $< 220 >$ and $< 331 >$ reflections. A scale factor was used in order to compare the behaviour of the measured reflectivity as a function of T to the theoretical calculations. We also tried to fit the data using Eqs. (2.21) for the reflectivity and (2.49) for the absorption, letting the C_2 parameter free. As is explained in [62] C_2 is an euristic parameter which depends only on the crystal material and not on any other quantity such as energy or Bragg planes. According to the same paper $C_2 = 12$ Å^{-2}eV^{-1} for copper. The fit parameter we obtained was $C_2 = 8.7$ Å^{-2}eV^{-1} at 100 meV and $C_2 = 2.6$ Å^{-2}eV^{-1} at 250 meV for both $< 220 >$ and $< 331 >$. This was of the same order as that reported in [62] at 100 meV, but much smaller at 250 meV, for both reflections. As the C_2 coefficient should not depend on E we can conclude that a fit of these data is not possible and this is the reason why, in Fig. 5.4, we report only the scaled reflectivity, without fit.

Fig. 5.4 shows that the agreement with theory is better at 100 meV than at 250 meV, and that at both energies it improves for the $< 331 >$ reflection. The only difference between $< 220 >$ and $< 331 >$ is the crystal orientation with respect to the beam: the neutron path in the $< 331 >$ case is longer because of the asymmetric angle formed by the Bragg planes and the crystal surface. The longer path makes absorption more important and the reflectivity increase is larger than for the symmetric $< 220 >$ reflection. For all measurements, excepting $< 220 >$ at 250 meV, the data are well fitted only for $T \geq 150\,K$. The disagreement at lower temperature is not easily understood. There could be several reasons. From the theoretical point of view, the calculation of the Debye Waller coefficient and the phonon cross-sections depends on the density of states. For all the calculations the Debye approximation has been used. However, we have also used the copper density of states as calculated by the Born-von Karman model, but the final result does not change. Probably the discrepancy with theory is due to the presence of multiple Bragg reflections: this is confirmed by the better agreement found at lower energy, where parasitic reflections are less important. This indicates that the efficiency of cooled monochromators for short

wavelength neutrons may not be as good as theoretically calculated.

The need to decrease and control the amount of multiple reflections drove us to repeat the measurements at lower energy. To this end, we used the T13A diffractometer at the ILL with 48 meV ($\lambda = 1.3$ Å) neutrons. We indexed the multiple Bragg reflections using the method described by Cole *et al.* [39] and implemented in the XOP's MAMON application [2]. The neutron energy was selected in such a way that this multiple reflection effect was minimized. By looking at Fig. 5.5 one can compare the amount of multiple reflections present at 100 meV (left) and 48 meV (right) as a function of the angle Φ drawn in Fig. 5.6 and which represents rotation around the diffraction vector. During the experiment the multiple reflections were monitored and reduced by rotating the azimuthal angle Φ of the crystal. We measured the trasmitted beam intensity T, as a function of the crystal rocking angle Θ, and for different values of Φ. The most suitable Φ angle was then chosen by maximising T. It was verified that for a such value of Φ the reflected intensity was also maximised. We used a perfect Ge <220> crystal monochromator and the beam was collimated to a value of 10'. The sample and geometry were the same as in the previous experiment on IN1. We measured the reflectivity of the <220> Bragg planes in transmission geometry and the Bragg angle was $\theta_B = 30.6^o$. The angular dependence of both the reflected and transmitted beams were recorded at $77\,K$, $115.5\,K$, $187\,K$, $233\,K$ and $289\,K$.

We fitted $R + T$ by using Eq. (2.25) in order to retrieve μ, then we fitted R with a Lorentzian R_{lor} plus a linear background. The angular dependence of R (after removing the background) and T are plotted in Fig. 5.7. The fitting results are also reported: the dashed line is $e^{-\mu d/\sin\phi}$; the solid lines are R_{lor} and $(e^{-\mu d/\sin\phi} - R_{lor})$. The fitted μ is reported in Table 2. The error on μ_{fit} is less than 1% i.e. smaller than the difference with the values μ_{calc} calculated by using Eqs. (2.47) and (2.49). We used μ_{fit} for retrieving the peak reflectivity and this was compared to the peak of R_{lor}. In conclusion the measured peak reflectivity is $\sim 20\%$ smaller than expected, and the observed gain at $77\,K$ is 12%, instead of the calculated 17%. By using also in this case, as shown in Table 1, the multi-phonon cross-section as calculated in the incoherent approximation, one finds a theoretical increase of the peak reflectivity of approximately 3%, which is much smaller than the value given using Freund's model and also smaller than wht we measured. This confirms that the incoherent approximation cannot be used at neutron energy of 48 meV.

An attempt to fit R, after convolution with the shape of the incident beam, did not succeed. This may be due to the unknown real shape of the incident beam, as well as to the non ideality of the crystal. This could also be the reason for the lower measured reflectivity. However, the test at 48 meV was evidently less affected by parasitic reflections: the values of absorption and reflectivity in Table 2 have approximately the same dependence on T as those calculated.

Some concluding remarks have to be made about these experiments at low temperature:

1) The measured gain in reflectivity is always smaller than expected and the agreement with calculations is worse at higher energy.

2) Better modelling, including parasitic reflections, is necessary.

4) At the same time new experiments should be done with more accuracy: the effect of multiple reflections can be investigated experimentally by recording Θ scans with automatic variation of Φ.

3) Other materials like germanium might show a good reflectivity gain at low temperature and it could be worthwhile measure them as well.

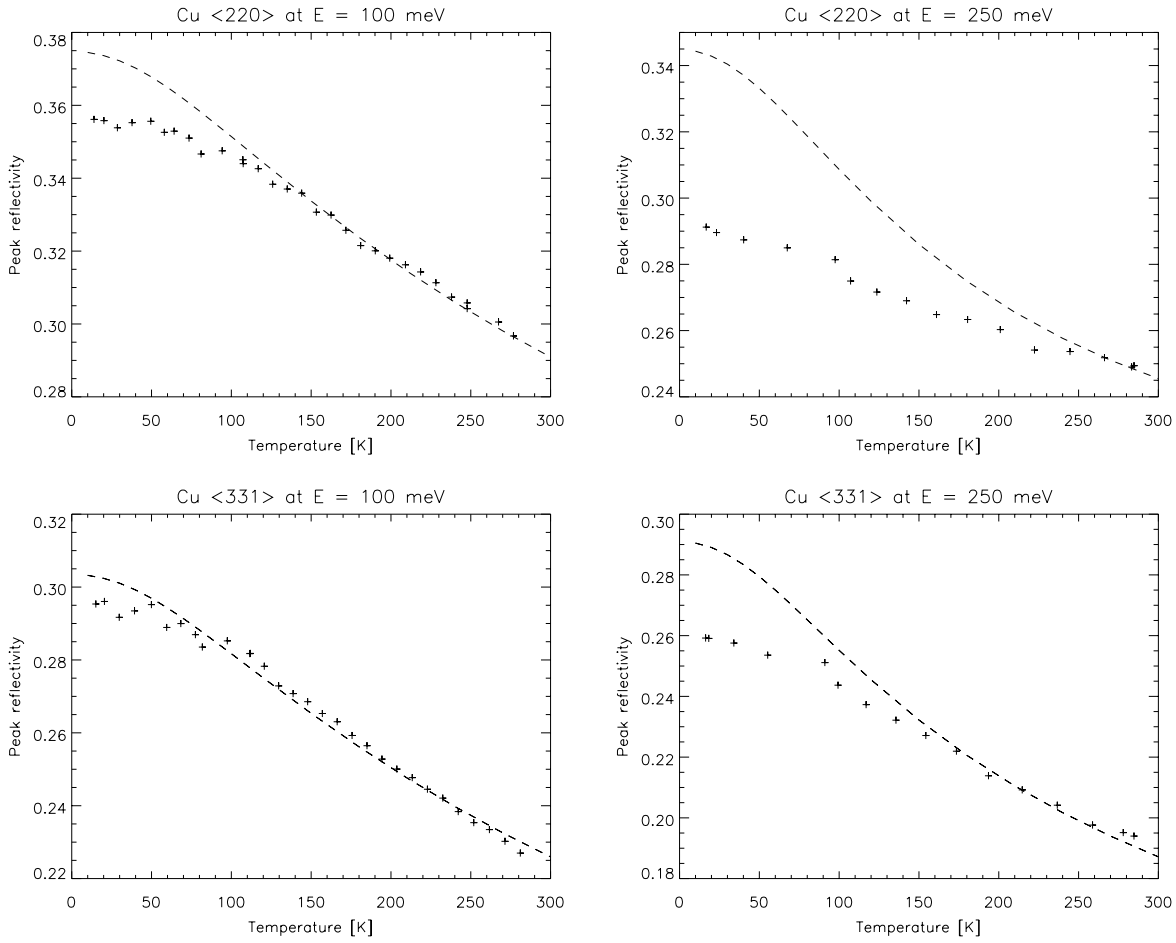

Figure 5.4: *Mosaic copper Cu-A: peak neutron reflectivity as a function of temperature in Laue geometry. The <220> reflection was measured in symmetric geometry and the <331> with an asymmetry angle of $\alpha = 13.3^o$. The + symbols are the measured values, multiplied by a scale factor. The dashed line is the theoretical reflectivity (see Eq. (2.21)) with the absorption coefficient μ given by Eq. (2.47) and with parasitic reflections neglected.*

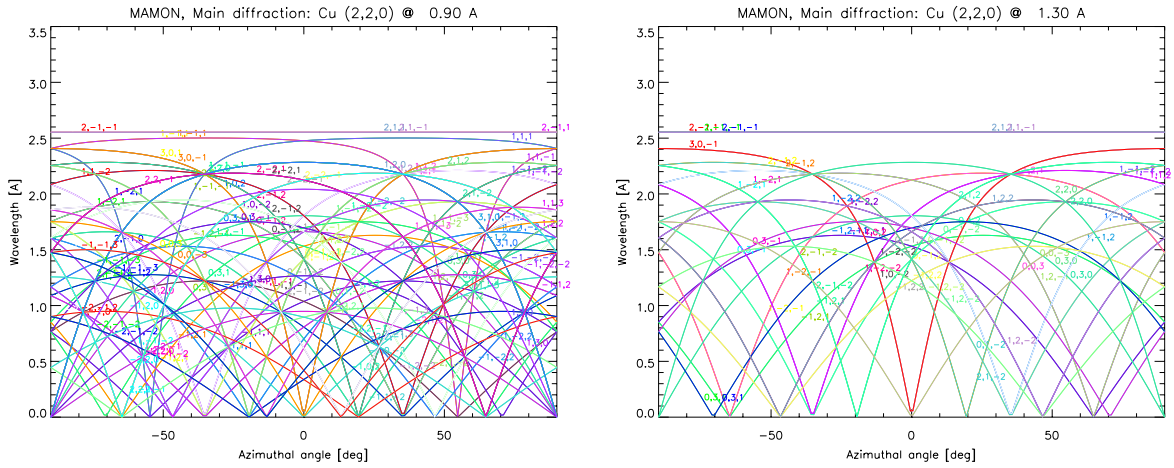

Figure 5.5: *Multiple reflection as a function of the azimuthal crystal angle* Φ *for Cu <220> at 100 meV (left) and 48 meV (right).*

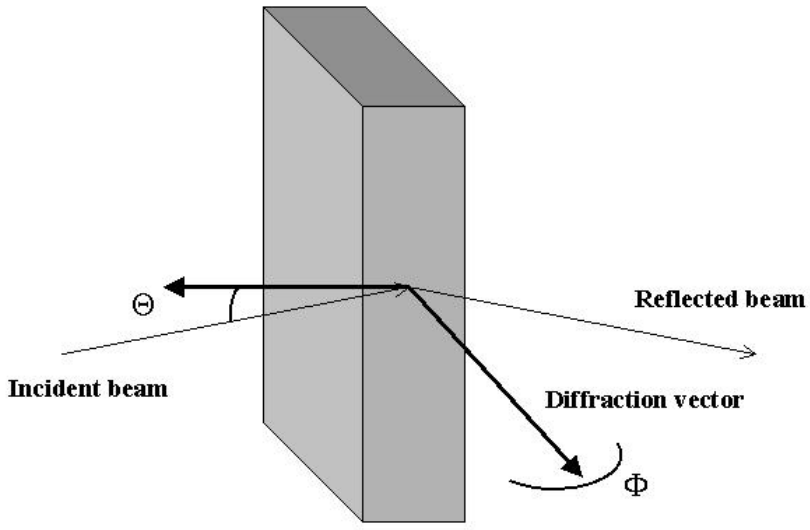

Figure 5.6: *Minimisation of multiple reflections by rotation of the* Φ *angle in Laue symmetric geometry.*

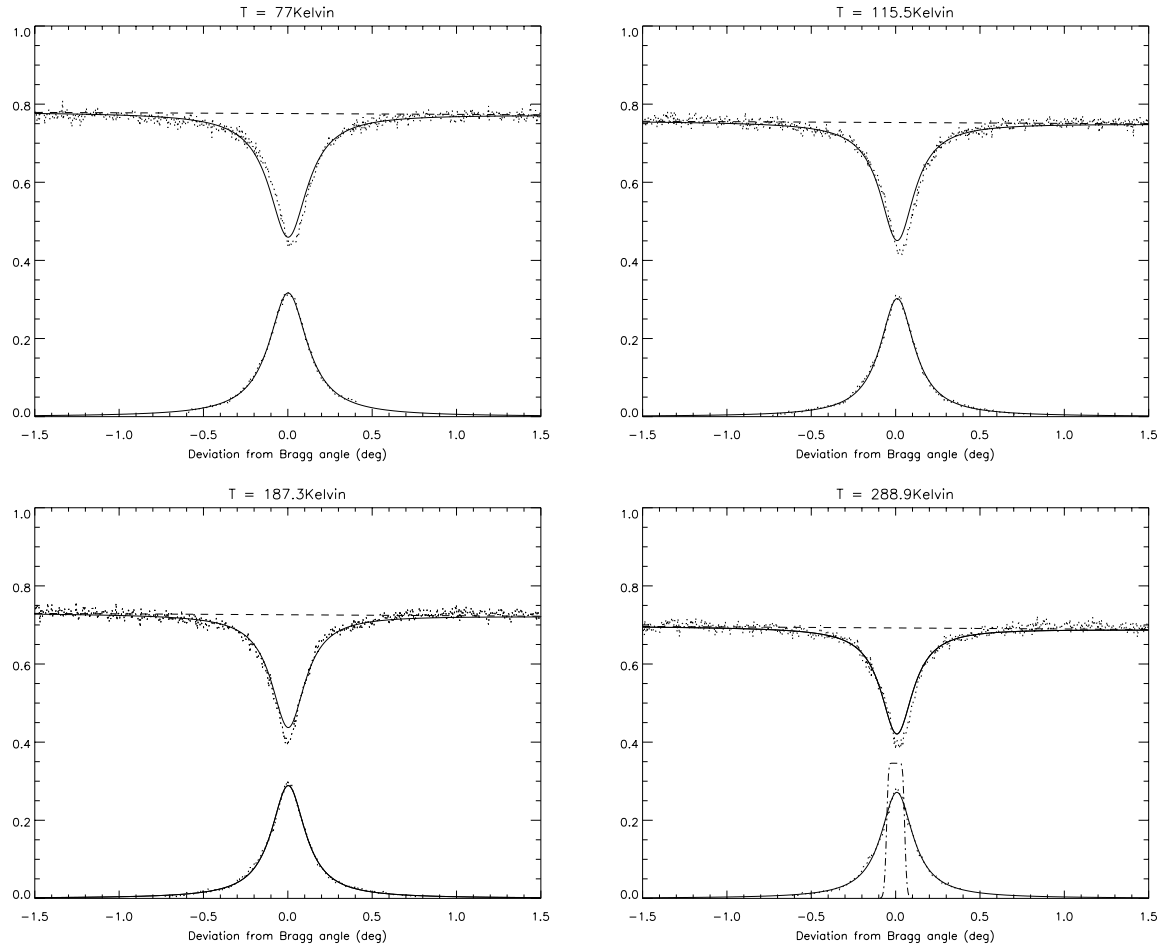

Figure 5.7: *Copper Cu-A at 48 meV, <220> reflection in Laue geometry. Angular dependence of the normalised transmitted and reflected beams for different values of temperature. The dotted lines are the measured T and R. The dashed line is the fit of $R + T = e^{-\mu d/\sin\phi}$ from which we obtained μ. The solid lines are the fit: a lorentzian R_{lor} for R and $(e^{-\mu d/\sin\phi} - R_{lor})$ for T. The dashed-dotted line in the last figure is the theoretical reflectivity for a mosaicity of 3' (FWHM).*

Table 2. *Neutron absorption and peak reflectivity for the Cu-A sample at 48 meV. The reflection used is the <220> in symmetric Laue geometry. Freund's [62] formulas have been used for calculating μ_{calc}.*

Temperature Kelvin	μ_{calc} [cm^{-1}]	μ_{fit} [cm^{-1}]	$R_{peak-calc}$	$R_{peak-meas}$
77	0.307	0.2735	0.388	0.317
115.5	0.3275	0.306	0.376	0.302
187.3	0.368	0.345	0.363	0.289
232.8	0.3935	0.366	0.356	0.279
288.9	0.424	0.396	0.346	0.271

5.4 X-ray reflectivity and topographic study

The good performance of artificial mosaic copper for monochromatising neutron beams is well established. In spite of this, the production process of these crystals (growth, cutting and pressing) can lead to the formation of inhomogeneities or grains which are witnessed by the impossibility to fit the rocking curves with the ideal symmetric mosaic distribution [12]. The possible presence of inhomogeneities has the effect of decreasing the reflectivity of these samples. This is generally true for other kinds of mosaic crystals, although the production technique has improved a lot in recent years, for example in the case of Heusler polarizing crystals [90]. In this thesis we report an x-ray study on two copper samples produced at the ILL monochromator laboratory from which non-ideality appears evident: however, this behaviour is not to be considered common to all the samples produced with the same technique [91]. As mentioned in section 2.4, the reflectivity of a mosaic crystal is also affected by the finite size of the small perfect mosaic blocks of which it is composed. The purpose of this x-ray study is to show the presence of both kinds of defects (inhomogeneity and primary extinction) and analyse the crystal homogeneity with an optimal spatial resolution. Due to the lower intensity and higher divergence of neutron sources, these types of characterisation could be performed using neutrons, but with much more effort than needed at a synchrotron source. The reflectivity curves and diffraction topographs were recorded at the ESRF beamline ID15A, described in section 5.2.

We will see that the agreement with the mosaic crystal model described in section 2.4 is very approximate. First of all the crystals do not show an ideal mosaic distribution $W(\theta - \theta_B)$ with Gaussian or Lorentzian shape, but always a combination of the two (pseudo-Voigt function). Almost all the rocking curves have an asymmetric shape and a combination of pseudo-Voigt functions is needed in order to fit them. The asymmetric mosaic distribution means that grains are present along the beam path in the crystal. Moreover, the mosaic parameters mosaicity η and scattering factor Q, as obtained from the fit for the same sample, depend on the photon energy, the set of Bragg planes and position in the crystal. In this sense, we will speak of "crystal inhomogeneity" or "non-ideality". We recall that the Q factor is not really related to the mosaic distribution W, but it determines the secondary extinction coefficient $\sigma = Q \times W(\theta = \theta_B)$. According to Zachariasen [37], a reduced Q', as obtained from the fit, means that primary extinction is present in the small perfect crystal blocks forming the crystal, thus decreasing secondary extinction and reflectivity. The correction to Q is a function of the ratio between crystallite size and primary extinction depth. In our experiments we always find corrected values for Q' which do not give a constant value t_0 for the crystallite size of a given sample, but t_0 changes with the energy, Bragg indices and position. Therefore we find different values for the crystallite size, when measuring rocking curves at different energies, Bragg indices or positions, due to the fact that we look at different directions and volumes in the bulk

crystal. As a matter of fact, we can simply look at the correction factor needed to fit Q as further proof of the crystal non-ideality and inhomogeneity.

This study was carried out on the samples Cu-D and Cu-E described in Table A. The diffraction profiles, and the corresponding fits, are plotted in Figs. 5.8 and 5.10. The mosaic distribution $W(\theta - \theta_B)$ resulting from the fit was a pseudo-Voigt function with a Lorentzian (60%) and Gaussian (40%) having the same FWHM η. For both samples, and for each of the diffraction profiles, the fit could only be performed for negative or positive angles (with respect to the Bragg angle) because of the asymmetric shape. This asymmetry could be due to the presence of grains. The fit gives a mosaicity of $\eta = 0.13^o$ for the $< 111 >$ reflection and an average correction for Q of ~ 0.6 for the Cu-D sample. On average we have $\eta = 0.22^o$ and a correction of Q of ~ 0.9 for the Cu-E sample. For both samples, but even more for Cu-D, the fitted value of η changed with the measured reflection. Since η is the intrinsic mosaicity it should not depend on the $< hkl >$ indices. The reason for the different observed values is that we sample different scattering volumes for each $< hkl >$. The mosaicity, expecially for Cu-D, then changes by several *arcmin* in different volume elements of the same crystal. This is clearly shown by the diffraction profile of the $< 222 >$ reflection in Fig. 5.8 (right): the fit was performed assuming that the mosaic distribution was a combination of the pseudo-Voigt function mentioned above, with $\eta = 0.07^o$, plus, for $\theta \leq \theta_B$, a Gaussian shifted by 0.05^o and with $\eta^{left} = 0.25^o$. The fact that this mosaic distribution could not be used to fit the $< 111 >$ reflectivity of the same sample means that the diffracting volumes seen by the beam for the two reflections are different, because of the different incidence angles.

The surface and contour plots in Figs. 5.9 and 5.11 represent reflectivity as a function of angle and Y coordinate along the crystal length as shown in Fig. 5.1, so they can give an idea of the crystal homogeneity along this direction. The spatial resolution of these plots corresponds to the beam footprint on the crystal, which, in the case of Cu-D $< 111 >$, was 0.8 mm (incident beam 20 μm wide). The footprint was 4 mm for the $< 111 >$ and 1.3 mm for the $< 333 >$ in the case of Cu-E (incident beam 100 μm wide). The inhomogeneities observed in these crystals most probably are not due to surface defects, because the samples were polished before the experiments.

5.4.1 Measured and simulated topographs

In this section we try to clarify the interpretation of the measured x-ray topographs. By looking at Fig. 5.3 one realizes that their shape and intensity can be explained by using geometrical arguments and also by considering the parameters governing extinction in the crystal: the absorption and secondary extinction coefficients as reported in Table 3. However this task is easier if we compare the experimental topographs with those simulated

with the *MOSAIC* program.

The experimental topographs of the two samples, as a function of the Bragg indices and angles of incidence, are shown in Figs. 5.12 to 5.17. A beam width of 100 μm was used in all cases, except for Fig. 5.13 where the slit width was reduced to 20 μm. A qualitative comparison between the two samples shows that for Cu-D the images are thinner than for Cu-E: this is due to the smaller mosaicity (i.e. smaller extinction length). The images of Cu-D look homogeneous, except for the presence in some of them of a double structure. This means that there are regions which are traversed by the beam and contribute to diffraction but which suffer the presence of macroscopic misorientations or grains. The misoriented zones are represented by the "black" regions of the topographs which occur between two zones where the intensity is different from zero. This is more evident in Fig. 5.13 because the slit was thinner and the image is "cleaner", although there is less intensity. Concerning Cu-E, the type of inhomogeneity looks more "granular" and in the case of the $< 333 >$ reflection in Fig. 5.17 we have again a double structure which indicates the presence of regions which are not diffracting. The different type of inhomogeneity observed in the two crystals is related to the different mosaicity.

The theoretical absorption and extinction lengths for a sample having $\eta = 0.1^o$ are reported in Table 3: it is useful to recall that they represent respectively the average path-lengths traveled by the incident beam, in the forward direction, before being absorbed or diffracted. The secondary extinction length for other values of mosaicity can easily be calculated by recalling that $l_{ext} = \sigma^{-1}$, with $\sigma = Q \times W(\theta = \theta_B)$ (see section 2.4), then the secondary extinction length is proportional to mosaicity $l_{ext} \propto \eta$. These values are not directly used in the simulations, but they are valid in a statistical sense. However, in the simulations the total path traveled by each photon is used for calculating the weight of that photon due to absorption:

$$weight = e^{-path \times \mu} \tag{5.1}$$

Therefore the true absorption length is related to μ, which is an input parameter for the simulations. The simulated topographs shown in Figs. 5.18, 5.20 and 5.21 concern the diffracted beam at the angular position corresponding to the exact Bragg angle. They are the images of the diffracted beam at a distance of 30 cm from the crystal as schematically shown in Fig. 5.3. The incident beam had a wavelength spread similar to that of our experiment and a divergence of 20 μrad. The x-axis in the topographs is the Z coordinate along the scattering direction, in the plane of image, as reported in Fig. 5.3. The images represent all scattered photons and do not take into account absorption: each point is a photon and the *weight* due to absorption is not considered.

The easiest way to compare simulations to experiment is computing the topograph profiles, as schematically drawn in Fig. 5.3. In the case of the simulations, we will call these profiles "histograms". If we simply make histograms of photons without using the weight in Eq. (5.1), we obtain the $h(Z)$ histograms reported for example in the left column in Fig. 5.19. We cannot compare these to experiment, because of the high absorption. The simulated weighted histograms $h_{weighted}(Z)$, reported in the column on the right, are calculated by assigning a *weight* or *probability* to each diffracted photon equal to the expression in Eq. (5.1). Therefore $h_{weighted}(Z)$ is the analog of the experimental profile.

First we can check the effect of the beam size on the histograms in order to say how this affects the results. The only difference between Fig. 5.20 and the first row in Fig. 5.18 is the beam size: 1 μm in the first case and 100 μm in the second. The comparison shows that the profiles do not change with changing the incident beam size. We can then say that the beam penetration effect is larger than the beam size effect. The topographs of sample Cu-E in Figs. 5.15, 5.16 and 5.17 can be compared to the simulated images in Fig. 5.21, obtained for $\eta = 0.21^o$. The result, reported in Fig. 5.22, shows that the agreement between simulation and experiment is excellent for the $< 111 >$ and $< 222 >$ reflections and less good for the $< 333 >$, because of noise on the experimental image.

By assuming an exponential decay, we can write an hypothetical shape for the histograms h and $h_{weighted}$:

$$h \propto e^{-\sigma l} \tag{5.2}$$

$$h_{weighted} \propto e^{-(\mu+\sigma)l} \tag{5.3}$$

where μ and σ are the absorption and secondary extinction coefficients, respectively, and l is the average length traveled in the forward direction by photons arriving at the detector. In practice we assume that the histogram behaviour is simply dictated by the attenuation law in the bulk crystal. A more precise estimation for the decay should be made by recalling that the transmitted intensity T across the crystal depth is given by Eq. (2.24). According to this equation, the transmitted intensity across the crystal in Bragg symmetric geometry and with $\mu = 0$, for a pathlength equal to l, should be:

$$T(l) = \frac{1}{1 + \sigma l} \tag{5.4}$$

We will assume that the profile of the topographic images would be proportional to $T(l)$ in the case of zero absorption:

$$h(l) \propto \frac{1}{1+\sigma l} \tag{5.5}$$

By using a simple geometrical consideration which neglects the effect on the beam path due to multiple scattering, we can substitute in the previous equations: $l = Z/\sin 2\theta_B$ with the Z axis drawn in Fig. 5.3 as before. We have verified that the non-weighted histograms are well described by Eq. (5.5): the fit results are the dotted lines in Fig. 5.19 and the fitted values of l_{ext}, reported in the figure caption, are of the same order of magnitude as those in Table 3.

For the $h_{weighted}$ histograms, instead, it is clear that the extinction is mostly due to absorption, and the Z range over which they differ from zero should be approximately equal to $1/\mu \sin(2\theta_B)$, i.e. a fraction a of mm. This behaviour, i.e. the predominance of absorption on secondary extinction, is confirmed by the results reported in Fig. 5.22: the profiles of the experimental images for Cu-E, at the top of the reflectivity curve, are reported together with the simulation results. The agreement is very good: in spite of the presence of grains or inhomogeneities (confirmed by the shape of the diffraction profiles and by the images analysed previously in this section) the sample diffracts according to expectations.

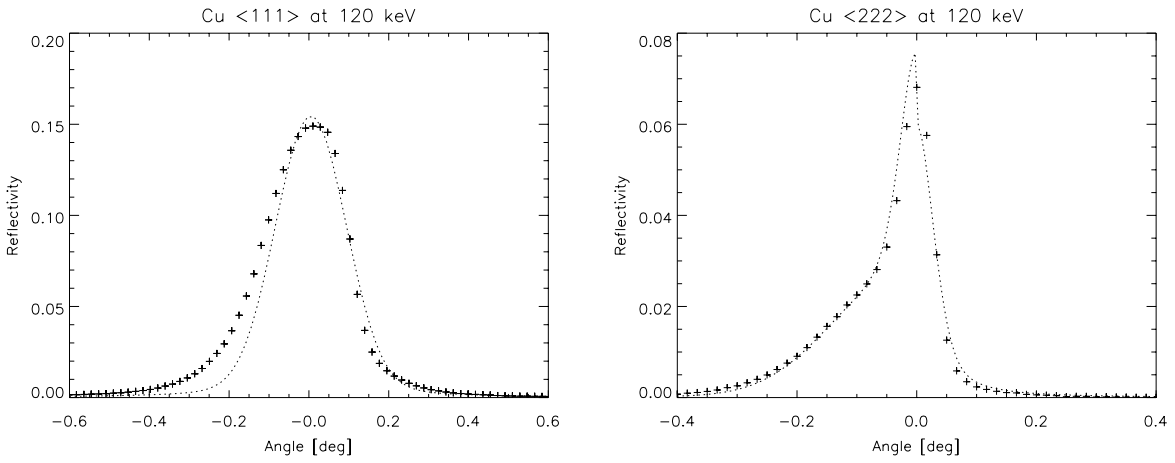

Figure 5.8: *Experimental X-ray reflectivity versus* $(\theta - \theta_B)$ *of the copper sample Cu-D at* $E = 120$ *keV (+ symbols). The fit (dotted lines) was performed using Eq. (2.23) with two free parameters: mosaicity* η *and the Q factor. The mosaic distribution was a psudo-Voigt function. LEFT: <111> reflection with* $\theta_B = 1.4^o$*. The fit (performed for* $(\theta - \theta_B) \geq 0$*) gave:* $\eta = 12'$*,* $Q = 0.68 \times Q_{theor} = 0.0042\ cm^{-1}$*. RIGHT: <222> reflection with* $\theta_B = 2.8^o$*. The fit results are:* $\eta = 4'$*,* $Q = 0.54 \times Q_{theor} = 0.0007\ cm^{-1}$*. For* $(\theta - \theta_B) \leq 0$ *the mosaic distribution was the pseudo-Voigt function plus a gaussian with FWHM equal to* $\eta_2 = 15'$*.*

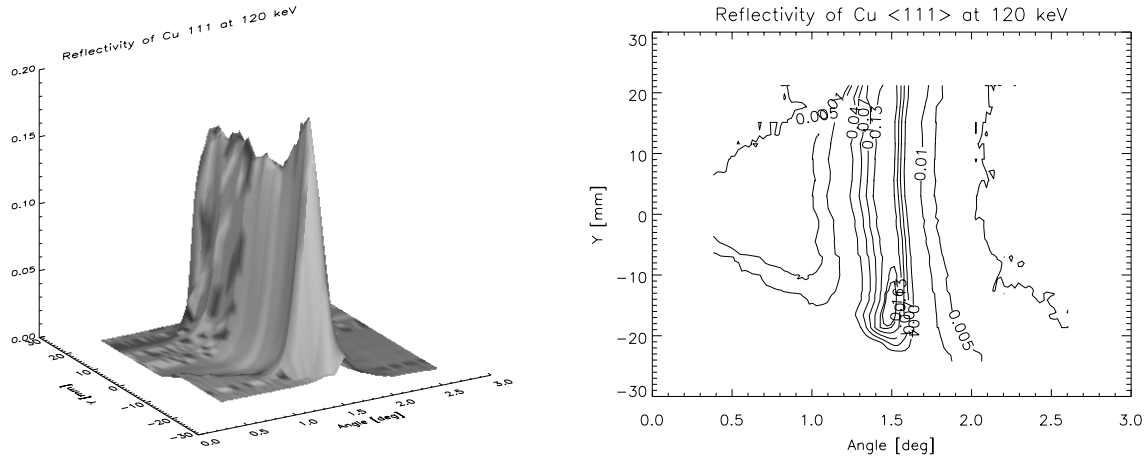

Figure 5.9: *Cu-D. LEFT: rocking curves at different values of the Y coordinate along the crystal surface using a beam width of 20 μm. RIGHT: Contour plot of graphic on the left.*

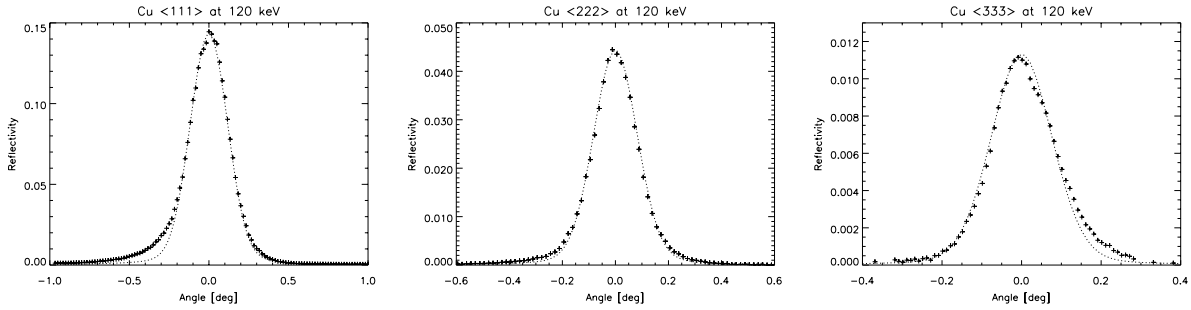

Figure 5.10: *X-ray reflectivity versus $(\theta - \theta_B)$ of the <111>, <222> and <333> reflections from copper sample Cu-E (+ symbols). The fit parameters were the mosaicity η and the Q factor. The mosaic distribution was a combination of a Gaussian and a Lorentzian. The parameters were as follows: $\eta_{<111>} = 16'$, $Q_{<111>} = 0.82 \times Q_{theor} = 0.0051\ cm^{-1}$, $\eta_{<222>} = 11'$, $Q_{<222>} = 0.95 \times Q_{theor} = 0.00123\ cm^{-1}$ and $\eta_{<333>} = 10'$, $Q_{<333>} = Q_{theor} = 0.000385\ cm^{-1}$.*

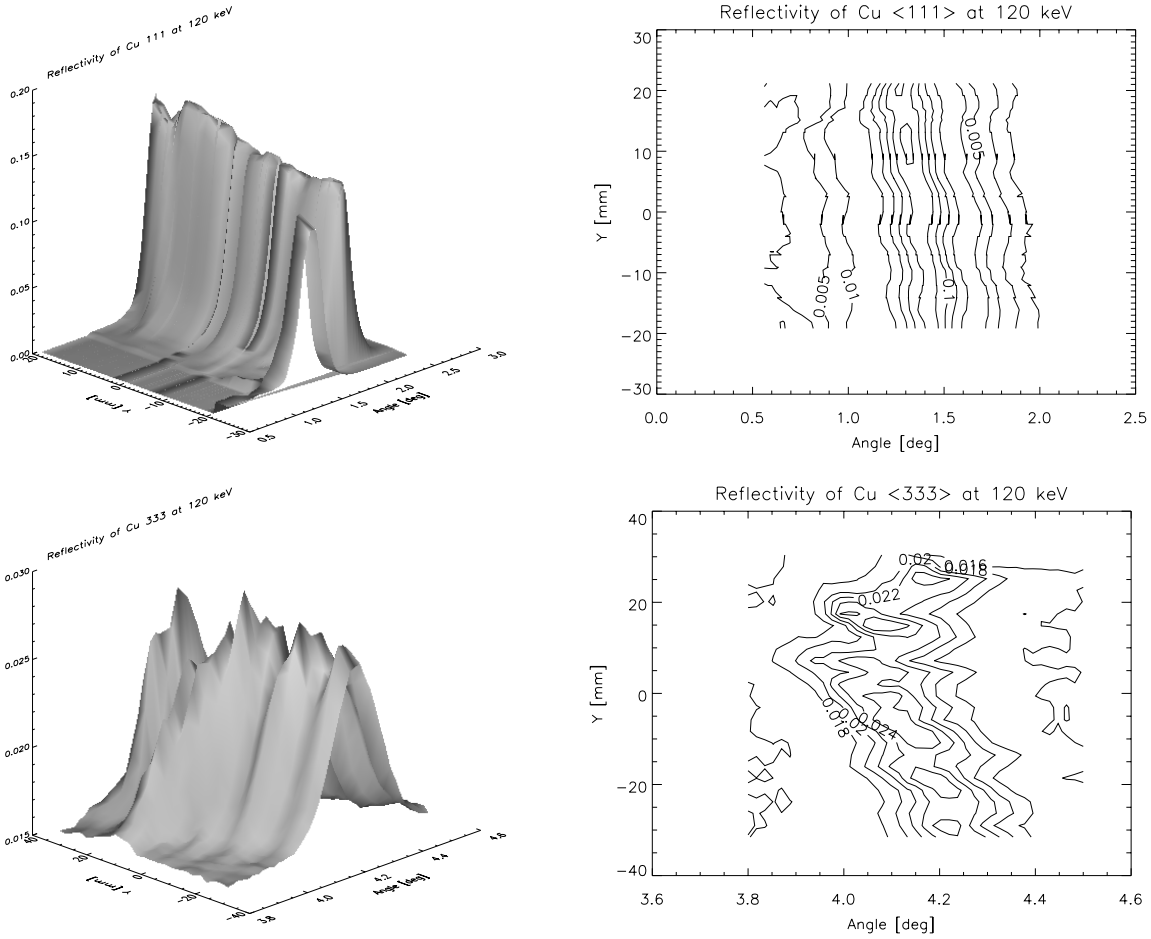

Figure 5.11: *Cu-E. LEFT: rocking curves at different values of the Y coordinate along the crystal surface using a beam width of 100 μm. RIGHT: Contour plot of graphic on the left.*

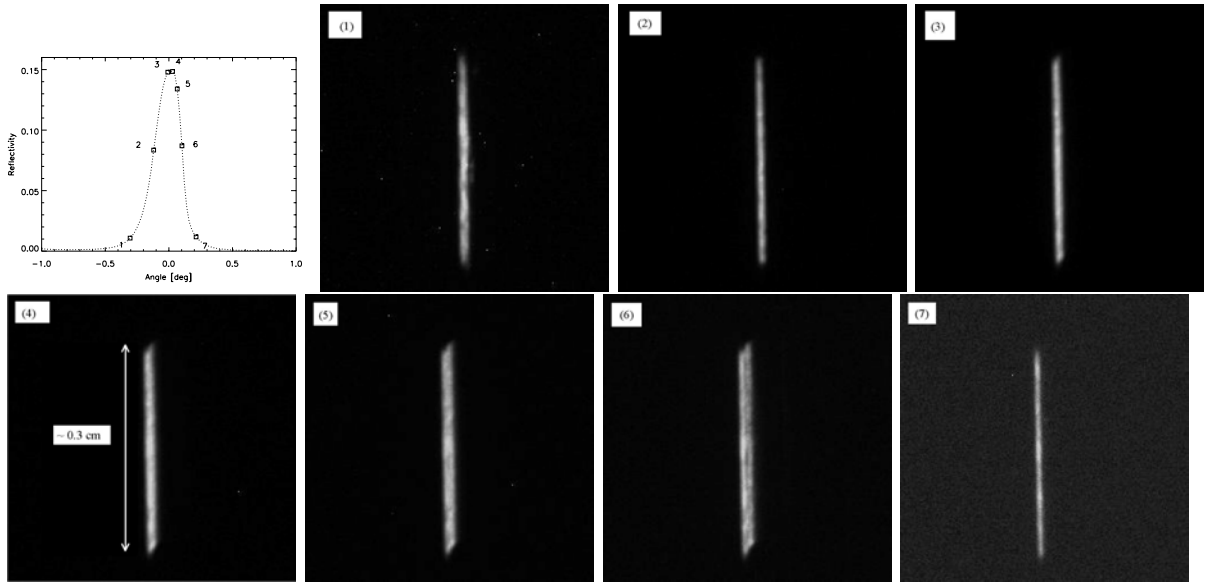

Figure 5.12: *X-ray topographs of Cu-D <111> at E = 120 keV. The angular positions at which the topographs were recorded are indicated in the plot on the top-left. The Bragg angle at this energy is 1.4° and the slit width was 100 μm.*

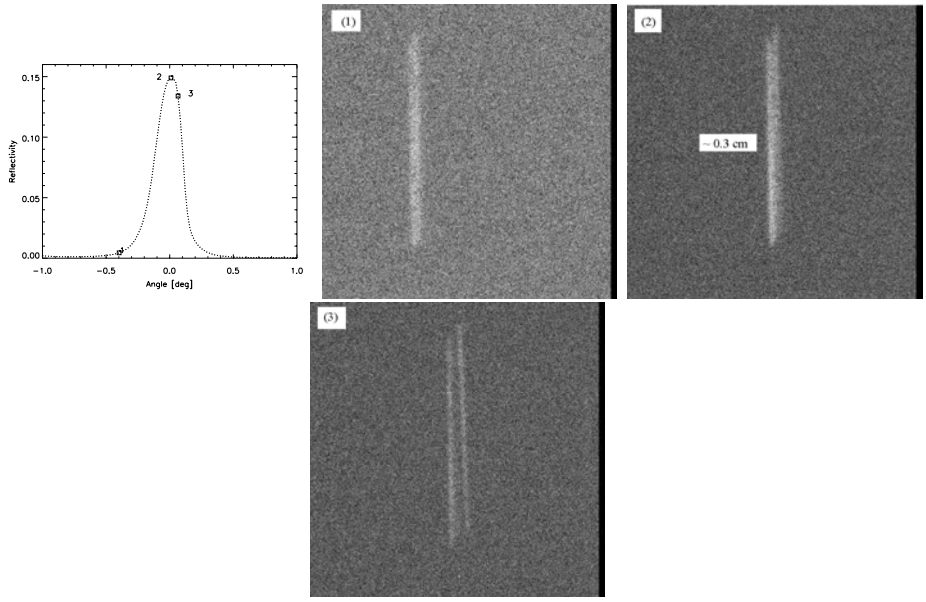

Figure 5.13: *Same as Fig. 5.12 but with a beam size of 20 μm.*

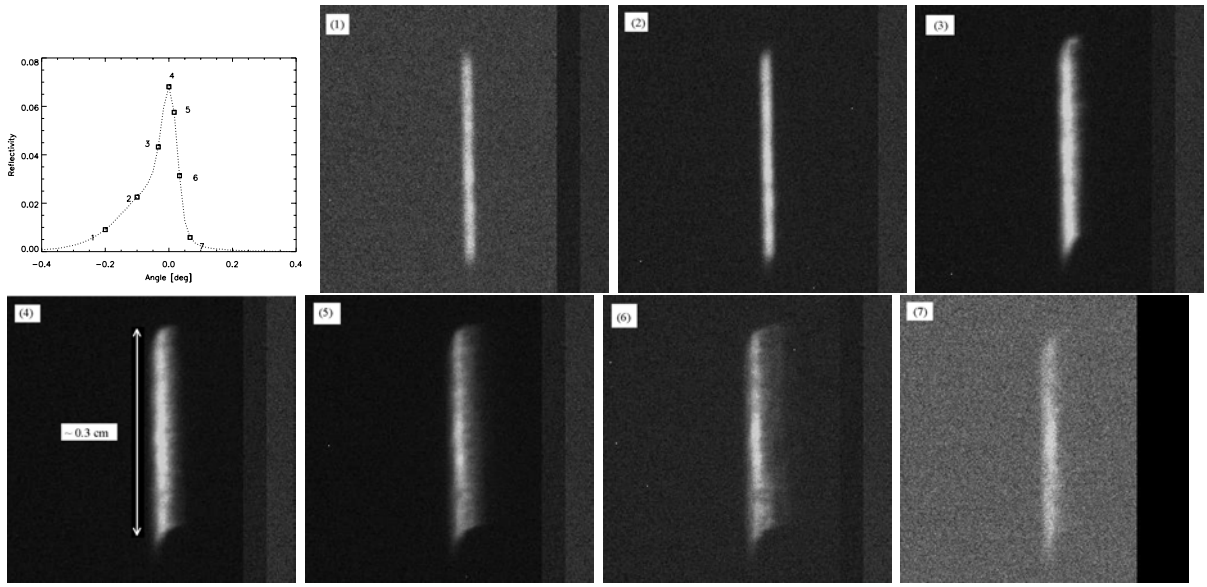

Figure 5.14: *X-ray topographs of Cu-D <222> at E = 120 keV. The angular positions at which the topographs were recorded are indicated in the plot on the top-left. The Bragg angle at this energy is 2.8° and the slit width was 100 μm.*

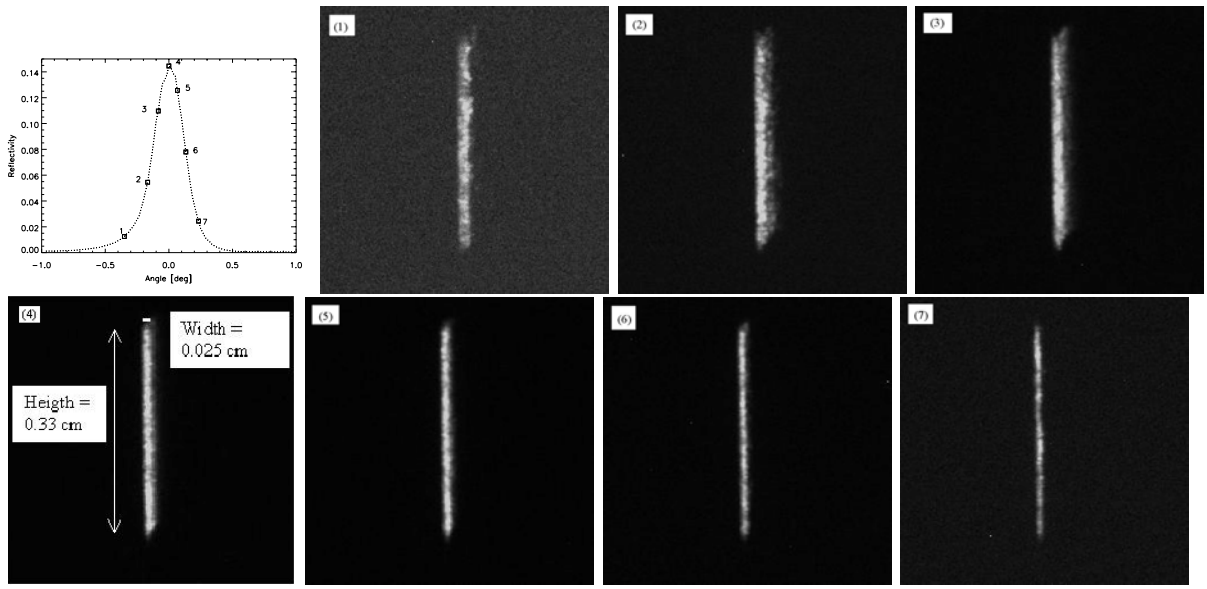

Figure 5.15: *X-ray topographs of Cu-E <111> at E = 120 keV. The angular positions at which the topographs were recorded are indicated in the plot on the top-left. The Bragg angle at this energy is 1.4° and the slit width was 100 μm.*

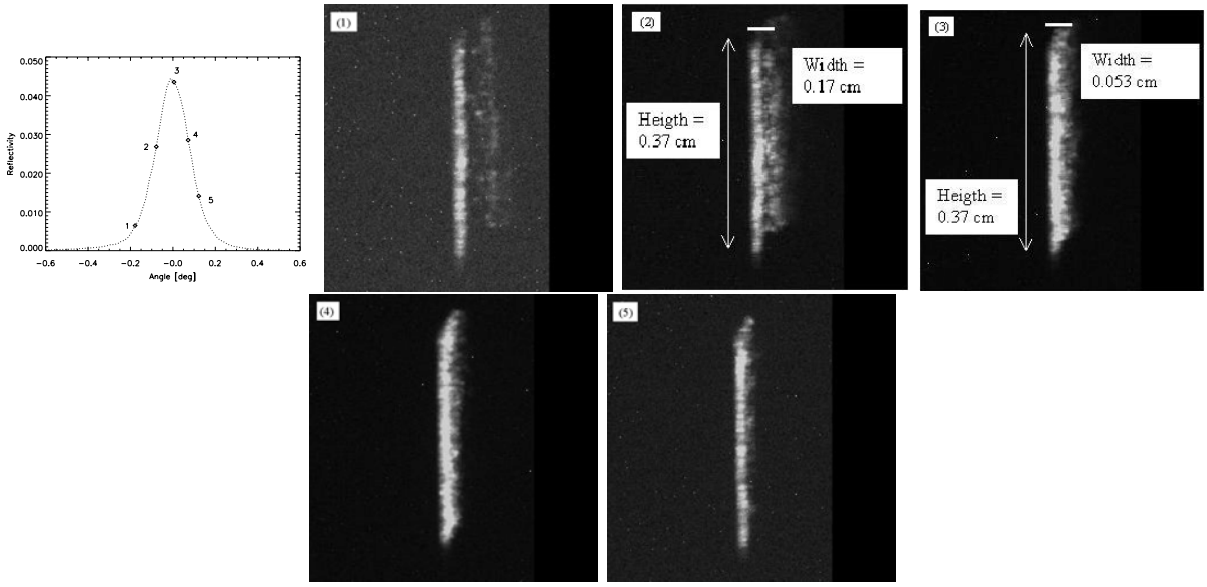

Figure 5.16: *X-ray topographs of Cu-E <222> at E = 120 keV. The angular positions at which the topographs were recorded are indicated in the plot on the top-left. The Bragg angle at this energy is 2.8º and the slit width was 100 μm.*

Table 3. *High energy X-ray primary extinction, absorption and secondary extinction lengths as a function of the energy and the reflection indices. The absorption length was calculated considering both photoelectric absorption and Compton scattering. The secondary extinction length was calculated for a mosaicity of η = 0.1º and the Debye Waller factor was not considered. The values in the second and third columns determine the spatial range of the topographic images.*

Energy keV	Reflection	Primary extinction length [μm]	True absorption length [cm]	Secondary extinction length [cm]
96	<200>	0.56	0.248	0.253
96	<400>	1.86	0.248	1.39
96	<600>	4.17	0.248	4.64
120	<111>	0.455	0.389	0.302
120	<222>	1.41	0.389	1.45
120	<333>	3.15	0.389	4.80
136	<200>	0.561	0.482	0.509
136	<400>	1.87	0.482	2.815
136	<600>	4.18	0.482	9.42

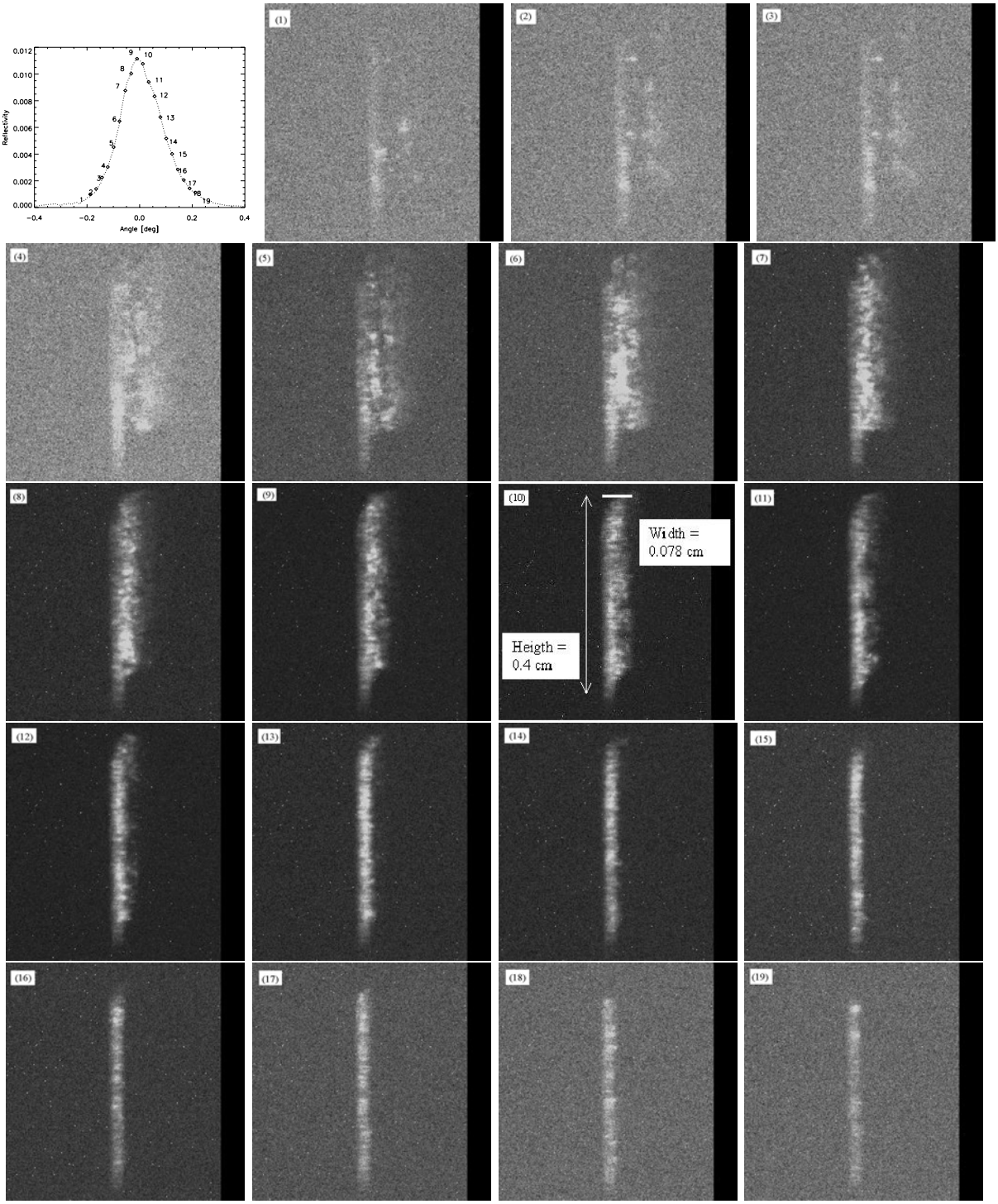

Figure 5.17: *X-ray topographs of Cu-E <333> at E = 120 keV. The angular positions at which the topographs were recorded are indicated in the plot on the top-left. The Bragg angle at this energy is 4.3° and the slit width was 100 μm.*

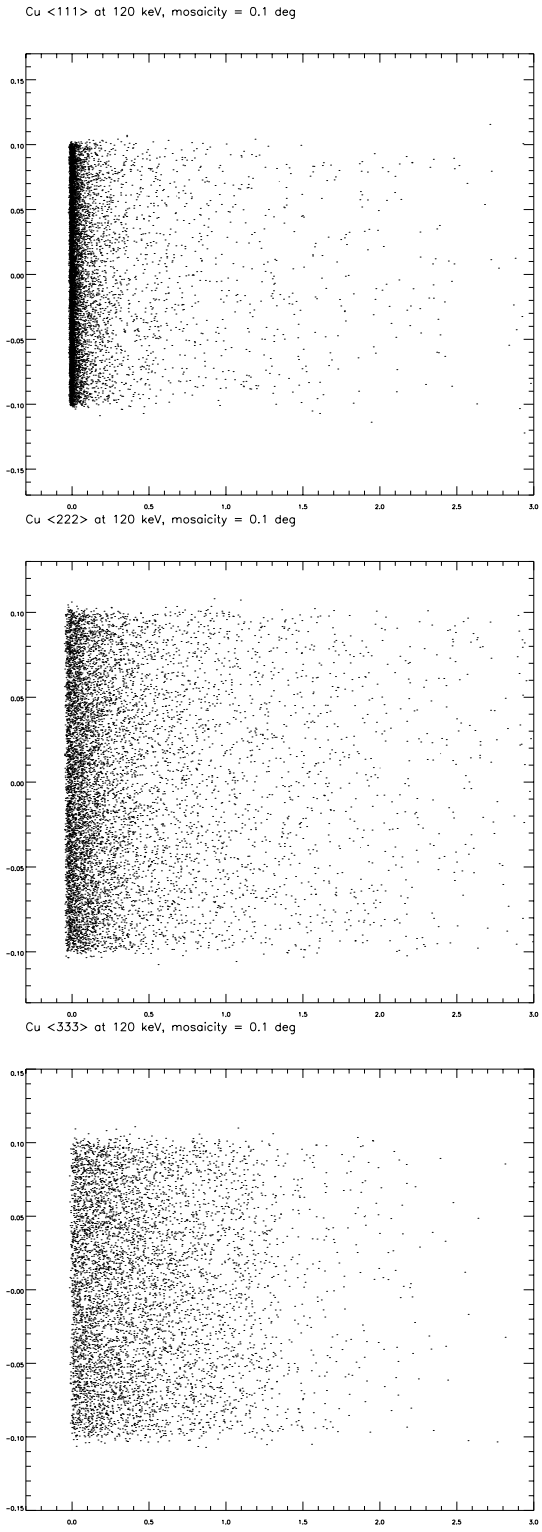

Figure 5.18: *Simulated x-ray topographs of the <111>, <222> and <333> reflections from copper at E = 120 keV. The incident beam is 100 μm wide and 2 mm high and has a divergence of 20 μrad. The crystal mosaicity is η = 0.1° and the image plane is 30 cm from the crystal. Each point corresponds to a diffracted ray but the individual ray weights due to absorption are not shown. The axes are the coordinates at the image plane perpendicular to scattering (vertical axis) and parallel (horizontal axis Z). Units are cm.*

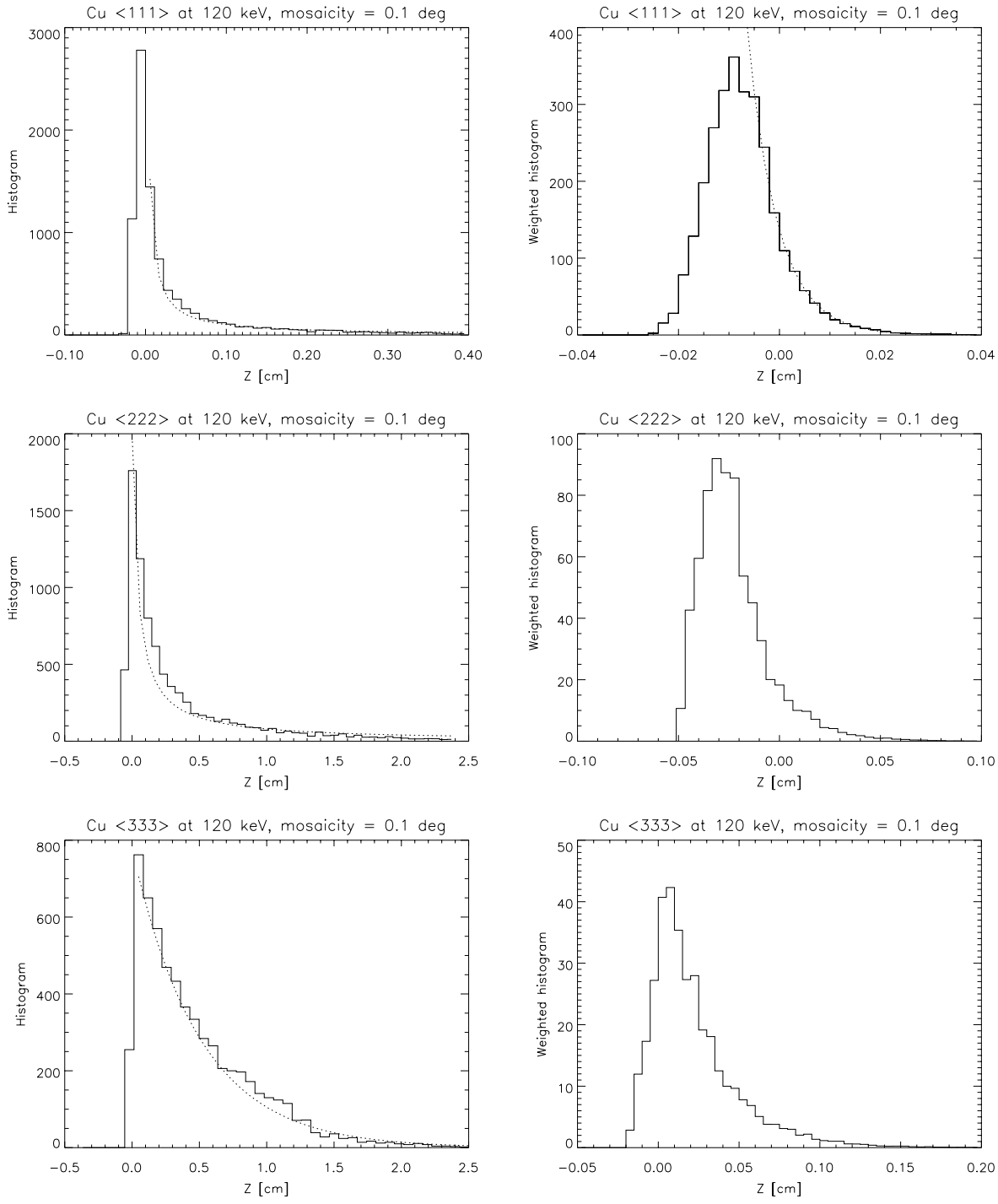

Figure 5.19: *LEFT COLUMN: histograms of the image in Fig. 5.18. The dotted line is the fit using Eq. (5.5) and giving* $l_{ext}^{<111>} = 0.20$ *cm,* $l_{ext}^{<222>} = 0.41$ *cm,* $l_{ext}^{<333>} = 3.3$ *cm which are of the same order of magnitude as the theoretical values in Table 3. RIGHT COLUMN: histograms of the simulated topograph, weighted using Eq. (5.1). These histograms could be directly compared with the experimental topographs.*

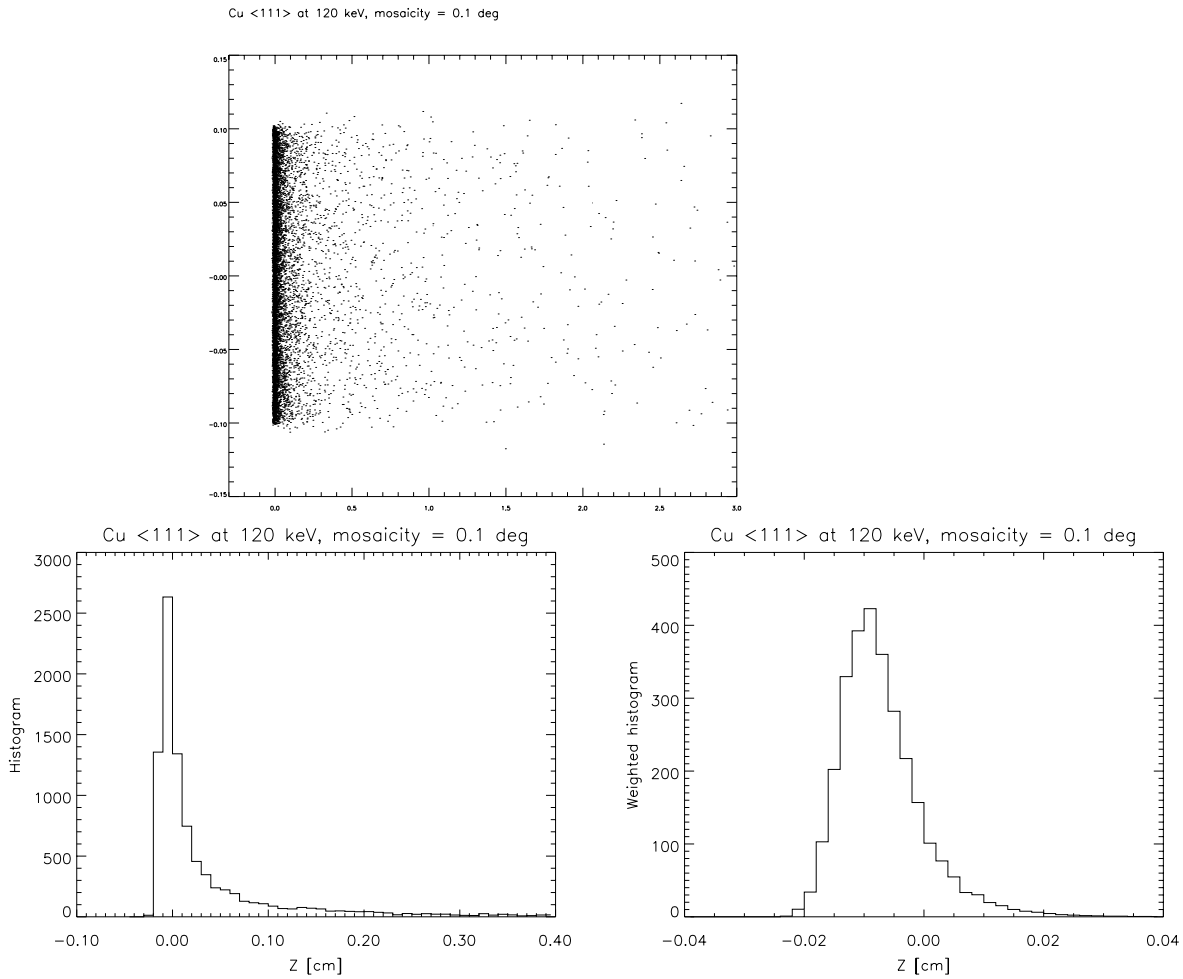

Figure 5.20: *Same as Figs. 5.18 and 5.19, but with a narrower beam: 1 μm.*

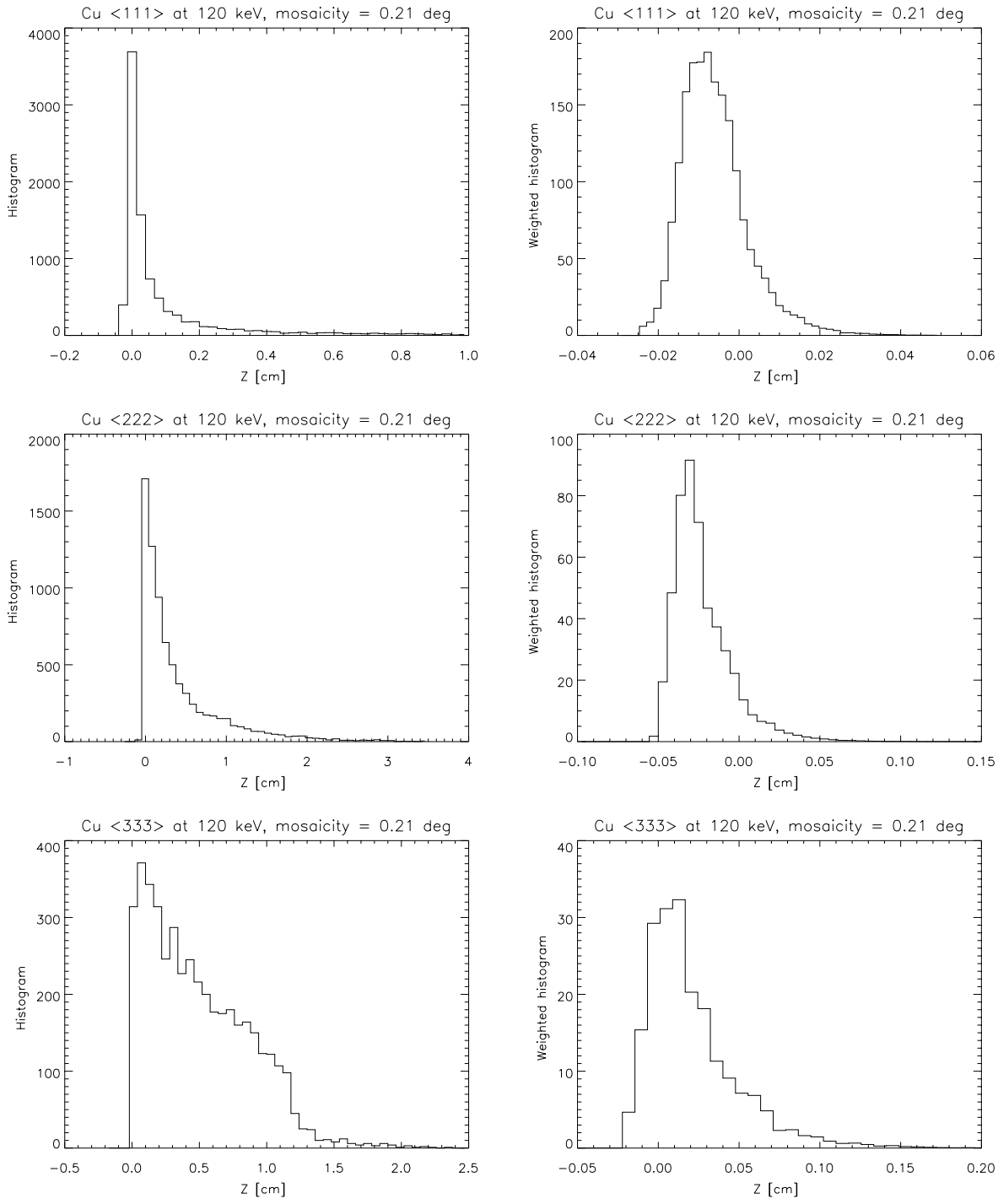

Figure 5.21: *Same as Fig. 5.19, but with a different mosaicity: $\eta = 0.21^o$.*

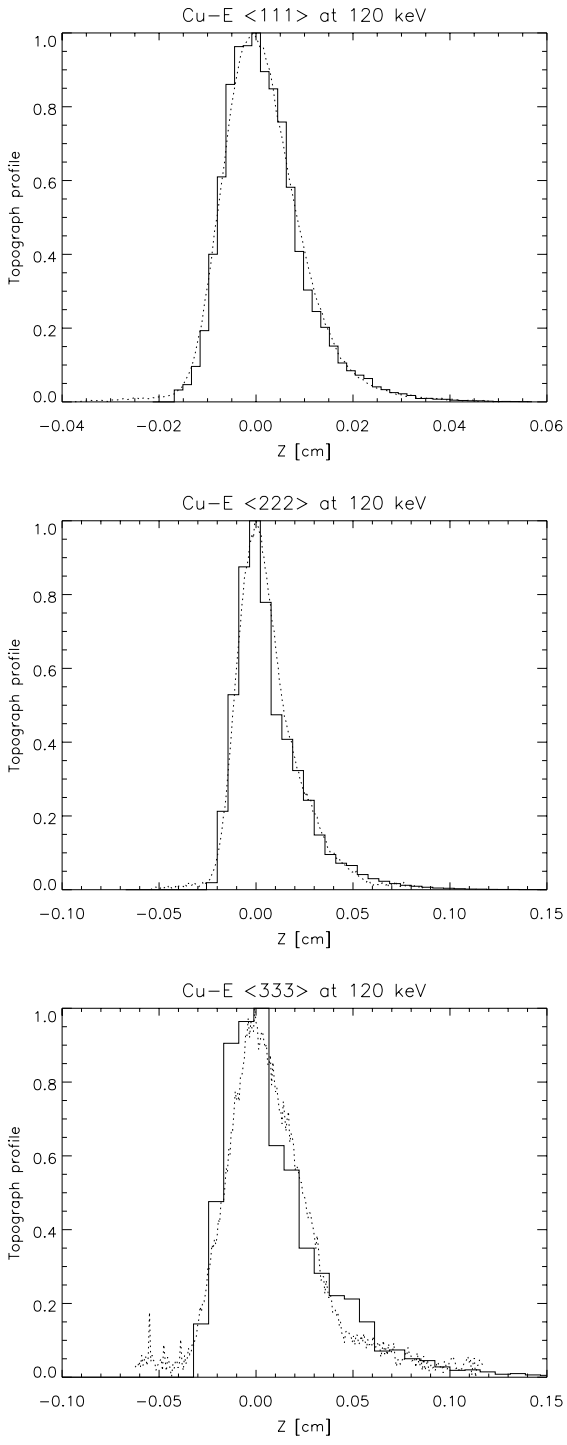

Figure 5.22: *Dotted lines: profiles of the experimental topographs for the <111>, <222> and <333> reflections of the copper sample Cu-E, recorded at the nominal Bragg angles. They were calculated from topographs (4), (3) and (10), respectively, in Figs. 5.15, 5.16 and 5.17. The histograms are the results of the simulations, also shown in the second column of Fig. 5.21.*

5.5 Summary and conclusions

Copper is one of the most used crystal monochromators for neutrons. It has a good coherent scattering cross-section and the absorption by nuclei is negligible. Moreover large crystal with good crystalline properties are easily produced. The ILL has its own facility for producing Cu mosaic crystals and they supplied us with several samples.

In the first part of this Chapter we have compared the real temperature dependent reflectivity of copper mosaic crystals with the valued predicted by the theory. We aimed, with these neutron experiments, at measuring the increase of reflectivity when lowering the crystal temperature down to the liquid helium or nitrogen temperatures. We have experimentally observed an increase of diffracted intensity. However it is difficult to exactly quantify the temperature effect, because of the presence of spurious effects, like parasitic multiple Bragg reflections. The comparison with the theories, described in Chapter 2, are not satisfactory. The Freund's formalism is able to reproduce the experimental data in the temperature range [100, 300] K for relatively "low" incident neutron energy. At lower temperature or in the case of high energy the model fails.

We have characterized copper crystals, made for neutron applications, using synchrotron radiation. The aim was to obtain accurate diffraction profiles and to study the homogeneity of the crystals. X-ray reflectivity and topographs were recorded for two crystals with different values of mosaicity. The results of the data analysis can be summarised as follows:

i) the mosaic distribution of both samples is better represented by a pseudo-Voigt function instead of a simple Lorentzian or Gaussian function. This could suggest that using by "default" Gaussian distributions of crystallites in mosaic crystal calculations is not appropriate, in particular for crystals like copper, in which the mosaicity is artificially created by deformation and annealing.

ii) The sample Cu-D, with $\eta \sim 8'$, was far from showing an ideal mosaic crystal behaviour because of two reasons: the presence of strong primary extinction (demonstrated by the correction coefficient to be made for the Q scattering factor) and presence of large grains (demonstrated by the asymmetric rocking curves).

iii) The sample Cu-E, with $\eta \sim 13'$, was more homogeneous and presented an almost symmetrical reflectivity.

iv) X-ray diffraction topography gives in principle valuable information on the crystal homogeneity: however, although high energy x-ray beams were used ($E = 120$ keV), the strong absorption only allowed us to investigate depths of the order of fractions of

mm, hence the complete bulk crystal, which contributes to the intensity of the diffracted neutrons, was not accessible. The topographs, recorded using high energy and highly collimated x-ray beams, do show the lack of homogeneity, of different type for the two crystals because of the different mosaicity. These details cannot be seen with neutrons, because of the much larger beam divergence and dimension of the beams. Rocking curves recorded using micrometric x-ray beams have different shapes in different positions of the crystal revealing then the sample inhomogeneity. We have also demonstrated that a quantitative analysis of the topographs can be carried out using our *MOSAIC* code.

Chapter 6

Experimental - Germanium and graphite

6.1 Use and production of germanium assembled crystals

Germanium crystals, like copper and silicon, are available in large quantities at a relatively low price. Moreover germanium (like silicon) has the diamond structure and the reflections having $h + k + l = 4n \pm 2$, with n an integer, are forbidden. Therefore, it is a suitable neutron monochromator when second order contamination has to be avoided. Both germanium and silicon have long coherence lengths, i.e. they are perfect on a long scale. In order to use them as neutron monochromators, some kind of distortion has to be introduced to produce integrated intensities similar to those of graphite or copper mosaic crystals. In principle, the high-temperature plastic deformation of large perfect germanium crystals leads to a microstructural change with a resulting mosaic structure. The main difficulty is to achieve mosaic crystals with a spatially homogeneous microstructure starting from a perfect single crystal. It happens that the crystal faces can "stick" in the hot-press and then gliding of the crystal planes as a whole is prevented. This is the reason for the presence of substructures in the crystals. These substructures can be observed using diffraction of hard x-rays (see [92] for the case of copper). When used as neutron monochromators, because the beams are large and divergent, the presence of substructures can have two effects: lowering the peak reflectivity and producing a non-uniform wavelength and intensity distribution of the reflected neutron beam. The resulting homogeneity of plastic deformed crystals depends critically on the thickness, and this is the reason why the *stacked wafer method* is being developed in many neutron laboratories including the ILL [93, 94]. The method is as follows: a given number of perfect germanium

wafers, approximately 1 mm thick, are first deformed by bending and reflattening several times and then glued in a hot press using thin aluminium or tin foils. The bending and flattening procedure is done in such a way as to achieve the desired mosaic spread. The same method can be used to assemble crystals which have virtually no mosaicity, but are simply plastically bent: in this case the wafers are bent only once and glued. Among the advantages of these monochromators is the possibility to obtain an anisotropic mosaic spread, which prevents neutron losses in the plane perpendicular to scattering. Finally, a sputtering method has been developed which replaces the use of tin or aluminium foils for gluing and which makes alignment of the wafers more precise [95]. In this section x-ray and neutron tests on two samples will be presented: the first one plastically bent and the second one flat and mosaic. The neutron experiments were performed at the T13A diffractometer of the ILL. The beam from the reactor, transported by the beam tube, was monochromated by a Ge $< 311 >$ monochromator. In this way, since the measurements reported here concern diffraction by the Ge $< 311 >$ planes (in Bragg symmetric geometry), the recorded diffraction profiles were not influenced by the incident beam divergence. The x-ray data were recorded at the ESRF high energy beamline ID15A and the experiment set-up was the same as used for copper, already described in section 5.2. As shown in Fig. 6.1, because of the extended incident beam, the diffraction profiles are still the convolution of the intrinsic profiles with the beam size. This introduces some uncertainties when discussing the reflectivity of the bent sample. The error on the experimental points representing the reflectivity as a function of the crystal angle was of the order of 2% for the neutron data and smaller for the x-ray. The integrated intensities diffracted by these two kinds of crystals are comparable: while the flat mosaic has the same applications as the mosaic copper, the bent crystal is of course more suitable when focusing is needed.

6.2 Germanium assembled bent crystal

Neutron experiment. The neutron reflectivity of the $< 311 >$ symmetric reflection from the sample Ge-A with $\lambda = 2$ Å ($\theta_B = 36^o$) and $\lambda = 1.75$ Å ($\theta_B = 31^o$), is reported in Fig. 6.2. In order to know how much the diffraction profiles suffer from convolution with the beam size we have to calculate the Bragg angle spread $\Delta\theta$ seen by the incoming beam, because of bending and finite beam size, as schematically shown in Fig. 6.1. The beam size was 1 mm, so $\Delta\theta \leq 0.02^o$. This value of $\Delta\theta$ is 10 times smaller than the width of the measured diffraction profile, so we will neglect, to a first approximation, the effect of the beam size on the reflectivity. The bending of the Bragg planes and the mosaicity of this sample were measured at the hard X-ray diffractometer at the ILL [89]. We found that $R = 5.7$ m and the mosaicity of the single wafers was practically negligible. In spite of this,

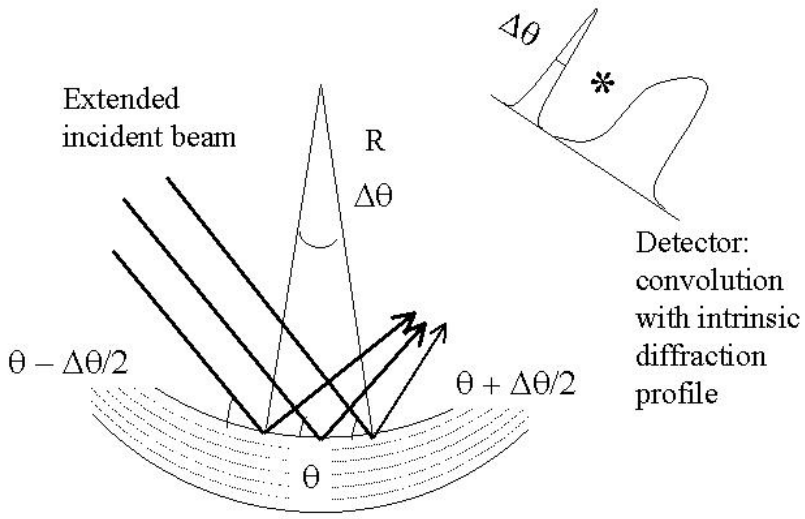

Figure 6.1: *The ideal reflectivity of a bent crystal must be convoluted with the effect of* $\Delta\theta$ *due to the beam size.*

we found that the diffraction profile could only be fitted if we introduce some mosaicity in the model. For example, at $\lambda = 2$ Å, the peak reflectivity is $\sim 60\%$. If the crystal were perfectly bent, according to the *lamellar model* which predicts the reflectivity of a bent perfect crystal, it would have a peak reflectivity of 98%. The lower peak reflectivity is explained by the presence of a mosaic distribution of the Bragg planes, which can be due to the cutting of the wafers and to the gluing. The fitting procedure was performed using Eq. (2.41) for the reflectivity predicted by the *layer coupling model* and letting free three parameters: mosaicity, equivalent thickness d and attenuation coefficient. As for the flat crystals (copper in the previous Chapter and HOPG in the next section), a more rigorous fit would require us to also let the Q factor free. We recall that, according to Zachariasen [37], a decreased Q, with respect to the theoretical value, accounts for primary extinction in the small perfect crystallites and has the effect of lowering the peak reflectivity without changing the shape of the diffraction profile. In other words, correcting Q is essential when diffraction is governed by secondary extinction due to mosaicity, and we want to correct for primary extinction. In our case the peak reflectivity is well fitted without correcting the Q parameter. Actually, this is true at $\lambda = 1.75$ Å, but at $\lambda = 2$ Å, the fitted peak reflectivity is lower. In order to reproduce it better, one should introduce a lower value of mosaicity, but then there would be a discrepancy between the fit and the tails of the measured profile. However, the small value of mosaicity found by fitting could also originate from the convolution with the beam shape discussed above, and not be exactly due to the crystal mosaicity.

There is a discrepancy between the real crystal thickness $d = 10$ mm and the fitted *reduced*

thickness $d = 7$ mm. This explanation is not straightforward. One might simply say that it is the thickness of the crystal volume seen by the beam, or the thickness corresponding to that crystal part which has not been damaged in the assembling process. Since the total width of the diffraction profile is determined by the thickness and the bending radius R, we cannot leave d out of consideration in the fitting.

The need to fit μ comes from the simple consideration that the diffraction profile of bent crystals is asymmetric because of attenuation: for each different incidence angle, the beam will fulfill the condition for Bragg reflection at a different depth and the Bragg diffracted beam intensity will decrease according to the value of μ and the path in the crystal. The slope of the diffraction profile on the left side of the peak is thus very precisely determined by the value of the attenuation coefficient. For the bent sample Ge-A, the fitted absorption coefficient is $\mu_{fit} = 1$ cm^{-1} at 2 Å and $\mu_{fit} = 0.75$ cm^{-1} at 1.75 Å, whereas the theoretical value is $\mu_{theor} \sim 0.14$ cm^{-1} in both cases. The diffraction profiles, for a crystal with the theoretical attenuation, are shown as dashed lines. The reason for the observed increase of μ is not clear. In spite of the non-ideal behaviour, this sample has a very good peak and integrated reflectivity and can be seen as a good candidate for being used as focusing monochromator.

X-ray experiment. The X-ray experiments on this crystal were performed at a photon energy of 120 keV, in Bragg symmetric geometry. The beam footprint on the crystal for the $< 311 >$ reflection was 3 mm. The x-ray rocking curve of the bent Ge is shown in Fig. 6.3. As for the neutron case, the peak reflectivity (18%) is lower than that predicted by the *lamellar theory* for a similar bent perfect crystal (31%). Therefore the rocking curve could only be reproduced by using the *layer coupling* model, which is valid for mosaic bent crystals, and the fitted mosaicity was very small: $\eta = 1.4'$. We also fitted absorption because the experimental FWHM was narrower than the theoretical value and, as explained above, this is due to absorption. The result was $\mu = 2.2$ cm^{-1}, whereas the theoretical value is $\mu_{theor} = 1.8$ cm^{-1}. The incident beam size was 100 μm, the footprint on the crystal was $F = 3.3$ mm and the angular spread seen by the incoming beam because of its finite size was $\Delta\theta \sim \tan^{-1}(F/R) = 0.03^o$. The resulting fit does not then say that there is some mosaicity but just that, in order to fit the experimental data to theory, one has to convolute the reflectivity of the ideal bent perfect crystal with the shape of the incident beam. When doing this, one realizes that the convoluted shape of the reflectivity is wider than that measured. We will then assume that the fit of the data (without convolution) with the model for the perfect mosaic crystal is more suitable.

Some considerations of the homogeneity of the crystal can be obtained from the plot of the rocking curves at different positions Y along the crystal shown in Fig. 6.4. The contour plot shows that there is an approximately linear variation of the angular position of the Bragg peak corresponding to the bending radius $R = 5.7$ m. The width of the rocking

curve along Y is constant, but the peak reflectivity decreases with decreasing Y: this is probably the effect of a smaller diffracting volume due to the limited crystal length (6 cm).

As in case of copper, the topographs shown in Fig. 6.5 do not show many details because of high absorption. However some structures are evident in the images labelled (1) and (2). The histogram obtained from the simulated topograph at the nominal Bragg angle in Fig. 6.6 is in very good agreement with the experimental profile. It is interesting to note that even though the crystal is bent, the profile is symmetric because the beam is extended.

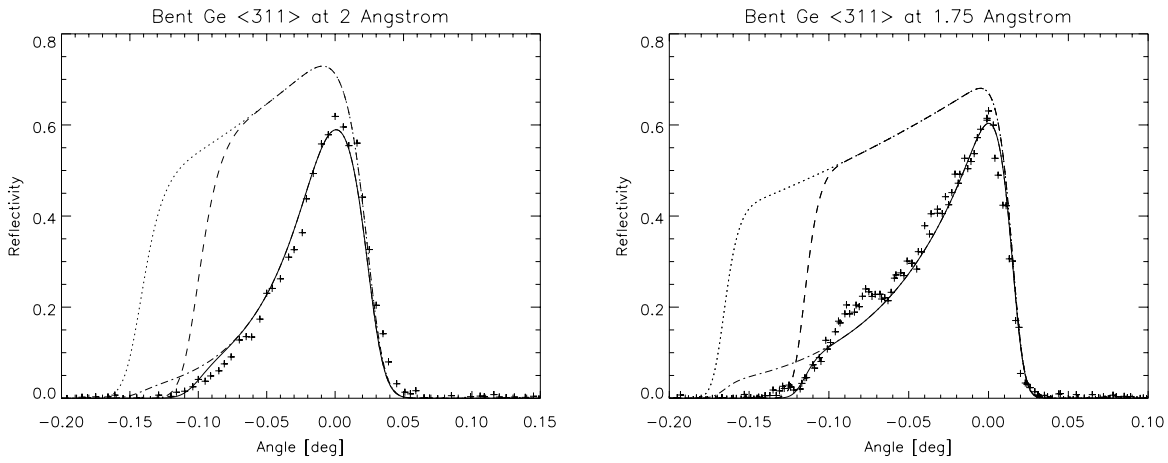

Figure 6.2: *Experimental neutron reflectivity versus* $(\theta - \theta_B)$ *(+ symbol) of the bent crystal Ge-A at 2 Å (left) and 1.75 Å (right). The layer coupling model was used for the fit with three free parameters: mosaicity, equivalent thickness and absorption coefficient. The equivalent thickness used for the fit (solid line) is 7 mm. The other parameters are:* $\eta_{2A^\circ} = 1.8'$, $\eta_{1.75A^\circ} = 1'$, $\mu_{fit,2A^\circ} = 1\ cm^{-1}$ *and* $\mu_{fit,1.75A^\circ} = 0.75\ cm^{-1}$. *The actual crystal thickness was of 10 mm and the calculated absorption coefficients are* $\mu_{theor,2A^\circ} = 0.145\ cm^{-1}$ *and* $\mu_{theor,1.75A^\circ} = 0.14\ cm^{-1}$. *The dashed lines are the calculated diffraction profiles with the nominal absorption coefficient; the dotted lines with the nominal absorption and thickness and the dot-dashed lines are calculated with the nominal thickness and fitted absorption coefficient.*

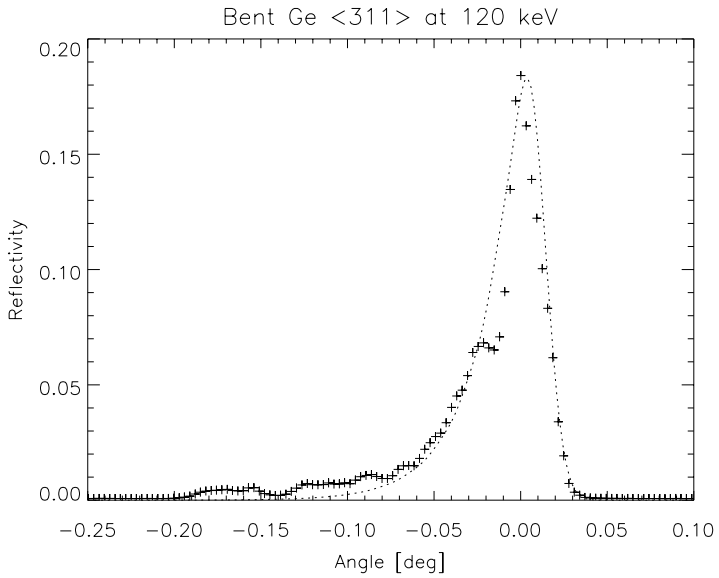

Figure 6.3: *X-ray reflectivity versus* $(\theta - \theta_B)$ *of the <311> reflection from the assembled bent crystal Ge-A. The photon energy was 120 keV. The radius of curvature is* $R = 5.7$ *m. The dotted line is the reflectivity according to the layer coupling model with the parameters:* $\eta = 1.4' = 0.02^o$ *and* $\mu = 2.2\ cm^{-1}$ *(whereas* $\mu_{theor} = 1.8\ cm^{-1}$*).*

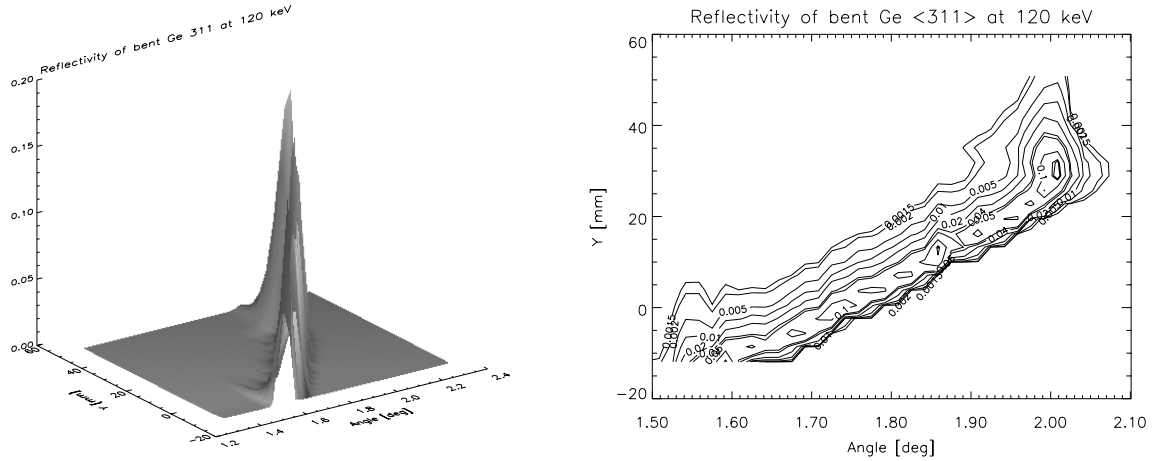

Figure 6.4: *LEFT: rocking curves along the crystal surface for the same case as Fig. 6.3. RIGHT: contour of the plot on the left. The bending of the Bragg planes to* $R = 5.7$ *m is proved by the shift of the peak along Y.*

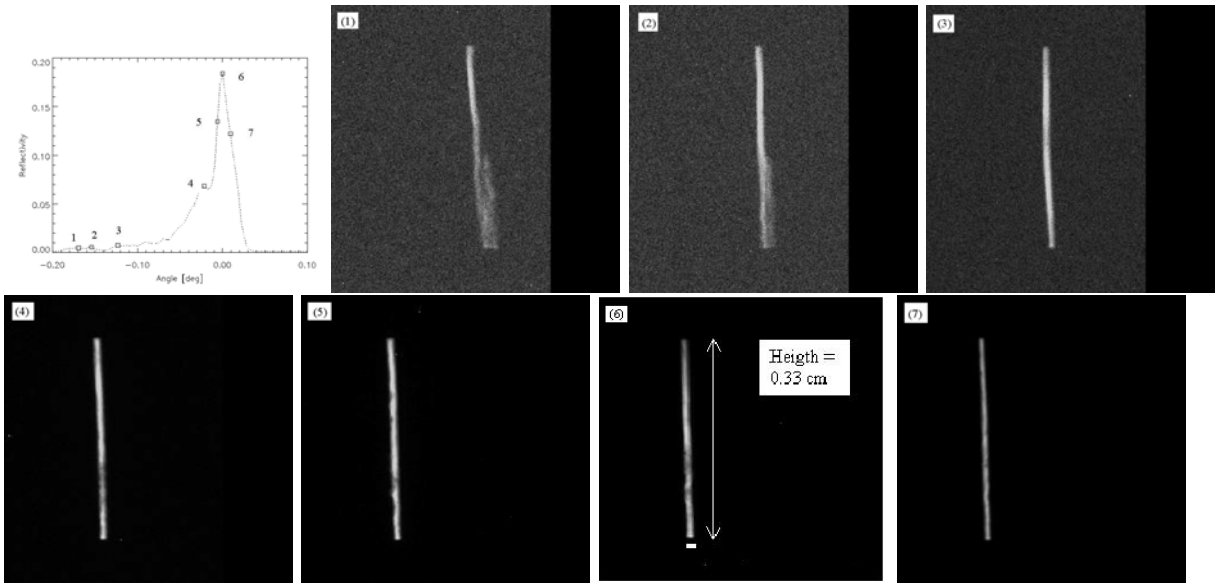

Figure 6.5: *X-ray topographs of the assembled bent <311> Ge-A at E = 120 keV. The angular positions at which the topographs were recorded are indicated as squares in the plot in the first row. The Bragg angle at this energy is 1.7° and the slit width was 100 μm.*

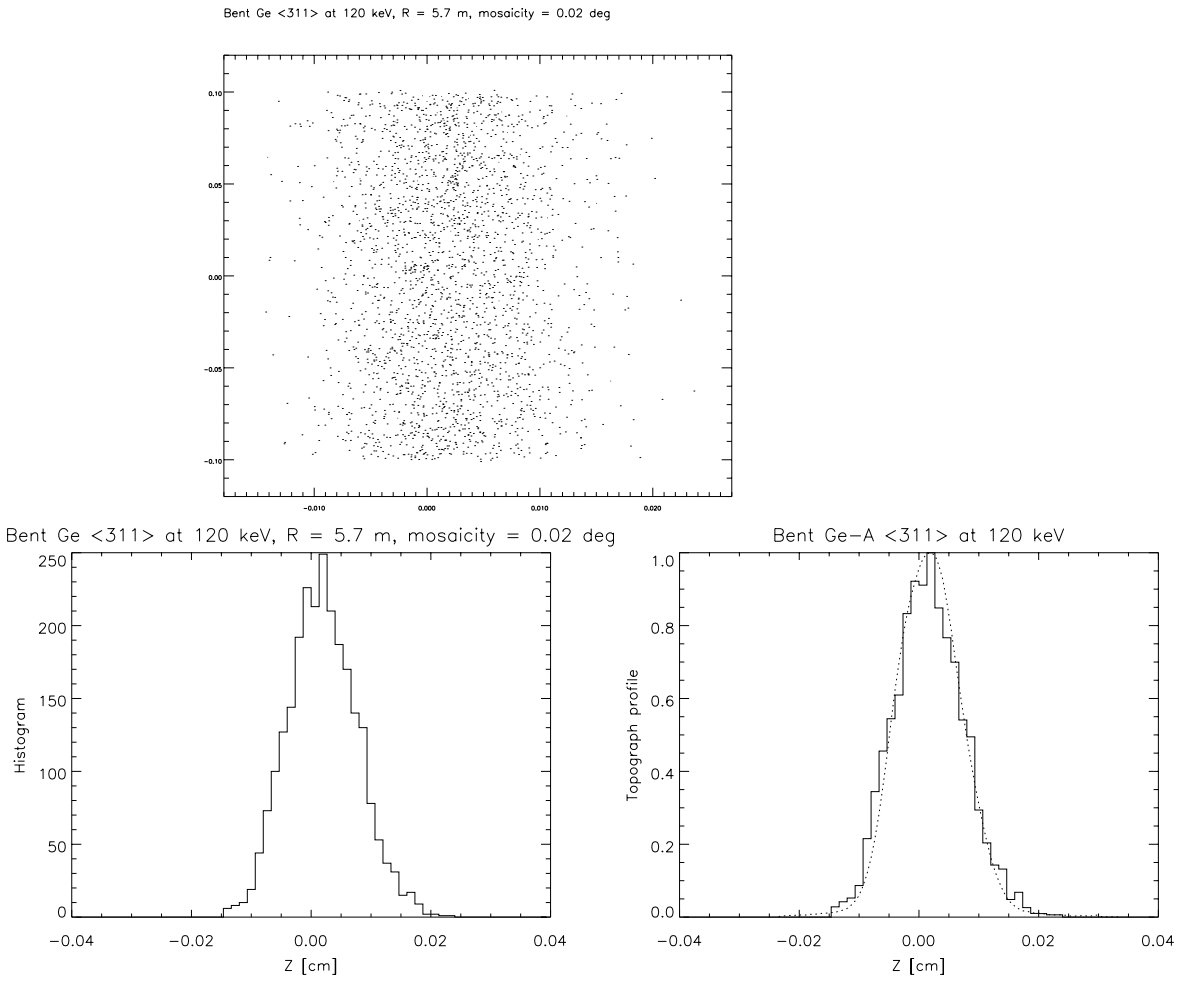

Figure 6.6: *TOP: simulated x-ray topograph of the <311> reflection from bent germanium at E = 120 keV at the exact Bragg angle. The incident beam is 100 μm wide and 2 mm high and has a divergence of 20 μrad. The crystal radius of curvature is R = 5.7 m, the mosaicity is η = 0.02° and the image plane is 30 cm from the crystal. Every point corresponds to a diffracted photon; the image is not weighted with absorption. The axes are the coordinates at the image plane perpendicular to scattering (vertical axis) and parallel (horizontal axis Z). Units are cm. BOTTOM LEFT: histogram of the image. BOTTOM RIGHT: the solid line is the histogram of the simulated topograph, weighted using Eq. 5.1 with the absorption coefficient equal to the value obtained by the fit of the rocking curve. The dotted line is the profile of the experimental image n° (6) in Fig. 6.5.*

6.3 Germanium assembled flat crystal

Neutron experiment. The flat sample described in this section was obtained by stacking 10 germanium wafers, 1 mm thick, which were previously bent and reflattened to achieve the desired mosaicity. Thus, as mentioned in the introduction to the Chapter, the resulting mosaicity should be anisotropic, with an average width η larger in the direction of deformation. The two neutron rocking curves shown in Fig. 6.7 were measured by rotating the azimuthal angle Φ of the crystal by 90^o. Therefore they demonstrate the different mosaicity when using two perpendicular scattering planes. The anisotropic mosaic distribution can be seen from the different widths of the rocking curves: the theoretical diffraction profiles shown in the plots were obtained using $\eta \sim 4.2'$ for the reflectivity in the plane corresponding to the deformation process, and $\eta \sim 2.1'$ for the perpendicular direction. In order to properly fit the reduced peak reflectivity, we used $Q = 0.3 \times Q_{theor} = 0.00093$ cm^{-1} and $Q = 0.15 \times Q_{theor} = 0.000465$ cm^{-1} respectively. The two different Q factors obtained from the fit indicate that the mosaic model we use is very approximate for this crystal. In theory, a smaller Q means a larger crystallite size, but in the case of the machined crystal this is just a measure of the imperfection. The surface plot in Fig. 6.8 represents reflectivity as a function of angle and Y coordinate along the crystal length. It does not show many details because of little spatial resolution of the beam (few mm). However, the contour plot shows a displacement of the peak along Y, as if there was a residual bending of the Bragg planes in the bulk crystal.

X-ray experiment. The x-ray rocking curves, measured at photon energies of 120 and 90 keV for the $< 311 >$ and $< 933 >$, are reported in Fig. 6.9. All the plots show the presence of grains, thus the fit was done by using a mosaic distribution $W(\theta - \theta_B)$ given by the sum of two pseudo-Voigt functions with different FWHMs η and η_2, shifted of Δ one with respect to the other. These parameters are reported in the same figure. The sample has an average mosaicity of $\sim 5'$, similar to that found with neutrons. The presence of inhomogeneities is also proved by the diffraction profiles recorded for the $< 311 >$ at 90 and 120 keV along the crystal surface as shown in Fig. 6.10: the peak reflectivity decreases by more than 50% over 10 mm. Furthermore, the surface plot at 90 keV shows some ripples. They are probably due to the fact that the wafers do not have a perfect flat shape because of the machining process. Contrary to the neutron data in Fig. 6.8, in the x-ray case in Fig. 6.10 the position of the Bragg peak does not change with Y, so a possible residual bending is present in the crystal bulk but not at the surface.

Different topographs, for several incidence angles, are shown in Figs. 6.11 for $E = 120$ keV and 6.12 for 90 keV. For this crystal we observe multiple structures, which are different from those seen for copper and for the bent Ge sample. An interesting question is whether the illuminated zones correspond to different wafers or if they are a proof of the ripples

that appear also in the surface plot already discussed. We can assess this by comparing the simulation results to for example the image (5) in Fig. 6.12, corresponding to $(\theta - \theta_B) = 0.08^o$, and where the structures are more visible. The *MOSAIC* program keeps track of the maximum depth reached by the simulated photon trajectories in the crystal. The simulation shows that rays having reached a maximum penetration depth of 10 mm, i.e. the total crystal depth, can reach the image position. Nevertheless, by weighting the probability of observation of these trajectories with Eq. (5.1), we find that, because of high attenuation, only those rays having a maximum penetration depth of approximately 0.4 mm have a non negligible probability of being observed at the detector. Then, according to the simulation result, the structures do not correspond to the wafer separation, but most probably to ripples in the first crystal wafer.

Finally, a comment on the simulated topographs in Fig. 6.13 and on the comparison with the experimental profiles in Fig. 6.14: the agreement is worse than that for the bent germanium because here we used the theoretical attenuation coefficient. In the case of the bent crystal we used the fitted value of μ and the simulated profiles were in very good agreement with the experiment.

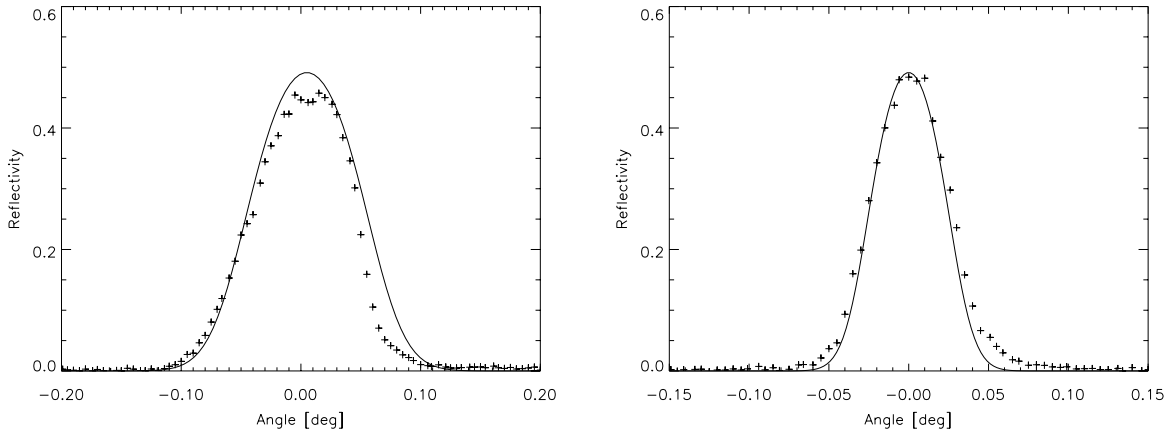

Figure 6.7: *Experimental neutron reflectivity versus* $(\theta - \theta_B)$ *(+ symbol) of the flat crystal Ge-B at 1.64 Å. LEFT: the scattering plane corresponds to the direction in which the wafers were machined. RIGHT: scattering plane perpendicular to the direction in which the wafers were machined. For the calculated reflectivity (solid line) we used* $Q = 0.3 \times Q_{theor} = 0.00093\ cm^{-1}$ *and* $\eta = 4.2'$ *(LEFT) and* $Q = 0.15 \times Q_{theor} = 0.000465\ cm^{-1}$ *and* $\eta = 2.1'$ *(RIGHT).*

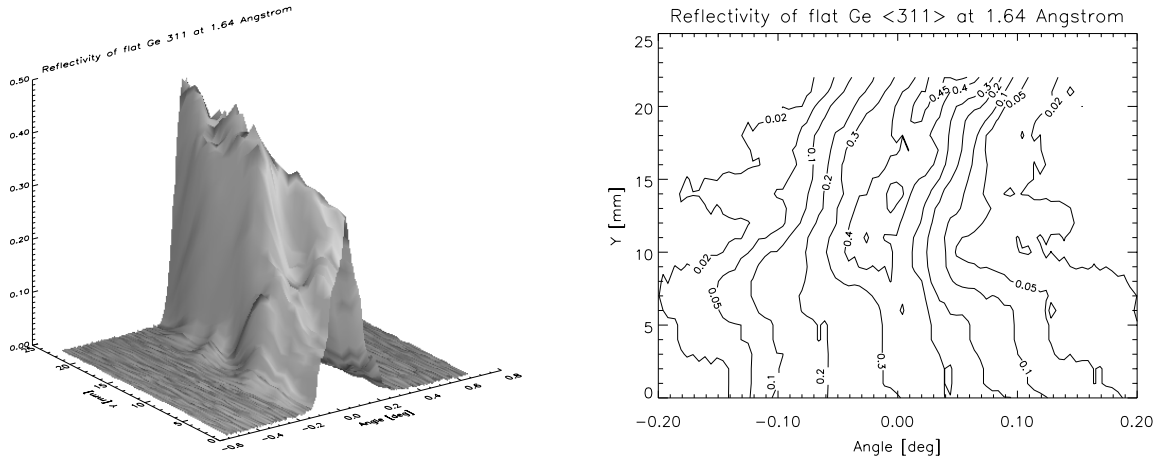

Figure 6.8: *Same as plot on the left in Fig. 6.7. LEFT: rocking curve recorded along the crystal surface. RIGHT: contour of the plot on the left.*

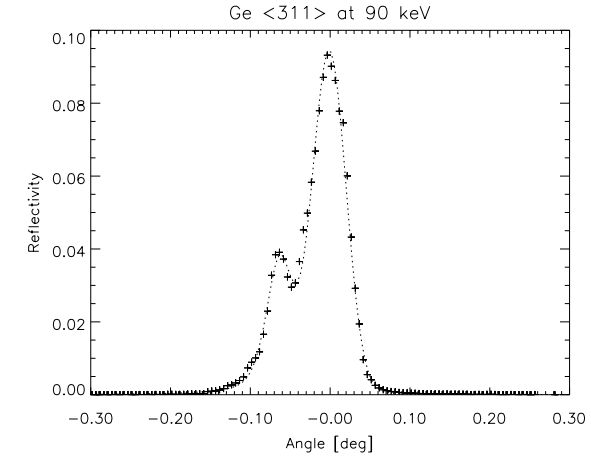

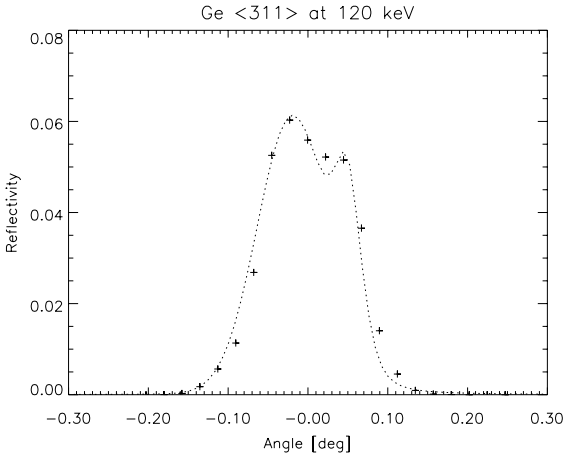

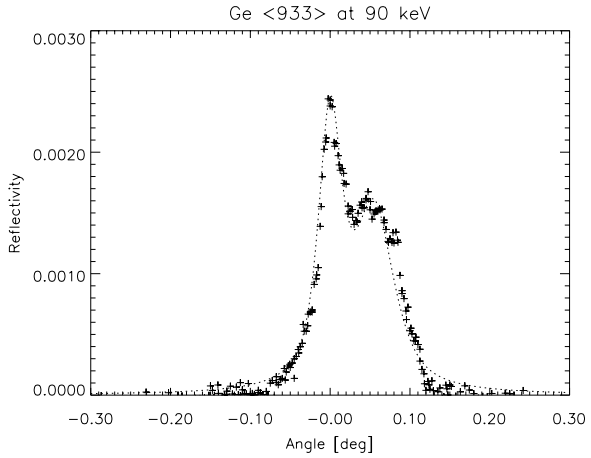

Energy [keV]	90	90	120
Reflection	311	933	311
θ_B [deg]	2.3	7	1.7
μ [cm^{-1}]	3.4	3.4	1.8
η [arcmin]	2.9	2.1	6
η_2 [arcmin]	2.4	3.6	2.4
Δ [arcmin]	-3.7	3.3	4.2
Q_{theor} [cm^{-1}]	1.3D-3	7.0D-5	7.0D-4
Q_{fit} [cm^{-1}]	1.05D-3	6.8D-5	6.5D-4

Figure 6.9: *X-ray reflectivity versus* $(\theta - \theta_B)$ *of the assembled flat crystal Ge-B (+ symbols). TOP: <311> reflection at 90 and 120 keV. BOTTOM LEFT: <933> reflection at 90 keV. BOTTOM RIGHT: parameters used for calculating the theoretical reflectivity (dotted lines) using a mosaicity distribution* $W(\theta - \theta_B)$ *with two separate peaks. The free parameters were the two FWHMs* η *and* η_2 *of* W*, the peak separation* Δ *and the* Q *scattering factor.*

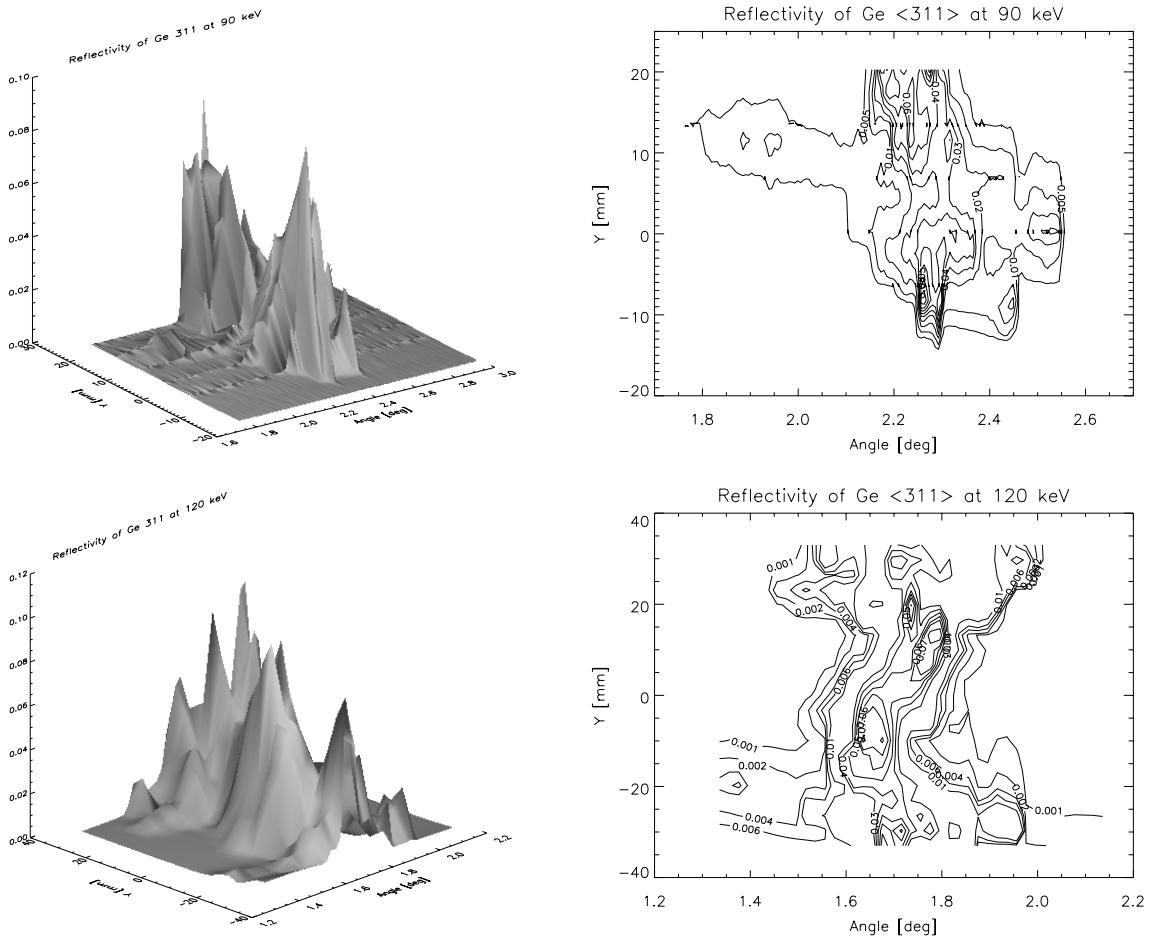

Figure 6.10: *LEFT: rocking curves recorded as a function of Y along the crystal surface for the case already shown in Fig. 6.9. The structures appearing on the tails, more visible for the upper surface plot, are due to real imperfections and not to noise or erroneous normalisation. RIGHT: contours of the plots on the left.*

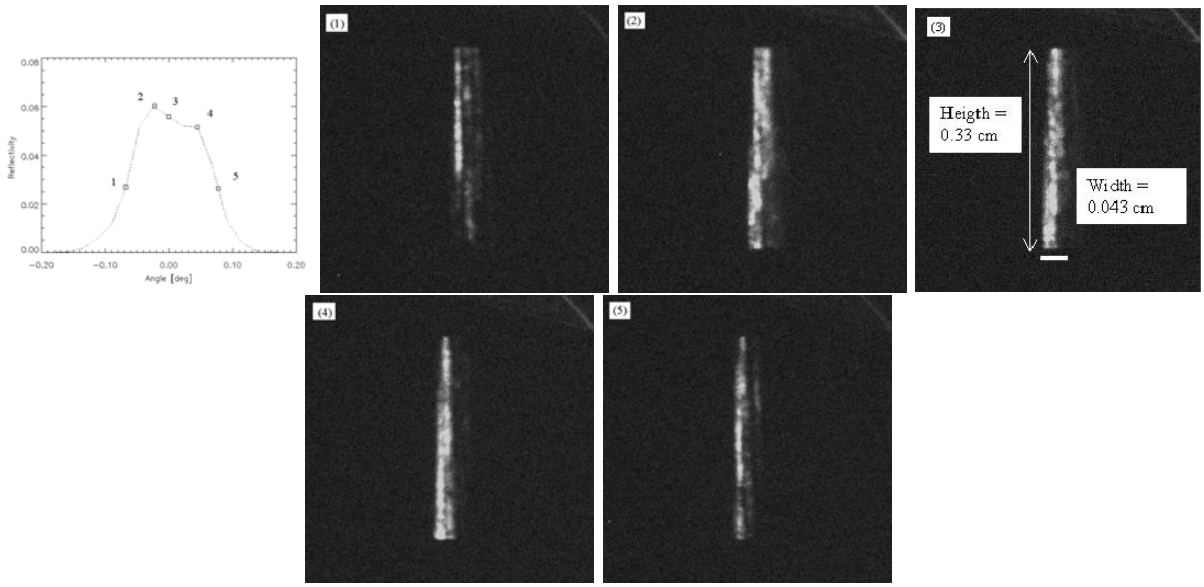

Figure 6.11: *X-ray topographs of the assembled flat crystal Ge-B at E = 120 keV for the <311> Bragg planes. The angular positions at which the topographs were recorded are indicated as squares in the plot in the first row. The Bragg angle at this energy is 1.7º and the slit width was 100 μm.*

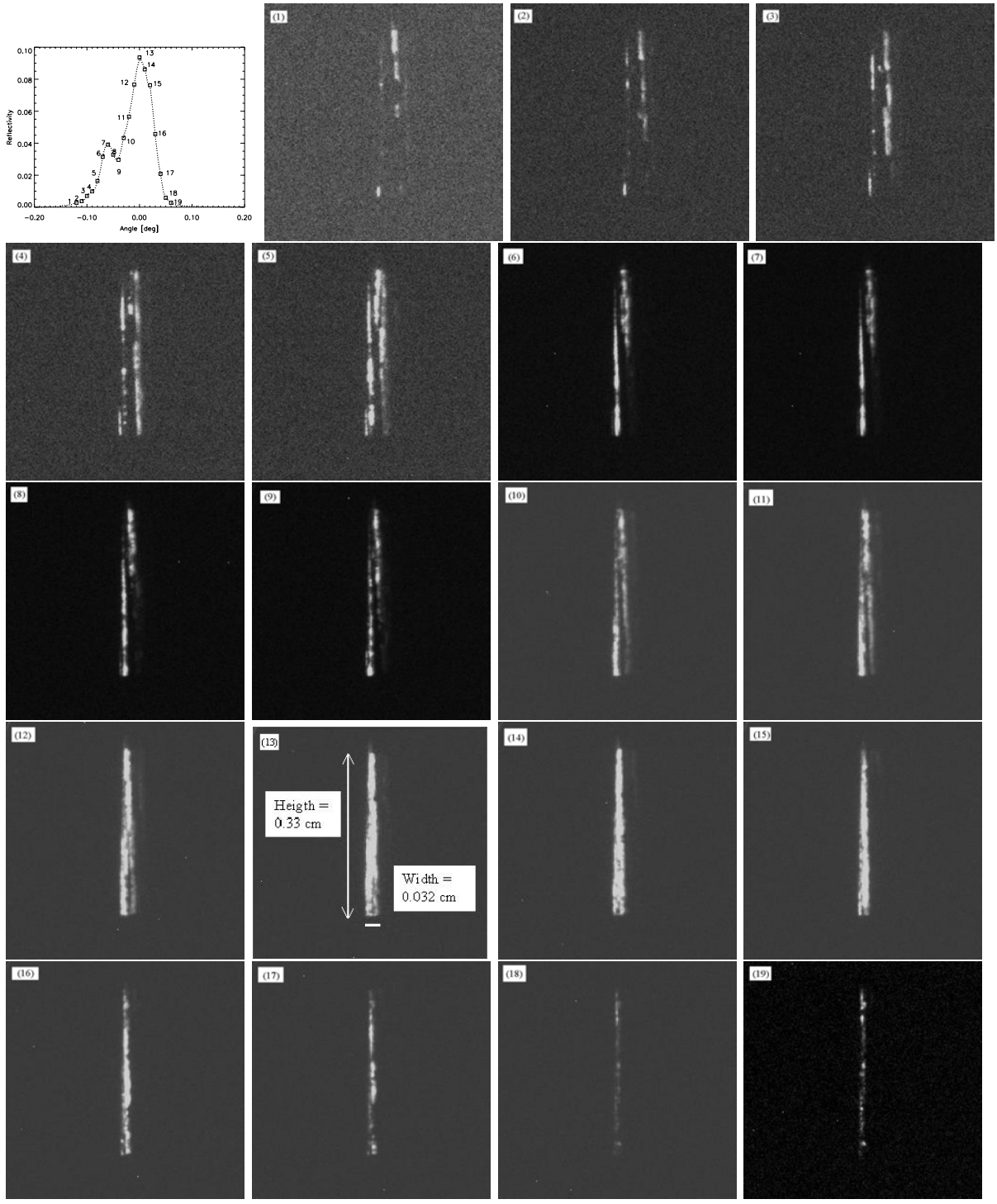

Figure 6.12: *X-ray topographs of the assembled flat crystal Ge-B at E = 90 keV for the <311> Bragg planes. The angular positions at which the topographs were recorded are indicated as squares in the plot in the first row. The Bragg angle at this energy is 2.3º and the slit width was 100 μm.*

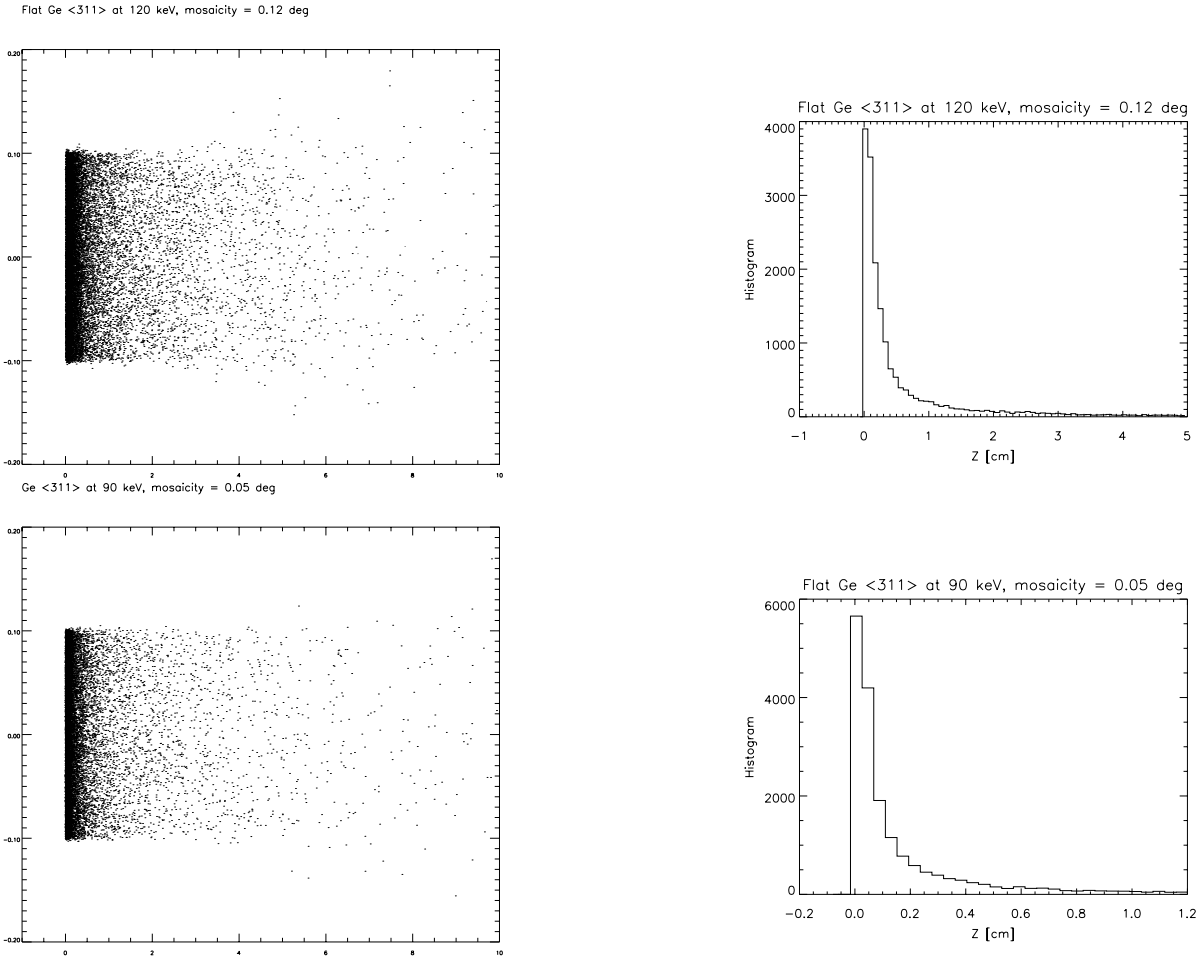

Figure 6.13: *Simulations for the <311> reflection from flat germanium at E = 120 keV (TOP) and E = 90 keV (BOTTOM). LEFT: simulated x-ray topograph at the nominal Bragg angle. The incident beam is 100 μm wide and 2 mm high and has a divergence of 20 μrad. The crystal mosaicity is η = 0.12° (TOP) and η = 0.05° (BOTTOM) and the image plane is 30 cm from the crystal. Every point corresponds to a diffracted photon; the image is not weighted with absorption. The axes are the coordinates at the image plane perpendicular to scattering (vertical axis) and parallel (horizontal axis Z). Units are cm. RIGHT: histogram of the image on the left.*

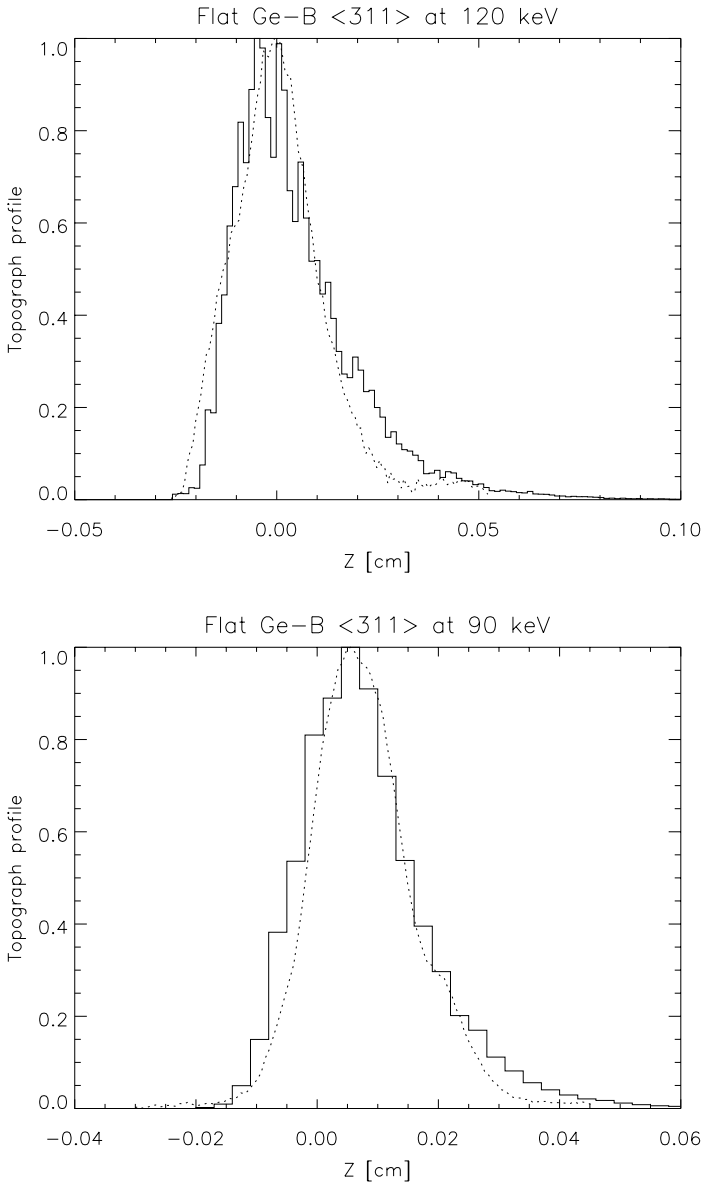

Figure 6.14: *Comparison between the experimental topograph profiles (dotted lines) and the histograms of the simulated topographs reported in Fig. 6.13, weighted by using Eq. 5.1 and the absorption coefficient given by the theory. TOP: profile of the experimental image n^o (3) in Fig. 6.11. BOTTOM: profile of the experimental image n^o (13) in Fig. 6.12.*

6.4 X-ray reflectivity of highly oriented pyrolitic graphite

Pyrolytic graphite is generally considered to be a nearly ideal imperfect crystal. Extensive studies of its diffracting properties have been made in the past [46, 96] but, to our knowledge, a complete analysis of its reflectivity as a function of energy and index of reflection does not exist. The reflection and transmission profiles in Fig. 6.15 and 6.16 were measured using synchrotron radiation at the BM5 beamline at ESRF. The divergence of the beam in the scattering plane was negligible and its dimensions were fixed at 0.1 mm $\times$ 0.1 mm. The curves were measured using a Si diode detector. We used a sample of thickness d = 0.5 mm produced by Optigraph (Russia) and measured the <002> and <004> reflections in Bragg symmetric geometry at 12, 22, 32 and 42 keV (λ=1.03, 0.56, 0.39 and 0.295 Å). We tested the sample homogeneity by recording diffraction topographs at all reflections and energies mentioned above. First the attenuation coefficient μ was obtained by fitting the tails of T, then these values were used to fit the rocking and transmission curves simultaneously with Eqs. (2.23) and (2.24). The fitting parameters were mosaicity η and the scattering factor Q and a gaussian function was used for the mosaic distribution $W(\theta - \theta_B)$. The theoretical and the fit parameters are shown in Table 1. The fit performed on the tails of T is good (thus giving reliable values for the attenuation coefficient) except for the case of the <002> reflection at $E \geq 22$ keV: one possible reason for this inaccurate fit may be that the Bragg angles are quite small (see Table 1) and the presence of possible defects or inhomogeneities on the surface affects the beam. The fit of the rocking curves, on the other hand, is very accurate for the <004> reflection but not for the <002>: the fitted peak reflectivity of the principal reflection is always smaller than the measured one. The mosaicity, as obtained from the fit, was equal to $\eta = 0.32^o \pm 0.01^o$. The rocking curves that we measured confirm the almost ideal behaviour of this sample, especially when compared to the copper and germanium crystals already discussed. The rocking curves are highly symmetric and we used a purely Gaussian function for fitting the mosaic distribution for all values of energy and Bragg indices. The correction factor for the Q coefficient is, on average, equal to ~ 0.7. By using Eq. (4.46a) of Zachariasen [37] and using the corrected Q, as obtained by the fit of the $< 002 >$ reflection at 12 keV, we can extrapolate the value of the crystallite size $t \sim 1.2$ μm. The primary extinction depths, instead, are t_{ext} = 1.1 and 3.7 μm respectively for the $< 002 >$ and $< 004 >$ reflections.

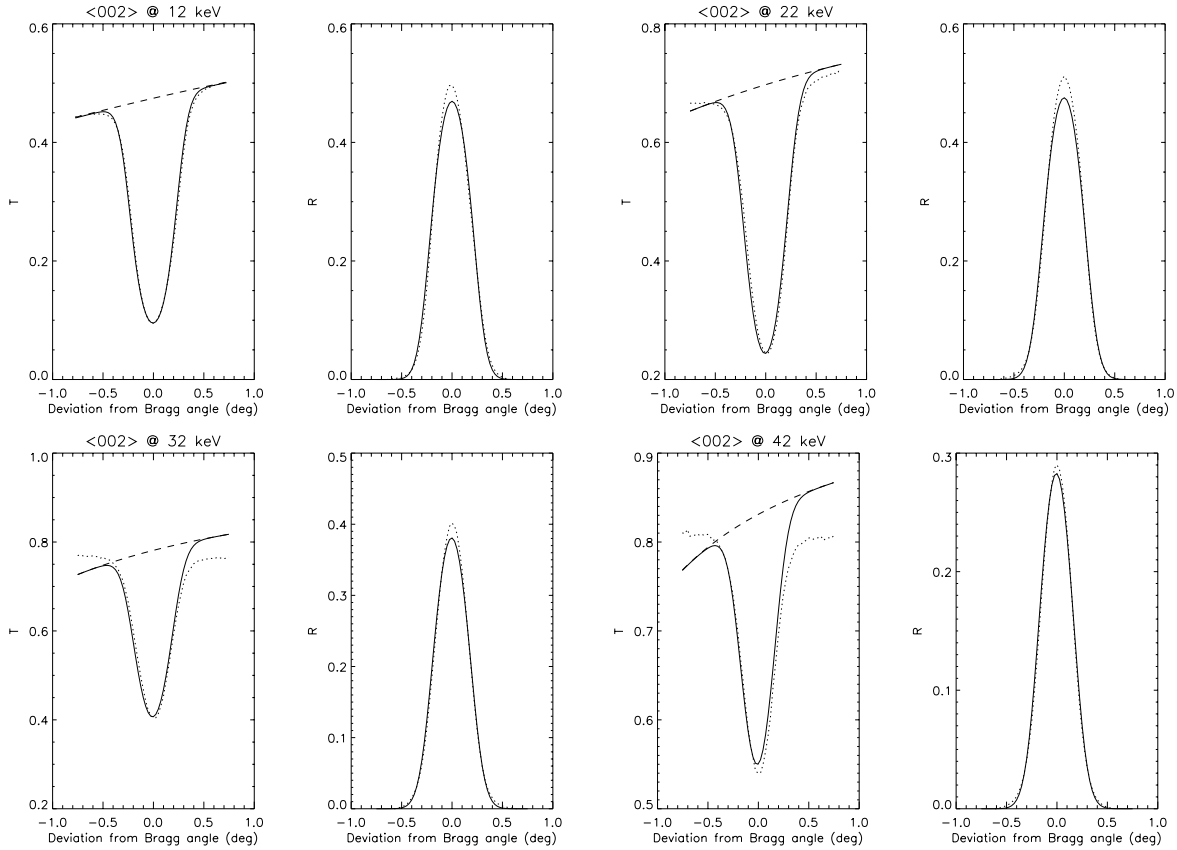

Figure 6.15: *Graphite sample HOPG-A: normalised transmission and reflectivity as a function of the X-ray energy for the <002> reflection. The dotted line is the experiment. The dashed lines superimposed on the T profiles represent the fit of the tails of T to determine the values of the attenuation coefficient μ. The fitted μ was then used to fit R and T simultaneously (solid lines) with two free parameters: the Q scattering factor and mosaicity η. The theoretical and fit parameters are reported in Table 1.*

Table 1. *Parameters of the pyrolitic graphite sample HOPG-A: Bragg angles, X-ray attenuation coefficient and Q factor.*

Energy keV	Reflection	θ_{Bragg} degrees	μ_{calc} cm^{-1}	μ_{fit} cm^{-1}	Q_{calc} cm^{-1}	Q_{fit} cm^{-1}
12	<002>	8.88	2.84	2.31	0.0638	0.0470
12	<004>	18.	2.84	2.31	0.00809	0.00584
22	<002>	4.83	0.73	0.61	0.0211	0.0163
22	<004>	9.69	0.73	0.67	0.00314	0.00227
32	<002>	3.32	0.49	0.29	0.00963	0.0061
32	<004>	6.65	0.49	0.44	0.00156	0.00116
42	<002>	2.53	0.425	0.16	0.005615	0.00265
42	<004>	5.06	0.425	0.32	0.000926	0.0007

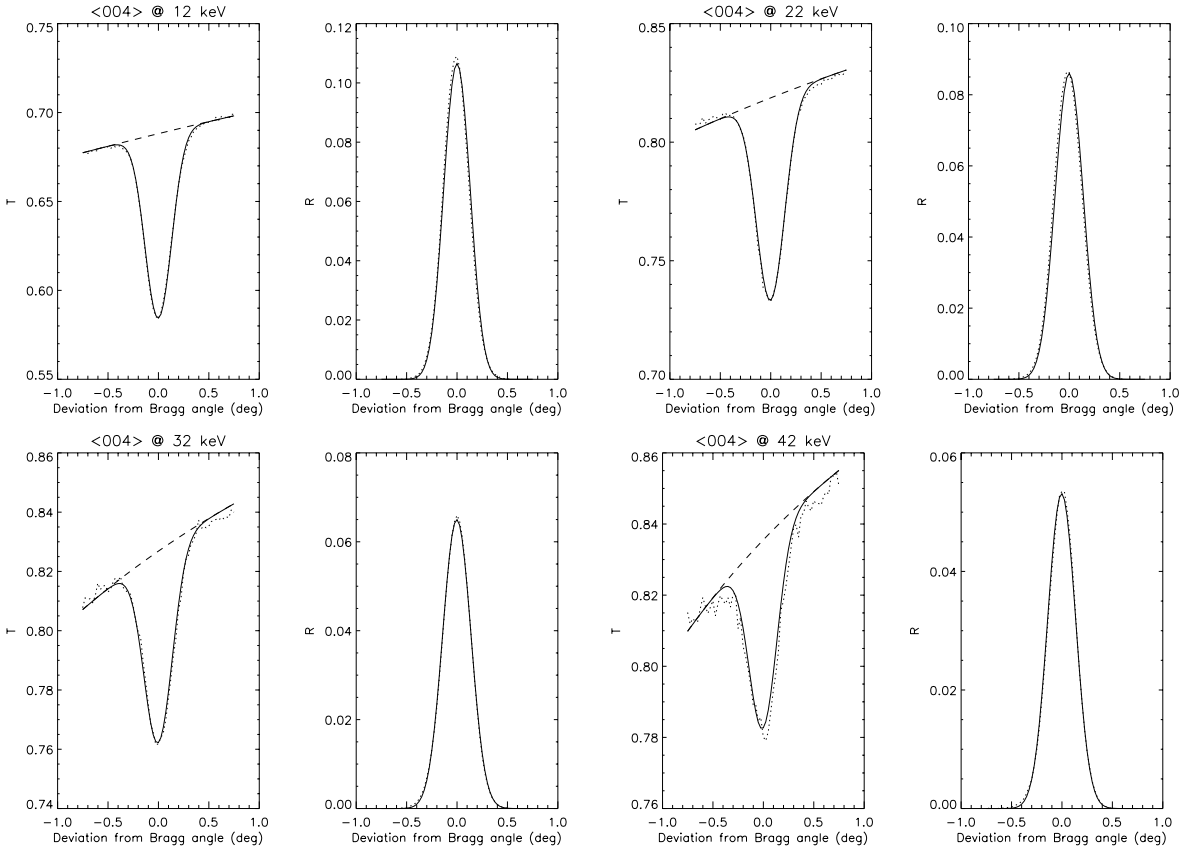

Figure 6.16: *Same as Fig. 6.15 for the <004> reflection.*

6.5 Summary and conclusions

In this Chapter we have discussed experiments carried out on three kinds of crystals: assembled bent germanium, flat germanium, and highly oriented pyrolitic graphite. These crystals were chosen because of their interesting properties when used as neutron monochromators or analysers. Germanium is a semiconductor with the diamond structure. Hence it is very rigid and it is difficult to obtain crystals with suitable mosaic distributions. For this reason a new class of germanium crystals obtained assembling thin germanium wafers is being developed. We studied both flat and bent assembled crystals. Pyrolitic graphite can be considered as a "standard" example of mosaic crystal. It is perhaps the best ideal imperfect crystal available.

This chapter closes a large study aiming at comparing the recorded reflectivity of real crystals (the two germanium assembled crystal, the copper crystals in the previous Chapter and HOPG): it shows that there exist mosaic crystals, such as HOPG, which diffract in almost perfect agreement with the theory presented in Chapter 2, and for which the reflectivity is perfectly fitted by assuming that they have a Gaussian mosaic distribution; on the other side, assembled crystals are very roughly modelled by the theoretical formulas. In the assembled crystals a high degree of inomogeneity can be found when looking at different parts of the crystal with a micrometric x-ray beam. This effect, also observed in copper, cannot be seen with neutrons, because of the poorer characteristics (in terms of size and collimation) of neutron beams. The peak intensity measured experimentally with neutrons is usually smaller than what is theoretically expected. The neutron reflectivity is an average over the whole diffracting bulk, and the high degree of inomogeneity at a microscopic scale, that we measured with x-rays, can be considered as a good argument to explain this reduction of intensity.

The analysis and fit of the neutron rocking curves of bent germanium tell us that important parameters, like attenuation, could be altered by the deformation and assembling process of the crystal, and no longer correspond to the theoretical values. This effect is responsible for the reduction of the final integrated reflectivity.

The analysis of the flat assembled germanium, on the other hand, shows that the deformation process used for obtaining the desired mosaicity, leads to a final crystal in which the mosaic distribution is not smooth, but is composed of at least two peaks. The wafers (both the superficial ones that we investigated with x-rays and the bulk ones, "seen" by neutrons) do not return to the flat shape thay had before being machined. All these problems make the interpretation of the germanium reflectivity more difficult than that of copper and HOPG.

Chapter 7

Summary and conclusions

Imperfect crystal monochromators and analysers are used in a large number of neutron scattering instruments. The diffraction properties of these crystals have a strong influence on the quality of the neutron beams diffracted by the crystal monochromator or analyser. Hence, understanding these properties is necessary when choosing the kind of crystal to be used in an instrument or simply when wanting to describe the instrument performance. This thesis has looked into the detailed description of mosaic and bent crystals from several points of view:

1) In Chapter 2 we have given a review of the theories describing the reflectivity of perfect, mosaic, bent and gradient crystals and mentioned the approximations needed by the models. We have shown two possible approaches for calculating, in an approximate way, the neutron beam attenuation due to thermal diffuse scattering. We have implemented the analytical formulas for reflectivity, transmissivity and attenuation in computer codes which will be released to the neutron community. We believe this is an important contribution to the development of neutron optics software tools.

2) An exact description of all the properties (beam intensity, spatial, angular and energy distributions) of the beam diffracted by a crystal is obtained by using the Monte Carlo method. In Chapter 3 we have shown how to apply this method to mosaic and bent crystals. Our codes are original tools and they are able to simulate a large variety of crystals. Moreover, they have been benchmarked against analytically calculated reflectivities and also measurements, like x-ray topographs. An example of application of the BENT Monte Carlo code is shown in Chapter 4, where some simulation results for the new *Strain Imager* instrument in construction at the ILL are discussed.

3) An experimental study concerning several types of crystals has allowed us to recognize which crystal properties are close to the theoretical expectations, and which are not. The knowledge of the detailed x-ray and neutron diffraction by some of these samples

allows reproducing their reflectivity, for example, both using analytical and numerical methods, provided that realistic parameters (attenuation, primary extinction and real mosaic distribution) are used in the calculation. The experimental data discussed in Chapters 5 and 6 have shown that detailed crystal simulations have to take into account also parasitic Bragg scattering.

A preliminary conclusion about this thesis is the following: there are differences between the real and the ideal crystal behaviour; we have investigated some non-ideal aspects and have been able to describe them, both with simulations and using analytical fitting. More detailed conclusions require recalling the main results, hence we will summarize them here trying to keep a global view of the work.

Neutron reflectivity of mosaic copper versus temperature.

The study of the temperature dependent reflectivity of mosaic crystals is an interesting subject, to assess the advantages of using cooled monochromators and analysers. The accurate prediction of the reflectivity gain of cooled mosaic crystals is important because this has to be compared to the high cost of the cryogenic system. We summarize, in Table 1, the peak reflectivity increase, at low temperature, measured using a copper crystal, in Laue geometry. The good improvement observed for the asymmetric $< 331 >$ reflection, suggests that this study is interesting and should be performed also with other crystals. However, the very partial agreement with the calculation results, indicates that less approximated models should be used. We observed experimentally how parasitic reflections can affect data: their effect changes with changing the neutron energy, the Bragg indices and the crystal azimuthal angle. An improvement of the data presented in this thesis would be obtained by repeating the experiments, on copper and also other crystals, and especially improving the data analysis, with corrections for the intensity added or subtracted by the parasitic reflections. This could be done using the model discussed in [40].

Table 1. *Measured and calculated increase of the neutron reflectivity (with respect to room temperature) for mosaic copper in Laue geometry.*

Reflection	T K	Energy meV	Experiment	Freund's model	Approximated multi-phonon
220	77	48	12%	17%	3%
	15	100	18%	24%	13%
	15	250	18%	35%	33%
331	15	100	31%	34%	14%
	15	250	33%	55%	35%

Characterisation of HOPG, copper and germanium.

The comparison of the data concerning different crystals as highly oriented pyrolitic graphite (HOPG), copper and assembled germanium shows how the different techniques used to produce these crystals strongly influence their reflectivity and homogeneity. In order to characterise crystals, it is important to use high quality beams, in terms of monochromaticity, collimation and small size (to access small crystal volumes). Hence, in this thesis, we present more experiments performed with x-rays than neutrons, because of the better angular and energy resolution of the photon beams produced by third generation synchrotrons. The x-ray data we measured using a HOPG sample has shown that the reflectivity and transmission curves are very well fitted provided that a correction is introduced accounting for primary extinction (see the example in Fig. 7.1). We used a purely Gaussian function for fitting the mosaic distribution and did not detect any inhomogeneity. The fitting parameter η, representing mosaicity, has only slight variations for different reflections and energy values. This means that the usual model used for simulating HOPG works well, if the effect of primary extinction is considered.

The situation drastically changes when considering tha x-ray characterisation of mosaic copper: depending on the sample, the mosaicity, the Bragg angle and the beam position on the crystal, we obtain different results in terms of homogeneity and primary extinction effects. The $< 222 >$ reflection (Fig. 7.2), measured with $E = 120$ keV, has a reflectivity which is affected by primary extinction and inhomogeneities of the mosaic distribution for the sample Cu-D, but is very close to the ideal result for the Cu-E sample. The different behaviour (also witnessed by the topographs shown in Chapter 6 for the two samples) is most probably due to the different deformation process used to produce the mosaicity.

The presence of defects in mosaic copper crystals has been known for a long time, but important progress has been done in the growing, cutting and machining technique. It is an interesting question whether the results of the detailed characterisation described in this thesis, limited to a few samples, can be used for modeling other crystals produced in a similar way. We believe that the study of the real crystal structure, even if limited to few crystals of good quality, helps to conclude if modeling (analytical or numerical) is close to reality or not. As an example, none of the copper samples that we analysed had a mosaic distribution $W(\theta - \theta_B)$ of Gaussian shape. Since this distribution determines the peak reflectivity and the total width of the diffraction profile, it is important to use a realistic distribution $W(\theta - \theta_B)$ for the simulations. The use of a simple Gaussian profile would lead to inaccurate results.

This characterisation is instructive for the case of the crystals made of assembled germanium wafers. Our measurements show the presence of defects and, for the flat crystal, of residual bending of the glued wafers (Fig. 7.3). The use of this kind of crystals for

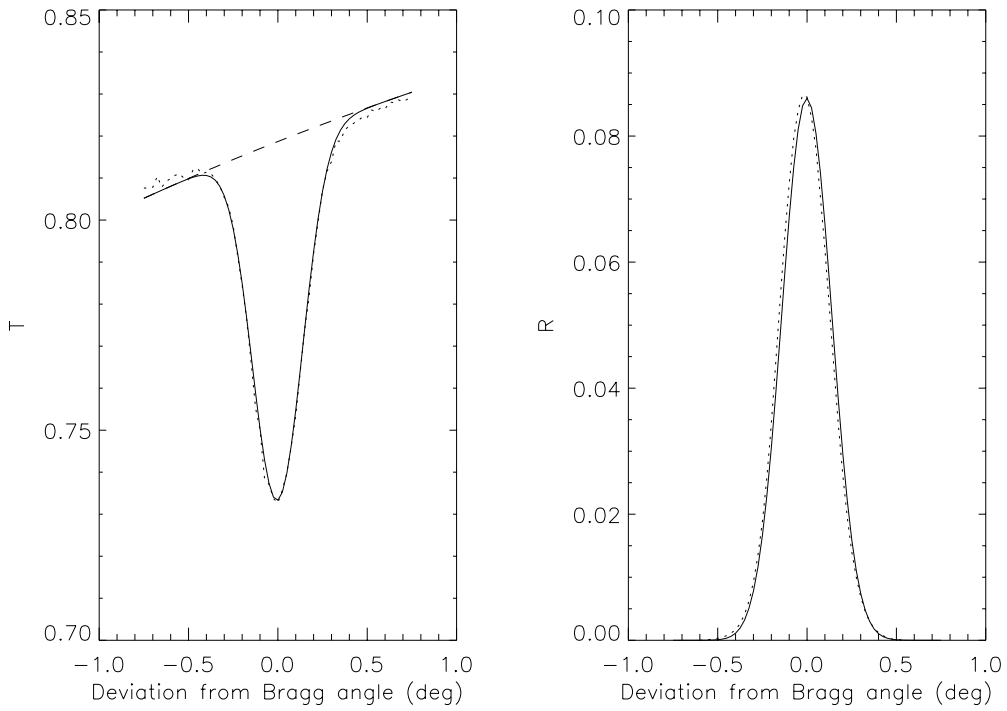

Figure 7.1: *Graphite sample HOPG-A: normalised transmission (left) and reflectivity (right) as a function of* $(\theta - \theta_B)$ *for the <004> reflection. The photon energy is E = 22 keV. The dotted line is the experiment. The dashed line superimposed on the T profiles represents the fit of the tails of T to determine the values of the attenuation coefficient* μ*. The fitted* μ *was then used to fit R and T simultaneously (the solid lines are the fit results) with two free parameters: the Q scattering factor and mosaicity* η*. The theoretical and fit parameters are reported in Table 1 in Chapter 6.*

monochromating neutrons is possible because of the high average mosaicity.

A pictorial view of the different kind of inhomogeneities found for copper and germanium is given by x-ray diffraction topography (Fig. 7.4). The presence of grains in visible in both cases, but, in the case of germanium, we observe imperfections that are probably ripples due to the wafer machining process.

Both neutron and x-ray data (Fig. 7.5) concerning the Ge-A assembled bent crystal show that a good fit is possible, using the *layer coupling model* [56], by letting the mosaicity η and the attenuation coefficient μ as free parameters. However, the μ_{fit} parameter is higher than the theoretical value, especially for the neutron data. This makes the neutron integrated reflectivity as low as 60% of the theoretical reflectivity. A more accurate fit of the data would require to study in more detail other effects which have not been considered here, in particular the presence of parasitic reflections. As an example, for germanium $< 311 >$ at $\lambda = 2$ Å the $< 111 >$ reflection can also be excited.

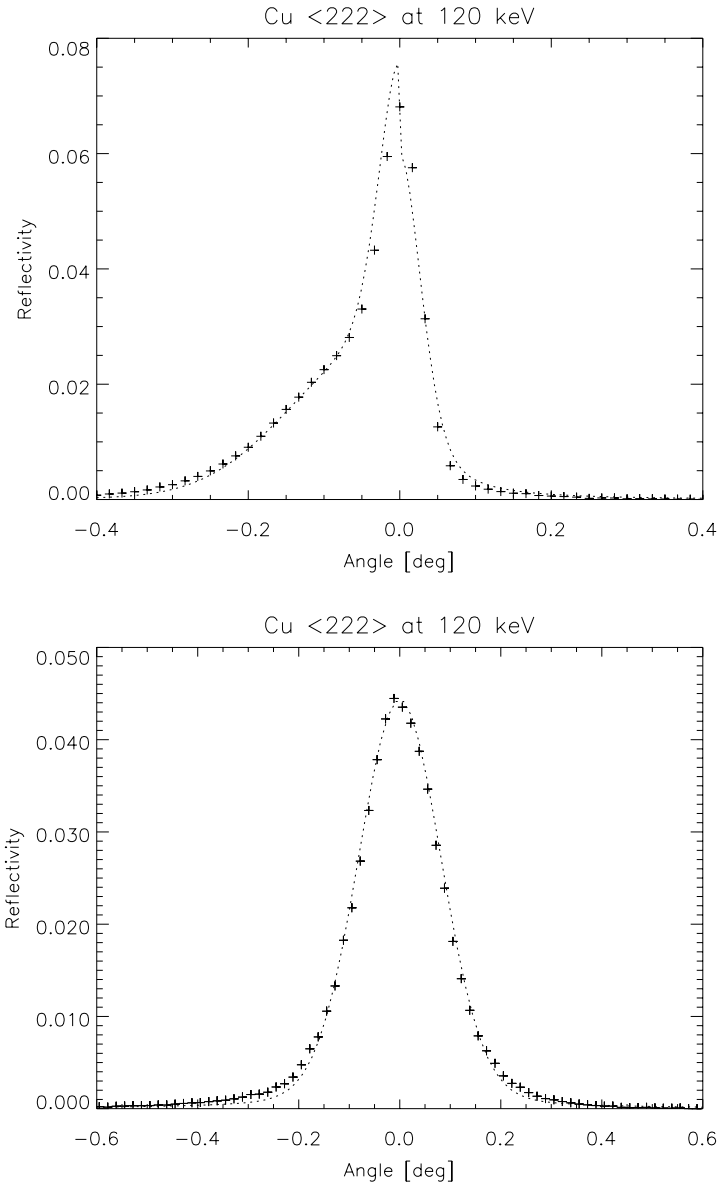

Figure 7.2: *Experimental x-ray reflectivity versus* $(\theta - \theta_B)$ *for the copper samples Cu-D (top) and Cu-E (bottom) (+ symbols). The fit (dotted lines) was performed using Eq. (2.23) with two free parameters: the mosaicity* η *and the* Q *factor. The mosaic distribution was a pseudo-Voigt function. The plot on the top was fitted by adding a Gaussian part to* $W(\theta - \theta_B)$*, for* $(\theta - \theta_B) \leq 0$*.*

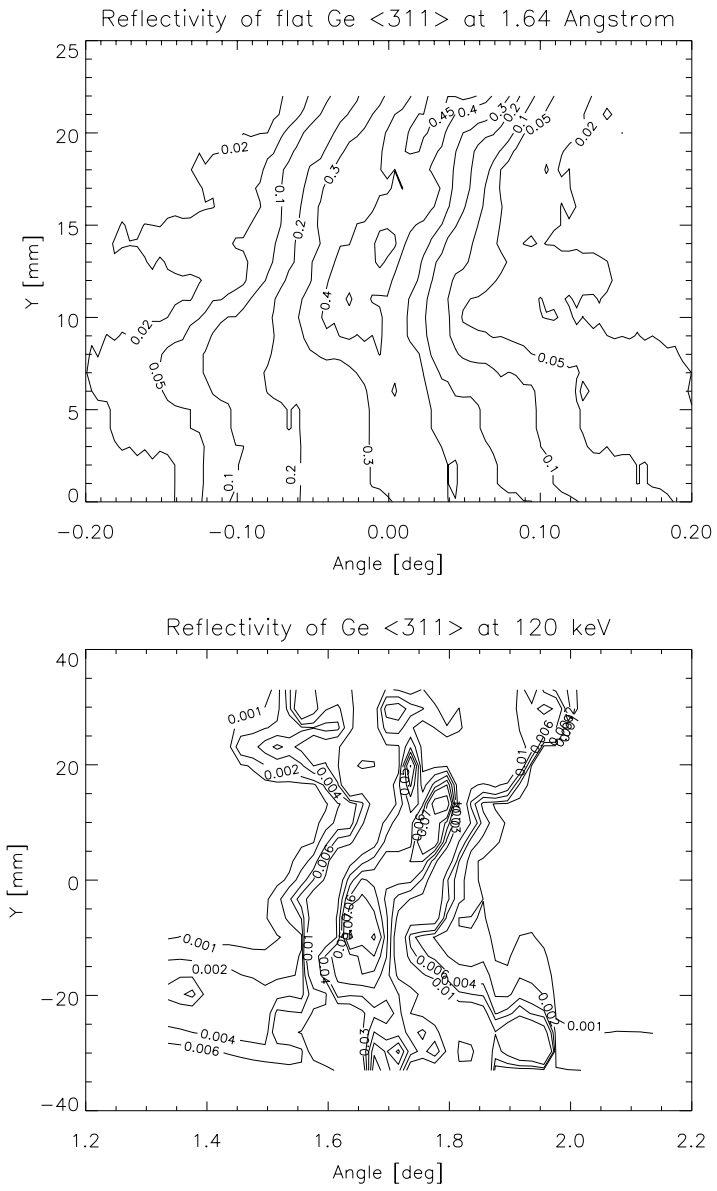

Figure 7.3: *Flat assembled crystal Ge-B: the contour plots represent the reflectivity as a function of the rotating angle and Y coordinate along the crystal surface. TOP: neutron reflectivity. BOTTOM: x-ray reflectivity.*

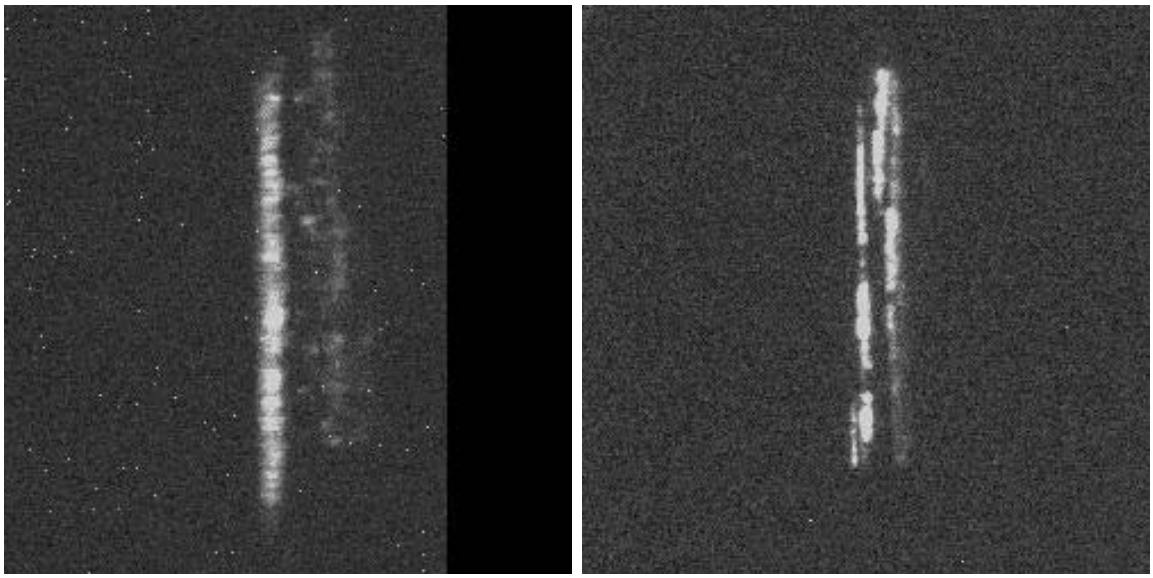

Figure 7.4: *X-ray topographs of Cu-E <222> at E = 120 keV (left) and of the assembled flat crystal Ge-B at E = 90 keV for the <311> reflection (right). Both topographs were recorded for $\theta < \theta_B$ (approximately 15% of the peak reflectivity). They are on the same scale and the image height is $\sim$ 3.5 mm.*

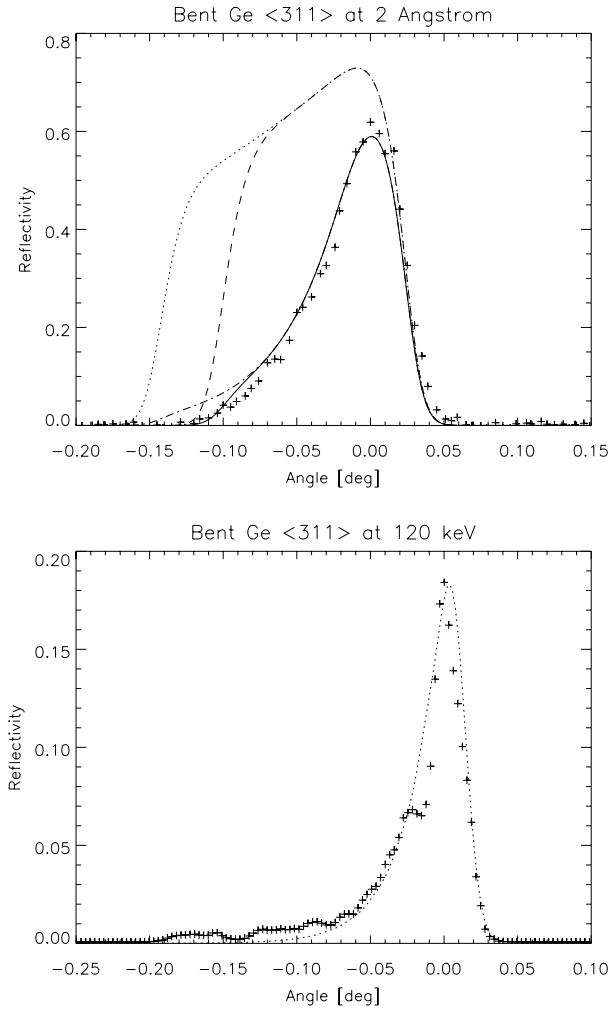

Figure 7.5: *The + symbols are the experimental neutron (top) and x-ray (bottom) reflectivity versus* $(\theta - \theta_B)$ *of the bent crystal Ge-A. The layer coupling model was used for the fit (Eq. (2.41)) with three free parameters: mosaicity, equivalent thickness and attenuation coefficient. TOP: the theoretical attenuation coefficient for Ge is* $\mu_{theor} = 0.145$ cm^{-1}. *The dashed line is the calculated diffraction profile with the nominal attenuation coefficient; the dotted line with the nominal* μ *and thickness; the dot-dashed line is calculated with the nominal thickness and fitted attenuation* ($\mu_{fit} = 1$ cm^{-1}); *the solid line is the fit with the thickness as a free parameter. BOTTOM: the dotted line is the reflectivity according to the layer coupling model with the parameters:* $\eta = 1.4' = 0.02^o$ *and* $\mu_{fit} = 2.2$ cm^{-1} *(whereas* $\mu_{theor} = 1.8$ cm^{-1}*).*

Monte Carlo modelling.

Many of the data presented in the previous sections of these Conclusions have been compared and fitted with theoretical formulas. These formulas allow calculating the reflectivity and transmission profiles of bent and mosaic crystals. However, the analytical methods can only partially explain some of the features observed in real crystals. In order to model and simulate a neutron instrument in detail, more sophisticated simulations must follow the unavoidable preliminary calculations (which can be graphical or analytical). Our original contribution to this problem was the development of Monte Carlo codes, which are described in detail in Chapter 3. This method allows a detailed description of the particle path in the mosaic and/or bent crystal. An original result, that probably cannot be obtained with other methods, is the computation of the average number of scattering events N_{multi} undergone by the simulated particles or the average depth $< \tau >$ reached in the crystal. We have shown in Chapter 3 a comparison between these quantities for mosaic and bent crystals having similar reflection profiles: the values obtained for $< \tau >$ are comparable, but for a mosaic crystal N_{multi} can be some orders of magnitude larger. We recall this result, in the case of the mosaic crystal, in Fig. 7.6.

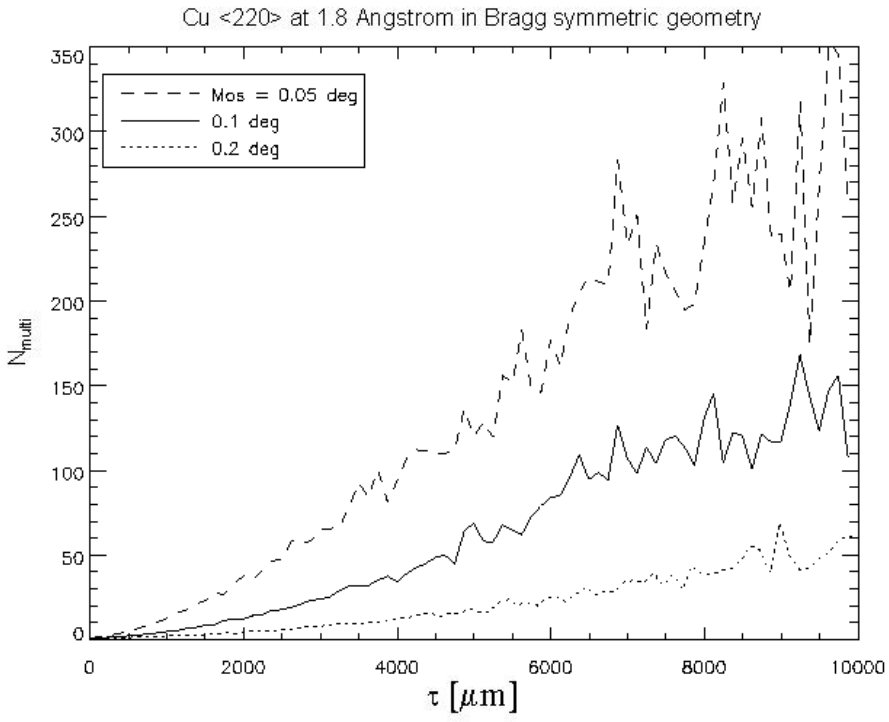

Figure 7.6: *Number of scattering events N_{multi} versus the maximum depth τ reached by reflected particles, for some values of the mosaicity η. These data correspond to the exact Bragg angle and Bragg symmetric geometry.*

In Chapter 4 we have shown how this method can be applied to the simulation of the new *Strain Imager* instrument of the ILL, where the crystal module is linked to other elements, as the equivalent source, the radial oscillating collimator, and the ideal polycrystalline

sample. This instrument will be based on the use of bent crystal monochromators: we believe that a decisive improvement of the accuracy of the calculations, in terms of intensity and resolution, would be achieved by describing the crystals in the most realistic way. The use of mosaic bent germanium (obtained by plastic bending) might not give the expected increase of intensity with respect to an elastically bent crystal, because of the imperfections (inhomogeneity or others) introduced by the deformation process. We have experimentally observed these effects and described them in Chapter 6.

A final successful application of the codes was the comparison between the measured and simulated data concerning the profiles of the x-ray diffraction topographs. We summarize these results in Fig. 7.7 for the three kinds of crystals used: mosaic copper, flat and bent assembled germanium. The very good agreement we found is explained by the fact that, in the simulations, we used parameters as attenuation coefficient, mosaicity and crystallite thickness (related to the primary extinction correction), obtained by fitting the rocking curves. The agreement is worse for the case of the flat germanium crystal because it was not possible to fit the μ coefficient, and the theoretical value had to be used instead.

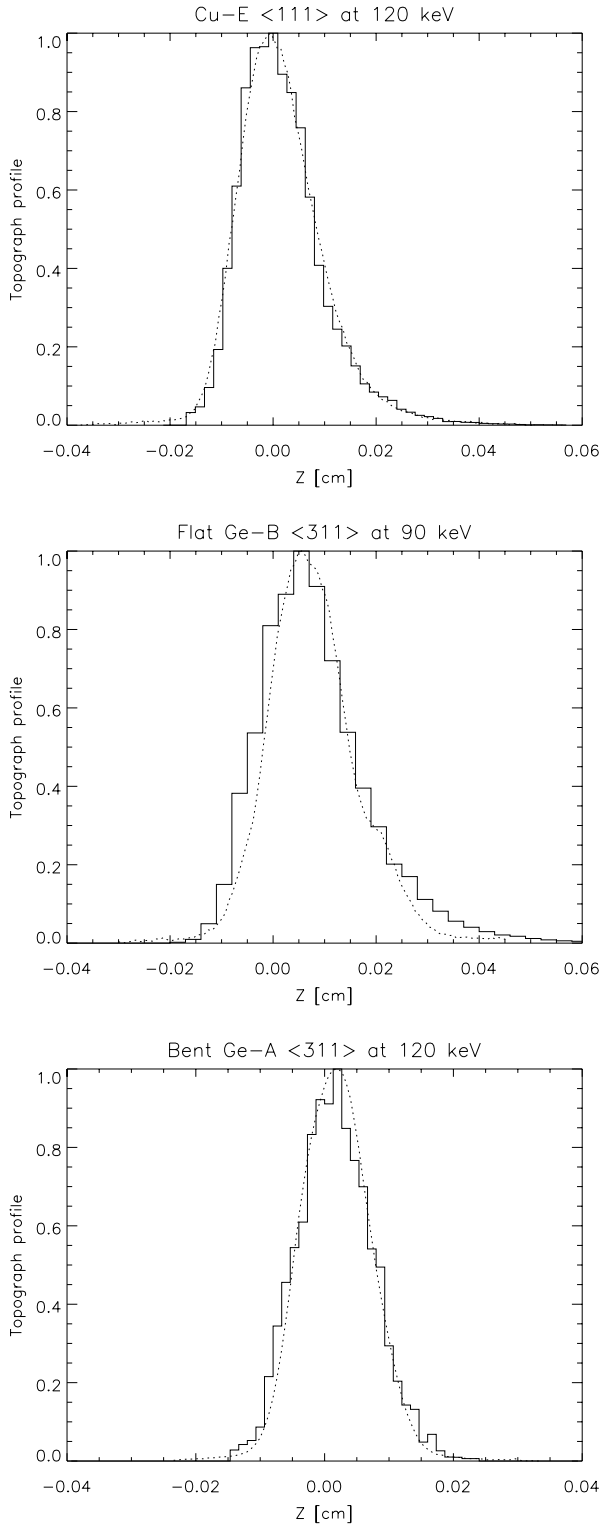

Figure 7.7: *Dotted lines: profiles of the experimental x-ray topographs recorded at the nominal Bragg angles. TOP: <111> reflection of the copper sample Cu-E at 120 keV. CENTER: <311> reflection of the flat germanium sample at 90 keV. BOTTOM: <311> reflection of the bent germanium sample at 120 keV. The histograms are the simulation results.*

The results that we have recalled in these conclusions show that Bragg diffraction by imperfect crystals can be described successfully by theories and Monte Carlo simulations. However, depending on the type of crystal, there can be undesired effects. The possible inhomogeneities of the mosaic distribution reduce the crystal reflectivity and also the quality of the diffracted beam. Our Monte Carlo codes are able to simulate these imperfections: the method can be applied to real crystal, provided that a realistic knowledge of the type and distribution of the imperfections is known. Another important reason for the decrease of the crystal reflectivity is primary extinction: also in this case, if the size of the crystallites is known, the numerical simulation gives precise values of the real reflectivity. A very well known problem is the decrease of efficiency of imperfect crystals because of parasitic reflections: the estimation of this effect is possible and its approximated calculation will probably be implemented in a future version of *XOP for neutrons* and of our Monte Carlo codes.

Finally, the possibility to accurately simulate bent crystals has to be recalled: due to the large penetration lengths of neutrons in crystals, the focusing effect by bent crystals suffers the presence of aberrations and the usual laws of optics are approximated. Only with realistic simulations of the beam path in the bulk crystal (i.e., with a full Monte Carlo simulation), we can describe focusing by non-ideal crystals.

In this thesis we have shown examples of all the effects that contribute to make the crystal reflectivity different from that predicted by the usual simplified models. We believe that the informations we collected during the development of this study can help in understanding real crystals. The calculation tools that we developed already contain these informations. However, they can surely be improved. Because the sources of imperfections and defects are many and difficult to predict, the results presented in this thesis and the release of these codes to the neutron community will hopefully contribute to the design and simulation of new neutron instruments using crystal analysers and monochromators.

Conclusions

Dans cette thèse, nous avons étudié de façon détaillée la diffraction par les cristaux imparfaits. En particulier, nous nous sommes concentrés sur des cristaux réels présentant un intérêt pour l'instrumentation neutronique, et qui sont employés comme monochromateurs ou analyseurs. Nous voulions étudier aussi les limites de l'applicabilité des modèles théoriques couramment utilisés pour décrire la diffraction de Bragg par ces cristaux. Le travaux sont présentés en deux parties complémentaires. D'abord, une partie expérimentale, plutôt étendue, visant à étudier la diffraction par nos échantillons, dans des conditions optimales, afin d'obtenir des données expérimentales comparable aux résultats théoriques. Pour cela, nous avons mesuré les profils de réflectivité de neutrons, mais aussi de rayons X et des topographies de rayons X. L'utilisation du rayonnement de synchrotron nous a permis de mieux évaluer la diffraction à un niveau microscopique, un genre d'information qui n'est pas disponible en employant des faisceaux de neutrons conventionnels. Deuxièmement, nous avons développé des programmes Monte Carlo qui simulent la diffraction par les cristaux imparfaits. Après avoir expliqué dans l'introduction les motivations pour étudier ces cristaux, et comment ce problème est situé dans le contexte général de la modélisation des instruments de neutrons, nous avons passé en revue, dans le chapitre 2, les théories décrivant la diffraction (et l'absorption) dans les cristaux parfaits, mosaïques et courbés. Une étape nécessaire était le développement de programmes de calcul théorique. Ces programmes peuvent être employés pour des calculs préliminaires de profils de réflectivité. Nous les avons appliqués à l'analyse des données expérimentales. Cependant, les méthodes analytiques peuvent seulement partiellement expliquer certains effets observés dans des cristaux réels.

Afin de modéliser et simuler un instrument de neutrons en détail, des simulations plus sophistiquées doivent suivre les calculs préliminaires (graphiques ou analytiques). Notre contribution originale à ce problème était le développement des codes de Monte Carlo décrits dans le chapitre 3. L'originalité est dans la description détaillée de la trajectoire des particules dans le cristal mosaïque et/ou courbé.

Dans le chapitre 4, nous avons montré comment cette méthode peut être appliquée à la simulation du nouvel instrument *Strain Imager* en construction à l'ILL, où la fonction du cristal est liée à d'autres éléments, par exemple un collimateur focalisant et oscillant et un échantillon polycristallin. Cet instrument sera basé sur un monochromateur constitué de cristaux courbés. Une amélioration décisive du calcul de l'intensité et de la résolution pourrait être effectuée, en décrivant les cristaux de la manière la plus réaliste, en connaissant les défauts typiques de ces cristaux. L'utilisation du germanium mosaïque et courbé (obtenu par déformation plastique) ne pourrait probablement pas donner l'augmentation prévue de l'intensité par rapport à un cristal courbé élastiquement, en raison des imperfections (inhomogénéités ou autres) données par le processus de déformation. Nous avons

observé ces effets et les avons décrits au chapitre 6. Aux chapitres 5 et 6, nous avons présenté des travaux expérimentaux détaillés sur des cristaux courbés en germanium, et des cristaux mosaïques en cuivre, germanium et graphite pyrolitique hautement orienté. Ceci a prouvé que, seulement dans le cas du graphite pyrolitique, une distribution de la mosaïque parfaitement gaussienne est acceptable, et les théories usuelles peuvent être appliquées ainsi. Dans le cas des cristaux en cuivre et germanium, la distribution de la mosaïque est mieux décrite par une fonction pseudo-Voigt et est en général asymétrique.

Les données expérimentales ont montré plusieurs effets qui sont bien connus mais sont rarement considérés dans la modélisation. Le premier est la présence de diffractions multiples parasites, difficiles à quantifier dans des cristaux mosaïque. La seconde est l'extinction primaire qui dépend de la taille finie des blocs parfaits (cristallites) qui composent le cristal mosaïque. Un troisième effet est la variation de la mosaïcité η en changeant l'énergie ou les plans de Bragg : la seule explication de cet effet est que les cristaux de germanium et de cuivre sont inhomogènes. Ces faits contribuent à la diminution de l'efficacité du cristal monochromateur et doivent être pris en compte pour des calculs réalistes.

Une partie très intéressante est l'étude des cristaux de germanium courbés, obtenus par assemblage de petites lames déformées plastiquement. La largeur des profils de diffraction de cristaux courbés dépend du rayon de courbure et de l'épaisseur. L'inclinaison est une fonction du coefficient d'atténuation μ. Les profils calculés ont été adaptés aux profils expérimentaux en affinant quelques paramètres comme le coefficient d'atténuation : les valeurs ainsi déterminées pour μ ont différé des prévisions théoriques. L'atténuation inopinément élevée du faisceau incident par le cristal de germanium suggérerait d'effectuer des mesures de basse température afin de déterminer, à partir du changement de cette inclinaison, combien d'absorption vient de la diffraction par les phonons et combien par les réflexions parasites.

En conclusion, les travaux analytiques, numériques et expérimentaux que nous avons menés pour la préparation de cette thèse nous ont fait comprendre les propriétés de diffraction de plusieurs types de cristaux imparfaits. Le développement des codes qui reproduisent les formules théoriques est utile, mais la description détaillée finale du cristal n'est obtenue qu'en employant la méthode de Monte Carlo. Afin d'obtenir une description réaliste, des paramètres réalistes doivent être employés pour les simulations. Nous avons montré que, dans les cristaux réels, des paramètres importants comment le coefficient d'atténuation, la taille des cristallites et la forme de la distribution de mosaïcité peuvent être différents de ceux prévus. Nous avons rapporté leurs valeurs "réelles" (obtenues à partir des expériences) dans certains cas et avons prouvé que leur connaissance est importante pour décrire la performance du cristal, et par conséquent de l'instrument de neutrons.

Appendix A

Appendix - Formal treatment of the dynamical theory of diffraction

For an infinite perfect crystal, the average of the coherent scattering length determining the optical potential in Eq. (2.17) is given by:

$$\langle b(\mathbf{r})\rangle = b\sum_h \tilde{F}_h e^{-i\mathbf{K_h}\cdot\mathbf{r}} \tag{A.1}$$

where b is the average bound coherent scattering length and $\tilde{F}_h = F_h/F_0$ is the normalised structure factor. The optical potential can then be written as:

$$v(\mathbf{r}) = v_0\sum_h \tilde{F}_h e^{-i\mathbf{K_h}\cdot\mathbf{r}} \tag{A.2}$$

where $v_0 = \frac{2\pi\hbar^2}{m}\rho b$ is the average value of $v(\mathbf{r})$ within a unit cell. The solution of the Schrödinger equation (2.16) is a superposition of plane waves outside the crystal

$$\psi(\mathbf{r}) = \sum ae^{i\mathbf{k}\cdot\mathbf{r}} \tag{A.3}$$

with $E = (\hbar k)^2/2m$, and a superposition of Bloch waves inside the crystal

$$\psi(\mathbf{r}) = \sum A(\mathbf{r})\, e^{i\mathbf{K}\cdot\mathbf{r}}. \tag{A.4}$$

Since $A(\mathbf{r})$ has the lattice periodicity, it can be expanded in the form

$$A(\mathbf{r}) = \sum_h A_h e^{-i\mathbf{K_h}\cdot\mathbf{r}} \tag{A.5}$$

and the coefficients A_h satisfy the equations:

$$D_h A_h = \xi\sum_{h'} \tilde{F}_{h-h'} A_{h'} \tag{A.6}$$

where $h-h'$ corresponds to a reciprocal lattice vector $\mathbf{K}_{h-h'} = \mathbf{K}_h - \mathbf{K}_{h'}$ and the D_h and ξ coefficients are given by:

$$D_h = 1 - \frac{(\mathbf{K} - \mathbf{K}_h)^2}{k^2} \tag{A.7}$$

$$\xi = \frac{v_0}{E} = \frac{4\pi}{k^2}\rho b. \tag{A.8}$$

The solution of Eq. (A.6) determines the *dispersion surface* $\mathbf{K} = \mathbf{K}(k)$ and the allowed values of $\mathbf{K}$, called *tie points* are calculated by applying the boundary conditions. At thermal neutron energies, the parameter ξ is very small. We have $\mathbf{K} = \mathbf{k}[1 + O(\xi)]$, then:

$$D_h = \frac{2\mathbf{k}\cdot\mathbf{K}_h - K_h^2}{k^2} + O(\xi) \tag{A.9}$$

and:

$$D_h A_h = O(\xi) \tag{A.10}$$

Eqs. (A.9) and (A.10) show that for $h = 0$ and h such that the Bragg law is satisfied, $2\mathbf{k}\cdot\mathbf{K_h} = K_h^2$, $D_h = O(\xi)$ and $A_h = O(1)$. For cases in which the Bragg law is not satisfied $D_h = O(1)$ and $A_h = O(\xi)$. This means that the nature of the solution depends on the number of reciprocal lattice vectors $\mathbf{K}_h$ for which the Bragg law is simultaneously satisfied for a given incident wave vector $\mathbf{k}$.

If the Bragg law is not satisfied for any $\mathbf{K}_h$, then $D_0 = \xi$ and we have the so-called *one-wave* solution:

$$\psi(\mathbf{r}) = A_0 \sum \left(e^{i\mathbf{K}\cdot\mathbf{r}} + \xi \sum_{h\neq 0} \frac{\tilde{F}_h}{D_h} e^{i(\mathbf{K}-\mathbf{K}_h)\cdot\mathbf{r}} + O\left(\xi^2\right) \right) \tag{A.11}$$

Thus, $\psi(\mathbf{r})$ is the superposition of the internal transmitted wave, with wave vector $\mathbf{K}$, plus a Bragg reflected wave, with wave vector $\mathbf{K} - \mathbf{K}_h$, from each reciprocal lattice site with $h \neq 0$. This is one of the main aspects of the dynamical theory: since the crystal refractive index differs from that of the surrounding medium, $n = K/k \sim 1 - \xi^2$, all possible Bragg reflections are excited, with an amplitude of the order of ξ relative to that of the transmitted wave. The intensity of each component of the Bragg reflected wave is $\sim \xi^2$, so it is negligible and we can write:

$$\psi(\mathbf{r}) = A_0 \sum e^{i\mathbf{K}\cdot\mathbf{r}} \tag{A.12}$$

If the Bragg condition is satisfied for only one value $\mathbf{K}_h$ of the reciprocal lattice vector, the Eq. (A.6) becomes:

$$D_{h'} A_{h'} = \xi \left(\tilde{F}_{h'} A_0 + \tilde{F}_{h'-h} A_h \right) + O\left(\xi^2\right) \tag{A.13}$$

The last equation is valid for $h' = 0, h$ and can be re-written as:

$$\begin{aligned}(D_0-\xi)\,A_0-\xi\tilde{F}_{-h}A_h&=0\\-\xi\tilde{F}_hA_0+(D_h-\xi)\,A_h&=0\end{aligned}\tag{A.14}$$

These equations describe the multiple Bragg reflections in a perfect crystal in the *two wave case*. They have a solution if:

$$(D_0-\xi)\,(D_h-\xi)-\xi^2\tilde{F}_h\tilde{F}_{-h}=0\tag{A.15}$$

Then:

$$X=\frac{A_h}{A_0}=\frac{D_0-\xi}{\xi\tilde{F}_{-h}}=\frac{\xi\tilde{F}_h}{D_h-\xi}\tag{A.16}$$

and the coherent wave can be written as:

$$\psi\left(\mathbf{r}\right)=A_0\sum\left(e^{i\mathbf{K}\cdot\mathbf{r}}+Xe^{i(\mathbf{K}-\mathbf{K}_h)\cdot\mathbf{r}}+\xi\sum_{h'\neq0,h}\frac{\tilde{F}_{h'}+X\tilde{F}_{h'-h}}{D_{h'}}e^{i(\mathbf{K}-\mathbf{K}_{h'})\cdot\mathbf{r}}+O\left(\xi^2\right)\right)\tag{A.17}$$

As in the one-wave case, the terms proportional to ξ are negligible and only the reflected wave having $h=h'$ is of the same order of the transmitted wave, so we can write:

$$\psi\left(\mathbf{r}\right)=A_0\sum\left(e^{i\mathbf{K}\cdot\mathbf{r}}+Xe^{i\mathbf{K}'\cdot\mathbf{r}}\right)\tag{A.18}$$

with:

$$\mathbf{K}'=\mathbf{K}-\mathbf{K}_h\tag{A.19}$$

The last equation implies that:

$$D_h=\alpha D_0+\xi\beta\tag{A.20}$$

with:

$$\begin{aligned}\alpha&=1-\frac{K_{hz}}{k_z}\\\beta&=\frac{2\mathbf{k}\cdot\mathbf{K}_h-K_h^2}{\xi k^2}\end{aligned}\tag{A.21}$$

where we have assumed that the crystal incidence surface lies in the $z=0$ plane.
We can write the refractive indices for the internal transmitted and reflected waves as:

$$\begin{aligned}n^2&=1-D_0\\n'^2&=1-D_h\end{aligned}\tag{A.22}$$

The solution of the dispersion equation (A.15) is:

$$D_{0\pm}=\xi\left[1+\gamma\pm\left(\gamma^2+\delta\right)^{\frac{1}{2}}\right]\tag{A.23}$$

$$D_{h\pm} = \alpha\xi\left[1 + \gamma \pm \left(\gamma^2 + \delta\right)^{\frac{1}{2}}\right] + \beta \tag{A.24}$$

with:

$$\gamma = \frac{1 - \alpha - \beta}{2\alpha} \qquad \delta = \frac{\tilde{F}_h \tilde{F}_{-h}}{\alpha} \tag{A.25}$$

Eqs. (A.23) and (A.24) show that both D_0 and D_h have two possible solutions, then the coherent wave is the superposition of four plane waves:

$$\psi(\mathbf{r}) = A_+\left(e^{i\mathbf{K}_+\cdot\mathbf{r}} + X_+ e^{i\mathbf{K}'_+\cdot\mathbf{r}}\right) + A_-\left(e^{i\mathbf{K}_-\cdot\mathbf{r}} + X_- e^{i\mathbf{K}'_-\cdot\mathbf{r}}\right) \tag{A.26}$$

where:

$$\mathbf{K}_\pm = \mathbf{k} - \frac{k^2}{2k_z} D_{0\pm}\hat{\mathbf{z}} \qquad \mathbf{K}'_\pm = \mathbf{K}_\pm - \mathbf{K}_h \tag{A.27}$$

Eq. (A.26) shows that, due to refraction in the crystal, the refractive indices for the transmitted and reflected waves are double valued, then there are four waves propagating in the crystal. This is the essential difference between the dynamical theory and the kinematical theory, in which refraction is neglected and there is no distinction between the internal and external waves. According to the dynamical theory, the external incident wave produces two internal transmitted waves with wave vectors $\mathbf{K}_\pm$ and two reflected waves with $\mathbf{K}'_\pm$.

The behaviour of the coherent wave is known, provided that the coefficients $A_\pm$ are determined. In order to do this, one has to write the boundary conditions. The crystal shape for which the boundary problem can easily be solved is that of a slab of thickness d. If we neglect the finite length, this is also the shape of crystals commonly used as monochromators. The approximation is good if the real length is much larger than the thickness. Another approximation lies in omitting the effect of partial reflection and refraction of the incident wave. This effect is appreciable only at very small grazing angles of the order of 0.2^o or less, then the approximation is good. In order to solve the boundary problem, we will choose the $z = 0$ plane as the entrance crystal surface and the $z = d$ plane as the crystal exit surface for the transmitted beam. The internal wave is described by the Eq. (A.26), and the external one will be:

$$\psi(\mathbf{r}) = \begin{cases} a e^{i\mathbf{k}\cdot\mathbf{r}} & \text{if } z < 0 \\ a' e^{i\mathbf{k}'\cdot\mathbf{r}} + a'' e^{i\mathbf{k}''\cdot\mathbf{r}} & \text{if } z > d \end{cases} \tag{A.28}$$

for the *Laue or transmission geometry* and:

$$\psi(\mathbf{r}) = \begin{cases} ae^{i\mathbf{k}\cdot\mathbf{r}} + a'e^{i\mathbf{k}'\cdot\mathbf{r}} & \text{if } z < 0 \\ a''e^{i\mathbf{k}''\cdot\mathbf{r}} & \text{if } z > d \end{cases} \tag{A.29}$$

for the *Bragg or reflection geometry.*
The rigorous boundary conditions would require that both $\psi(\mathbf{r})$ and $\nabla\psi(\mathbf{r})$ be continuous at the crystal surface, but since we neglect reflection at boundary, the condition on $\nabla\psi(\mathbf{r})$ can be neglected and the continuity of $\psi(\mathbf{r})$ at $z = 0$ and $z = d$ gives:

$$\begin{aligned} \mathbf{k}' = \mathbf{k} - \mathbf{K}_h - \xi\frac{\beta}{\alpha}\frac{k^2}{2k_z}\hat{\mathbf{z}} \\ \mathbf{k}'' = \mathbf{k} \end{aligned} \tag{A.30}$$

and the amplitudes for the Laue case are:

$$\begin{aligned} A_+ &= -\frac{X_-}{X_+ - X_-}a \\ A_- &= \frac{X_+}{X_+ - X_-}a \\ a' &= -X_+X_-\frac{Y_+ - Y_-}{X_+ - X_-}ae^{i\xi\frac{\beta}{\alpha}\frac{k^2}{2k_z}d} \\ a'' &= \frac{X_+Y_- - X_-Y_+}{X_+ - X_-}a \end{aligned} \tag{A.31}$$

In the Bragg geometry we have:

$$\begin{aligned} A_+ &= -\frac{X_-Y_-}{X_+Y_+ - X_-Y_-}a \\ A_- &= \frac{X_+Y_+}{X_+Y_+ - X_-Y_-}a \\ a' &= X_+X_-\frac{Y_+ - Y_-}{X_+Y_+ - X_-Y_-}a \\ a'' &= Y_+Y_-\frac{X_+ - X_-}{X_+Y_+ - X_-Y_-}a \end{aligned} \tag{A.32}$$

with $Y_\pm = e^{-i\frac{k^2}{2k_z}D_{0\pm}d}$.
In both Laue and Bragg case the reflectivity and the transmissivity are given by:

$$R = |\alpha||\frac{a'}{a}|^2 \tag{A.33}$$

$$T = |\frac{a''}{a}|^2 \tag{A.34}$$

where $|\alpha| = \frac{sin\phi'}{sin\phi}$ is the asymmetry factor which depends on the incoming and outcoming angles ϕ and ϕ'. The explicit form of the solutions is:

$$R_{Laue} = |\alpha||X_+X_-\frac{Y_+ - Y_-}{X_+ - X_-}|^2 \tag{A.35}$$

$$T_{Laue} = |\frac{X_+Y_- - X_-Y_+}{X_+ - X_-}|^2 \tag{A.36}$$

$$R_{Bragg} = |\alpha||X_+X_-\frac{Y_+ - Y_-}{X_+Y_+ - X_-Y_-}|^2 \tag{A.37}$$

$$T_{Bragg} = |Y_+Y_-\frac{X_+ - X_-}{X_+Y_+ - X_-Y_-}|^2 \tag{A.38}$$

Case of zero absorption. In this case b is real and $F^*_{hkl} = F_{\bar{h}\bar{k}\bar{l}}$, then the quantities α, β, γ and δ are real. From Eqs. (A.35) it follows that:

$$R + T = 1 \tag{A.39}$$

$$R\left(x,y\right)_{Laue} = \frac{\sin^2\left(x\sqrt{y^2+1}\right)}{y^2+1} \tag{A.40}$$

$$R\left(x,y\right)_{Bragg} = \begin{cases} \frac{\sinh^2\left(x\sqrt{1-y^2}\right)}{1-y^2+\sinh^2\left(x\sqrt{1-y^2}\right)} & \text{if } y^2 < 1 \\ \frac{\sin^2\left(x\sqrt{y^2-1}\right)}{y^2-1+\sin^2\left(x\sqrt{y^2-1}\right)} & \text{if } y^2 > 1 \end{cases} \tag{A.41}$$

where $y^2 = \frac{\gamma^2}{|\delta|}$ and $x^2 = \left(\frac{\xi k^2 d}{2kk_z}\right)^2 |\delta|$. In the case where we want to calculate the diffraction profile as a function of the crystal angle, we have that y is related to the deviation from the Bragg angle θ_h and x to the ratio between the crystal thickness and the primary extinction depth:

$$y = \frac{\theta - \theta_h}{\chi_h} + \psi_h \tag{A.42}$$

$$x = \frac{\pi d}{t_h}$$

In symmetric geometry we have:

$$\psi_h = \begin{cases} 0 & \text{Laue case} \\ \pm|\tilde{F}_h|^{-1} & \text{Bragg case} \end{cases} \tag{A.43}$$

$$t_h = \frac{\pi V_0}{\lambda|F_h|}\sqrt{\sin\phi\sin\phi'} \tag{A.44}$$

$$\chi_h = \frac{\lambda^2|F_h|}{\pi V_0 \sin 2\theta_h}\sqrt{\frac{\sin\phi'}{\sin\phi}}$$

For both Laue and Bragg geometry the reflectivity is an even function of y, but only in the Bragg symmetric geometry it also is a symmetric function of $(\theta - \theta_h)$. In all other cases the rocking curve is not symmetric about the Bragg angle because $\psi_h \neq 0$.
Thin crystals. If the crystal thickness is much smaller than the primary extinction depth, i.e. if $d \ll t_h$, then the range of y values for which reflectivity is non zero is $y \gg 1$ and we can neglect the ψ_h contribution in y and write, for both the Laue and Bragg cases:

$$R(x,y) = \left(\frac{\sin xy}{y}\right)^2 \tag{A.45}$$

Thick crystals. If the crystal is thick, i.e. $d \gg t_h$, the reflectivity is non zero in a small interval $|y| \leq 1$, or $|\theta - \theta_h| \leq \chi_h \sim 10^{-6}$ rad. $R(x,y)$ has a very narrow peak and oscillates very rapidly as a function of y. By performing averages on these oscillations, one can retrieve what would be the measured reflectivity profile of a perfect crystal. The result is that for $x \gg 1$, in the Bragg geometry, the reflectivity is equal to 1 for $|y| \leq 1$. This peak width is called the *Darwin width*. In the Laue case the reflectivity has a Lorentzian shape with a peak equal to 0.5.

Bibliography

[1] http://www.ill.fr/pages/menu_g/docs/millennium_programme.pdf

[2] M. Sánchez del Río and R.J. Dejus, "XOP: Recent developments", *SPIE proceedings* **3448**, pp. 340-345, 1998.

[3] L. Alianelli, M. Sánchez del Río, R. Felici *et al.* "XOP for neutrons", *In preparation.*

[4] J.W.M. Du Mond "Theory of the use of more than two successive x-ray crystal reflections to obtain increased resolving power." *Phys. Rev.* **52**, pp. 872-883, 1937.

[5] J.R.D. Copley "The joy of acceptance diagrams" *J. Neutron Res.* **1**, pp. 21-36, 1993.

[6] M. Popovici, A. Stoica and I. Ionita "Optics of curved-crystals neutron spectrometers. I. Three axis sprectrometers." *J. Appl. Cryst.* **20**, pp. 90-101, 1987.

[7] M.J. Cooper and R. Nathans "The resolution function in neutron diffractometry. I. The resolution function of a neutron diffractometer and its application to phonon measurements." *Acta Cryst.* **23**, pp. 357-367, 1967.

[8] B. Dorner "The normalization of the resolution function for inelastic neutron scattering and its applications." *Acta Cryst.* **28**, pp. 319-327, 1972.

[9] M. Sánchez del Río, S. Bernstorff, A. Savoia and F. Cerrina "A conceptual model for ray tracing calculations with mosaic crystals" *Rev. Sci. Instrum.* **63(1)**, pp. 932-935, 1992.

[10] http://www.hmi.de/projects/ess/vitess/

[11] P.A. Seeger and L.L. Daemen, "Mosaic crystal algorithm for Monte Carlo", *Physica A*, 2002, in press.

[12] J.R. Schneider, "Interpretation of rocking curves measured by γ-ray diffractometry", *J. Appl. Cryst.* **7**, pp. 547-554, 1974.

[13] A.K. Freund and J.B. Forsyth, "Materials problems in neutron devices", *Treatise on materials and technology* **Vol. 15**, pp. 471-488, 1979.

[14] C. May, P. Klimanek and A. Magerl, "Plastic bending of thin berillium blades for neutron monochromator", *Nucl. Instr. and Meth.* **A 357**, pp. 511-518, 1995.

[15] M. Popovici and W.B. Yelon, "Focusing monochromators for neutron diffraction", *J. Neutron Res.* **3**, pp. 1-25, 1995.

[16] J. Kulda and J. Saroun, "Elastically bent silicon monochromator and analyzer on a TAS instrument", *Nucl. Instr. and Meth.* **A 379**, pp. 155-166, 1996.

[17] http://www.ill.fr/YellowBook/IN13/

[18] J. Mesot, S. Janssen, L. Holitzner and R. Hempelmann, "FOCUS: Time-Of-Flight Spectrometer for Cold Neutron at SINQ", *J. Neutr. Res.* **3**, pp. 293-310, 1996.

[19] http://www.isis.rl.ac.uk/molecularspectroscopy/iris/

[20] M.L. Crow, "Characterization of mica crystals as reflectors for an ultracold neutron doppler converter", *Physica B* **241-243**, pp. 110-112, 1998.

[21] M. Sánchez del Río, A.Ya Faenov, T.A. Pikuz, A. Souvorov and A.K. Freund, "Hard X-ray reflectivity of spherically bent mica crystals", *AIP Conference proceedings* **521**, pp. 287-292, 2000.

[22] J. Saroun and J. Kulda, "RESTRAX - a program for TAS resolution calculation and scan profile simulation", *Physica B: Condensed Matter* **234-236**, pp. 1102-1104, 1997.

[23] P.A. Seeger, L.L. Daemen, T.G. Thelliez and R.P. Hjelm, "Neutron instrument simulations in the next millennium", *Physica B: Condensed Matter* **283**, pp. 433-435, 2000.

[24] http://strider.lansce.lanl.gov/NISP/Welcome.html

[25] D. Wechsler, G. Zsigmond, F. Streffer, J.A. Stride and F. Mezei, "Monte-Carlo simulations for instrumentation at pulsed and continuous sources", *Physica B: Condensed Matter* **276-278**, pp. 71-71, 2000.

[26] K. Nielsen and K. Lefmann, "Monte Carlo simulations of neutron-scattering instruments using McStas", *Physica B: Condensed Matter* **283**, pp. 426-432, 2000.

[27] http://neutron.risoe.dk/mcstas/

[28] C. Welnak, G.J. Chen and F. Cerrina, "SHADOW: a synchrotron radiation and x-ray optics simulation tool", *Nucl. Instr. and Meth.* **A347**, pp. 344-347, 1994.

[29] http://www.nanotech.wisc.edu/shadow/shadow.html

[30] J.F. Briesmeister, "MCNP – A General Monte Carlo N-Particle Transport Code", *Los Alamos National Laboratory report LA-13709-M*, 2000.

[31] http://www-xdiv.lanl.gov/XCI/PROJECTS/MCNP/

[32] P.A. Seeger and L.L. Daemen, "Numerical solution of Bloch's equation for neutron spin precession", *Nucl. Instr. and Meth.* **A457**, pp. 338-346, 2001.

[33] W.H. Bragg, "The intensity of reflection of X-rays by crystals", *Phil. Mag.* **27**, pp. 881, 1914.

[34] S.W. Lovesey, "Theory of neutron scattering from condensed matter", *Clarendon Press, Oxford*, 1984.

[35] V.F. Sears, "Neutron Optics", *Oxford University Press*, 1989.

[36] V.F. Sears, "Neutron Scattering Length and Cross Section", *Neutron News* **3**,pp. 29-37, 1992.

[37] W.H. Zachariasen, "Theory of X-ray Diffraction in Crystals", *Dover, New York*, 1945.

[38] B.W. Batterman and H. Cole, "Dynamical diffraction of X-rays by perfect crystals", *Rev. Mod. Phys.* **36**, pp. 681-717, 1964.

[39] H. Cole, F.W. Chambers and H.M. Dunn, "Simultaneous Diffraction: Indexing Umweganregung Peaks in Simple Cases", *Acta Cryst.* **15**, pp. 138-144, 1962.

[40] D.A. O'Connor and J. Sownowski, "Parasitic multiple Bragg scattering" *Acta Cryst.* **14**, pp 292-297, 1961.

[41] J.E. White, "X-ray diffraction by elastically deformed crystals", *J. Appl. Phys.* **21**, pp. 855-859, 1950.

[42] H. Maier-Leibnitz, "Einige Vorschläge für die Verwndung von Zusammengesetzten Monochroamtorkristallen für Neutronenbeugungs und Streumessungen", *Ann. Acad. Sci. Fenncae, Phys. VI* **267**, pp. 2-17, 1967.

[43] B. Alefeld, "Ein perfekter Kristall mit Temperaturgradient als Neutronenmonochromator", *Z. Physik* **228**, pp. 454-464, 1969.

[44] G.E. Bacon and R.D. Lowde, "Secondary Extinction and Neutron Crystallography", *Acta Cryst.* **1**, pp. 303-314, 1948.

[45] V.F. Sears, "Bragg Reflection in Mosaic Crystals. I. General solution of the Darwin Equations", *Acta Cryst.* **A53**, pp. 35-45, 1997.

[46] A.K. Freund, A. Munkholm and S. Brennan, "X-Ray Diffraction Properties of Highly Oriented Pyrolitic Graphite", *SPIE proceedings* **2856**, pp. 68-79, 1996.

[47] A. Freund, P. Guinet, J. Mareschal, F. Rustichelli and F. Vanoni, "Cristaux à gradient de maille", *J. of Crystal Growth* **13/14**, pp. 725-730, 1972.

[48] F. Rustichelli, "Study of a composite neutron monochromator system consisting of crystals with a gradient of the lattice spacing", *Nucl. Instr. and Meth.* **83**, pp. 124-130, 1970.

[49] A. Magerl, "Towards still better monochromators", *Physica B* **213-214**, pp. 917-921, 1995.

[50] A. Erko, I. Packe, W. Gudat, N. Abrosimov and A. Firsov, "A crystal monochromator based on graded SiGe crystals", *Nucl. Instr. and Meth. A* **467-468**, pp. 623-626, 2001.

[51] N.W. Abrosimov, "Single crystal growth of $Si_{1-x}Ge_x$ by the Czochralski technique", *J. Crystal Growth* **166**, pp. 657-662, 1996.

[52] D. Taupin, "Théorie dynamique de la diffraction des rayons X par les cristaux deformés", *Bull. Soc. Fr. Mineral. Cristallogr.* **87**, pp. 469-511, 1964.

[53] S. Takagi, "A dynamical theory of diffraction for a distorted crystal", *J. Phys. Soc. Jap.* **26**, pp. 1239-1253, 1969.

[54] B. Klar and F. Rustichelli, "Dynamical neutron diffraction by ideally curved crystals", *Il nuovo Cimento* **Vol. 13, N. 2**, pp. 249-271, 1973.

[55] J. Gronkowsky, "Propagation of x-rays in distorted crystals under dynamical diffraction", *Phys. Rep.* **206**, pp. 1-41, 1991.

[56] Hua-Chen Hu, "A layer-coupling model for neutron reflectivity and transmissivity calculation in deformed mosaic crystals", *J. Appl. Cryst.* **25**, pp. 731-736, 1992.

[57] G. Hölzer, O. Wehrhan and E. Förster, "Characterization of flat and bent crystals for X-ray spectroscopy and imaging.", *Crys. Res. Technol.* **33(4)**, pp. 555-567, 1998.

[58] G. Albertini, A. Boeuf, G. Cesini, S. Mazkedian, S. Melone and F. Rustichelli, "A simple model for dynamical neutron diffraction by deformed crystals", *Acta Cryst.* **A 32**, pp. 863-868, 1976.

[59] G. Placzek, "The scattering of Neutron by Systems of Heavy Nuclei", *Phys. Rev.* **86**, pp. 377-388, 1952.

[60] C.J. Carlile, M.A. Adams, P.S.N. Krishna, M. Prager, K. Shibata, P. Westerhuijs, "Less background, better contrast by cooling analyser crystals", *Nucl. Instr. and Meth. A* **338**, pp. 78-82, 1994.

[61] N. Wakabayashi, R.M. Nicklow, S. Katano, Y. Ishii, H.R. Child, H.G. Smith and J.A. Fernandez-Baca, "Calculation of thermal diffuse scattering", *Physica B* **241-243**, pp. 320-322, 1998.

[62] A.K. Freund, "Cross-sections of materials used as neutron monochromators and filters", *Nucl. Instr. and Meth.* **213**, pp. 495-501, 1983.

[63] W. Marshall and S.W. Lovesey, "Theory of thermal neutron scattering", *Clarendon Press, Oxford*, 1971.

[64] V.F. Turchin , "Slow neutrons", *Israel Program for Scientific Translations*, 1965.

[65] K. Binder, "Total Coherent Cross Sections for the Scattering of Neutrons from Crystals", *Phys. Stat. Sol.* **41**, pp. 767-779, 1970.

[66] J. Tickner, "Particle transport in inhomogeneous media" in *Advanced Monte Carlo for Radiation Physics, Particle Transport Simulation and Applications, Proc. of the Monte Carlo 2000 Conference, Lisbon* , *Springer-Verlag*, 2001.

[67] G.E. Ice and C.J. Sparks, "Mosaic crystals x-ray spectrometer to resolve inelastic background from anomalous scattering experiments", *Nucl. Instr. and Meth. A* **291**, pp. 110-116, 1990.

[68] M. Sánchez del Río, M. Gambaccini, G. Pareschi, A. Taibi, A. Tuffanelli, and A. Freund, "Focusing properties of mosaic crystals", *SPIE proceedings* **3448**, pp. 345-345, 1998.

[69] A.D. Stoica and M. Popovici, "On the neutron reflectivity of bent perfect crystals", *J. Appl. Cryst.* **22**, pp. 448-454, 1989.

[70] Hua-Chen Hu, "Neutron diffraction in flat and bent mosaic crystals for asymmetric geometry", *J. Appl. Cryst.* **26**, pp. 251-257, 1993.

[71] Th. Pirling and S. Rowe, "A strain imager at the ILL", *ILL Annual Report*, 2000.

[72] J. Saroun and Th. Pirling, "Optimisation of focusing monochromator for the neutron strain-scanner at a supermirror guide", *ILL internal report.*

[73] G. Bruno, "Comparison between a Ge and a Cu monochromator for the Strain Imager", *ILL internal report.*

[74] G. Bruno, "Cut of the Ge monochromator of the Strain Imager", *ILL internal report.*

[75] Th. Pirling, "Specifications of a horizontal fixed curvature mosaic Cu monochromator for the Strain Imager", *ILL internal report.*

[76] F.N. Chukhovskii and M. Krisch, "The lens equation for Bragg diffraction optics. The general case of asymmetrical reflection", *J. Appl. Cryst.* **25**, pp. 211-213, 1992.

[77] R.H. Scherm and E. Kruger, "Bragg optics - focusing in real and k-space", *Nucl. Instr. and Meth.* **A 338**, pp. 1-8, 1994.

[78] M. Sánchez del Río, "Ray tracing simulations for crystal optics", *SPIE proceedings* **3448**, pp. 230-245, 1998.

[79] L.D. Cussen, "On the resolution of neutron scattering instruments", *J. Appl. Cryst.* **33**, pp. 1399-1404, 2000.

[80] E. Farhi, *Private communication*, 2002.

[81] Th. Pirling, "Neutron strain scanning at interfaces: an optimised beam optics to reduce surface effects", *Mat. Sci. Forum*, **347-349**, pp. 107-112, 2000.

[82] B. Hamelin, "Synthetic mosaic copper monochromators", *ILL annual report*, 1996.

[83] B. Dorner, "Measurements of absolute reflectivities of mosaic crystals and their wavelength dependence", *J. Appl. Cryst.* **4**, pp. 185-190, 1971.

[84] http://www.ill.fr/YellowBook/IN1/

[85] http://www.esrf.fr/exp_facilities/ID15A/handbook/handbook.html

[86] http://www.esrf.fr/exp_facilities/BM5/main/main.php

[87] L. Alianelli, M. Sánchez del Río, A. Ivanov, B. Hamelin, R. Felici, I.Anderson, "Reflectivity test at low temperature on a mosaic copper crystal", *ILL Experimental Report*, TEST $N°464$, 2000.

[88] L. Alianelli, M. Sánchez del Río and R. Felici, "Study of models for ray-tracing simulations of thermal neutron monochromators", *SPIE proceedings* **4509**, pp. 135-144, 2001.

[89] P. Bastie and B. Hamelin, "La méthode de Laue refocalisée à haute énergie: une technique d'étude en volume des monocristaux ", *Journal de Physique IV* **6**, pp. C4/13-C4/21, 1996.

[90] P. Courtois, "Characterization of Heusler crystals for polarized neutron monochromators", *Physica B* **267-268**, pp. 363-366, 1999.

[91] P. Courtois, *Private communication*, 2002.

[92] A. Freund, "A neutron monochromator system consisting of deformed crystals with anisotropic mosaic structure", *Nucl. Instr. and Meth.* **124**, pp. 93-99, 1975.

[93] J.D. Axe, S. Cheung, D.E. Cox, L. Passell, T. Vogt, and S. Bar-Ziv, "Composite germanium monochromators for high resolution neutron powder diffraction applications", *J. Neutr. Res.* **2**, pp. 85-94, 1994.

[94] T. Vogt, L. Passell, S. Cheung and J.D. Axe, "Using wafers stacks as neutron monochromators", *Nucl. Instr. and Meth. A* **338**, pp. 71-77, 1994.

[95] J. Schefer, M. Medarde, S. Fischer, R. Thut, M. Koch, P. Fischer, U. Staub, M. Horisberger, G. Böttger and A. Dönni, "Sputtering method for improving neutron composite germanium monochromators", *Nucl. Instr. and Meth. A* **372**, pp. 229-232, 1996.

[96] A. Tuffanelli, M. Sánchez del Río, G. Pareschi, M. Gambaccini, A. Taibi, A. Fantini and M. Ohler, "A comparative characterization of Highly Oriented Pyrolitic Graphite by means of diffraction topography", *SPIE proceedings* **3773**, pp. 192-198, 1999.